coatings

Special Issue Reprint

Novel Coatings for Corrosion Protection

Edited by
Qiang Wei and Chaoqun Xia

mdpi.com/journal/coatings

MDPI

Novel Coatings for Corrosion Protection

Novel Coatings for Corrosion Protection

Guest Editors

Qiang Wei
Chaoqun Xia

MDPI
Basel • Beijing • Wuhan • Barcelona • Belgrade • Novi Sad • Cluj • Manchester

Guest Editors

Qiang Wei	Chaoqun Xia
School of Mechanical Engineering	School of Materials Science and Engineering
Hebei University of Technology	Hebei University of Technology
Tianjin	Tianjin
China	China

Editorial Office
MDPI AG
Grosspeteranlage 5
4052 Basel, Switzerland

This is a reprint of the Special Issue, published open access by the journal *Coatings* (ISSN 2079-6412), freely accessible at: https://www.mdpi.com/journal/coatings/special_issues/novel_corrosion_protection.

For citation purposes, cite each article independently as indicated on the article page online and as indicated below:

Lastname, A.A.; Lastname, B.B. Article Title. *Journal Name* **Year**, *Volume Number*, Page Range.

ISBN 978-3-7258-4441-8 (Hbk)
ISBN 978-3-7258-4442-5 (PDF)
https://doi.org/10.3390/books978-3-7258-4442-5

Contents

About the Editors . . . . **vii**

Preface . . . . **ix**

Jie Ma, Qiang Wei, Hongbo Fan, Zhengpan Qi and Ning Hu
Mechanical Properties Evolution and Damage Mechanism of Kevlar Fiber under Ozone Exposure in Near-Space Simulation
Reprinted from: *Coatings* **2022**, *12*, 584, https://doi.org/10.3390/coatings12050584 . . . . **1**

Leoš Doskočil, Pavlína Šomanová, Jiří Másilko, Martin Buchtík, Michaela Hasoňová, Lukáš Kalina and Jaromír Wasserbauer
Characterization of Prepared Superhydrophobic Surfaces on AZ31 and AZ91 Alloys Etched with $ZnCl_2$ and $SnCl_2$
Reprinted from: *Coatings* **2022**, *12*, 1414, https://doi.org/10.3390/coatings12101414 . . . . **13**

Qingqing Hu, Aijuan Lv, Yukang Ma, Yan Wang, Haoyi Zhang, Xin Mi and Qiang Xiao
In Situ Polymerization to Boron Nitride-Fluorinated Poly Methacrylate Composites as Thin but Robust Anti-Corrosion Coatings
Reprinted from: *Coatings* **2021**, *11*, 1518, https://doi.org/10.3390/coatings11121518 . . . . **33**

Jianxing Yu, Xin Liu, Yang Yu, Haoda Li, Pengfei Liu, Ruoke Sun, et al.
Numerical Analysis of High-Velocity Oxygen Fuel Thermal-Spray Process for Fe-Based Amorphous Coatings
Reprinted from: *Coatings* **2021**, *11*, 1533, https://doi.org/10.3390/coatings11121533 . . . . **47**

Hongyun Deng, Kuixue Xu, Shuguang Liu, Chaofeng Zhang, Xiongwei Zhu, Haoran Zhou, et al.
Impact of Engineering Surface Treatment on SurfaceProperties of Biomedical TC4 Alloys under a SimulatedHuman Environment
Reprinted from: *Coatings* **2022**, *12*, 157, https://doi.org/10.3390/coatings12020157 . . . . **64**

Peiyi Tong, Qiang Wei, Ning Hu and Xueguang Chen
Asynchronous Synergistic Damage Effect of Atomic Oxygen and Space Micro Debris on Kapton Film
Reprinted from: *Coatings* **2022**, *12*, 179, https://doi.org/10.3390/coatings12020179 . . . . **79**

Hugo Mora-Sanchez, Florian Pixner, Ricardo Buzolin, Marta Mohedano, Raúl Arrabal, Fernando Warchomicka and Endzhe Matykina
Combination of Electron Beam Surface Structuring and Plasma Electrolytic Oxidation for Advanced Surface Modification of Ti6Al4V Alloy
Reprinted from: *Coatings* **2022**, *12*, 1573, https://doi.org/10.3390/coatings12101573 . . . . **93**

Xiaolin Zhang, Yi Ding, Honglu Ma, Ruibin Zhao, Liangquan Wang and Fanyong Zhang
Microstructure and Mechanical Properties of Co-Deposited Ti-Ni Films Prepared by Magnetron Sputtering
Reprinted from: *Coatings* **2023**, *13*, 524, https://doi.org/10.3390/coatings13030524 . . . . **116**

Pengfei Ma, Jiaoli Li, Ying Zhuo, Pu Jiao and Genda Chen
Coating Condition Detection and Assessment on the Steel Girder of a Bridge through Hyperspectral Imaging
Reprinted from: *Coatings* **2023**, *13*, 1008, https://doi.org/10.3390/coatings13061008 . . . . **128**

Zunqi Xiao, Zhizhong Jiang, Lin Luo, Yi Wan, Aixue Liu, Bin Zhang, et al.
Protection of 316L Steel Against LBE Corrosion by a $CaO\text{-}MgO\text{-}Al_2O_3\text{-}SiO_2$ Glass–Ceramic Coating
Reprinted from: *Coatings* **2024**, *14*, 1371, https://doi.org/10.3390/coatings14111371 . . . . **141**

About the Editors

Qiang Wei

Qiang Wei is a professor and Ph.D./Master's Supervisor at the Department of Intelligent Manufacturing Engineering, Hebei University of Technology, where he also serves as the department director. Additionally, he is the deputy director of the Key Laboratory of Cross-scale Intelligent Equipment Technology of Hebei Province. He obtained his Ph.D. in Materials Science from Harbin Institute of Technology in July 2005. From August 2005 to June 2018, he worked at Tianjin University, holding positions such as Lecturer, Associate Professor, Master's Supervisor, and Doctoral Supervisor. In July 2018, he joined the School of Mechanical Engineering at Hebei University of Technology. He concurrently holds multiple academic roles, including member of the Space Materials Professional Committee of the Chinese Society of Space Science, Expert Reviewer for the China Association for Science and Technology's science and technology talent awards, Vice President of the Hebei Aerospace Society, and Editorial Board Member of the journal *Spacecraft Environmental Engineering*. Over the years, he has been deeply involved in research on spacecraft environmental engineering, focusing on the digitalization and intelligentization of spacecraft service evaluation and its low-cost commercialization. He has received two second prizes of the Tianjin Science and Technology Progress Award and one China Invention and Innovation Award. As the technical lead, in 2020, he was responsible for the development, launch, and operation and maintenance of the "Yuan Guang" scientific experiment satellite of Hebei University of Technology.

Chaoqun Xia

Chaoqun Xia is currently a professor and Ph.D./Master's Supervisor at the School of Materials Science and Engineering, Hebei University of Technology. Born in 1990, he obtained his Ph.D. in Metallic Materials Engineering from Yanshan University. His research primarily focuses on high-performance lightweight metallic materials, including the development of and investigation of the mechanisms of novel high-performance Zr and Ti alloys, the preparation and application of bulk amorphous/nanocrystalline alloys, and the corrosion behavior and protection of metallic materials.

Prof. Xia has led two national-level projects and six provincial/ministerial-level projects. He has authored over 70 high-impact papers published in prestigious journals such as *Corrosion Science*, *Journal of Materials Science and Technology*, and *Materials Science and Engineering: A*. His research contributions have been acknowledged with several awards, including the First Prize of the Hebei Provincial Science and Technology Progress Award, the Third Prize of the Hebei Provincial Science and Technology Progress Award, and the Hebei Excellent Doctoral Dissertation Award.

Beyond his academic endeavors, Prof. Xia serves as a Youth Editor for *Rare Metals and Iron and Steel Research* and a Young Scientist Committee Member for *Advanced Powder Materials*, as well as holding additional academic positions, such as Committee Member of the Heat Treatment Professional Committee of the Hebei Mechanical Engineering Society. He is also an active member of several professional societies, including the Chinese Materials Research Society, the Chinese Society for Corrosion and Protection, and the Chinese Nonferrous Metals Society. Furthermore, Prof. Xia has been invited to serve as a reviewer for a number of leading international journals, including *Corrosion Science*, *Materials and Design*, *Journal of Alloys and Compounds*, and *Materials Letters*.

Preface

Welcome to this Special Issue of *Coatings*, which is devoted to presenting the latest advancements and applications in surface modification and protective coatings. This carefully curated collection of 10 articles examines a wide range of materials, including metals, alloys, polymers, and composites. Our objective is to provide an in-depth overview of cutting-edge techniques and materials that are being developed to address key challenges in corrosion resistance, wear reduction, and environmental adaptability.

Contributions from distinguished researchers in the field cover topics ranging from high-velocity oxygen fuel (HVOF) spraying and electron-beam surface structuring to the utilization of innovative coating materials, such as boron nitride-fluorinated poly methacrylate composites. The articles explore applications across aerospace engineering, biomedical implants, and other domains, emphasizing groundbreaking solutions that enhance material properties and ensure reliability in demanding and challenging environments.

We extend our gratitude to all the authors who have contributed their expertise and research findings, making this Special Issue an invaluable resource for scientists, engineers, and industry professionals. We trust that this compilation will stimulate further research and development, advancing the frontiers of innovation in surface modification and protective coatings.

Qiang Wei and Chaoqun Xia
Guest Editors

coatings

Article

Mechanical Properties Evolution and Damage Mechanism of Kevlar Fiber under Ozone Exposure in Near-Space Simulation

Jie Ma [1], Qiang Wei [2,3,*], Hongbo Fan [4], Zhengpan Qi [2] and Ning Hu [2,3,*]

[1] School of Materials Science and Engineering, Hebei University of Technology, Tianjin 300401, China; majie_1230@126.com
[2] School of Mechanical Engineering, Hebei University of Technology, Tianjin 300130, China; zhengpan_qi@hebut.edu.cn
[3] State Key Laboratory of Reliability and Intelligence Electrical Equipment, Hebei University of Technology, Tianjin 300401, China
[4] Department of Vehicle and Electrical Engineering, Army Engineering University of PLA, Shijiazhuang 050003, China; ffhhbboo@163.com
* Correspondence: weiqiang@hebut.edu.cn (Q.W.); ninghu@hebut.edu.cn (N.H.)

Abstract: The stratospheric airship, a long-term floating vehicle in near-space, has become a new hotspot in aerospace exploration. The airship's envelope material is vulnerable to ozone exposure in near-space and degrades. This paper used typical Kevlar fiber as the research material for an ozone exposure experiment in a near-space simulated environment. The results showed that the elongation of the Kevlar fiber decreased and the elastic modulus increased after ozone exposure. The tensile strength of fiber decreased gradually with an increase in ozone concentration and exposure time. When ozone concentration increased from 0 pphm to 1000 pphm, the tensile strength of fiber decreased from 2397 MPa to 2059 MPa. With increasing ozone exposure time from 0 h to 1000 h under ozone concentration 1000 pphm, the tensile strength of fiber decreased from 2332 MPa to 1954 MPa. The hydrogen bonds and partial amide groups in the fiber structure were damaged, and the surface chemical functional groups of the Kevlar fiber were reassembled under ozone exposure. Low molecular weight oxidation products, including -COO- structures, formed on the surface of the Kevlar fiber. This work explores the ground simulation method in a near-space environment and enriches the service data of airship envelope materials.

Keywords: near-space; ozone; kevlar fiber; mechanical properties; damage mechanism

1. Introduction

Near-space, 20–100 km above sea level, is the space where aviation and aerospace converge and has gradually become more utilized and developed in the fields such as science, technology, and military applications [1–3]. Near space vehicle has many advantages, such as a highly effective cost ratio, good maneuverability, and low technical difficulty of payload updating and maintenance for both high dynamic and low dynamic aircraft. At present, various approaches for developing near-space vehicles have been proposed. A stratospheric airship is an important fixed-point platform that, with geosynchronous satellites, can be used as an effective supplement for satellites and aircraft. It has great advantages in military reconnaissance, space early warning, communication relay, and space exploration [4].

The efficiency of the airship, such as buoyancy height, duration of flight, payload, service life, etc., is directly affected by the mechanical properties of the envelope materials that are the main structural materials of the airship [5–7]. A high-performance envelope involves a variety of special functional materials such as high specific strength fabric, high barrier materials, adhesives, anti-aging agents, etc. In recent years, with the advance in fiber manufacturing technology, Kevlar and other fibers with excellent mechanical properties and good heat resistance have emerged [8–13].

Kevlar fiber has excellent properties such as high strength, high modulus, and high temperature resistance. Due to these characteristics, it can be used as the main structural reinforcement layer of airship envelope materials to enhance the mechanical strength of envelope materials [14]. In addition to its applications in the aerospace field, Kevlar fiber is also widely used in tires, bulletproof devices, sports equipment, high-strength rope, and other products [15,16]. With the appearance of Kevlar fiber and other new airship envelope materials, the environmental effect and service reliability of envelope materials have become one of the key scientific and technological issues in the long-term service of airships in the face of a complex and changeable near-space environment. Near-space spans multiple atmospheric layers, including the ozone and ionosphere, and encounters solar ultraviolet radiation, high temperature, particle radiation, aero-thermal and re-entry plasma, meteoroids, and other environments [17]. Envelope materials are vulnerable to ozone in the near-space atmosphere and deteriorate in quality, as shown in Figure 1 [18]. The ozone content can vary from 0.4 mg/m^3 at the maximum to 0.2 mg/m^3 at the minimum level. Therefore, the environmental effect of ozone on the airship envelope material in near-space should not be ignored [19,20].

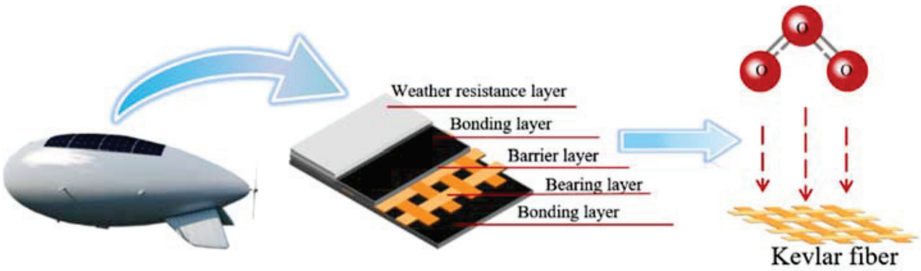

Figure 1. Schematic diagram of Kevlar fiber of airship envelope eroded by ozone in near-space.

Similar to the space environment, the environmental conditions in near-space are especially extreme, with environmental conditions that do not exist on the ground. In order to systematically study the environmental adaptability of vehicle materials in near-space, ground simulation studies need to be carried out. The traditional natural environment test method has a long test cycle, which is not well equipped to meet the needs of equipment development, testing, and evaluation. Although the laboratory simulated environment test method has the advantage of a short test cycle, it cannot reflect the failure law in the real environment [21–23].

The accelerated test method for the ground simulated environment accelerates the deterioration of equipment or material properties by appropriately strengthening some environmental factors under natural environmental conditions. It combines the advantages of the natural environment test and laboratory simulation environment test and has the favorable characteristics of reality, reliability, and short test period [24,25]. Thus, establishing a reasonable ground acceleration test method is an important foundation for evaluating the environmental adaptability of near-space vehicles in the exploration stage.

This study used typical high-performance Kevlar fabrics as envelope research materials for ground-level ozone accelerated test research. The change law of mechanical properties of Kevlar fiber was characterized, and the change mechanism of surface micromorphology and molecular structure was analyzed in an ozone environment. This work will enrich the data of airship envelope materials in a near-space environment and provide a useful reference for ground simulation and life prediction technology in a near-space environment.

2. Materials and Methods

2.1. Materials

The experimental material used in this paper was orange Kevlar fiber (Para-aramid fiber, DuPont, DE, USA). The molecular structure formula of the Kevlar fiber is shown in Figure 2. The fiber contains a benzene ring structure and amide group. The conjugation effect of the benzene ring and amide group leads to greater rigidity of the molecular chain, so Kevlar fiber has excellent mechanical properties [26,27]. Each Kevlar cord used in this paper was braided using three fiber bundles composed of many small fiber monofilaments, as shown in Figure 3.

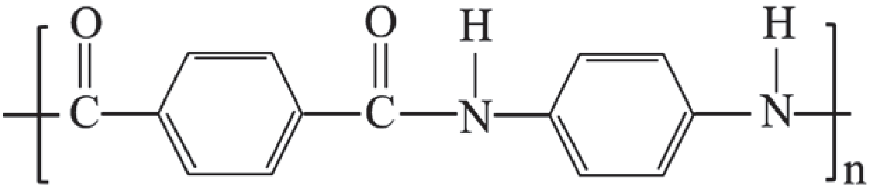

Figure 2. Molecular structure formula of Kevlar fiber.

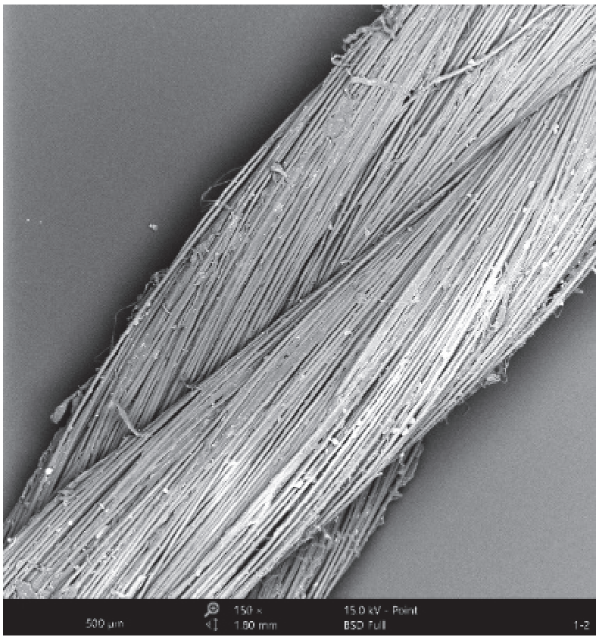

Figure 3. Multi-level structure diagram of Kevlar fiber.

Kevlar monofilament with a diameter of about 12 µm was used as the research object in this experiment. The fiber monofilament selected randomly was fixed on cowhide coordinate paper with acrylic adhesive (TA-868) and paralleled to the long edge of the paper frame. Then, 2 pieces of kraft paper with a length and width of 35 mm were glued to both ends of the cowhide coordinate paper. The preparation process of fiber monofilament and the sample after molding are illustrated in Figure 4.

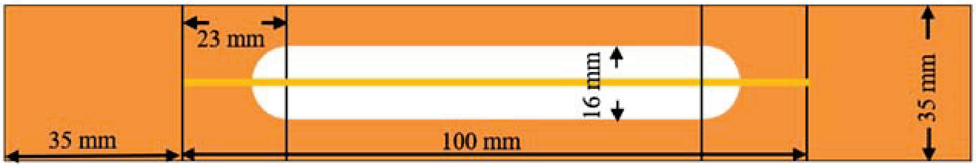

Figure 4. Schematic diagram of fiber monofilament tensile processing and molding sample.

2.2. Testing and Characterization

The mechanical properties of Kevlar fiber monofilament were tested with a universal tensile testing machine (INSTRON 3365, Boston, MA, USA). According to ASTM C 1557-2003 [28], the upper and lower ends of the paper frame were fixed between the two fixtures of the tensile testing machine before the experiment, and the fiber was straightened with 0.4 N force to ensure that the fiber was straight before the test. Then, the fiber was loaded at a speed of 0.01 mm/s, and the tensile test was carried out until the fiber broke. The ultimate load was obtained as the tensile strength of a single filament [29].

The surface morphology of the Kevlar fiber monofilament was observed by ultra-high-resolution thermal field emission scanning electron microscope (JSM-7610F, JEOL, Tokyo, Japan), and its acceleration voltage was 3 kV. Before observation, the sample surface was sprayed with gold (palladium gold alloy with a particle size of about 20 nm was selected). The surface attenuated total reflection FT-IR spectroscopic of the fiber monofilament was characterized by Fourier transform infrared spectrometer (VERTEX80V, Bruker, Billerica, MA, USA). The element types, chemical bonds, and relative contents on the sample surface were identified by X-ray photoelectron spectroscopy (Escalab 250Xi, Thermo Fisher Scientific Inc., Waltham, MA, USA). The excitation source adopted a monochromatic Al target, and the best spatial resolution was 1 μm. The signal was accumulated for 5–10 cycles, and the charge correction was carried out with C 1s at 285.0 eV binding energy as the energy standard.

2.3. Ozone Exposure

The ozone exposure test was carried out using an ozone aging test chamber (GH-150, Future Science and Technology Application Research, Tianjin, China), which can adjust the ozone concentration range from 10 to 1000 pphm. In this test, Kevlar fiber monofilament samples were placed into the ozone aging test chamber for the ozone exposure test at room temperature (25 °C), and the correlation between fiber strength, ozone concentration, and exposure times was investigated. Within 100 h, ozone concentrations were 0, 100, 300, 500, 800, 1000 pphm (equivalent to 0, 2.14, 6.43, 10.71, 17.14, 21.43 mg/m^3 after unit conversion). At 1000 pphm ozone concentration, the exposure time was 0, 100, 300, 500, and 1000 h, respectively. To increase the validity of the test results, 3 samples were selected as a group for each test condition. A set of 3 samples was averaged to determine the final test results.

3. Results and Discussion

3.1. Mechanical Properties Characterization

For ozone concentrations of 0, 100, 300, 500, 800, and 1000 pphm, the Kevlar fiber's stress–strain relationship before and after 100 h exposure tests are shown in Figure 5a. The stress and strain of Kevlar fiber showed a linear relationship, relating to the fact that the molecular structure of Kevlar fiber is composed of rigid molecular chains [30]. After ozone exposure, the elongation of Kevlar fiber decreased, and the elastic modulus increased. The tensile strength of fiber decreased gradually with the increase in ozone concentration. When ozone concentration was 0 pphm, the tensile strength of the fiber was 2397 MPa. However, the tensile strength of the fiber reduced to 2059 MPa, when ozone concentration was 1000 pphm.

For ozone exposure times of 0, 100, 300, 500, and 1000 h, the Kevlar fiber's stress–strain relationship before and after 1000 pphm ozone exposure tests are shown in Figure 5b. By comparing Figure 5a,b, it can be seen that the relationship between mechanical properties and ozone exposure time at a certain concentration was similar to the relationship between mechanical properties and ozone concentration at a certain time. Namely, after the ozone exposure test at a concentration of 1000 pphm for a different time, the elongation of the Kevlar fiber also decreased. The elastic modulus increased, and the tensile strength of fiber decreased gradually with the increase of ozone exposure time. With increasing ozone exposure time from 0 h to 1000 h under ozone concentration 1000 pphm, the tensile strength of fiber decreased from 2332 MPa to 1954 MPa.

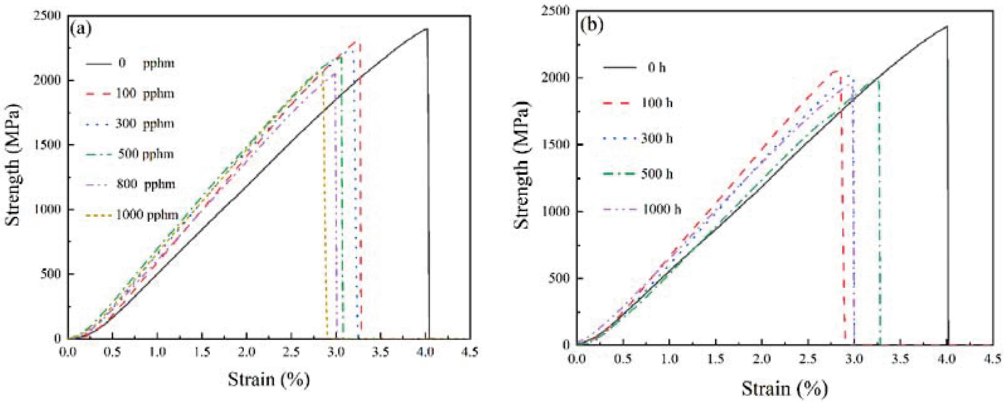

(**a**) (**b**)

Figure 5. Stress–strain relationship of Kevlar fiber in ozone environment: (**a**) When the exposure time of ozone was 100 h, different ozone concentrations, (**b**) When the ozone concentration was 1000 pphm, different ozone exposure times.

The strength of the Kevlar fiber is one of the important indexes of airship envelope material. Figure 6 examines the correlation between the tensile strength of the fiber and ozone concentration and exposure time. It can be seen from the figure that with the increase in ozone concentration (Figure 6a), or the exposure time in the ozone environment (Figure 6b), the strength of the Kevlar fiber had a trend of rapid decrease at first and then gradually gentle. The curves of the relationship between the tensile strength of the fiber, ozone concentration, and exposure time could be fitted as follows:

$$\sigma_{t100} = 1973 + \frac{464}{[1 + (\frac{C}{303})^{0.74}]} \tag{1}$$

$$\sigma_{c1000} = 1895 + \frac{455}{[1 + (\frac{T}{91})^{0.75}]} \tag{2}$$

where σ_{t100} is the strength (MPa) of Kevlar fiber when the ozone exposure time is 100 h; σ_{c1000} is the strength (MPa) of Kevlar fiber when ozone concentration is 1000 pphm; C denotes ozone concentration (pphm), and T represents ozone exposure time (h).

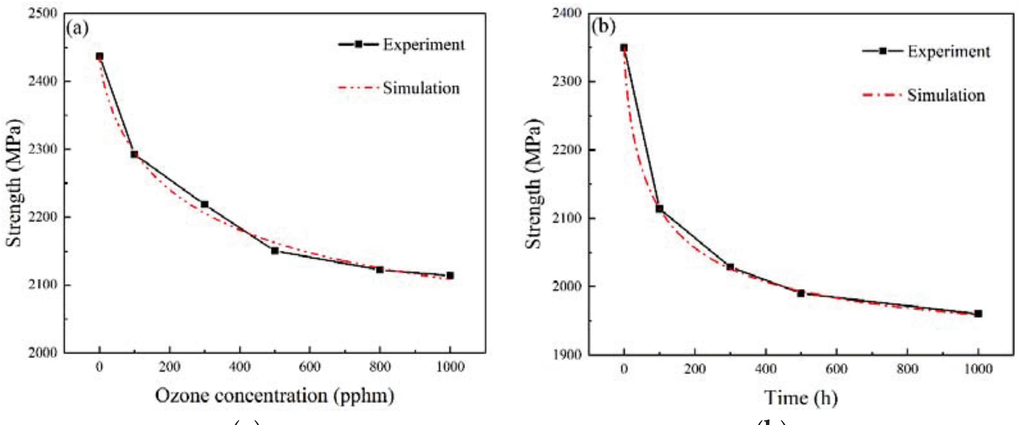

(**a**) (**b**)

Figure 6. Correlation between the tensile strength of the Kevlar fiber and ozone concentration and exposure time: (**a**) Stress and ozone concentration, (**b**) Stress and ozone exposure time.

From Formulas (1) and (2), the strength of Kevlar fiber corresponding to ozone concentration (under the condition of exposure time of 100 h) and ozone exposure time (under the condition of ozone concentration of 1000 pphm) in a certain range could be obtained.

SPSS statistical software (version 26.0) was used to analyze the correlation between ozone concentration, ozone exposure test time, and the tensile strength of Kevlar fibers. The results showed a highly negative correlation between ozone concentration and tensile strength ($\gamma = -0.986$), and there was a significant negative correlation between the time of ozone exposure test and tensile strength ($\gamma = -0.688$). This showed that the test data were within a reasonable error range.

3.2. Morphology Analysis

Macroscopic pictures of the Kevlar fiber surface before and after ozone exposure are shown in Figure 7. Before the ozone exposure tests, the sample surface looked smooth (as shown in Figure 7a). This is mainly because the surface layer of the fiber is composed of rigid molecules with high crystallinity for lots of intermolecular hydrogen bonds [31]. After ozone exposure, the surface morphology of the Kevlar fiber gradually coarsened and even peeled off with the increase in ozone exposure time. After 100 h of ozone exposure, the surface of the fiber formed depression and bulge morphology (as displayed in Figure 7b). As the ozone exposure time was further extended, the degree of surface roughness increased (as shown in Figure 7c,d). When ozone exposure time reached 1000 h, the fiber surface appeared wrinkled and even peeling, as shown in Figure 7e. The variation of fiber surface might be related to the local movement of molecular chains and the reduction in free volume [32].

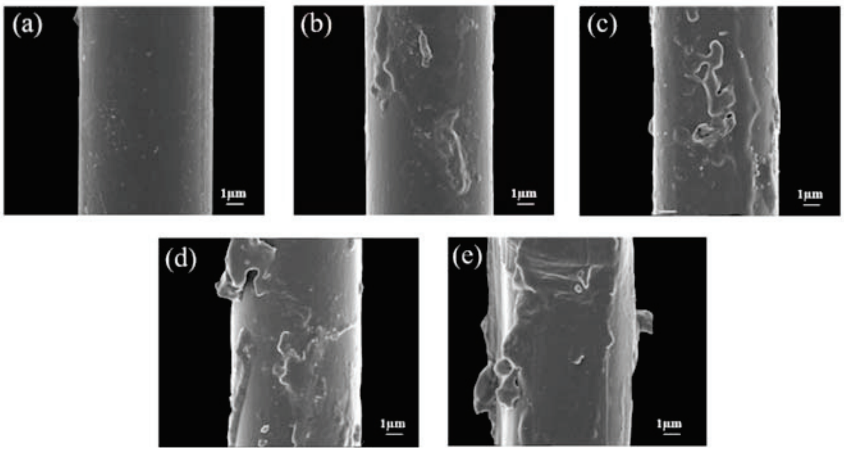

Figure 7. Macroscopic picture of Kevlar fibers before (**a**), and after ozone exposure for 100 h (**b**), 300 h (**c**), 500 h (**d**), 1000 h (**e**).

3.3. Surface Structure Characterization

Figure 8 is the FT-IR spectroscopic of the Kevlar fiber before and after ozone exposure and shows the positions of the absorption peaks of the main functional groups. The FT-IR spectroscopic of the original Kevlar fiber is shown in Figure 8a. The wide peak near 3320 cm^{-1} is the stretching vibration absorption peak of the hydrogen bond formed by the association of the N-H bond and C=O bond in the aramid structure. The vibration absorption peak (amide I band) near 1640 cm^{-1} is the stretching vibration characteristic absorption peak of the aramid amide bond (C=O). The absorption peaks near 1520 cm^{-1} (amide II band) and 1403 cm^{-1} (amide III band) correspond to the cooperative vibration peak of the C-N and N-H bond [33]. The absorption peak near 1315 cm^{-1} (amide III band) expresses the characteristic absorption peak of ph-N ("ph" stands for phenyl group; phenyl is the group left after removing a hydrogen atom from any carbon in benzene molecule.). The absorption peaks near 819 cm^{-1} and 654 cm^{-1} indicate the presence of a benzene ring structure [34,35].

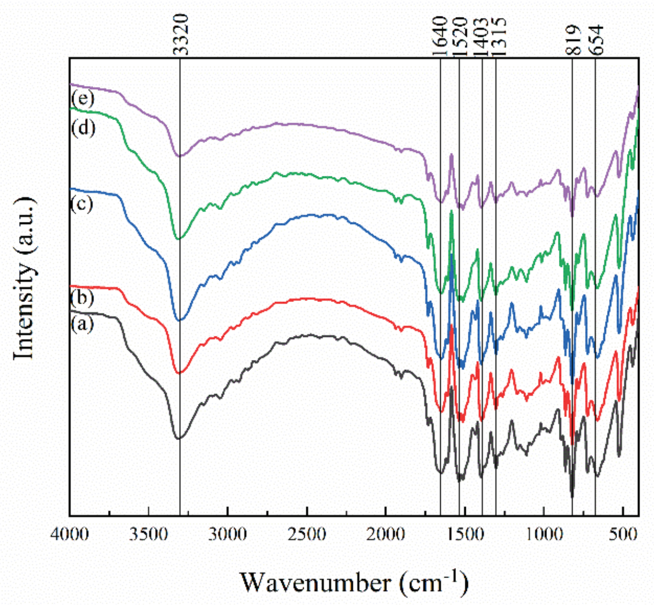

Figure 8. FT-IR spectra of Kevlar fiber before (**a**), and after ozone exposure to atomic oxygen for 100 h (**b**), 300 h (**c**), 500 h (**d**), 1000 h (**e**).

When Kevlar fibers were exposed to ozone tests, as summarized in Figure 8b–e, the absorption peaks mentioned above still existed, but the relative intensity of each vibration absorption peak gradually weakened with ozone exposure time. The intensity ratio of each absorption peak is given in Table 1. The relative intensity ratio of hydrogen bond absorption peak near 3320 cm^{-1} decreased after ozone exposure, while the intensity ratio of amide group absorption peaks near 1315 cm^{-1}, 1403 cm$^{-1,}$ and 1520 cm^{-1} increased after 100 h of ozone exposure. It indicates that after ozone exposure, the hydrogen bond formed by the amide group between the lateral molecular chains was damaged, and the macromolecular main chain binding would further be enhanced. Therefore, the elastic modulus of the fiber increased when the fiber was stretched. This was also consistent with the above test results of the mechanical properties of Kevlar fiber.

Table 1. Intensity ratio of absorption band before and after ozone exposure.

Exposure Time (h)	**Intensity Ratio of Absorption Band (%)**				
	Amide Group				**Hydrogen Bond**
	1315 cm^{-1}	**1403 cm^{-1}**	**1520 cm^{-1}**	**1640 cm^{-1}**	**3320 cm^{-1}**
0	3.78	1.01	1.25	3.34	45.57
100	4.78	6.78	4.25	7.13	10.86
300	4.71	6.38	3.88	6.58	8.93
500	4.80	6.14	3.86	5.90	11.20
1000	4.70	6.17	3.55	5.96	10.10

X-ray photoelectron spectroscopy (XPS) was used to analyze the changes of surface elements and chemical bonds of samples to understand further the damage mechanism of samples exposed to ozone. Figure 9 is XPS full scan spectra of Kevlar fibers before and after ozone exposure. The peaks of photoelectron energy spectra at about 285, 400, and 532 eV are attributed to C, N, and O atoms, respectively [36]. C, N, and O are the main chemical components of the Kevlar fiber surface; their relative chemical composition is shown in Table 2. After exposure to ozone tests, the relative content of oxygen element on the Kevlar fiber surface showed an overall trend of increase. The O/C ratio was about 0.18 before and after 100 and 300 h of ozone exposure and increased to 0.21 after 500 and 1000 h of ozone exposure. This phenomenon can be attributed to the strong oxidation capacity of ozone, which introduced a large number of oxygen atoms to the surface of the Kevlar fiber, resulting in partial oxidation of the molecular chain on the surface of the fiber.

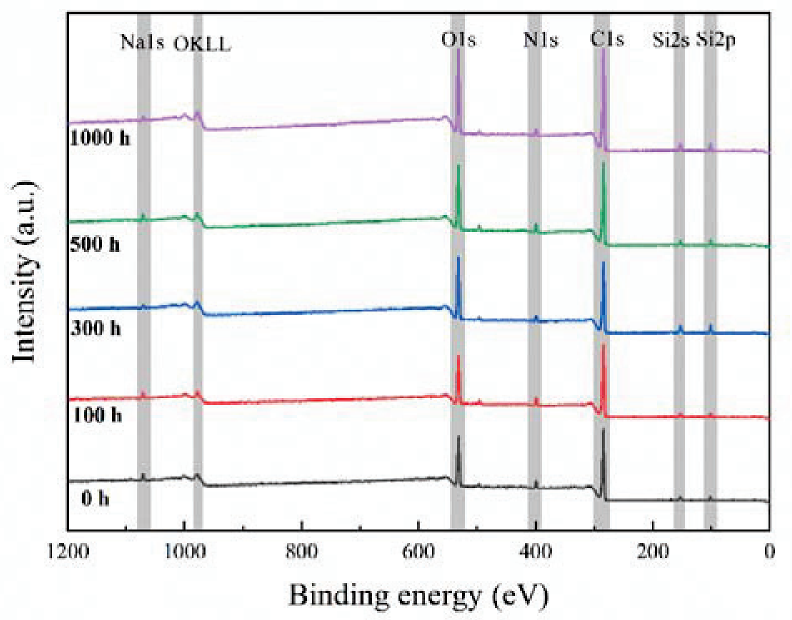

Figure 9. XPS full scan spectra of Kevlar fibers before and after ozone exposure at different time.

Table 2. Relative content of elements before and after ozone exposure.

Exposure Time (h)	Surface Composition (at. %)			Atom Ratio
	C	N	O	O/C
0	77.3	8.9	13.8	0.18
100	76.3	9.8	13.9	0.18
300	77.3	9.0	13.7	0.18
500	75.4	8.8	15.9	0.21
1000	75.9	8.1	16.0	0.21

The high-resolution spectra of C1s and the peak fitting curves by XPSEAK software (version 4.1) before and after exposure to ozone for 100, 300, 500, and 1000 h are summarized in Figure 10. As can be seen from Figure 10a, the C1s high-resolution spectrum of the original Kevlar fiber can be decomposed into 3 fitting peaks with binding energy near 285, 286, and 288 eV, corresponding to the chemical states of C atoms in -C-C-, -C-N-, and -C=O functional groups respectively. After ozone exposure, the C1s high-resolution spectrum can be fitted to 4 separate peaks, as shown in Figure 10b–e. The fitted peak added with binding energy near 289 eV was attributed to the -COO- functional group [36,37]. It can be seen from Table 3 and Figure 10f that the content of the -COO- functional group on the Kevlar fiber surface was correlated with ozone exposure time. With increasing ozone exposure time, the percentage of -COO- functional group first increased and reached the maximum value of 8.82% after 500 h of ozone exposure. However, when the ozone exposure time was further extended to 1000 h, the percentage of the -COO- functional group decreased. This phenomenon was attributed to the partial peeling of the surface layer on the Kevlar fiber, and a partial sub-surface was exposed as a new surface (as shown in Figure 7).

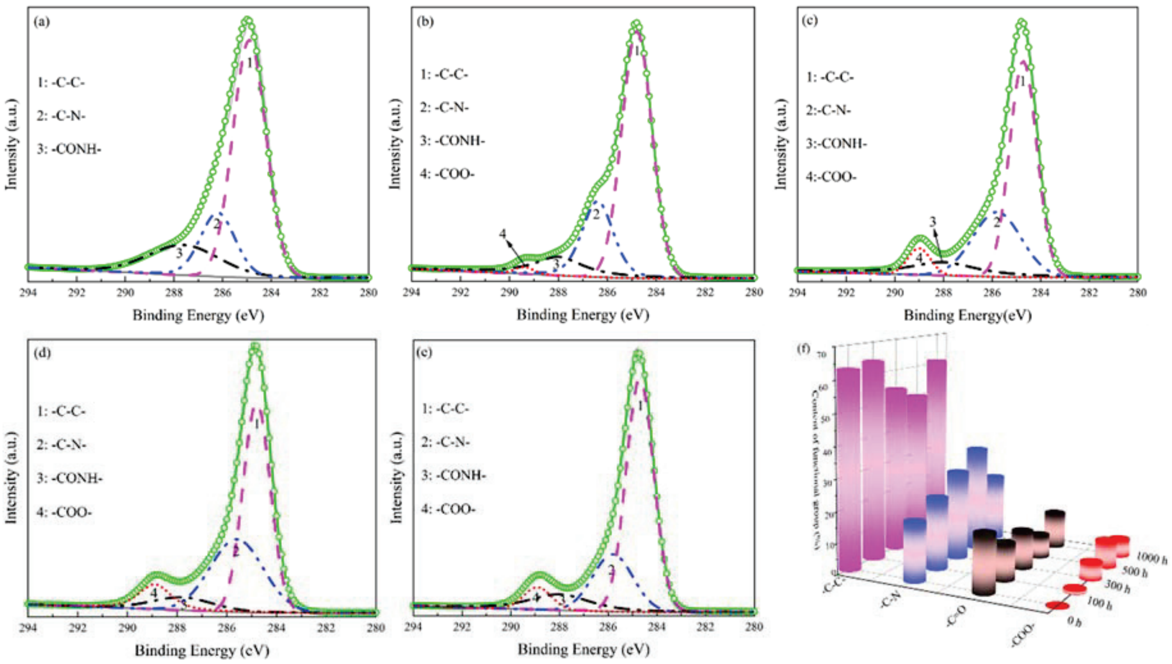

Figure 10. High-resolution XPS spectra for Kevlar fibers before (**a**), and after ozone exposure to atomic oxygen for 100 h (**b**), 300 h (**c**), 500 h (**d**), 1000 h (**e**) and content of functional group of C1s peaks for Kevlar fibers (**f**).

Table 3. Functional groups on the Kevlar fibers surface before and after ozone exposure.

Exposure Time (h)	Content of Functional Group (%)			
	-C-C-	-C-N-	-CONH-	-COO-
0	62.81	18.73	18.46	0.00
100	64.07	22.95	11.88	1.10
300	53.80	28.50	12.21	5.49
500	49.98	33.72	7.48	8.82
1000	60.85	21.58	11.76	5.81

According to the test and analysis results above, partial chemical functional groups on the surface of the Kevlar fiber recombined, induced by ozone molecules. The interaction between the Kevlar fiber and ozone molecules can be roughly divided into two stages, including hydrogen bond destruction and amide bond damage. The reaction mechanism is shown in Figure 11.

There is a hydrogen bond between the H atom and O atom in the molecular chain of the Kevlar fiber. Ozone is composed of an oxygen molecule and an oxygen atom. The 4 electrons are shared by 3 oxygen atoms, so the central oxygen appears with a partial positive charge, and the terminal oxygen has a partial negative charge. At the initial stage of ozone exposure (100 h), the hydrogen bond is destroyed. Due to the lone pair of electrons provided by the O atom in the amide group, the ozone molecule forms a coordination bond with it. Meanwhile, -NH is released from the binding of the hydrogen bond, which is manifested in an increase in the content of the C-N group, and the electron density of the amide group increases. Finally, the crystal regularity of the molecular chain of aramid fiber is destroyed [38]. This is consistent with the results of the infrared analysis.

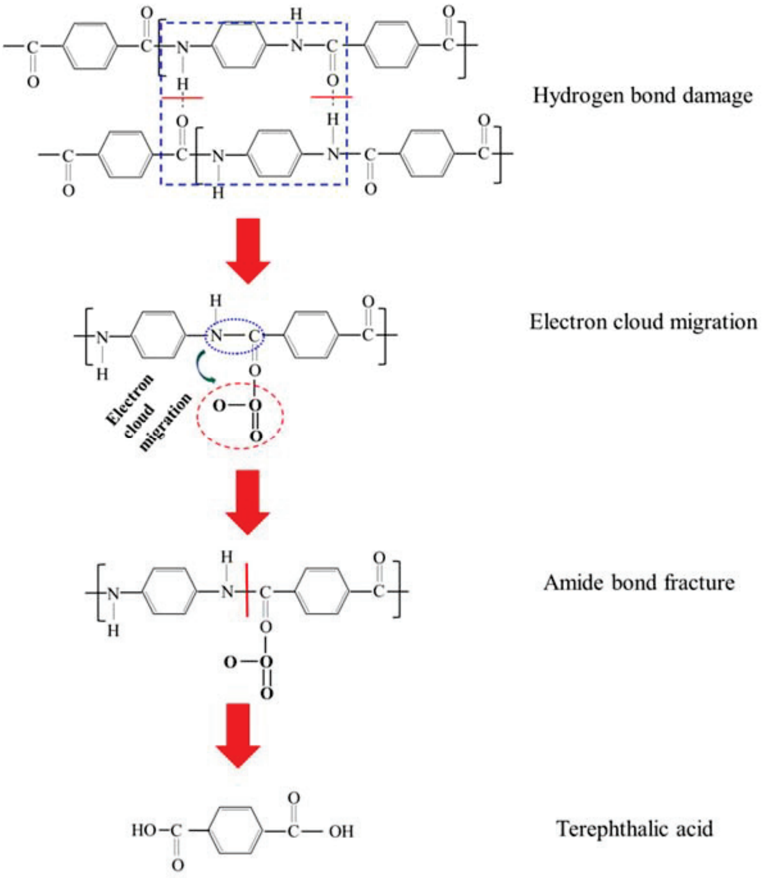

Figure 11. The reaction mechanism of Kevlar fiber in an ozone environment.

The amide bonds (-CONH-) in the Kevlar fiber molecule possessed a certain electronegativity, which was vulnerable to attack and damage from the positively charged oxygen atom in the ozone molecule. With the extension of ozone exposure time, part of the amide bonds was broken, and end groups were oxidized to form a -COO- structure, such as small molecular weight products containing carboxylic acid groups -COOH [35,39].

4. Conclusions

The mechanical properties and damage mechanism of Kevlar fiber were investigated by ground simulation of a near-space ozone environment in this paper. After ozone exposure tests, the elongation of the Kevlar fiber decreased, and the elastic modulus increased. The tensile strength of fiber decreased gradually with an increase in ozone concentration and exposure time. When ozone concentration increased from 0 pphm to 1000 pphm, the tensile strength of fiber decreased from 2397 MPa to 2059 MPa. With increasing ozone exposure time from 0 h to 1000 h under ozone concentration 1000 pphm, the tensile strength of fiber decreased from 2332 MPa to 1954 MPa.

With the increase in ozone exposure time, the surface morphology of the Kevlar fiber gradually roughened and even peeled off. The hydrogen bonds and amide groups connected by rigid molecular chains in the fiber structure were damaged and aged.

After ozone exposure, the relative contents of oxygen and O/C ratio on the surface of the Kevlar fiber increased. At the initial stage of ozone exposure (100 h), hydrogen bonds were broken. Due to the lone pair electrons provided by O atoms in the amide group, ozone molecules formed coordination bonds with it, and the hydrogen bonds formed by the amide groups in the lateral molecular chains were broken. The chemical functional groups on the surface of the Kevlar fiber were reorganized under long-term ozone conditions. The positively charged oxygen atoms in the ozone molecule further destroyed the electronegative amide bonds, forming the -COO- structure, such as low molecular weight oxidation products containing carboxylic acid groups. Therefore, this study on the damage behavior of Kevlar fiber exposed to ozone has reference value for designing and developing promising airship envelope materials with good weather resistance.

Author Contributions: Conceptualization, Q.W., methodology, Q.W. and H.F.; investigation, J.M. and Z.Q., writing—original draft preparation, J.M., writing—review and editing, J.M. and Q.W., supervision, Q.W. and Z.Q., project administration, Q.W. and N.H., funding acquisition, Q.W. and N.H. All authors have read and agreed to the published version of the manuscript.

Funding: This work was supported by the Natural Science Foundation of Hebei Province (Grant No.: E2019202106), the National Natural Science Foundation of China (Grant No.: 51873146 and 81873316), and the Fund for Innovative Research Groups of the Natural Science Foundation of Hebei Province (Grant No. A2020202002).

Institutional Review Board Statement: Not applicable.

Informed Consent Statement: Not applicable.

Data Availability Statement: Data is contained within the article.

Conflicts of Interest: The authors declare no conflict of interest.

References

1. Liu, Y.Y.; Liu, Y.X.; Liu, S.Z.; Tan, H.F. Effect of Accelerated Xenon Lamp Aging on the Mechanical Properties and Structure of Thermoplastic Polyurethane for Stratospheric Airship Envelope. *J. Wuhan Univ. Technol.-Mater. Sci. Ed.* **2014**, *29*, 1270–1276. [CrossRef]
2. Chen, F.G.; Chen, G.G.; Liu, K.H. Analysis of Near Space Environment and Its Effect. *Equip. Environ. Eng.* **2013**, *10*, 71–75. [CrossRef]
3. Jamison, L.; Sommer, G.S.; Porche, I.R., III. High-Altitude Airships for the Future of The Force Army. *Rand Corp.* **2006**, *75*, 151–155.
4. Kang, W.; Suh, Y.; Woo, K.; Lee, I. Mechanical property characterization of film-fabric laminate for stratospheric airship envelope. *Compos. Struct.* **2006**, *75*, 151–155. [CrossRef]
5. Fei, C.; Wang, Z.Q.; Zhou, X.Y.; Wang, F. Research Status of Near Space Airship Envelop Materials. *Fiber Compos.* **2016**, *33*, 24–26.
6. Said, M.A.; Dingwall, B.; Gupta, A.; Seyam, A.M.; Mock, G.; Theyson, T. Investigation of ultra violet (UV) resistance for high strength fibers. *Adv. Space Res.* **2006**, *37*, 2052–2058. [CrossRef]
7. Qiu, Z.; Chen, W.; Gao, C. Initial configuration and nonlinear mechanical analysis of stratospheric nonrigid airship envelope. *J. Aerosp. Eng.* **2019**, *32*, 04018155. [CrossRef]
8. Chen, L. Study on Comprehensive Performance of Several High-Performance Fibers. Ph.D. Thesis, Beijing University of Chemical Technology, Beijing, China, 2016.
9. Dobb, M.G.; Johnson, D.J.; Saville, B.P. Supramolecular Structure of a High-modulus polyaromatic fiber (Kevlar 49). *J. Polym. Sci. Polym. Phys. Ed.* **2010**, *15*, 2201–2211. [CrossRef]
10. Maekawa, S.; Nakadate, M.; Takegaki, A. On the Structures of the Low Altitude Stationary Flight Test Vehicle. *J. Aircr.* **2013**, *44*, 662–666. [CrossRef]
11. Liu, T.M.; Zheng, Y.S.; Hu, J. Surface modification of aramid fibers with novel chemical approach. *Polym. Bull.* **2011**, *66*, 259–275. [CrossRef]
12. Xi, M.; Li, Y.L.; Shang, S.Y.; Li, D.H.; Dai, X.Y. Surface modification of aramid fiber by air DBD plasma at atmospheric pressure with continuous on-line processing. *Surf. Coat. Technol.* **2008**, *202*, 6029–6033. [CrossRef]
13. Yue, C.Y.; Padmanabhan, K. Interfacial studies on surface modified Kevlar fiber/epoxy matrix composites. *Compos. Part B Eng.* **1999**, *30*, 205–217. [CrossRef]
14. Yu, C.C.; Chen, Y.J.; Wu, C.Y. Effect of Relative Humidity on Adsorption Breakthrough of CO_2 on Activated Carbon Fibers. *Materials* **2017**, *10*, 1296. [CrossRef]
15. Kamedulski, P.; Lukaszewicz, J.P.; Witczak, U. The Importance of Structural Factors for the Electrochemical Performance of Graphene/Carbon Nanotube/Melamine Powders towards the Catalytic Activity of Oxygen Reduction Reaction. *Materials* **2021**, *14*, 2448. [CrossRef]
16. Irshad, H.M.; Hakeem, A.S.; Raza, K.; Baroud, T.N.; Ehsan, M.A.; Ali, S.; Tahir, M.S. Design, Development and Evaluation of Thermal Properties of Polysulphone-CNT/GNP Nanocomposites. *Nanomaterials* **2021**, *11*, 2080. [CrossRef]
17. Bing, Y.; Jian, Y.; Li, X.; Zhao, Y. The operating environment of near-space and its effects on the airship. *Spacecr. Environ. Eng.* **2008**, *25*, 555–557.
18. Mabee, A.E. Ozone Effects on Construction Materials for The Stationary High-Altitude Relay Platform (SHARP) Aircraft. Ph.D. Thesis, University of Toronto (Canada), Toronto, ON, Canada, 1991.
19. Zhang, Y.; Wang, Y.; Wang, C. Light weight optimization of stratospheric airship envelope based on reliability analysis. *Chin. J. Aeronaut.* **2020**, *33*, 2670–2678. [CrossRef]

20. Mai, R.Q.; Wang, C.G.; Tan, H.F. Effect of Near Space Environment on Mechanical Properties of Airship Envelope Woven Materials. *Equip. Environ. Eng.* **2020**, *17*, 1–5.
21. Yang, X.R.; Zhang, L.W.; Zhang, Y.Z. Natural Accelerated Environmental Test Technologies. *Equip. Environ. Eng.* **2004**, *1*, 7–11. [CrossRef]
22. Ni, L.; Chemtob, A.; Barghorn, C.C.; Moreau, N.; Bouder, T.; Sebastien, C.; Nadine, P. Direct-to-metal UV-cured hybrid coating for the corrosion protection of aircraft aluminum alloy. *Corros. Sci.* **2014**, *89*, 242–249. [CrossRef]
23. Chen, Z.C.; Li, H.S.; Zhang, P.S.; Zhou, Y.R. Highly Accelerated Ground Simulation Technology of Space Ultraviolet Radiation. *Equip. Environ. Eng.* **2021**, *18*, 57–61.
24. Yimit, M.; Abla, S.; Zhang, S.; Sawut, A.; Di, S.X. Research on Experimental Methods of UV Artificially Accelerated Photoaging of Drip Irrigation Tape. *China Plast.* **2013**, *27*, 89–93.
25. Wang, D.; Zhang, T.F.; Yang, X.H. Equivalent Relationship of Aviation Coatings Gloss Loss between Natural Exposure and Accelerated Aging Test. *Equip. Environ. Eng.* **2020**, *17*, 82–86.
26. Li, B.T.; Xing, L.Y.; Zhou, Z.G.; Jiang, Z.G.; Chen, X.B. Study on Mechanical Properties of High-Performance Envelope Materials. *J. Mater. Eng.* **2010**, *12*, 1–13. [CrossRef]
27. Yuan, H.; Wang, W.; Yang, D.; Zhou, X.; Zhao, Z.; Zhang, L.; Wang, S.; Feng, J. Hydrophilicity modification of aramid fiber using a linear shape plasma excited by nanosecond pulse. *Surf. Coat. Technol.* **2018**, *344*, 614–620. [CrossRef]
28. American Society for Materials and Testing. *Standard Test Method for Tensile Strength and Young's Modulus of Fibers*; ASTM: West Conshohocken, PA, USA, 2003.
29. Liu, Y.X. Study on Photoaging Behavior and Protection of Vectran Fibers. Ph.D. Thesis, Harbin Institute of Technology, Harbin, China, 2014.
30. Levchenko, A.A.; Antipov, E.M.; Plate, N.A.; Stamm, M. Comparative analysis of structure and temperature behavior of two Copolyimides-Regular KEVLAR and statistical ARMOS. *Macromol. Symp.* **1999**, *146*, 145–151. [CrossRef]
31. Leal, A.A.; Deitzel, J.M.; Gillespie, J.W. Assessment of compressive properties of high-performance organic fibers. *Compos. Sci. Technol.* **2007**, *67*, 2786–2794. [CrossRef]
32. Jin, Z.; Luo, Z.; Yang, S.; Lu, S. Influence of complexing treatment and epoxy resin coating on the properties of aramid fiber reinforced natural rubber. *J. Appl. Polym. Sci.* **2015**, *132*, 42122. [CrossRef]
33. Xiong, L.; Yu, W.D. Application to the study on FTIR microspectroscopy in high-performance fibers. *J. Donghua Univ.* **2004**, *30*, 92–97. [CrossRef]
34. Li, G.J.; Li, M.Y. The performance study on the Kevlar twaron fabric. *New Chem. Mater.* **2011**, *8*, 118–121. [CrossRef]
35. Ban, H.J. Structure Design of Integrated Rope-Coring Soft Bag and Ultraviolet Protection. Ph.D. Thesis, Harbin Institute of Technology, Harbin, China, 2015.
36. Su, M.; Gu, A.J.; Liang, G.Z.; Yuan, L. The effect of oxygen-plasma treatment on Kevlar fibers and the properties of Kevlar fibers/bismaleimide composites. *Appl. Surf. Sci.* **2011**, *257*, 3158–3167. [CrossRef]
37. Zhang, Y.H.; Jiang, Z.X.; Huang, Y.D.; Li, Q. The modification of Kevlar fibers in coupling agents by γ-ray co-irradiation. *J. Fibers Polym.* **2011**, *12*, 1014–1020. [CrossRef]
38. Li, C. Study of Complexation on Surface Modification of Kevlar Fiber. Ph.D. Thesis, Guizhou University, Guizhou, China, 2015.
39. Zhang, Y.; Jin, X.D.; Sun, S.B.; Tian, Y.L. Research Progress on Surface Modification of Polymer Materials Based on Ultraviolet-Ozone. *J. Mater. Sci. Technol.* **2021**, *23*, 1–17. [CrossRef]

coatings

Article

Characterization of Prepared Superhydrophobic Surfaces on AZ31 and AZ91 Alloys Etched with $ZnCl_2$ and $SnCl_2$

Leoš Doskočil *, Pavlína Šomanová, Jiří Másilko, Martin Buchtík, Michaela Hasoňová, Lukáš Kalina and Jaromír Wasserbauer

Materials Research Centre, Faculty of Chemistry, Brno University of Technology, Purkyňova 464/118,
612 00 Brno, Czech Republic
* Correspondence: doskocil@fch.vut.cz

Abstract: Superhydrophobic surfaces were prepared using a two-step method that involved the etching of AZ31 and AZ91 magnesium alloys and then modifying the etched alloys with stearic acid. Magnesium alloys etched with $ZnCl_2$ and $SnCl_2$ exhibited surfaces roughened with micro- and nanoscale hierarchical structures consisting of two chemically distinct regions ($Zn/Zn(OH)_2$ or Sn/SnO_2 and $Mg(OH)_2$). An optimum etching time of ten minutes was chosen for both etchants. Superhydrophobic surfaces with the highest contact angle were prepared when stearic acid reacted with the etched alloys at 50 °C for 4 h. Stearic acid was bound as zinc stearate and magnesium stearate on Mg alloys etched with $ZnCl_2$ and $SnCl_2$ solutions, respectively. The superhydrophobic process on AZ31 alloys etched with $ZnCl_2$ and $SnCl_2$ improved the corrosion resistance in phosphate buffered saline (PBS) solution compared to bare AZ31 alloy, with the use of $ZnCl_2$ etchant leading to better results. An improvement in the corrosion resistance of AZ91 alloy was observed when the stearic-acid-modified AZ91 alloy was etched with $SnCl_2$. In contrast, the use of $ZnCl_2$ etchant to pretreat AZ91 alloy resulted in a significant deterioration in corrosion properties compared to bare AZ91 alloy. The microstructure of the Mg alloy had an impact on the etching and modification process. On the basis of the findings, a characterization of the chemistry of etching magnesium alloys and the formation of superhydrophobic surfaces was proposed. Magnesium alloys were prepared with superhydrophobic surfaces, incorporating antibacterial metals, features which may increase their potential for use in medical applications.

Keywords: AZ31 alloy; AZ91 alloy; chemical etching; corrosion resistance; superhydrophobic surface

---

1. Introduction

Magnesium and its alloys have considerable application potential and could become some of the most important engineering materials of the 21st century. Currently, magnesium materials are finding applications in the automotive, aerospace, and electronics industries, as well as in biomedicine [1]. The attractiveness of magnesium and its alloys is due to their favorable properties, such as low density, high specific strength, favorable thermal and electrical conductivity, favorable electromagnetic shielding ability, excellent castability, biocompatibility, and biodegradability [2]. Unfortunately, their main drawback is their poor corrosion resistance, which limits the wider use of magnesium materials in practice. In order to overcome this problem, various coatings, including fluoride coatings, Ni-P coatings, plasma electrolytic oxidation coatings, calcium phosphate coatings, and layered double hydroxide coatings, are diligently being developed [3–9], as well as examined and studied from different points of view.

In the past decade, the preparation of superhydrophobic surfaces has become a very attractive area of research. Superhydrophobic surfaces are defined by a contact angle greater than 150° and a sliding angle of less than 10°. They perfectly repel water from the surface and this allows a significant improvement in the corrosion resistance of the superhydrophobic material [10,11]. Currently, a large number of methods are available to prepare a surface with superhydrophobic properties. One popular method is chemical etching, which is fast and simple and has a low cost [11]. The preparation of a superhydrophobic surface is usually carried out using a two-step method. First, surface roughening with micro- and nanoscale hierarchical structures is performed, and then the roughened surface is modified with a low-energy surface substance (e.g., stearic acid) [11,12]. These two processes are both prerequisites for the successful preparation of a superhydrophobic surface. Some authors have also shown that the preparation of superhydrophobic surfaces can be achieved using a one-step method [12,13].

The improvement of the corrosion resistance, and therefore the extension of the service life of the magnesium material, is explained as follows. The surface roughening combined with the low surface energy allows a large amount of air to be trapped between the protrusions of the rough surface, resulting in an air cushion that prevents corrosive media with aggressive ions (e.g., Cl^-) from attacking the surface [14]. Another possible reason for the improved corrosion resistance of superhydrophobic materials relates to capillarity. Li et al. assumed that water can be forced out of the pores of a superhydrophobic surface by Laplace pressure [15]. Superhydrophobic surfaces are also attractive due to their antibacterial properties [16]. They inhibit the adhesion of bacteria to the implant surface by means of a layer of trapped air and they consequently reduce bacterial infection in the body. It is reported that antibacterial suppression is essential during the initial stages after surgery. Moreover, the effectiveness may be enhanced by the release of an antibacterial agent from the superhydrophobic material. For these reasons (the presence of anti-corrosion and antibacterial properties), superhydrophobic surfaces on magnesium materials are particularly attractive for application in the medical field [16].

The chemical etching of magnesium alloys can be carried out using simple inorganic salts, such as $ZnCl_2$, $MnSO_4$, $FeCl_3$, or $CuCl_2$ [17–20]. The current authors have already shown that these etchants can lead to the successful preparation of a superhydrophobic surface on AZ31 alloy under mild conditions. The etching process is kept below 100 °C for a short period of time and similar reaction conditions are applied for the modification process [17–20]. Stearic acid is most commonly used to achieve a superhydrophobic state, as it is non-toxic and readily available [21]. Stearic acid also has the advantage, as Mensink has shown, of reducing low density lipoprotein (LDL) cholesterol formation compared to other saturated fatty acids, such as myristic acid or palmitic acid [22]. The antibacterial properties of magnesium materials can be enhanced if the superhydrophobic surface is prepared by means of an etchant containing a cation that has an antibacterial effect [23]. The elemental metal and/or metal salt is deposited on the surface of the magnesium alloy during the etching process and can subsequently interact with bacteria [17–20,23]. Zn^{2+}, Cu^{2+}, or Sn^{2+} are known to have antibacterial ability, while Zn^{2+} also exhibits osteogenic activity, which is advantageous for orthopedic implants [23]. Therefore, the selected etchants in this work were $ZnCl_2$ and $SnCl_2$ [22]. To the best of our knowledge, there is a lack of research addressing the preparation of superhydrophobic surfaces on magnesium alloys with a heterogeneous microstructure, such as AZ91 alloy, using inorganic salts as etchants. An exception is the work of Song et al. [24], who chemically etched bare AZ61 alloy with $CuSO_4$ solution at 80 °C for 10 min. Their paper indicated that the original microstructure of AZ61 alloy had an impact on the resulting surface morphology after etching and that modification with stearic acid led to the preparation of a superhydrophobic surface with a contact angle of 151.3°. Unfortunately, the corrosion characteristics were not investigated [24].

The aim of the present work was to prepare superhydrophobic surfaces on AZ31 and AZ91 alloys using a two-step method. The magnesium alloys were etched with $ZnCl_2$ and $SnCl_2$ solutions to produce a roughened surface with a micro- and nanoscale hierarchical structure. In this work and for the first time, $SnCl_2$ was used as an etchant for magnesium alloys. The choice of the etchants was motivated by a desire to exploit the antibacterial properties of Zn and Sn, which could provide added value to the prepared superhydrophobic magnesium alloys. Superhydrophobic surfaces were obtained by causing a reaction between the etched magnesium alloys and stearic acid. In this work, optimal conditions for the preparation of superhydrophobic surfaces were determined and attention was paid to the effect of the etchant used ($ZnCl_2$, $SnCl_2$) and the etching time on the surface roughening of the alloys. Two different microstructures were examined to determine the influence of material bases on the process: cast AZ91 magnesium alloy, with a heterogeneous microstructure, and wrought AZ31 alloy, which can be considered to be homogeneous. Prior to this work, no study involving the preparation of a superhydrophobic surface via the chemical etching of AZ91 alloy has been published. The corrosion resistance of superhydrophobic surfaces on different alloys was tested by potentiodynamic measurements and electrochemical impedance spectroscopy in phosphate buffered saline (PBS) solution, which is used as one type of simulated solution for in vitro experiments. The chemical characterization of superhydrophobic surfaces using spectrometric methods was also carried out and, subsequently, the chemistry of etching magnesium alloys and the formation of superhydrophobic surface was characterized. On the basis of their observations, the authors also formulated a description of the chemical reactions taking place during the etching and modification process. The work demonstrates a possible strategy for the protection of magnesium materials with different microstructures for biomedical applications because pretreatment with $ZnCl_2$ or $SnCl_2$ followed by modification with stearic acid allows for increased corrosion protection as well as the production of nanoscale crystals of metals and their salts with antibacterial properties.

2. Materials and Methods

2.1. Materials

Rolled sheet AZ31 and cast AZ91 magnesium alloys were used in this work. The elemental compositions of the alloys were determined using a Glow-Discharge Optical Emission Spectroscopy (GDOES; Spectrumat GDS 750, Spectruma Analytik GmbH, Hof, Germany) and is listed in Table 1. Samples with dimensions of 20 mm × 20 mm × 5 mm were ground with 800, 1200, and 2500 grit SiC paper, rinsed with deionized water and isopropanol, and dried with hot air. The following chemicals were used: $ZnCl_2$ (Lach-Ner, min. 98%), $SnCl_2{\cdot}2H_2O$ (Lachema, min. 98%), absolute ethanol (VWR, 99.8%), isopropanol (KOVSHOP, 99.9%), NaCl (Lach-Ner, 99.9%), Na_2HPO_4 (PENTA, 99.9%), KCl (Lachema, min. 98%), and KH_2PO_4 (Lach-Ner, 99.9%).

Table 1. The elemental compositions of AZ31 and AZ91 magnesium alloys (GDOES analysis).

Content (wt.%)	Al	Zn	Mn	Si	Fe	Sn	Zn	Mg
AZ31	3.60	1.34	0.28	0.03	0.002	0.01	-	Bal.
AZ91	8.80	0.81	0.32	0.01	0.004	-	0.01	Bal.

2.2. Preparation of the Superhydrophobic Surface

The superhydrophobization process was performed using a two-step method involving chemical etching followed by surface modification with stearic acid in ethanol (Figure 1). It was partly adopted from the work of Xie et al. [17], who prepared a superhydrophobic coating on AZ31 alloy etched with $ZnCl_2$.

Etching was performed with two different etchants by immersing the samples of magnesium alloys in 0.25 M $ZnCl_2$ or 0.25 M $SnCl_2$ for 2 and 10 min each. The samples were then rinsed with deionized water, sonicated in deionized water for 10 min, and dried in an oven for 20 min at 50 °C to remove residual water. The superhydrophobic surface was prepared in an ethanol solution of 0.05 M stearic acid. The etched samples were immersed in the solution at 50 or 60 °C for 1, 2, 3, 4, and 5 h to determine the optimum conditions for the preparation of the superhydrophobic surface.

2.3. Characterization

A scanning electron microscope (SEM, JEOL JSM-7600, Tokyo, Japan) with an energy dispersive X-ray spectroscope (EDS, Oxford Instruments plc, Abingdon, UK) was used to characterize the surface morphology and elemental composition of the etched samples and the superhydrophobic surfaces.

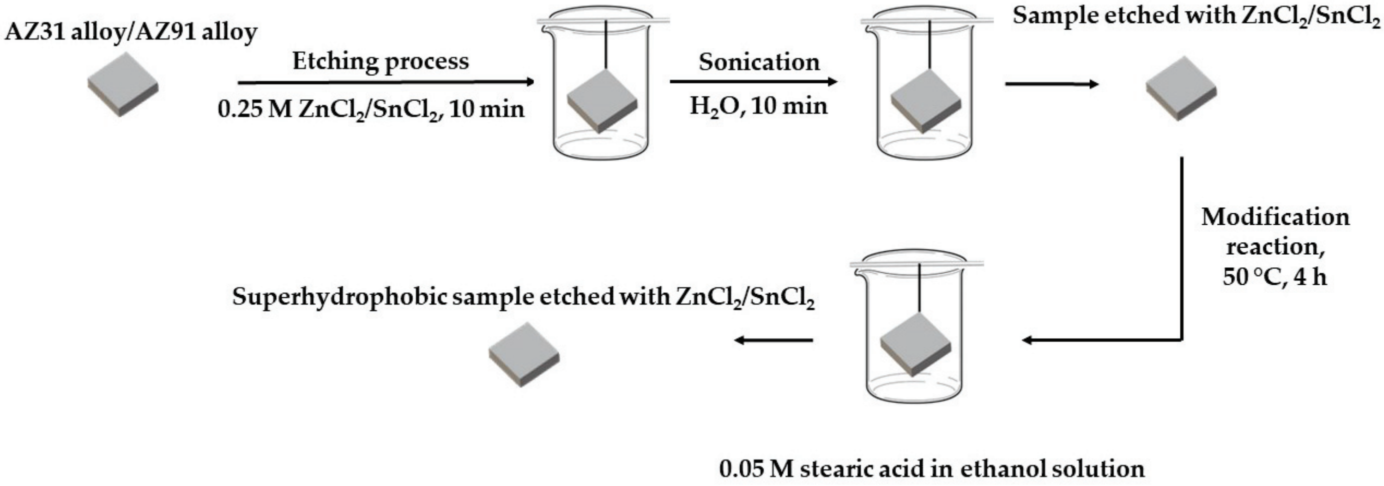

Figure 1. Schematic illustration of the superhydrophobic surface preparation process on AZ31 and AZ91 alloys etched with $ZnCl_2$ and $SnCl_2$ under optimal conditions.

The wetting properties of the surface were measured with a contact angle meter (DataPhysics Instruments, OCA 20, Filderstadt, Germany) using the sessile drop method. The volume of deionized water drops was about 5 µL. A total of ten contact angle values were measured at different spots on the sample surface at room temperature. The resulting contact angle value was calculated as the arithmetic mean. The contact angle was analyzed by SCA 20 software. The sliding angle was determined using in-house instruments. The superhydrophobic sample was placed on a tilting stage and a drop of water was applied to the surface. Then, the stage was slowly tilted at a rate of 1.5°/s. Once the droplet began to slide, the sliding angle was recorded.

Potentiodynamic measurements and electrochemical impedance spectroscopy (EIS) on superhydrophobic samples and ground magnesium alloys were performed using a Bio-Logic VSP-300 potentiostat (BioLogic, Seyssinet-Pariset, France). Measured samples with an exposed area of 1 cm^2 served as the working electrode. The saturated calomel electrode (SCE) was used as the reference electrode and Pt mesh as the counter-electrode. Phosphate buffered saline (PBS) solution with pH 7.4 was used as a corrosion medium in the corrosion cell with a volume of 200 mL. The composition of this solution was 8.00 g/L NaCl, 0.2 g/L KCl, 1.44 g/L Na_2HPO_4, and 0.24 g/L KH_2PO_4. Open circuit potential (OCP) variations with time were recorded during 30 min of exposure. Afterwards, potentiodynamic measurements were performed in the potential range from −200 mV to 200 mV vs. OCP at a scan rate of 1 mV/s. Only cathodic branches of the polarization curves were used to evaluate the corrosion current density. EIS measurements were performed at the OCP with a perturbation amplitude of 10 mV and a scan frequency range from 100 kHz to 10 mHz. The measurement time was 24 h.

The phase composition of the superhydrophobic samples, etched samples, and bare alloys was analyzed by X-ray diffraction (XRD; Panalytical, Malvern, UK). The X-ray source was Cu $K\alpha_1$ radiation (λ = 1.540598 Å), which was operated at a voltage of 40 kV and a current of 30 mA within the range of 5° and 90° 2θ at a scanning rate of 0.01313° 2θ time per step of 46 s.

Fourier transform infrared spectroscopy (FTIR; Nicolet iS50, Thermo Fisher Scientific, Madison, WI, USA) was used to analyze the superhydrophobic samples, etched samples, bare alloys, and stearic acid. Measurements were performed in absorbance mode with the attenuated total reflection technique (ATR) across a spectral range of 4000–400 cm^{-1} and with a resolution of 4 cm^{-1}. A total of 256 scans were performed on each sample.

X-ray photoelectron spectroscopy (XPS; Axis Supra, Kratos Analytical Ltd., Manchester, UK) was used to analyze the superhydrophobic samples. A monochromatic Al Kα source operated at 225 W. High-resolution spectra were obtained using an analysis area of 300 µm × 700 µm and 20 eV pass energy. The Kratos charge neutralizer system was used for all analyses. XPS spectra were analyzed using CasaXPS software (version 2.3.15) and have been charge-corrected to the main line of carbon C 1s (C–C; C–H) set to 284.8 eV. A standard Shirley background was used for all sample spectra.

3. Results and Discussion

3.1. Morphology

SEM-EDS analysis was employed to obtain detailed information on surface roughening due to etching in terms of morphology and the resulting elemental composition. Knowledge of the surface can be useful for the successful preparation of a superhydrophobic surface and understanding its properties.

Surface analysis of AZ31 alloy etched for 10 min with the $ZnCl_2$ solution revealed a rough surface with pits and cracks (Figure 2A). Much of the surface was covered with clusters of fine nanoscale crystals, some of which had a well-developed hexagonal shape (Figure 2B). Elemental analysis by EDS indicated that the crystals were composed of $Zn(OH)_2$ (Table 2). The detection of a relatively high chlorine content can be related to $Mg_2Cl(OH)_2$, $MgCl_2$, and/or the etchant residue of $ZnCl_2$. The presence of $Mg_2Cl(OH)_2$ was indicated by XRD analysis; see below. $MgCl_2$ could be formed by the interaction between Cl^- etchant and Mg^{2+} ions released during the etching of the alloy. The detection of chlorine may also indicate the presence of zinc chloride hydroxide [25]. The surface of the etched AZ31 alloy also included regions of zinc dendrites (detail not shown) formed by the interaction of magnesium alloys with the $ZnCl_2$ etchant solution, as described below. The occurrence of elemental zinc was also detected by XRD analysis. In addition to the regions containing zinc compounds, the surface of the etched alloy was also composed of regions of $Mg(OH)_2$ (Table 2) with typical plate-like crystals of about 15 nm in thickness (Figure 2C). Comparison of the EDS analyses of etched and bare magnesium alloys demonstrated that the surface was heavily oxidized during the etching process (Table 2). The observed micro- and nanoscale hierarchical structures consisting of two chemically distinct regions ($Zn/Zn(OH)_2$ and $Mg(OH)_2$) satisfy the crucial condition for the preparation of a superhydrophobic surface [14]. Compared to the alloy surface etched for 10 min, the surface of the alloy etched for 2 min (Figure 2D–F) appeared to be less roughened, exhibiting therefore shallower pits, and less covered with clusters of zinc compound crystals. The surface also contained cracks. The region formed by $Zn/Zn(OH)_2$ crystals, as determined from EDS analysis (Table 2), is shown in Figure 2E. The $Mg(OH)_2$ structure (Table 2) appeared to be less porous (Figure 2F) than that observed for the longer etching time (Figure 2C). In both cases, coarser structures were created compared to those created after the longer etching time. The etching time of 2 min resulted in a rather underdeveloped hierarchical structure compared to the longer etching time of 10 min.

The surface of AZ31 alloy etched with the $SnCl_2$ solution for 10 min was rough, containing shallow pits and cracks (Figure 3A). The etching effect of the $SnCl_2$ solution was lower than that of the $ZnCl_2$ solution, as the surface etched with $SnCl_2$ for 10 min was much less degraded than the surface etched with $ZnCl_2$ for 2 min. Similar to the surfaces etched with the $ZnCl_2$ solution, two chemically different regions occurred on the $SnCl_2$ etched surface. One of the regions consisted of a cluster of crystals (Figure 3B), which were attributed to elemental Sn and SnO_2 on the basis of EDS analysis (Table 2). The crystals were coarser than those observed on surfaces of alloys etched with the zinc solution. With respect to the detection of chlorine in the displayed region (Figure 3B), the presence of $Mg_2Cl(OH)_2/MgCl_2$ and $SnCl_2$ is assumed. The occurrence of Sn(OH)Cl cannot be completely excluded either [26]. The second characteristic region of etched AZ31 alloy was formed by $Mg(OH)_2$ crystals (Figure 3C, Table 2). The surface etched for 2 min was smoother than the surface etched for 10 min (Figure 3D). It contained fewer regions formed by clusters of crystals (Figure 2E) composed of Sn and SnO_2, as determined by EDS analysis (Table 2). Most of the surface of AZ31 alloy appeared to be composed of $Mg(OH)_2$ with poorly grown crystals (Figure 3F, Table 2). The results obtained suggest that the $SnCl_2$ solution provides an underdeveloped micro- and nanoscale hierarchical structure for both etching times of 2 and 10 min.

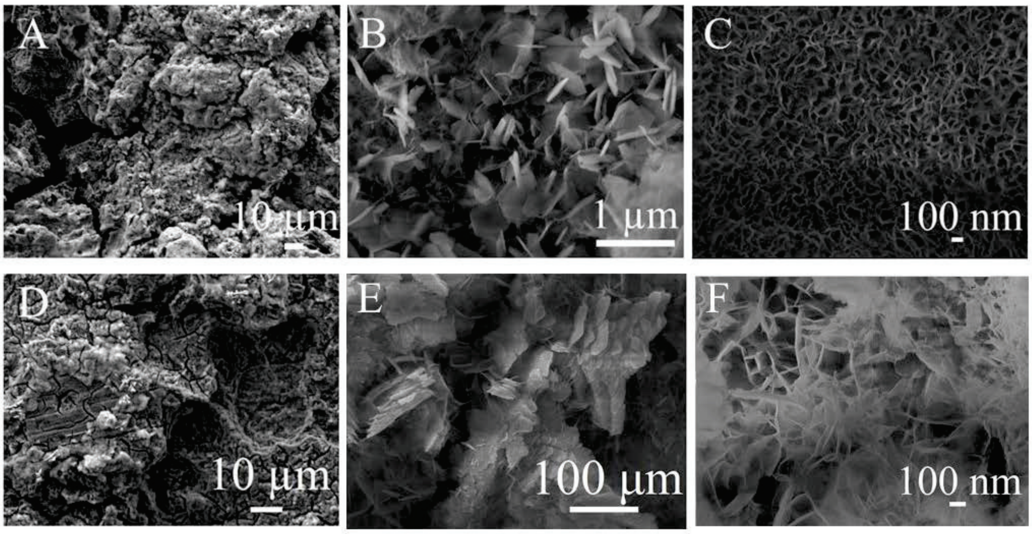

Figure 2. SEM images of AZ31 alloy etched with $ZnCl_2$ for 10 min (**A**–**C**) and 2 min (**D**–**F**). Details in (**B**,**E**) show the zinc-rich regions and details in (**C**,**F**) show the $Mg(OH)_2$ regions.

Table 2. Elemental composition determined by the EDS method for different regions subject to SEM analysis. The regions of elemental composition correspond to the SEM images; see Figures 2–5. The EDS analysis also includes the elemental composition of bare magnesium alloys. EDS energy spectra of magnesium alloys etched with $ZnCl_2$ and $SnCl_2$ for 2 and 10 min each are shown in Figure S3.

Alloy	**Etchant**	**Figure**	**Elements (at. %)**					
			O	**Mg**	**Al**	**Cl**	**Zn**	**Sn**
AZ31	-	-	-	96.98	2.67	-	0.35	-
	$ZnCl_2$	2B	55.34	3.34	0.71	8.47	32.15	-
		2C	24.58	2.73	0.66	2.64	69.38	-
		2E	33.82	8.57	0.82	2.29	54.49	-
		2F	57.59	32.99	2.07	2.46	4.88	-
	$SnCl_2$	3B	52.75	2.60	0.58	3.03	-	41.04
		3C	61.80	33.90	2.67	0.90	-	0.74
		3E	57.03	12.66	2.10	2.38	0.24	25.58
		3F	35.25	56.71	7.01	0.25	0.34	0.44
AZ91	-	-	-	94.86	4.62	-	0.11	-
	$ZnCl_2$	4B	63.24	18.04	6.95	0.64	11.13	-
		4C	51.02	24.90	9.36	3.22	11.5	-
		4E	50.25	24.47	4.26	0.95	20.07	-
		4F	36.19	58.21	4.32	1.28	-	-
	$SnCl_2$	5B	68.50	16.97	1.51	0.18	-	12.85
		5C	55.37	27.19	5.90	9.83	-	1.72
		5E	49.83	7.45	3.15	0.15	-	39.43
		5F	39.21	54.58	4.00	1.72	-	0.48

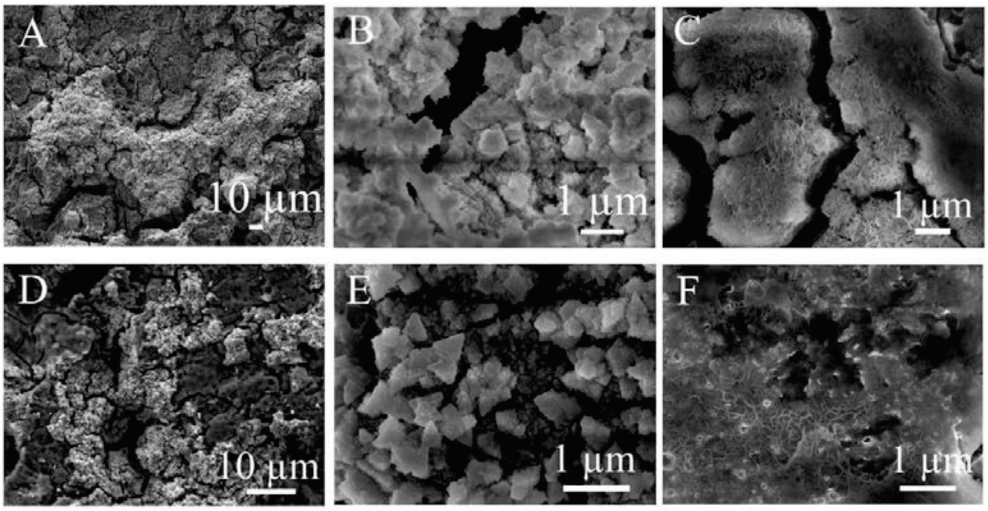

Figure 3. SEM images of AZ31 alloy etched with $SnCl_2$ for 10 min (**A**–**C**) and 2 min (**D**–**F**). Details in (**B**,**E**) show the tin-rich regions and details in (**C**,**F**) show the $Mg(OH)_2$ regions.

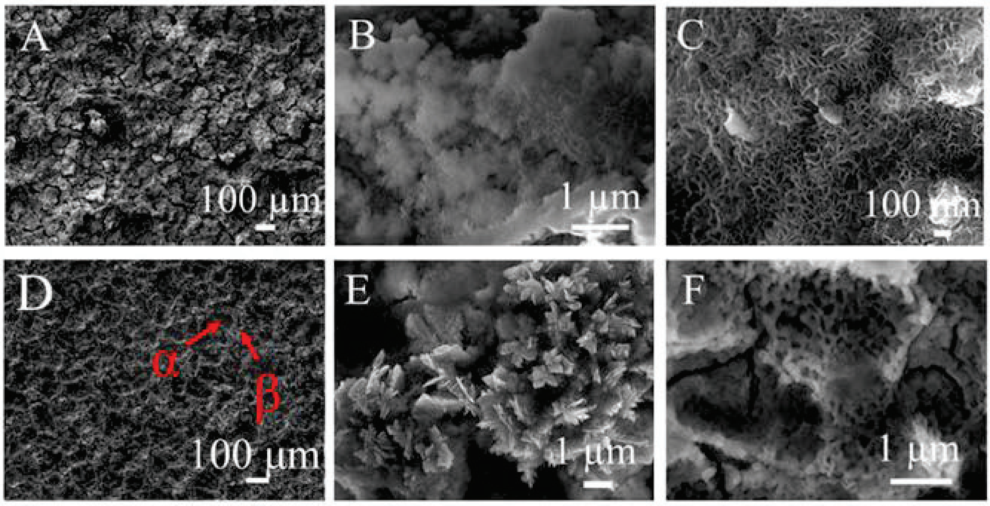

Figure 4. SEM images of AZ91 alloy etched with $ZnCl_2$ for 10 min (**A**–**C**) and 2 min (**D**–**F**). Details in (**B**,**E**) show the zinc-rich regions and details in (**C**,**F**) show the $Mg(OH)_2$ regions.

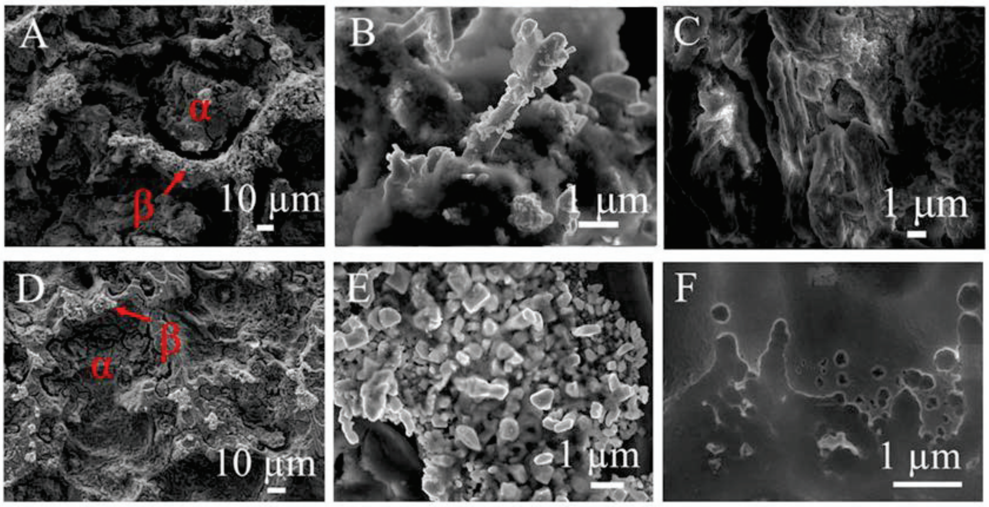

Figure 5. SEM images of AZ91 alloy etched with $SnCl_2$ for 10 min (**A**–**C**) and 2 min (**D**–**F**). Details in (**B**,**E**) show the tin-rich regions and details in (**C**,**F**) show the $Mg(OH)_2$ regions.

The surface of AZ91 alloy etched with the $ZnCl_2$ solution for 10 min was rough, containing cracks, with the original microstructure of the alloy no longer visible (Figure 4A). Figure 4B shows the area of nanoscale crystals attributed to $Zn(OH)_2$ on the basis of elemental analysis (Table 2). At the same time, areas of $Mg(OH)_2$ comprising platelet crystals with a thickness of about 13 nm were also present on the sample surface (Figure 4C). Another region (not shown) also contained elemental zinc. The surface of AZ91 alloy etched with the $ZnCl_2$ solution for 2 min (Figure 4D) revealed the original, recognizable AZ91 alloy microstructure, from which the α phase was preferentially dissolved. Observable residues of the β phase were retained due to its higher electrode potential compared to the electrode potential of the α phase (solid solution of elements in Mg) [4,23]. Figure 4E shows the zinc dendrites (Table 2) that were generally observed on the β phase residues. Figure 4F shows the structure of $Mg(OH)_2$ in the α phase region (Table 2).

The AZ91 alloy surface etched with the $SnCl_2$ solution for 10 min was characterized by a more pronounced degradation of the original microstructure compared to the surfaces etched for shorter times (Figure 5A,D). However, residues of the β phase and the corroded α phase were still distinguishable on the surface. Tin compounds created on the surface due to the reaction of the alloy with the etchant formed isolated islands of nanoscale crystals that preferentially occurred on the preserved β phase. Elemental analysis indicated that these regions (Figure 5B) were most probably composed of Sn and SnO_2; see Table 2. Once the Sn/SnO_2 crystals occupied the surface of the residues of the original β phase, they also began to grow on the surfaces of the degraded α phase. Similar behavior was also observed in a study of NiP deposition on AZ91 alloy [27]. The growth of the NiP coating was initiated on the β phase and subsequently extended to the α phase. The region of $Mg(OH)_2$ is shown in Figure 5C.

The AZ91 alloy surface etched with the $SnCl_2$ solution for 2 min was characterized by a more preserved original microstructure with few cracks. Tiny clusters of nanoscale elemental Sn and SnO_2 crystals were randomly located on the β phase of the original microstructure of the AZ91 alloy (Figure 5D,E, Table 2). The Sn/SnO_2 crystals appeared to be coarser compared to those observed on the surface etched for a longer time. This observation indicates that the microstructure of the magnesium alloy has an impact on the etching process and, as a consequence, can affect the wetting of the stearic-acid-modified surface. Figure 5F shows the region with a chemical composition of $Mg(OH)_2$, which was without observable crystal growth.

Additionally, the effect of a longer etching time (15 min) on surface morphology was investigated (see Figures S1 and S2). The results show that crystals containing zinc or tin were larger in size and that regions of $Mg(OH)_2$ were mostly poor in observable fine crystals. Moreover, magnesium alloys etched with $SnCl_2$ were more covered with Sn and SnO_2 crystals than those etched for shorter times, see EDS analysis in Table S1. Thus, surface analysis suggests that a longer etching time for both magnesium alloys does not provide roughening with micro- and nanoscale hierarchical structures.

The etched samples were immersed in a stearic acid solution to prepare superhydrophobic surfaces but SEM analysis showed that the resulting morphology resembled the etched samples. Since the effect of stearic acid on the surface morphology of the etched alloys was negligible, SEM images of the stearic-acid-modified samples are not presented here. This negligible effect is attributed to the formation of a very thin film on the surface of the etched alloys. Similar observations have also been reported by other authors [17,24]. The grafting of stearic acid onto the surfaces of etched samples was shown by FTIR spectrometry (see below).

3.2. *Effect of Etchant and Etching Time on the Creation of Superhydrophobic Surface*

The etched samples were modified by immersion in stearic acid solution at 50 °C for 4 h to obtain a superhydrophobic surface. As shown in Table 3, the pretreatment of the sample by etching had an effect on the degree of wetness on the modified surface. The measured contact angles were either close to 150° (highly hydrophobic properties) or above 150° (superhydrophobic properties). It should be noted that the bare AZ31 and AZ91 alloys had contact angles of 38.0° ± 3.8° and 40.8° ± 3.8°, respectively. These measured values agree with those published and demonstrate the hydrophilic nature of the alloy surface [28,29]. Images of water droplets on stearic-acid-modified magnesium alloys etched with $ZnCl_2$ and $SnCl_2$ are shown in Figure S4.

Table 3. Contact angles measured on stearic-acid-modified magnesium alloys etched under different etching conditions.

Alloys	**$ZnCl_2$**		**$SnCl_2$**	
	2 min	**10 min**	**2 min**	**10 min**
AZ31	150.1° ± 1.3°	151.3° ± 1.1°	147.2° ± 1.3°	150.2° ± 2.1°
AZ91	146.4° ± 1.3°	149.8° ± 2.1°	147.5° ± 1.1°	152.0° ± 1.5°

The $ZnCl_2$ etchant proved to be very effective in the case of AZ31 alloy because a superhydrophobic surface with a contact angle of about 150.1° was obtained on the sample etched for 2 min. Prolonging the etching time had a positive effect on increasing the contact angle (Table 3). This indicates that the $ZnCl_2$ solution can provide a rough surface with a hierarchical structure very quickly. This observation is consistent with the observed morphology, which showed a micro- and nanoscale hierarchical structure (Figures 2–5). Undoubtedly, the creation of the $Mg(OH)_2$ morphology with a large content of pores, which could be filled with air and prevent contact with a corrosive medium, could have played a supporting role in increasing the water repellency. AZ31 alloy etched with the $SnCl_2$ solution for 2 min probably acquired insufficient roughness, because the contact angle of the stearic-acid-modified surface was below 150°. The lower contact angle may be related to the lower degree of roughening than that formed by $ZnCl_2$ etching, as recognized by surface morphology analysis. The longer etching time (10 min) resulted in a reduction in surface wettability, because a slight increase in contact angle was observed. Nevertheless, when considering statistical deviations, the measured values of the contact angle were close to those indicating superhydrophobic properties. Unfortunately, increasing the etching time (15 min) resulted in a worsening of the contact angle value (see Table S2).

The contact angles measured for modified surfaces of AZ91 alloy etched with the $ZnCl_2$ solution for 2 and 10 min were lower than 150°. A longer time (15 min) did not result in a higher contact angle value, as shown in Table S2. In addition, $ZnCl_2$ appears to be an unsuitable etchant for AZ91 alloy. The contact angle for the stearic-acid-modified surface of AZ91 alloy etched with $SnCl_2$ for 2 min was about 147.5°; however, a superhydrophobic surface with a contact angle of about 152.0° was successfully prepared when AZ91 alloy was etched for 10 min using the $SnCl_2$ solution. This confirms that the $SnCl_2$ solution is able to provide the necessary micro- and nanoscale hierarchical structure for the preparation of a superhydrophobic surface, unlike the $ZnCl_2$ etchant. The longer etching time led to a decrease in the contact angle; see Table S2. Thus, the results suggest that an etching time of 10 min is sufficient for the pretreatment of AZ31 and AZ91 alloys using $ZnCl_2$ or $SnCl_2$ solutions in the context of producing surfaces with superhydrophobic properties.

3.3. Effect of Temperature and Time on the Preparation of a Superhydrophobic Surface

Etching conditions, including the choice of etchant and etching time, are important for the successful preparation of a superhydrophobic surface on magnesium alloys, as shown by the experiments above. In addition, the preparation of a superhydrophobic surface can also be dependent on the reaction conditions (temperature and time) when the etched magnesium alloy reacts with a low surface energy substance, such as stearic acid [11,12]. Hence, for an optimum etching time of 10 min, the effect of temperature and time on the reaction of stearic acid with etched samples was investigated.

Figure 6 shows the dependence of the contact angle on time (1–5 h) at 50 and 60 °C for a stearic-acid-modified surface on magnesium alloys etched with $ZnCl_2$ and $SnCl_2$ for 10 min.

It should be noted that the standard deviation of the contact angles was approximately 1.5° and the sliding angle of samples was below 10°.

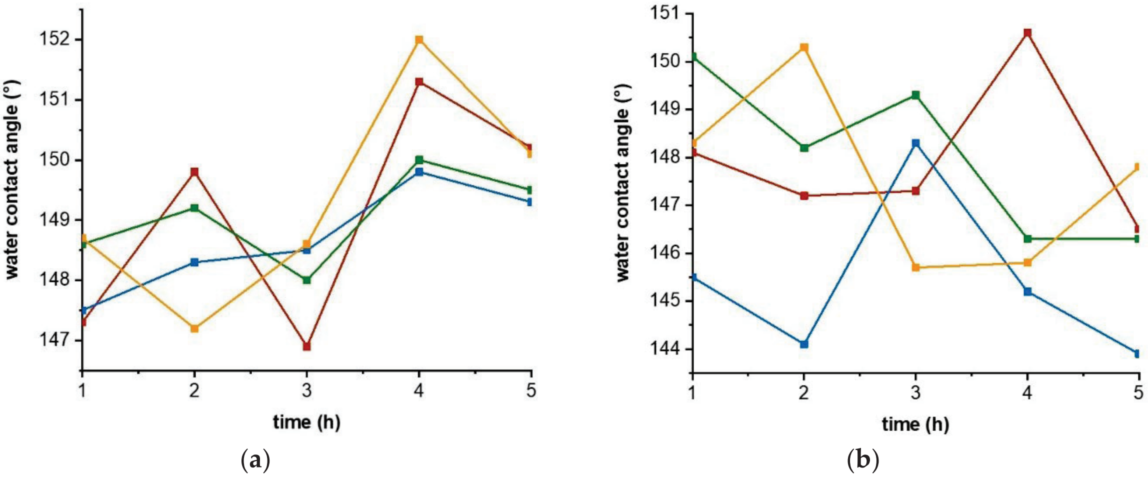

Figure 6. Contact angle as a function of time at 50 °C (**a**) and 60 °C (**b**). Contact angles were measured on stearic-acid-modified surfaces of AZ31 etched with $ZnCl_2$ (red) and etched with $SnCl_2$ (blue), and AZ91 etched with $ZnCl_2$ (green) and etched with $SnCl_2$ (orange).

Figure 6a shows the same trend for the curves for all samples modified at 50 °C. The contact angle on all surfaces initially increased until it reached a maximum value of about 150° at 4 h and then decreased. Finding a clear trend for the contact angle versus time at 60 °C was more difficult (Figure 6b). However, it appears that the contact angles decreased with increasing time. Furthermore, the contact angle values were slightly lower than those found at 50 °C. This indicates higher surface wettability with water and consequently poorer corrosion resistance. The observation of lower contact angle values at 60 °C for different reaction times could be explained by the predominance of the hydrolysis reaction of stearate and/or the higher solubility of metal stearate. The highest water repellency was observed for the surfaces prepared at 50 °C for 4 h; therefore, these conditions were chosen as optimal for the reaction with stearic acid.

3.4. Potentiodynamic Tests

The measured contact angles confirmed that superhydrophobic surfaces were prepared on etched magnesium alloys. In light of the obtained results, samples etched for 10 min and modified with stearic acid for 4 h at 50 °C were used for electrochemical measurements. Consequently, these investigated samples with superhydrophobic surfaces should have had a higher corrosion resistance than bare AZ31 and AZ91 alloys, because superhydrophobic surfaces prevent wetting by a corrosive solution. To verify the improved corrosion resistance of the prepared superhydrophobic surfaces, potentiodynamic polarization measurements were performed in PBS solution (Figure 7). The evaluated parameters, including corrosion current density (i_{cor}) and corrosion potential (E_{cor}), are summarized in Table 4.

The positions of the curves and the obtained i_{cor} and E_{cor} values indicate that the corrosion resistance of AZ31 alloy was improved by the preparation of a superhydrophobic surface (Figure 7a). The values of E_{cor} for both superhydrophobic samples were the same and were more positive than the E_{cor} of bare AZ31 alloy. This indicates a lower tendency to corrode after treatment, from a thermodynamic point of view. From the kinetic point of view, slightly better corrosion results were obtained for the samples prepared on AZ31 alloy etched with $ZnCl_2$ compared to AZ31 alloy etched with $SnCl_2$ because the corrosion current density was slightly lower (Table 4). This observation is consistent with the measured value of the contact angle for superhydrophobic surfaces. The superhydrophobic surface of AZ31 alloy etched with $ZnCl_2$ had a higher the contact angle (about 151.3°)

than the one etched with $SnCl_2$ (about 150.2°) and therefore it more effectively prevented contact with the corrosive environment. The improvement in corrosion resistance by the superhydrophobization process is also illustrated by the fact that the superhydrophobic surface on AZ31 etched with $ZnCl_2$ reduced the corrosion current density approximately nine times compared to bare AZ31 alloy.

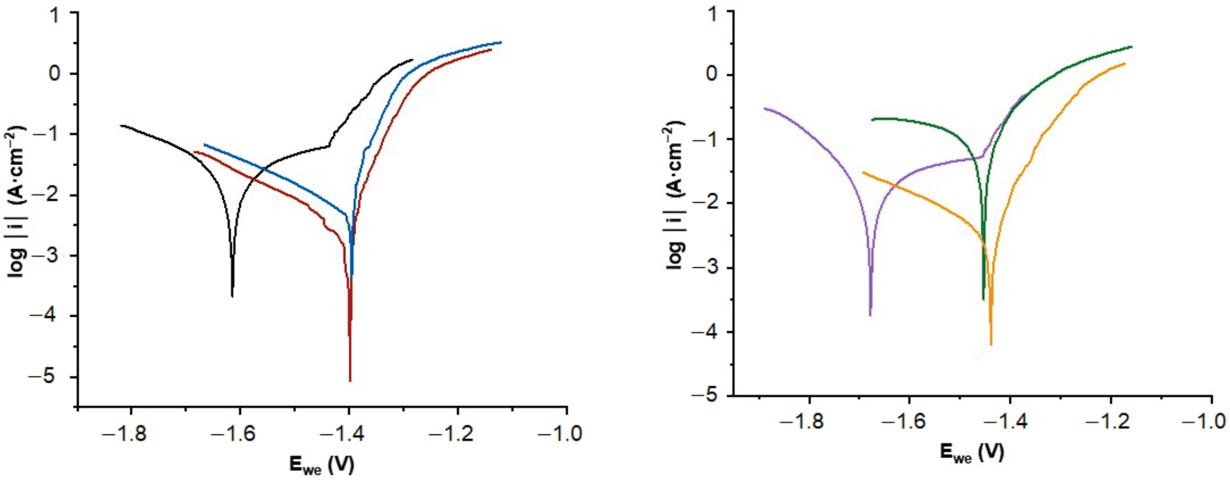

(**a**) (**b**)

Figure 7. Potentiodynamic polarization curves of the examined samples. On the left (**a**) are the curves for bare AZ31 alloy (black) and stearic-acid-modified AZ31 alloy etched with $ZnCl_2$ (red) and etched with $SnCl_2$ (blue). On the right (**b**) are curves for bare AZ91 alloy (violet) and stearic-acid-modified AZ91 alloy etched with $ZnCl_2$ (green) and etched with $SnCl_2$ (orange).

Table 4. Corrosion parameters obtained from potentiodynamic measurements.

Sample		**i_{cor} [μA/cm^2]**	**E_{cor} [mV]**
AZ31	Untreated	26.51	−1.61
	$ZnCl_2$ + modification	3.41	−1.40
	$SnCl_2$ + modification	5.46	−1.40
AZ91	Untreated	22.22	−1.68
	$ZnCl_2$ + modification	120.62	−1.45
	$SnCl_2$ + modification	4.89	−1.45

A different situation was observed in the case of AZ91 alloy (Figure 7b). Additionally, in this case, both the superhydrophobic surfaces on AZ91 alloy etched with $ZnCl_2$ and $SnCl_2$ had the same E_{cor} value and it was more positive than the E_{cor} of bare AZ91 alloy. However, a significant difference in the corrosion kinetics was observed. The prepared superhydrophobic surface on AZ91 alloy etched with $ZnCl_2$ exhibited significantly deteriorated corrosion resistance compared to bare AZ91 alloy, from the kinetic point of view, even though the resistance from the thermodynamic point of view was improved, as can be seen in Figure 7b and Table 4. In contrast, the superhydrophobic surface prepared on AZ91 alloy etched with $SnCl_2$ provided good corrosion protection against the corrosive environment, as the corrosion current density decreased approximately five times compared to the value for bare AZ91 alloy.

The corrosion deterioration observed in stearic-acid-modified AZ91 alloy etched with $ZnCl_2$ could be related to the nature of the surface, which exhibits the contact angle equal to 149.8° ± 2.1°. As a result, the corrosive environment could more easily come into contact with the surface. The corrosion reaction may have been facilitated by the formation of a galvanic cell between magnesium and zinc (or $Zn(OH)_2$) crystals, which had a higher electrode potential. Moreover, it can be assumed that the corrosive environment had easier access to the magnesium-rich α phase, since stearic acid reacted exclusively with $Zn/Zn(OH)_2$

during the superhydrophobization process (see FTIR analysis), which was mainly accumulated on β phase residues of AZ91 alloy (Figure 4A,D). Thus, a significant reduction in surface energy probably occurred in the areas where zinc was present. This observation suggests that the microstructure of magnesium alloys may affect the surface properties.

3.5. EIS Measurements

EIS data obtained after one day of exposure in PBS solution are shown in Figure 8. Nyquist plots were fitted using two different equivalent electrical circuits, which are shown in Figure 9. The model in Figure 9a was used for all samples except for the superhydrophobic surface of AZ91 alloy etched with $SnCl_2$. The equivalent electrical circuit shown in Figure 9a consisted of components representing the solution resistance (R_1), the resistance (R_2) and the constant phase element (Q_1) of the corrosion products and/or the superhydrophobic film, and the resistance (R_3) and the constant phase element (Q_3) of the electric double layer at the electrolyte and substrate interface. The second equivalent electrical circuit (Figure 9b) consisted of components representing the solution resistance (R_1), the constant phase element (Q_1) of the present corrosion layer, the resistance of the capacitance part (R_2), the inductance (L_3; the time-independent part of the circuit characterizing the inductive loop of the plot), and the resistance (R_3) of the inductive loop. The parameters evaluated by fitting the EIS data and the calculated polarization resistance values are summarized in Table 5. The polarization resistances were calculated according to the relations presented in Figure 9. The higher the polarization resistance values, the higher the corrosion resistance. The shapes of the Nyquist plots (Figure 8a) and the R_p values show that the superhydrophobic process resulted in improved corrosion resistance in PBS solution compared to bare AZ31 alloy. The corrosion resistance was of a comparable order of magnitude for both superhydrophobic samples. Figure 9b and the R_p values clearly show that only the superhydrophobic surface of AZ91 alloy etched with $SnCl_2$ resulted in better corrosion resistance. Even the superhydrophobic surface of AZ91 alloy etched with $ZnCl_2$ had a polarization resistance two orders of magnitude lower than bare AZ91 alloy. Moreover, the application of the other equivalent electrical circuit (Figure 9b) indicates that the corrosion of the sample was proceeded by a different corrosion mechanism. The EIS results are consistent with those of the potentiodynamic polarization measurements.

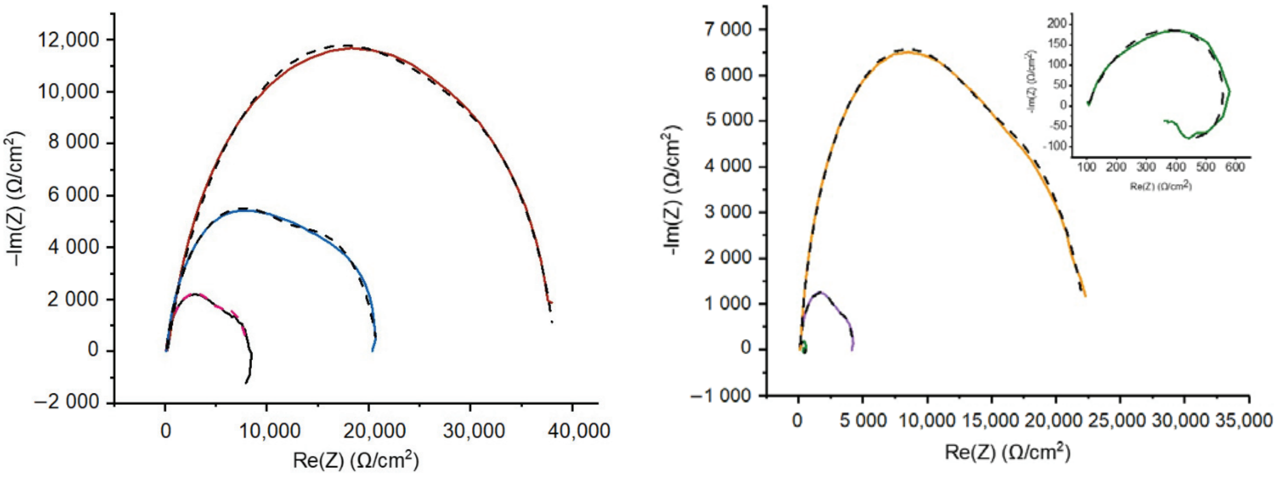

(**a**) (**b**)

Figure 8. (**a**) Nyquits plots and their fits (dashed curves) for AZ31 alloy samples: bare AZ31 alloy (pink), AZ31 alloy etched with $ZnCl_2$ and a superhydrophobic surface (red), and AZ31 alloy etched with $SnCl_2$ and a superhydrophobic surface (blue). (**b**) Nyquits plots and their fits (dashed curves) for AZ91 alloy samples: bare AZ91 alloy (pink), AZ91 alloy etched with $ZnCl_2$ and a superhydrophobic surface (yellow), and AZ91 alloy etched with $SnCl_2$ and a superhydrophobic surface (green).

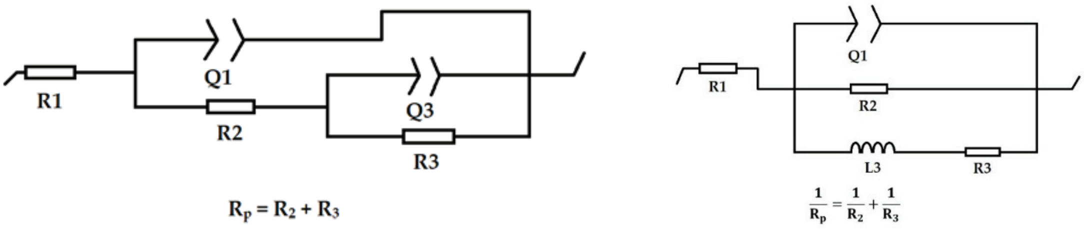

(**a**) (**b**)

Figure 9. Equivalent electrical circuits used for Nyquist plot evaluation and equations for the calculation of polarization resistance (R_p). The equivalent electrical circuit (**a**) was used for bare magnesium alloys, stearic-acid-modified AZ31/AZ91 alloy etched with $ZnCl_2$ and stearic-acid-modified AZ31 alloy etched with $SnCl_2$. The equivalent electrical circuit (**b**) was used for the superhydrophobic surface of AZ91 alloy etched with $SnCl_2$.

Table 5. The parameters evaluated by fitting the EIS data and the calculated polarization resistance values.

	Sample	R_1 [Ω]	Q_1 [$\mu F \cdot s^{(a-1)}$]	a_1	R_2 [Ω]	Q_3 [$mF \cdot s^{(a-1)}$]	L_3 (H)	a_3	R_3 [Ω]	R_p [Ω]
AZ31	Untreated	102	14	0.86	5514	398	-	0.91	2433	7947
	$ZnCl_2$ + modification	240	5.7	0.78	32,680	0.126	-	0.96	5444	38,124
	$SnCl_2$ + modification	124	4.6	0.84	13,747	0.085	-	0.84	6953	20,700
AZ91	Untreated	92	23	0.87	3071	807	-	0.88	1102	4173
	$ZnCl_2$ + modification	104	291	0.71	651	-	262	-	490	280
	$SnCl_2$ + modification	129	8	0.89	14,958	162	-	0.75	7496	22,454

3.6. XRD Analysis

The superhydrophobic samples, etched samples, and both bare magnesium alloys were characterized using the XRD method. The analysis revealed the presence of elemental zinc on surface of AZ31 and AZ91 alloys etched with the $ZnCl_2$ solution (Figure 10). No other chemical form of zinc was identified. Similarly, XRD analysis of magnesium alloys etched with $SnCl_2$ showed only the presence of elemental tin (Figure 10). These results are contrary to expectation arising from the EDS analysis. The absence of other forms of zinc and tin in the XRD spectra could be explained by the nanoscale size of crystals and/or their low abundance. The presented XRD spectra of superhydrophobic and etched samples did not differ from each other. The observed broad peak around 11° is undoubtedly related to the etching process, as the peak did not appear in the XRD spectra of bare alloys. On the basis of these results and the literature, the peak can probably be attributed to $Mg_2Cl(OH)_3 \cdot 4H_2O$ [17,30]. The absence of metal stearates in the XRD spectra can be explained by their amorphous nature or their low abundance on the surface. Their occurrence was revealed by FTIR analysis, as discussed below. This fact is not surprising since metal stearates are not commonly identified in XRD spectra, as indicated in the published literature [12,17,24]. The presence of zinc and tin on the surface of magnesium alloys can enhance the alloys' antibacterial properties, as these metals inhibit bacterial infection [23]. However, biological experiments would be needed to confirm this hypothesis. Xie et al. recently reported that the superhydrophobic AZ31 alloy surface with deposited zinc significantly enhanced biocompatibility and had lower cytotoxicity than AZ31 alloy [17].

3.7. FTIR Analysis

FTIR spectra recorded for stearic acid and superhydrophobic and etched samples are shown in Figure 11. FTIR spectra for bare AZ31 and AZ91 alloys are shown in Figure S5. Identification of the bands was made on the basis of the literature [31–33]. In all displayed FTIR spectra (with the exception of etched samples), very pronounced bands at 2914 and 2847 cm^{-1} were related to asymmetric and symmetric stretching in methylene groups.

Moreover, a shoulder of the asymmetric stretching at 2954 cm^{-1} in methyl groups was observed. Deformation vibrations of methylene groups were present at about 1460 cm^{-1}. The identification of predominantly methylene groups is consistent with the structure of the stearic acid/stearate molecule. The presence of long carbon chains derived from stearic acid was revealed by the band at 728 cm^{-1} and by the shoulder at the same wavenumber. Thus, FTIR analysis confirmed the presence of hydrophobic long-chain alkyl, which was present on the surfaces of all superhydrophobic samples.

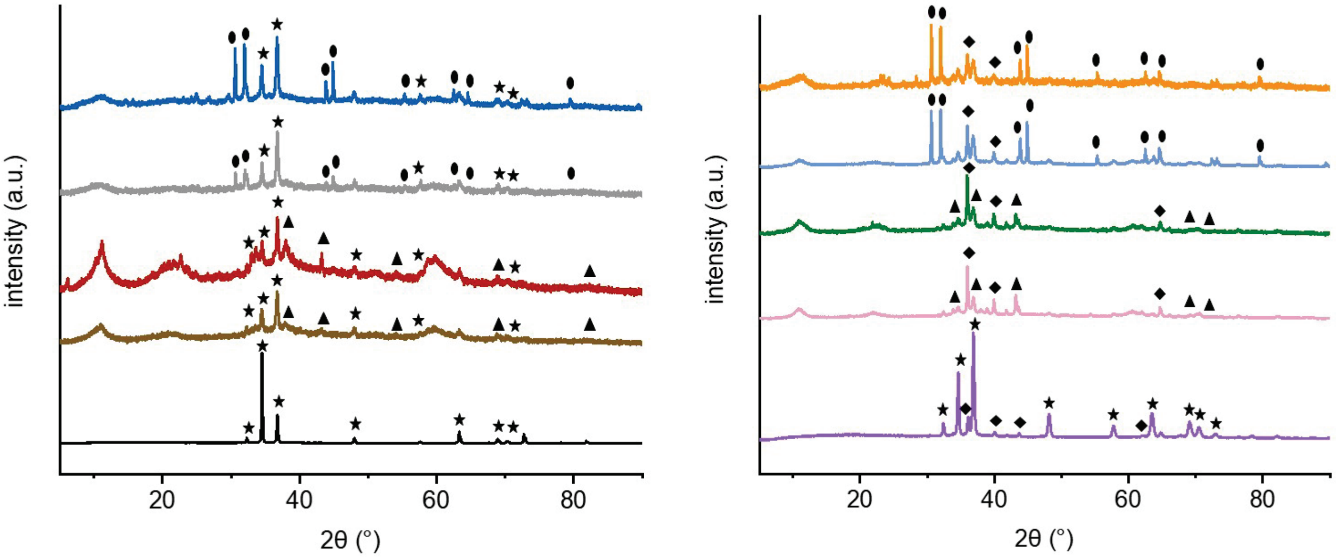

(**a**) (**b**)

Figure 10. (**a**) XRD spectra of AZ31 alloy samples: bare AZ31 alloy (black), AZ31 alloy etched with $ZnCl_2$ (brown) and etched with $SnCl_2$ (red), and AZ31 alloy etched with $ZnCl_2$ and a superhydrophobic surface (grey) and etched with $SnCl_2$ and a superhydrophobic surface (blue). (**b**) XRD spectra of AZ91 alloy samples: bare AZ91 alloy (violet), AZ91 alloy etched with $ZnCl_2$ (pink) and etched with $SnCl_2$ (light blue), and AZ91 alloy etched with $ZnCl_2$ and with a superhydrophobic surface (green) and etched with $SnCl_2$ and a superhydrophobic surface (orange). The peaks corresponding to tin, zinc, magnesium, and $Al_{12}Mg_{17}$ are shown by circles, triangles, stars, and diamonds, respectively.

In the FTIR spectrum of stearic acid, a strong band at 1698 cm^{-1} was present and corresponded to the asymmetric stretching of carboxyl groups. This characteristic band disappeared in the spectra of superhydrophobic samples and two new distinguishable bands appeared instead. These two bands situated in the range of 1530–1560 and 1390–1460 cm^{-1} were ascribed to asymmetric and symmetric stretching in metal carboxylate. The FTIR spectra of superhydrophobic magnesium alloys etched with the $ZnCl_2$ solution exhibited bands at 1538 and 1397 cm^{-1}, perfectly corresponding to the positions of the zinc stearate bands [32]. These bands were not present in the FTIR spectra of the etched magnesium alloys. It is noteworthy that Xie et al. [17] obtained magnesium stearate, as indicated by the bands of the published FTIR spectrum, although they applied the same method to AZ31 alloy. On the other hand, Zhang et al. [12] observed the formation of zinc stearate when they prepared a superhydrophobic surface on AZ31 alloy in a one-step method using $ZnCl_2$ and stearic acid. Their results suggest that the form of the stearate did not affect the value of the contact angle, as both works presented a contact angle of about 162°. The occurrence of zinc stearate in our investigated samples is also supported by XPS analysis; see below.

In the case of superhydrophobic magnesium alloys etched with $SnCl_2$, FTIR spectra revealed relatively broad bands centered at 1560 and 1465 cm^{-1}, predominantly indicating the presence of magnesium stearate instead of the expected stannous stearate [33]. A minority formation of stannate stearate cannot be completely ruled out because the band corresponding to the asymmetric vibration was slightly shifted to lower wavenumbers compared to the band corresponding to magnesium stearate [32,33]. It should be noted that the bands identified as carboxylates were not observed in the FTIR spectra of the etched magnesium alloys.

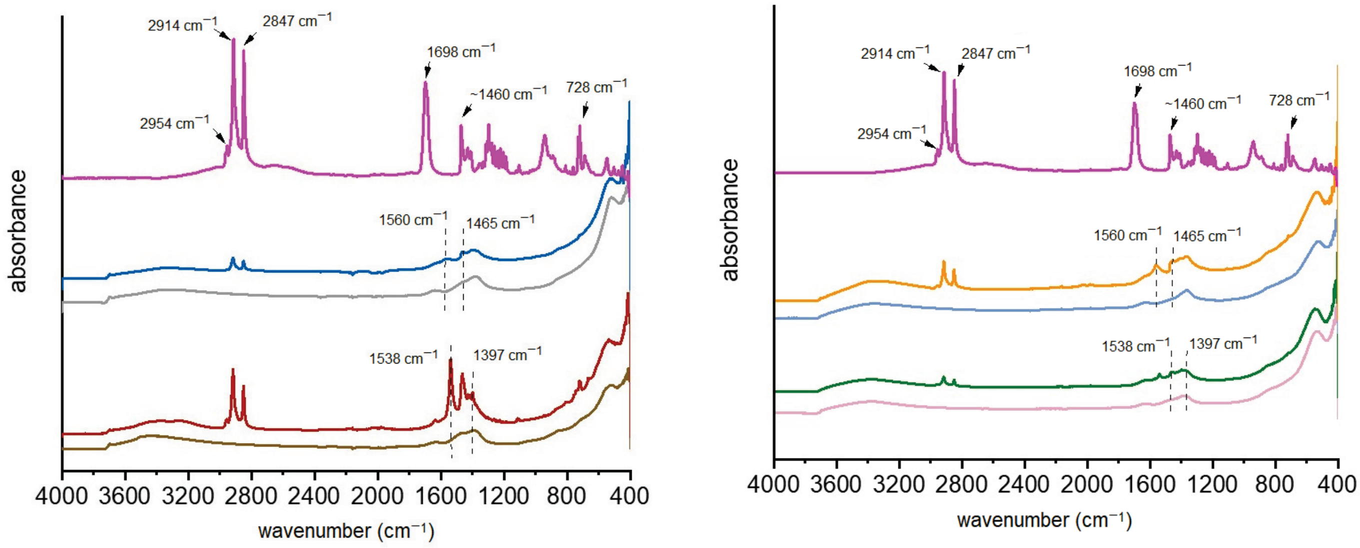

(**a**) (**b**)

Figure 11. (**a**) FTIR spectra of the following: stearic acid (purple), AZ31 alloy etched with $ZnCl_2$ (brown) and etched with $SnCl_2$ (grey), and superhydrophobic surfaces of AZ31 alloy etched with $ZnCl_2$ (red) and etched with $SnCl_2$ (dark blue). (**b**) FTIR spectra of the following: stearic acid (purple), AZ91 alloy etched with $ZnCl_2$ (pink) and etched with $SnCl_2$ (light blue), and superhydrophobic surfaces of AZ91 alloy etched with $ZnCl_2$ (green) and etched with $SnCl_2$ (orange).

3.8. XPS Analysis

XPS analysis was used to identify the chemical state of Mg, Zn, and Sn for the superhydrophobic samples. The Mg 1s spectra of stearic-acid-modified AZ31 and AZ91 alloys etched with $ZnCl_2$ (Figure 12) contained one strong peak at 1304.1 eV corresponding to the presence of $Mg(OH)_2$ [34]. The high-resolution XPS spectra of Zn 2p was characterized by two peaks assigned to Zn $2p_{1/2}$ and Zn $2p_{3/2}$. These two peaks, which appear due to the spin-orbit splitting, are well-separated and therefore only Zn $2p_{3/2}$ peaks can be considered for the assignment of zinc chemical state. Deconvolution of the Zn $2p_{3/2}$ peak for both superhydrophobic samples revealed the occurrence of one chemical state with a binding energy of 1022.4 eV, which was higher than the binding energy of Zn, ZnO, and $Zn(OH)_2$ [35]. Consequently, the binding value received was attributed to zinc stearate. These results are in agreement with the findings of FTIR analysis, which confirmed the presence of zinc stearate.

The Mg 1s spectrum of stearic-acid-modified AZ31 alloy etched with $SnCl_2$ (Figure 12a) contained a single peak with a binding energy of 1304.1 eV corresponding to $Mg(OH)_2$. The shift in binding energy to 1304.4 eV in the Mg 1s spectrum for stearic-acid-modified AZ91 alloy etched with $SnCl_2$ (Figure 12b) may be an indicator of the presence of magnesium stearate, which has a binding energy of about 1304.8 eV [36]. The high-resolution XPS spectra of Sn 3d comprised two peaks assigned to Sn $3d_{3/2}$ and Sn $3d_{5/2}$. For the same reasons as in the case of the Zn 2p XPS spectra, only the Sn $3d_{5/2}$ peaks were fitted. For stearic-acid-modified AZ31 alloy etched with $SnCl_2$ (Figure 12a), one peak with a binding energy of 486.7 eV was found to be attributed to SnO_2 [37]. By deconvolution of Sn $3d_{5/2}$ for the stearic-acid-modified AZ91 alloy etched with $SnCl_2$ (Figure 12b), two peaks with binding energies of 486.8 and 484.5 eV were found, which were attributed to SnO_2 and elemental tin, respectively [37]. The occurrence of tin and its oxide and $Mg(OH)_2$ is in agreement with previous spectrometric analyses. Unfortunately, the XPS analysis did not unambiguously identify magnesium stearate, which is assumed to be present in the samples based on FTIR analysis. On the other hand, stannous stearate was not observed at all in the XPS spectra. The inconclusive evidence of stearate in the XPS spectra can be explained by the fact that the signal was collected from an area very poor in stearate and/or by the interfering contribution of $Mg(OH)_2$ to the Mg 1s spectrum.

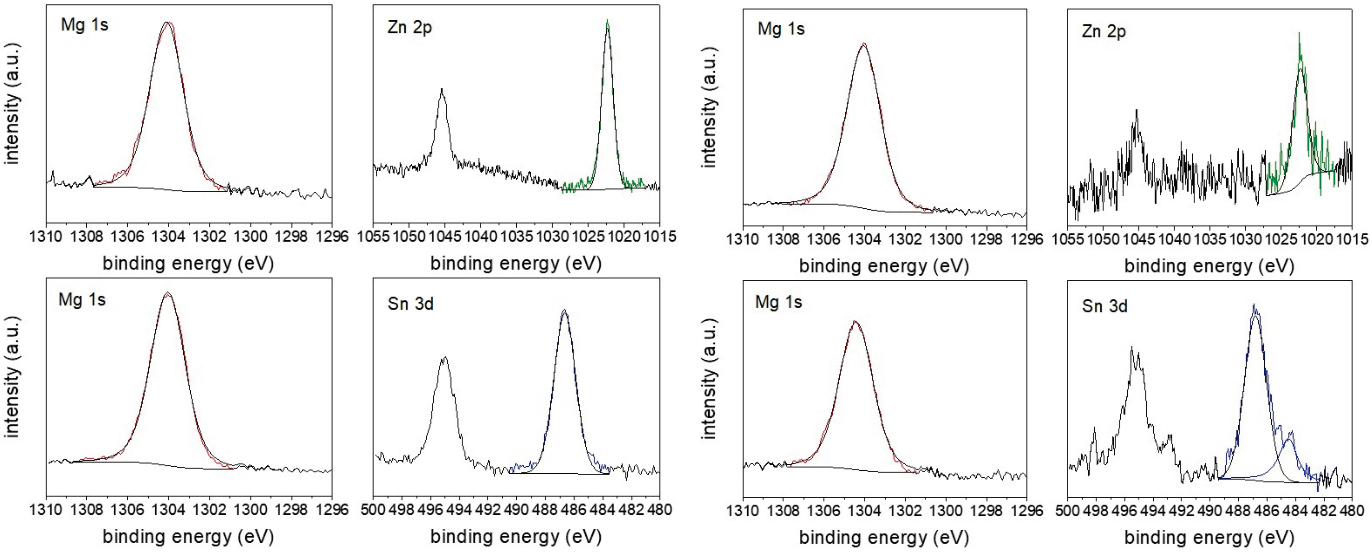

(**a**) (**b**)

Figure 12. (**a**) XPS spectra for the stearic-acid-modified AZ31 alloy etched with $ZnCl_2$ (top pair) and $SnCl_2$ (bottom pair); (**b**) XPS spectra for the stearic-acid-modified AZ91 alloy etched with $ZnCl_2$ (top pair) and $SnCl_2$ (bottom pair).

3.9. Chemism of the Etching and Preparation of Superhydrophobic Surface

On the basis of the results presented in this paper and published in the literature [12,17,24,26,27,38], reaction steps were proposed to describe the etching process and the reaction of the formed products with stearic acid.

The etchant $ZnCl_2$ underwent hydrolysis to form $Zn(OH)_2$ or ZnO and H^+ ions, which gave the solution an acidic pH. The process can be described by the following Equations (1) and (2).

$$ZnCl_2 + 2H_2O \leftrightarrow Zn(OH)_2 + 2HCl \quad (1)$$

$$ZnCl_2 + H_2O \leftrightarrow ZnO + HCl \quad (2)$$

The generated H^+ ions reacted with the magnesium (Equation (3)) contained in the α phase of the magnesium alloys (AZ31 and AZ91), while the other phases with higher electrode potentials remained more intact by corrosion. This led to the formation of a rough surface, as described above (Figures 2 and 4).

$$Mg + 2H^+ \rightarrow Mg^{2+} + H_2 \quad (3)$$

The reaction rate was undoubtedly facilitated by the higher temperature, as a relatively large heat was released during the hydrolysis.

The released H^+ ions could react with the formed ZnO to form Zn^{2+}, as described by Equation (4):

$$ZnO + 2H^+ \leftrightarrow Zn^{2+} + H_2O \quad (4)$$

The consumption of H^+ ions shifted the chemical equilibrium of both hydrolysis reactions to the right in favor of $Zn(OH)_2$ or ZnO.

The elemental zinc frequently observed in the form of dendrites was produced by the reaction of the etchant with the magnesium alloy (5).

$$ZnCl_2 + Mg \rightarrow Zn + MgCl_2 \tag{5}$$

In addition to the above reactions, corrosion reactions of the magnesium alloy with water and chloride ions could simultaneously take place according to the sequence of reactions (6) and (7):

$$Mg + 2H_2O \rightarrow Mg(OH)_2 + H_2 \tag{6}$$

$$Mg(OH)_2 + 2Cl^- \rightarrow MgCl_2 + 2OH^- \tag{7}$$

The XRD analysis indicated the presence of $Mg_2Cl(OH)_3$, which could have been formed during the etching process according to reaction (8) [30]:

$$3Mg(OH)_2 + Mg^{2+} + 2Cl^- \rightarrow 2Mg_2Cl(OH)_3 \tag{8}$$

The OH^- anions generated by the reaction (7), including those from the hydrolysis of $Mg(OH)_2$, could participate in the following interaction (9):

$$Zn^{2+} + 2OH^- \rightarrow Zn(OH)_2 \tag{9}$$

Zn(OH)Cl could theoretically be formed as a minor by-product of hydrolysis [25].

$$Zn^{2+} + H_2O + Cl^- \leftrightarrow Zn(OH)Cl + H^+ \tag{10}$$

During the superhydrophobic process, stearic acid interacted with Zn^{2+} ions to form zinc stearate (11), as shown by FTIR and XPS analysis.

$$Zn^{2+} + 2CH_3(CH_2)_{16}COOH \rightarrow Zn[CH_3(CH_2)_{16}COO]_2 + 2H^+ \tag{11}$$

Unfortunately, stearates are generally highly sensitive to pH and therefore can easily undergo hydrolysis in acidic or alkaline environments. This is a limitation of superhydrophobic surfaces prepared with stearic acid. On the other hand, since blood has a pH of about 7.4 due to its natural buffering system, the relatively long-term stability of stearates can be expected.

The reaction steps during etching with the $SnCl_2$ solution can be understood in a similar way. The hydrolysis of $SnCl_2$ could provide two stable compounds involving Sn(OH)Cl and SnO_2, as described by reactions (12) and (13):

$$Sn^{2+} + H_2O + Cl^- \leftrightarrow Sn(OH)Cl + H^+ \tag{12}$$

$$2Sn^{2+} + O_2 + 2H_2O \leftrightarrow 2SnO_2 + 4H^+ \tag{13}$$

The formation of $Sn(OH)_2$ (including $Sn(OH)_4$) is unlikely because its preparation from an aqueous solution has not yet been described in the literature [39]. The released H^+ ions reacted with magnesium, as described above by chemical Equation (3). Reducing the amount of H^+ ions shifted the chemical equilibrium of reactions (12) and (13) to the right, towards the products. This shift in equilibrium was visually observed by the precipitation of a white precipitate from the solution during etching. Similar to the previously described etchant, $SnCl_2$ reacted with the magnesium and was reduced to elemental tin (14), which was demonstrated by the XRD, the XPS, and the EDS analysis.

$$SnCl_2 + Mg \rightarrow Sn + MgCl_2 \tag{14}$$

Surface analysis in the case of cast AZ91 alloy showed that Sn/SnO_2 were mainly accumulated on the residues of the β phase (Figure 5A,D) because these sites had a higher electrode potential than the corroded magnesium-rich α phase. This was not observed in the case of wrought AZ31 alloy, since its microstructure is de facto homogeneous and composed of magnesium-rich grains. We believe that the observed phenomenon is associated with the different electrode potentials of the α and β phases. The dissolution of magnesium from the α phase produced electrons (15) that were consumed by Sn^{2+} ions on the β phase (16).

$$Mg \rightarrow Mg^{2+} + 2e^{-} \tag{15}$$

$$Sn^{2+} + 2e^{-} \rightarrow Sn \tag{16}$$

The occurrence of Sn^{4+} ions was demonstrated by XPS and EDS analysis; thus, elemental tin occurring on the surface of magnesium alloys did not reduce Sn^{4+} ions to Sn^{2+} according to chemical Equation (17), as would be inferred from standard electrode potentials.

$$Sn + Sn^{4+} \rightarrow Sn^{2+} + 2e^{-} \tag{17}$$

During the superhydrophobic process, stearic acid interacted with Mg^{2+} ions to form stearate, as indicated by FTIR analysis; this interaction can be described by Equation (18).

$$Mg^{2+} + 2CH_3(CH_2)_{16}COOH \rightarrow Mg[CH_3(CH_2)_{16}COO]_2 + 2H^{+} \tag{18}$$

Theoretically, stearic acid could also react to a minor extent with Sn^{2+} ions to form stannous stearate, as described by (19). However, it should be emphasized that stannous stearate in the superhydrophobic samples was not detected by any of the spectrometric methods used.

$$Sn^{2+} + 2CH_3(CH_2)_{16}COOH \rightarrow Sn[CH_3(CH_2)_{16}COO]_2 + 2H^{+} \tag{19}$$

Superhydrophobic surfaces of magnesium alloys etched with $ZnCl_2$ or $SnCl_2$ appear to be a possible strategy for the protection of magnesium materials in medicine applications. The prepared samples not only had enhanced corrosion resistance but also contained $Zn/Zn(OH)_2$ or Sn/SnO_2, which could improve the biological properties. The corrosion behavior was monitored in PBS solution in this work, but for a deeper evaluation it is desirable to perform long-term experiments in simulated physiological solutions with respect to the location of the magnesium implant in the body. The positive effect of $Zn/Zn(OH)_2$ or Sn/SnO_2 in superhydrophobic samples on biological properties also needs to be demonstrated and monitored as a function of time. Future work will therefore focus on these areas of research. Mechanical stability is a hot issue of superhydrophobic materials, which limits their long-term applications in practice [10]. However, the development of advanced magnesium implants may be a solution, as a superhydrophobic surface can provide biological protection, which is crucial at the beginning of implant placement in the body, and corrosion protection can continue through appropriate coatings on the surface of the magnesium material [23].

4. Conclusions

The chemical etching of magnesium alloys led to surface roughening with a micro- and nano-scale hierarchical structure. The surface morphology of magnesium alloys etched with $ZnCl_2$ or $SnCl_2$ contained regions of nanoscale $Zn/Zn(OH)_2$ or Sn/SnO_2 crystals and platelet-like $Mg(OH)_2$ crystals. AZ91 alloy etched with $SnCl_2$ also contained observable residues of the β phase of the original alloy microstructure, which preferentially contained Sn/SnO_2 crystals. Stearic acid bound to the surface of $ZnCl_2$- and $SnCl_2$-etched magnesium alloys in the form of zinc stearate and magnesium stearate, respectively. The superhydrophobic surfaces on AZ31 alloy etched with $ZnCl_2$ and $SnCl_2$ improved the corrosion resistance compared to bare AZ31 alloy. The improvement of the corrosion resistance of AZ91 alloy was observed only in the case of the superhydrophobic surface of the alloy etched with $SnCl_2$. The results show that the microstructure of magnesium alloys can have an impact on the surface roughening and consequently some physicochemical properties (wettability and corrosion resistance) of the surface modified with stearic acid. A sequence of reactions is proposed to describe the chemical processes during the etching of AZ31 and AZ91 alloys and their subsequent modification with stearic acid. Future research will focus on long-term corrosion tests and the investigation of biological properties, with an emphasis on the antibacterial effects of the presented superhydrophobic magnesium alloys.

Supplementary Materials: The following are available online at https://www.mdpi.com/article/10.3390/coatings12101414/s1, Figure S1: SEM images of AZ31 alloy etched with $ZnCl_2$ (A–C) and $SnCl_2$ for 15 min (D–F). Details B and E show the regions of zinc and tin, respectively, and details C and F show the $Mg(OH)_2$ regions.; Figure S2: SEM images of AZ91 alloy etched with $ZnCl_2$ (A–C) and $SnCl_2$ for 15 min (D–F). Details B and E show the regions of zinc and tin, respectively, and details C and F show the $Mg(OH)_2$ regions; Figure S3: EDS energy spectra of the magnesium alloys etched with $ZnCl_2$ and $SnCl_2$ for 2 and 10 min; Figure S4: Images of water droplets on (a) stearic acid-modified AZ31 alloy etched with $ZnCl_2$, (b) stearic acid-modified AZ31 alloy etched with $SnCl_2$, (c) stearic acid-modified AZ91 alloy etched with $ZnCl_2$, (d) stearic acid-modified AZ91 alloy etched with $SnCl_2$; Figure S5: FTIR spectra of bare AZ31 alloy (black) and bare AZ91 alloy (purple); Table S1: Elemental composition determined by the EDS method for different regions subject to SEM analysis. The regions of elemental composition correspond to the SEM images; see Figures S1 and S2; Table S2: Contact angles measured on stearic acid-modified magnesium alloys etched with $ZnCl_2$ and $SnCl_2$ for 15 min.

Author Contributions: L.D. and P.Š. conceived and designed the experiments; P.Š., M.B., J.M. and J.W. performed the experiments; P.Š., J.W., M.B., L.K., M.H. and J.M. analyzed the data; L.D. and P.Š. wrote the paper. All authors have read and agreed to the published version of the manuscript.

Funding: This work was supported by Specific University Research at FCH BUT, Project No. FCH-S-22-8012, Ministry of Education, Youth and Sports of the Czech Republic.

Institutional Review Board Statement: Not applicable.

Informed Consent Statement: Not applicable.

Data Availability Statement: The data supporting the results are contained within the article.

Conflicts of Interest: The authors declare no conflict of interest. The sponsors had no role in the design of the study; in the collection, analyses, or interpretation of data; in the writing of the manuscript; or in the decision to publish the results.

References

1. Esmaily, M.; Svensson, J.E.; Fajardo, S.; Birbilis, N.; Frankel, G.S.; Virtanen, S.; Arrabal, R.; Thomas, S.; Johansson, L.G. Fundamentals and advances in magnesium alloy corrosion. *Prog. Mater. Sci.* **2017**, *89*, 92–193. [CrossRef]
2. Saji, V.S. Organic conversion coatings for magnesium and its alloys. *J. Ind. Eng. Chem.* **2019**, *75*, 20–37. [CrossRef]
3. Dziková, J.; Fintová, S.; Kajánek, D.; Florková, Z.; Wasserbauer, J.; Doležal, P. Characterization and Corrosion Properties of Fluoride Conversion Coating Prepared on AZ31 Magnesium Alloy. *Coatings* **2021**, *11*, 675. [CrossRef]
4. Wasserbauer, J.; Buchtík, M.; Tkacz, J.; Fintová, S.; Minda, J.; Doskočil, L. Improvement of AZ91 Alloy Corrosion Properties by Duplex NI-P Coating Deposition. *Materials* **2020**, *13*, 1357. [CrossRef] [PubMed]
5. Buchtík, M.; Doskočil, L.; Brescher, R.; Doležal, P.; Másilko, J.; Wasserbauer, J. The Effect of Crystallization and Phase Transformation on the Mechanical and Electrochemical Corrosion Properties of Ni-P Coatings. *Coatings* **2021**, *11*, 447. [CrossRef]
6. Hadzima, B.; Kajánek, D.; Jambor, M.; Drábiková, J.; Březina, M.; Buhagiar, J.; Pastorková, J.; Jacková, M. PEO of AZ31 Mg Alloy: Effect of Electrolyte Phosphate Content and Current Density. *Metals* **2020**, *10*, 1521. [CrossRef]
7. Tomozawa, M.; Hiromoto, S. Microstructure of hydroxyapatite- and octacalcium phosphate-coatings formed on magnesium by a hydrothermal treatment at various pH values. *Acta Mater.* **2011**, *59*, 355–363. [CrossRef]
8. Tabish, M.; Yasin, G.; Anjum, M.J.; Malik, M.U.; Zhao, J.; Yang, Q.; Manzoor, S.; Murtaza, H.; Khan, W.Q. Reviewing the current status of layered double hydroxide-based smart nanocontainers for corrosion inhibiting applications. *J. Mater. Res. Technol.* **2021**, *10*, 390–421. [CrossRef]
9. Peng, F.; Wang, D.; Tian, Y.; Cao, H.; Qiao, Y.; Liu, X. Sealing the Pores of PEO Coating with Mg-Al Layered Double Hydroxide: Enhanced Corrosion Resistance, Cytocompatibility and Drug Delivery Ability. *Sci. Rep.* **2017**, *7*, 8167. [CrossRef]
10. Yao, W.; Wu, L.; Huang, G.; Jiang, B.; Atrens, A.; Pan, F. Superhydrophobic coatings for corrosion protection of magnesium alloys. *J. Mater. Sci. Technol.* **2020**, *52*, 100–118. [CrossRef]
11. Yeganeh, M.; Mohammadi, N. Superhydrophobic surface of Mg alloys: A review. *J. Magnes. Alloy.* **2018**, *6*, 59–70. [CrossRef]

12. Zhang, X.; Shen, J.; Hu, D.; Duan, B.; Wang, C. A rapid approach to manufacture superhydrophobic coating on magnesium alloy by one-step method. *Surf. Coat. Technol.* **2018**, *334*, 90–97. [CrossRef]
13. Zheng, T.; Hu, Y.; Pan, F.; Zhang, Y.; Tang, A. Fabrication of corrosion-resistant superhydrophobic coating on magnesium alloy by one-step electrodeposition method. *J. Magnes. Alloy.* **2019**, *7*, 193–202. [CrossRef]
14. Mohamed, A.M.A.; Abdullah, A.M.; Younan, N.A. Corrosion behavior of superhydrophobic surfaces: A review. *Arab. J. Chem.* **2015**, *8*, 749–765. [CrossRef]
15. Liu, T.; Chen, S.; Cheng, S.; Tian, J.; Chang, X.; Yin, Y. Corrosion behavior of super-hydrophobic surface on copper in seawater. *Electrochim. Acta* **2007**, *52*, 8003–8007. [CrossRef]
16. Falde, E.J.; Yohe, S.T.; Colson, Y.L.; Grinstaff, M.W. Superhydrophobic materials for biomedical applications. *Biomaterials* **2016**, *104*, 87–103. [CrossRef] [PubMed]
17. Xie, J.; Hu, J.; Fang, L.; Liao, X.; Du, R.; Wu, F.; Wu, L. Facile fabrication and biological properties of super-hydrophobic coating on magnesium alloy used as potential implant materials. *Surf. Coat. Technol.* **2020**, *384*, 125223. [CrossRef]
18. Xun, X.; Wan, Y.; Zhang, Q.; Gan, D.; Hu, J.; Luo, H. Low adhesion superhydrophobic AZ31B magnesium alloy surface with corrosion resistant and anti-bioadhesion properties. *Appl. Surf. Sci.* **2020**, *505*, 144566. [CrossRef]
19. Wang, H.; Wei, Y.; Liang, M.; Hou, L.; Li, Y.; Guo, C. Fabrication of stable and corrosion-resisted super-hydrophobic film on Mg alloy. *Colloids Surf. A Physicochem. Eng. Asp.* **2016**, *509*, 351–358. [CrossRef]
20. Zang, D.; Zhu, R.; Wu, C.; Yu, X.; Zhang, Y. Fabrication of stable superhydrophobic surface with improved anticorrosion property on magnesium alloy. *Scr. Mater.* **2013**, *69*, 614–617. [CrossRef]
21. Khalifeh, S.; Burleigh, T.D. Super-hydrophobic stearic acid layer formed on anodized high purified magnesium for improving corrosion resistance of bioabsorbable implants. *J. Magnes. Alloy.* **2018**, *6*, 327–336. [CrossRef]
22. Mensink, R.P. Effects of stearic acid on plasma lipid and lipoproteins in humans. *Lipids* **2005**, *40*, 1201–1205. [CrossRef]
23. Lin, Z.; Sun, X.; Yang, H. The Role of Antibacterial Metallic Elements in Simultaneously Improving the Corrosion Resistance and Antibacterial Activity of Magnesium Alloys. *Mater. Des.* **2021**, *198*, 109350. [CrossRef]
24. Song, J.; Lu, Y.; Huang, S.; Liu, X.; Wu, L.; Xu, W. A simple immersion approach for fabricating superhydrophobic Mg alloy surfaces. *Appl. Surf. Sci.* **2013**, *266*, 445–450. [CrossRef]
25. Tanaka, H.; Fujioka, A.; Futoyu, A.; Kandori, K.; Ishikawa, T. Synthesis and characterization of layered zinc hydroxychlorides. *J. Solid State Chem.* **2007**, *180*, 2061–2066. [CrossRef]
26. Pettine, M.; Millero, F.J.; Macchi, G. Hydrolysis of Tin(II) in Aqueous Solutions. *Anal. Chem.* **1981**, *53*, 1039–1043. [CrossRef]
27. Ambat, R.; Zhou, W. Electroless nickel-plating on AZ91D magnesium alloy: Effect of substrate microstructure and plating parameters. *Surf. Coat. Technol.* **2004**, *179*, 124–134. [CrossRef]
28. Safarpour, M.; Hosseini, S.A.; Ahadani-Targhi, F.; Vašina, P.; Alishahi, M. A transition from petal-state to lotus-state in AZ91 magnesium surface by tailoring the microstructure. *Surf. Coat. Technol.* **2020**, *383*, 125239. [CrossRef]
29. Zheng, T.; Hu, Y.; Zhang, Y.; Pan, F. Formation of a hydrophobic and corrosion resistant coating on magnesium alloy via a one-step hydrothermal method. *J. Colloid Interface Sci.* **2017**, *505*, 87–95. [CrossRef]
30. Lojka, M.; Jankovský, O.; Jiříčková, A.; Lauermannová, A.M.; Antončík, F.; Sedmidubský, D.; Pavlík, Z.; Pavlíková, M. Thermal Stability and Kinetics of Formation of Magnesium Oxychloride Phase 3Mg(OH)2·MgCl2·8H2O. *Materials* **2020**, *13*, 767. [CrossRef]
31. Doskočil, L.; Enev, V.; Pekař, M.; Wasserbauer, J. The spectrometric characterization of lipids extracted from lignite samples from various coal basins. *Org. Geochem.* **2016**, *95*, 34–40. [CrossRef]
32. Dou, Q.; Ng, K.M. Synthesis of various metal stearates and the corresponding monodisperse metal oxide nanoparticles. *Powder Technol.* **2016**, *301*, 949–958. [CrossRef]
33. Nep, E.I.; Conway, B.R. Preformulation studies on grewia gum as a formulation excipient. *J. Therm. Anal. Calorim.* **2012**, *108*, 197–205. [CrossRef]
34. Chubar, N. The influence of sulfate on selenite sorption on Mg-Al-CO3 layered double hydroxides prepared by fine inorganic sol-gel synthesis studied by X-ray photoelectron spectroscopy. *Appl. Surf. Sci.* **2018**, *459*, 281–291. [CrossRef]
35. Polyakov, N.A.; Botryakova, I.G.; Glukhov, V.G.; Red'kina, G.V.; Kuznetsov, Y.I. Formation and anticorrosion properties of superhydrophobic zinc coatings on steel. *Chem. Eng. J.* **2021**, *421*, 127775. [CrossRef]
36. Lebeau, D.; Beuvier, L.; Cornaton, M.; Miserque, F.; Tabarant, M.; Esnouf, S.; Ferry, M. Aging of magnesium stearate under high doses gamma irradiation and oxidative conditions. *J. Nucl. Mater.* **2015**, *460*, 130–138. [CrossRef]
37. Kwoka, M.; Ottaviano, L.; Passacantando, M.; Santucci, S.; Czempik, G.; Szuber, J. XPS study of the surface chemistry of L-CVD SnO_2 thin films after oxidation. *Thin Solid Films.* **2005**, *490*, 36–42. [CrossRef]
38. Niazi, S.; Olsen, E.; Nygård, S.H. Hydrolysis of eutectic compositions in the ZnCl2: KCl:NaCl ternary system and effect of adding ZnO. *J. Mol. Liq.* **2020**, *317*, 114069. [CrossRef]
39. Greenwood, N.N.; Earnshaw, A. *Chemistry of the Elements*, 1st ed.; Informatorium: Prague, Czech Republic, 1993; pp. 469–470.

coatings

MDPI

Article

In Situ Polymerization to Boron Nitride-Fluorinated Poly Methacrylate Composites as Thin but Robust Anti-Corrosion Coatings

Qingqing Hu [1], Aijuan Lv [1], Yukang Ma [1], Yan Wang [1], Haoyi Zhang [1], Xin Mi [2] and Qiang Xiao [1,*]

[1] Key Laboratory of the Ministry of Education for Advanced Catalysis Materials, Institute of Advanced Fluorine-Containing Materials, Zhejiang Normal University, Jinhua 321004, China; huqingqing@zjnu.edu.cn (Q.H.); lvaijuan@zjnu.edu.cn (A.L.); CopeeM@zjnu.edu.cn (Y.M.); wangyan1618@zjnu.edu.cn (Y.W.); zhanghy@zjnu.edu.cn (H.Z.)

[2] Beijing Thinvec Co. Ltd., Beijing 100176, China; technical@thinvec.com

* Correspondence: xiaoq@zjnu.edu.cn

Abstract: High-performance anti-corrosion coatings featuring easy processability and thin thickness are highly desired in industry. Yet, solution process coating often faces a sedimentation problem with particles which are used as reinforcement in coatings. In this contribution, boron nitride (BN) was modified by an acrylate silane coupling agent (KH-570) to obtain acrylated BN flakes. Afterwards, the acrylated BN flakes were in situ copolymerized with 2-(perfluorohexyl)ethyl methacrylate to synthesize BN-fluorinated poly methacrylate (PFBP) composites. The as-obtained PFBP composites can form stable coating solutions, in which sedimentation of BN flakes seldom happens. The coating solution can easily form uniform coatings on various substrates with nanoscale thickness, confirmed by scanning electron microscope (SEM). The corrosion resistance of the samples coated PFBP coatings in 3.5 wt.% sodium chloride solution was evaluated by electrochemical impedance spectroscopy (EIS). It is indicated that the incorporation of BN flakes greatly reduce the corrosion rate. Adhesion measurements and abrasion resistance test indicate the PFBP coating performs good adhesion to substrate and robustness. Through the in situ polymerization, acrylated BN flakes are connected with the polymer chain, which inhibits the sedimentation of BN in the coating solution. Additionally, the BN flakes dispersed in the fluorinated polymer act as barriers, improving the corrosion resistance of the coated samples.

Keywords: in situ polymerization; boron nitride; corrosion resistant; coating; fluorinated polymethacrylate; anti-moisture

1. Introduction

Anti-moisture and anti-corrosion for the metallic components are highly desirable in industry. Coating with polymeric film is one of the most effective and convenient methods to prevent the corrosion of metal. Through forming a water-repellent coating film as a barrier, polymer coatings protect the metal surface from corrosion [1]. At present, the protective polymeric coatings widely used in the electronic industry include fluorine-containing resin, epoxy resin, phenolic resin, etc. [2]. Among them, fluorine-containing resin features low surface energy, low water absorption, high hydrophobicity and high stability [3,4]. Compared to the widely used fluorinated resins, e.g., polytetrafluoroethylene (PTFE), which can be hardly dissolved in solvent, fluorinated polyacrylate is soluble in some fluorous solvents, resulting in an ease of processibility in forming films on substrate [5–7]. The coatings with high performance usually rely on high barrier property and good adhesion to substrate. Reinforcement with nanomaterials could improve the anticorrosion property of fluorinated polymer by inhibiting the permeation of corrosion media and forming superhydrophobic surface [7,8]. In recent years, the rise of graphene has aroused people's attention in the field of anticorrosion [9]. By virtue of the large high aspect ratio and impermeability to gases, graphene holds promise as an effective anticorrosion barrier when incorporated in anticorrosive coatings [10–13]. However, the high conductivity of graphene limits its long-term application in the protection of electronic products [14].

Boron nitride (BN), which has a layered structure similar to graphene, features high resistivity, excellent thermal conductivity and high impermeability [15–18]. Shen et al. demonstrated that monolayer BN exhibited much better long-term corrosion barrier performance than graphene [14]. Jiang et al. reported an in situ synthesis of BN coatings on substrates, which can effectively prevent the substrates from being oxidized or corrosion [19]. BN could also be added in polymeric coatings as filler, finding an improvement of anti-corrosion performance. Husain et al. illustrated that h-BN/PVA hybrid coatings showed an improved corrosion protection against simulated seawater media [20]. Additionally, incorporation into epoxy resin (EP) has verified BN is a good reinforcement material. To improve the compatibility of BN and the EP, non-covalent modification of BN has been made with various chemicals such as polydopamine (PDA) [21], carboxylated aniline trimer (CAT) [22] and tannins acid (TA) [23,24], etc. Oh et al. prepared BN/polymethyl methacrylate (PMMA) composites with high thermal conductivity using an in situ polymerization process. BN was bonded with vinyltriethoxysilane to introduce double bonds, and it was directly linked with the PMMA chains during the polymerization step. The BN/PMMA composites exhibited an obvious thermal conductivity enhancement, with a value that was 17.8 times higher than that of PMMA [25]. Very recently, He et al. initiated an in situ anionic polymerization of methyl methacrylate on the exfoliated BN nanosheets. The PMMA chains grafted on the BN nanosheets enhanced the solubility in solvent [26].

From the above, a great deal of work relating to the incorporation of layered materials (graphene, BN, etc.) into polymer coatings has been reported. However, seldom has work been focused on the incorporation of these layered materials into fluorinated polymethacrylate systems. In a fluorous composite coating system, which has low viscosity, sedimentation of the incorporated layered materials can hardly be avoided.

In this contribution, BN powder was firstly exfoliated to flakes using a wet ball-milling method followed by modification of 3-(trimethoxysilyl)propyl methacrylate (KH-570). Then, the acrylated BN flakes was in situ polymerized with 2-(perfluorohexyl)ethyl methacrylate (C6Rf) to obtain BN-fluorinated poly methacrylate (PFBP) composites by a precipitation polymerization method. The PFBP composites can be well dissolved in a fluorous solvent forming a stable suspension. BN flakes are covalently bonded to the polymer matrix, which on one hand, eliminates the possible appearance of voids between BN flakes and polymer; on the other hand, inhibits the sedimentation of BN from the coating solution. BN flakes are well dispersed in the polymer matrix and the formed PFBP coatings display greatly enhanced corrosion resistance property.

2. Material and Methods

2.1. Materials

Sodium chloride (NaCl) and boron nitride (BN) were purchased from Aladdin Chemical Co. Ltd., Shanghai, China. 3-(Trimethoxysilyl)propyl methacrylate (KH-570) was acquired from Yuanye Biological Technology Co. Ltd., Shanghai, China. Butyl acetate (BAC) and azodiisobutyronitrile (AIBN) were purchased from J&K Scientific Ltd., Shanghai, China. Hydrofluoroether 1-(ethoxy)nonafluorobutane (HFE-7200) was purchased from 3M China. 2-(perfluorohexyl)ethyl methacrylate (C6Rf) was supplied by Beijing Thinvec Co. Ltd., Beijing, China. Before experiments, all of the copper sheets and Q235 steel sheets were cleaned in an ultrasonic bath for several times in a sequence of acetone, anhydrous ethanol, and deionized water. AIBN was purified by recrystallization prior to use, while other reagents were used as-received.

2.2. In Situ Polymerization

The in situ polymerization process is illustrated in Scheme 1. A horizontal planetary milling was used for dispersion of BN, according to ref. [27]. In a typical run, 2 g of micron-sized BN powder mixed with 2 M aqueous NaOH solution were loaded into a stainless steel grinding bowl with steel balls. The BN/NaOH solution mixture was milled for 24 h. The ground product was rinsed with HCl solution and repeatedly washed with deionized water until the pH was close to neutral. After the sample was dried, it was dispersed in IPA and sonicated at 45 kHz for 1 h. Then, 2.5 g KH-570 and 0.4 g ammonia water were added, sonicated at 45 kHz for 1 h, followed by stirring at 60 °C for 12 h. The product was centrifuged at 2000 g for 10 min and the top 3/4 of the supernatant was filtered to recover the final product. The acrylated BN flakes was referred to as BN570.

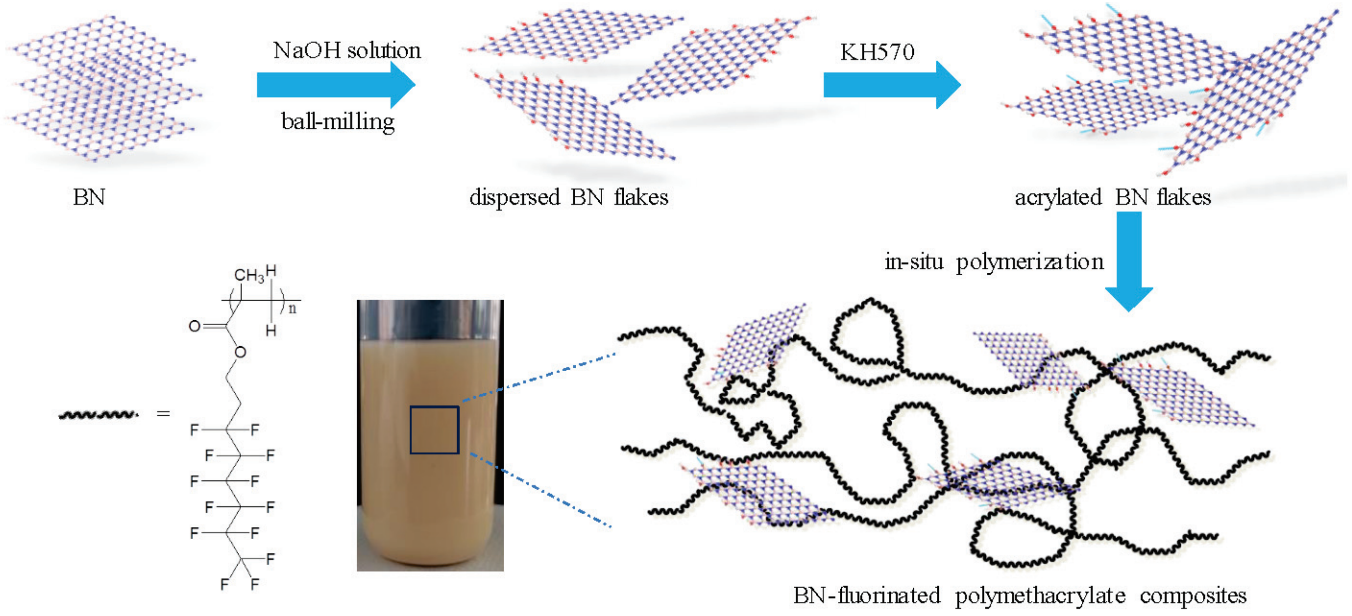

Scheme 1. Dispersion, acrylation of BN flakes and in situ polymerization to the PFPB composite coatings.

AIBN (0.085 g), C6Rf (5 g), KH-570 (0.287 g), BN570, BAC (15 g) were added into a polymerization tube. After purged with N_2, the mixture was heated at 70 °C for 24 h for polymerization. Then, the precipitate was collected, washed with ethanol and dried. The prepared BN-fluorinated poly methacrylate was referred to as PFBP-1, PFBP-2 and PFBP-3, according to the amount of BN570 of 0.045, 0.075 and 0.105 g, respectively. As a comparison, fluorinated poly methacrylate was synthesized through the same recipe but no BN was added, which was referred as to PF.

2.3. Preparation of Coating

The PFBP was dissolved in HFE-7200 to prepare coating solutions with concentrations of 1, 2.5 and 5 wt.%, which are referred to as 1PFBP, 2.5PFBP and 5PFBP, respectively. The PFBP composite was coated on Q235 carbon steel sheets or copper sheets by a simple casting method. After dried at room temperature, the test specimens were further treated in an oven at 80 °C for 3 h. The thickness of the coating was regulated by dropping 0.5 mL of the coating solution onto an O-ring circled area of the substrate.

2.4. Characterization

Fourier transform infrared (FTIR), and attenuated total reflection Fourier transform infrared (ATR-FTIR) spectra were collected using a Nicolet iS50 (Nicolet, Madison, WI, USA). Scanning electron microscopy (SEM) images were acquired on Hitachi S-4800 field emission scanning electron microscope (Hitachi, Tokyo, Japan) with an acceleration voltage of 10 kV. The static water contact angle (WCA) was measured using an optical contact angle meter (Dongguan Sindin SDC-100, Shengding, Dongguan, China).

2.5. Electrochemical Polarization Measurements

Electrochemical polarization measurements were performed on a CHI-604E, Chenhua electrochemical instrument (Chenhua, Shanghai, China). A three-electrode configuration was employed with the test specimen as the working electrode, a Pt plate as the counter electrode, and a saturated calomel electrode (SCE) as the reference electrode. The working electrode had an area of 1 cm^2, opening to 3.5 wt.% NaCl solution as the electrolytic solution. Prior to the measurements, the working electrode was immersed in the electrolytic solution for 20 min to establish a stable open circuit potential (OCP). Electrochemical impedance spectroscopy (EIS, Chenhua, Shanghai, China) measurements were carried out with the frequency range of 10^{-2}~10^5 Hz with alternating current signals. Zview software (version 3.10) was used for analyzing the EIS results within an error of 10%.

2.6. Adhesion Test

The adhesion between the coating and the substrate was tested according to Adhesion Test Procedure-ASTM 3359 [28]. In a typical run, the cutting tool was put on the coated copper sheet. The tool was pressed down and pulled to create a cross hatch pattern. Then, the coating was covered with 3M Scotch tape and the tape was smoothed so that it fitted closely with the coating. The tape was removed by pulling in a single smooth action at an angle of 180°. Finally, the surface of coating was inspected by a microscope to evaluate the adhesion by comparing with the ASTM description.

2.7. Abrasion Resistance Test

The abrasion resistance test was according to a simplified procedure of ISO 7784-2. The PFBP-coated specimen was loaded with a 60 g counterweight covered by non-woven cloth. Then, the counterweight was horizontally moved for various times. The abrasion resistance was evaluated by monitoring the water contact angle and the Tafel curves.

2.8. Salt Fog Corrosion Test

Prior to the corrosion tests, Q235 carbon steel with a working area of 5 cm^2 was rinsed with acetone and ethanol in an ultrasonic bath and dried in air. Then, the carbon steel was coated with PFBP composites. After cured at 80 °C for 3 h, the coated substrate was exposed in a salt spray. The salt fog test was carried out at a constant temperature of 35 °C, and the corrosion was recorded periodically [29].

3. Results and Discussion

The as-received BN powder exhibits morphology of particle, confirmed by the SEM and TEM images (Figure 1A,C). After the wet-milling with the NaOH solution followed by modification with KH-570, the morphology of the acrylated BN (BN570) becomes aggregates of BN flakes (Figure 1B). The dispersion of the BN flakes are further verified by the TEM image (Figure 1D). The well-dispersed BN flakes are beneficial to copolymerize with the fluorinated acrylate monomer and formed stable coating solution.

3.1. Sedimentation of Coating Solution

UV–vis spectrophotometry based on the Lambert–Beer law indicates that the absorbance is linearly related to the concentration of a solution [30]. As a result, the sedimentation of the PFBP coating solution can be evaluated by monitoring the absorbance and the sedimentation data are collected in Table S1. Here, 5 wt.% BN dispersed in HFE-7200 suspension shows a severe sedimentation with a settlement rate of about 84.9% after settling for 24 h. After BN is exfoliated and modified by KH-570, the value is greatly reduced to 16.7%. Furthermore, after the in situ polymerization, the as-prepared 5PFBP-2 coating solution (5 wt.%) shows a negligible settlement rate of 0.76%. The prepared BN-fluorinated polymethacrylate coating solution is quite stable, which is beneficial to the formation of uniform coating with high performance.

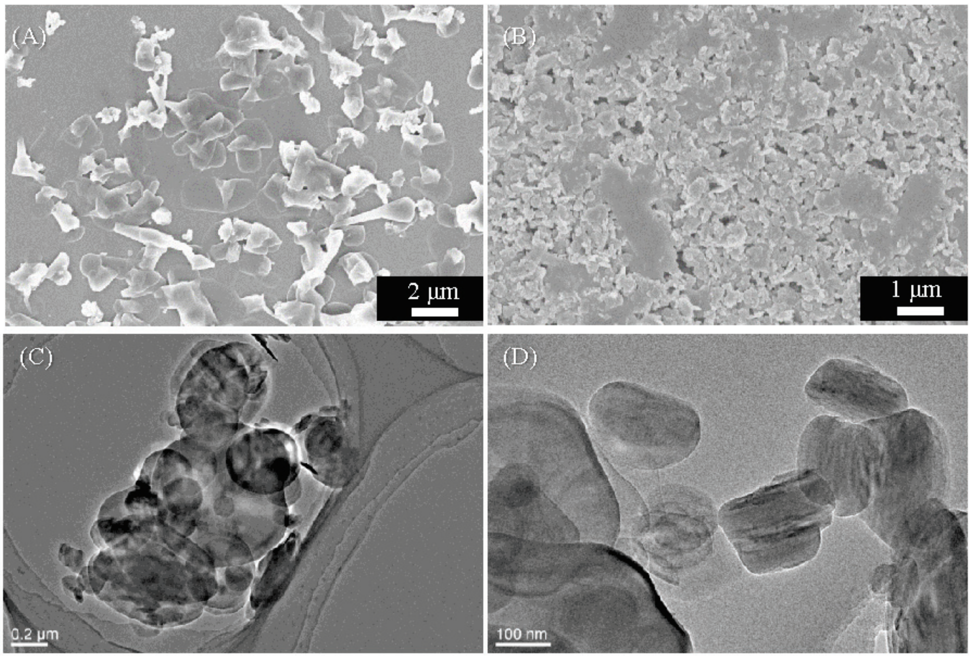

Figure 1. SEM and TEM images of BN (**A**,**C**) and BN570 (**B**,**D**).

3.2. Coating Composition

Figure 2a shows the FTIR spectra of KH-570, BN570, and BN. Two broad peaks at 1231 and 737 cm^{-1} can be observed, corresponding to the absorption bands of BN [25]. While the KH-570 modification of BN570 shows additional peaks at 2840~2950, 1640 and 1723 cm^{-1}, which are attributed to C–H, C=C and C=O, respectively. FTIR spectra confirm that the C=C bond has been successfully grafted on BN, providing the moiety for the in situ polymerization. ATR-IR spectra of the PFBP coatings present peaks at 1723 and 1400–1000 cm^{-1}, which are associated with the bond of C=O and C–F [31], respectively (Figure 2b). Additionally, absorption peak at 1640 cm^{-1} attributing to the stretch vibration of C=C disappears, indicating the completion of polymerization. However, the characteristic peaks of BN at 1231 and 737 cm^{-1} are not well resolved due to their very low content and thus being masked by the peaks of polymer.

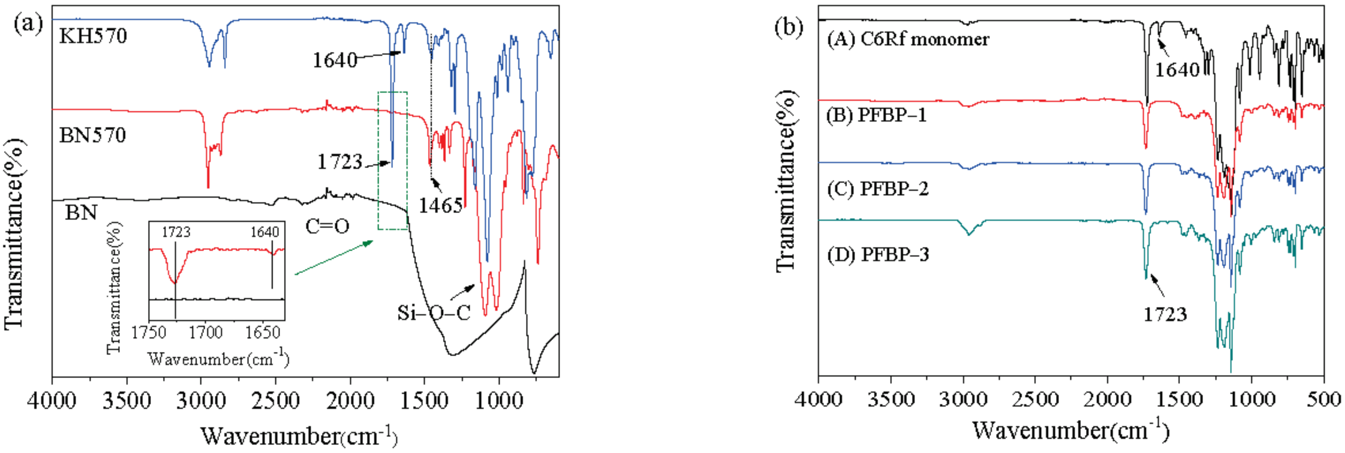

Figure 2. (**a**) FTIR spectra of KH570, BN570, and BN, inset is the enlargement of rectangle; (**b**) ATR-IR spectra of C6Rf monomer (A), PFBP-1 (B), PFBP-2 (C) and PFBP-3 (D).

3.3. Microstructures

From top-view of the PFBP coatings (Figure 3), one can see that the formed PFBP coatings are dense and flat. Some BN flakes are observed when increasing the content of BN570 in PFBP. Cross-sectional images indicate that all the coatings are uniform in thickness. PFBP-1, PFBP-2 and PFBP-3 coatings prepared from 1 wt.% coating solution show slightly increased thickness of 363, 394 and 414 nm, possibly due to the increase in the BN570 content. Additionally, an increase in the coating solution concentration leads to a thicker film. PFBP-2 coating solutions with concentrations of 2.5 wt.% and 5 wt.% produce coatings with thickness of 578 and 726 nm, respectively. The coating were peeled off from the substrate and embedded in a resin to obtain cross-sectional slices. It can be seen that the BN sheets (indicated by circles) are well distributed in the coatings (Figure 3F,G). The surface wettability of the coatings is tested by the measurements of water contact angle (WCA). All the PFBP coatings show hydrophobicity with close WCA around 110° (Figure 3, inset). The side chains of -CF2 connected to the main chain of acrylate through ester bonds contribute to the good hydrophobicity.

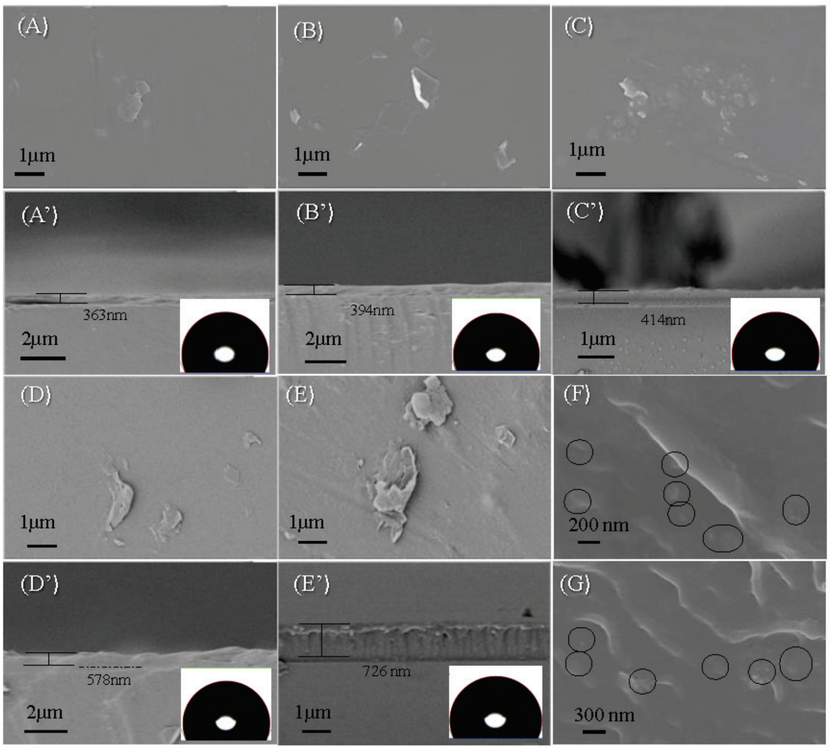

Figure 3. SEM images of top-view (**A**–**E**) and cross-section (**A′**–**E′**) of PFBP coatings prepared from different coating solutions. (**A**,**A′**) 1 wt.% PFBP-1 coating solution; (**B**,**B′**) 1 wt.% PFBP-2 coating solution; (**C**,**C′**) 1 wt.% PFBP-3 coating solution; (**D**,**D′**) 2.5 wt.% PFBP-2 coating solution; (**E**,**E′**) 5 wt.% PFBP-2 coating solution. Insets are photographs of water drop on the corresponding coatings; and cross section images of coating slices (**F**,**G**). The slices were prepared by embedding coatings in Technovit$^{®}$7100.

3.4. Electrochemical Corrosion Test

Electrochemical polarization is a conventional method to evaluate the corrosion resistance of coatings. A lower self-corrosion current density (I_{corr}) means a slower corrosion rate. As shown in Figure 4, the Tafel curve of the PF coated Cu sheet evidently shifts to the lower right corner, compared to that of the bare Cu sheet. This indicates that coating with fluorinated polymer greatly improves the corrosion resistance. PF coating with good hydrophobicity prevents the corrosive medium (3.5 wt.% NaCl aqueous electrolyte) from contacting the Cu substrate and thus inhibits the corrosion. By contrast, the Tafel curves of the BN incorporated PFBP coatings are positioned lower than that of the PF coating, which means that PFBP coatings display better corrosion resistance than the PF coating. When increasing the thickness of the coatings by using higher concentration coating solution, the Tafel curves further move to a lower position, implying the achievement of better corrosion resistance performance.

Corrosion data fitted from the Tafel curves are collected in Table 1. I_{corr} of PFBP-1, PFBP-2 and PFBP-3 coatings are remarkably decreased to be 0.05, 0.018 and 0.074 μA·cm^{-2}, respectively, much lower than that of bare Cu sheet and PF. It is also observed that all of the PFBP coating samples exhibit a maximum corrosion rate lower than 8.6 mm·year^{-1}, much slower than that for PF coating. Additionally, corrosion potential (E_{corr}) also indicates the corrosion trend. The more positive the E_{corr} is, the more difficult the corrosion inclines to be. The Tafel curves for the PFBP-coated Cu sheet give an E_{corr} higher than −171 mV, more positive than for bare Cu sheet and PF at −290 and −226 mV, respectively. Among the PFBP-2 coatings with different thickness, it can be observed that 5PFBP-2 shows the best corrosion resistance. The I_{corr} for 5PFBP-2 is 0.4 nA·cm^{-2}, which decreases two orders of magnitude compared to the 1PFBP-2.

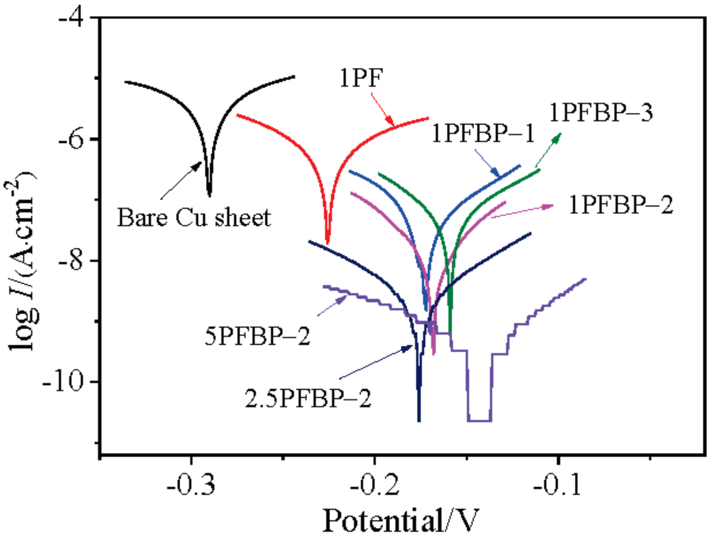

Figure 4. Tafel curves for bare Cu sheet and various coatings on Cu sheet.

Table 1. Electrochemical corrosion data from Tafel curves.

Coating	I_{corr}/(μA·cm^{-2})	E_{corr}/mV	R/10^{-4} (mm·year^{-1})
Bare Cu sheet	16.5	−290	—
1PF	1.86	−226	220
1PFBP-1	0.050	−171	5.70
1PFBP-2	0.018	−168	2.10
1PFBP-3	0.074	−159	8.60
2.5PFBP-2	0.004	−176	0.42
5PFBP-2	0.0004	−153	0.05

Note: I_{corr}: corrosion current; E_{corr}: corrosion potential; R: corrosion rate.

The electrochemistry corrosion behavior of the 5PFBP-2 coating is further investigated by analyzing the EIS data acquired through immersing the samples in 3.5 wt.% NaCl solution for 20 min, 16 h, 24 h, and 72 h, respectively, and the results are shown in Figure 5. After 16 h of immersion, the impedance of the 5PFBP-2 coated sample declines a little but the shape of Bode plots does not change and still keeps one time constant. Therefore, the curves can be fitted by the equivalent circuit model in Figure 5b. This indicated that the composite coating was effective in protecting the metal substrate from corrosion after even 16 h of immersion. With a prolonged immersion time of 24 h, two time constants appeared in the phase angle diagram and no longer conformed to the aforementioned equivalent circuit. Instead, the equivalent circuit model 2 in Figure 5b was used for fitting. The time constant at high frequency corresponds to the barrier performance of the coating [14,32], while the occurrence of one at low frequency indicates that the metal substrate has a corrosion reaction due to the infiltration of the corrosion medium [33,34]. Here, R_{ct} is the charge transfer resistance between the substrate and the electrolyte, CPE2 is the constant phase angle elements representing capacitive properties of the electric double layer. It can be seen that the EIS data are well fitted by the models. The fitted data are collected in Table S2. After 72 h of immersion, the R_c of the coating decreased by near three orders of magnitude compared to the one immersed for 20 min (Figure S1), indicating that the electrolyte penetrates across the coating and corrodes the metal substrate.

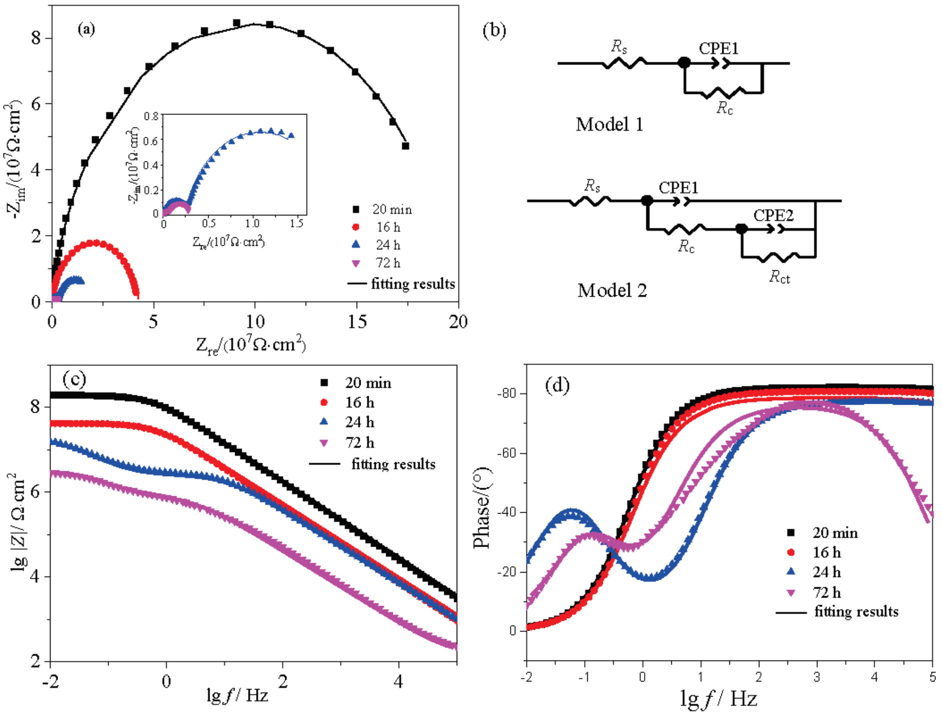

Figure 5. Nyquist (**a**) and Bode (**c**,**d**) plots of 5PFBP-2 coating immersed in 3.5 wt.% NaCl solution for different time, and the equivalent circuits used for fitting the Nyquist plots (**b**).

The electrochemical impedance spectra (EIS) measurements were used to investigate the electrochemical behaviors of bare Cu sheets and PFBP-coated samples. Figure 6 illustrates the Nyquist and Bode plots of the different coatings tested in NaCl solution (3.5 wt.%) at room temperature. The Nyquist plots construct a semi-circle, indicating that the electrode process is determined by the electrochemical step. The capacitive arc radius becomes remarkably larger after the Cu sheets are coated by the PF (Figure 6a, inset). The arc radius is even bigger when increasing the content of BN flakes. However, PFBP-3 with the highest BN content shows a reduced capacitive arc radius, indicating that excessive BN addition might deteriorate the barrier effect of the coating system [35]. This deteriorative trend is related to the aggregation of excessive fillers, supported by the SEM analysis results shown in Figure 3. For the PFBP-2 coatings, the thicker the coating is, the larger the capacitive arc radius is (Figure 6b). The impedance modulus at the lowest frequency (Z_f = 0.01 Hz) in Bode plot could be used as a semi-quantitative indicator of coating's barrier performance [32]. The values of coatings at Z_f = 0.01 Hz are collected in Table 2. Z_f values of PFBP are much higher than that of PF coating and bare copper sheet. Additionally, when increasing the thickness of PFBP coatings, the values at Z_f = 0.01 Hz are increased accordingly and improved to be 1.55×10^8 Ω·cm^2 for the 5PFBP-2 coating. The EIS data were fitted by model 1 in Figure 5b, where the R_c represents the charge transfer resistance, R_s is the solution resistance, and CPE1 is Constant Phase Angle Element 1. The fitted R_c values are summarized in Table 2. The R_c value is 25.06×10^4 Ω·cm^2 for the coating of 1PF. While for the coating of 1PFBP-1, the value of R_c rises sharply and finally reaches up to 209.44×10^4 Ω·cm^2 for 1PFBP-2. Additionally, an increase in the concentration of PFBP-2 coating to 5% leads to a larger R_c of 1.559×10^8 Ω·cm^2. These results confirm that the 5PFBP-2 composite coating offers the most effective protection among all coatings.

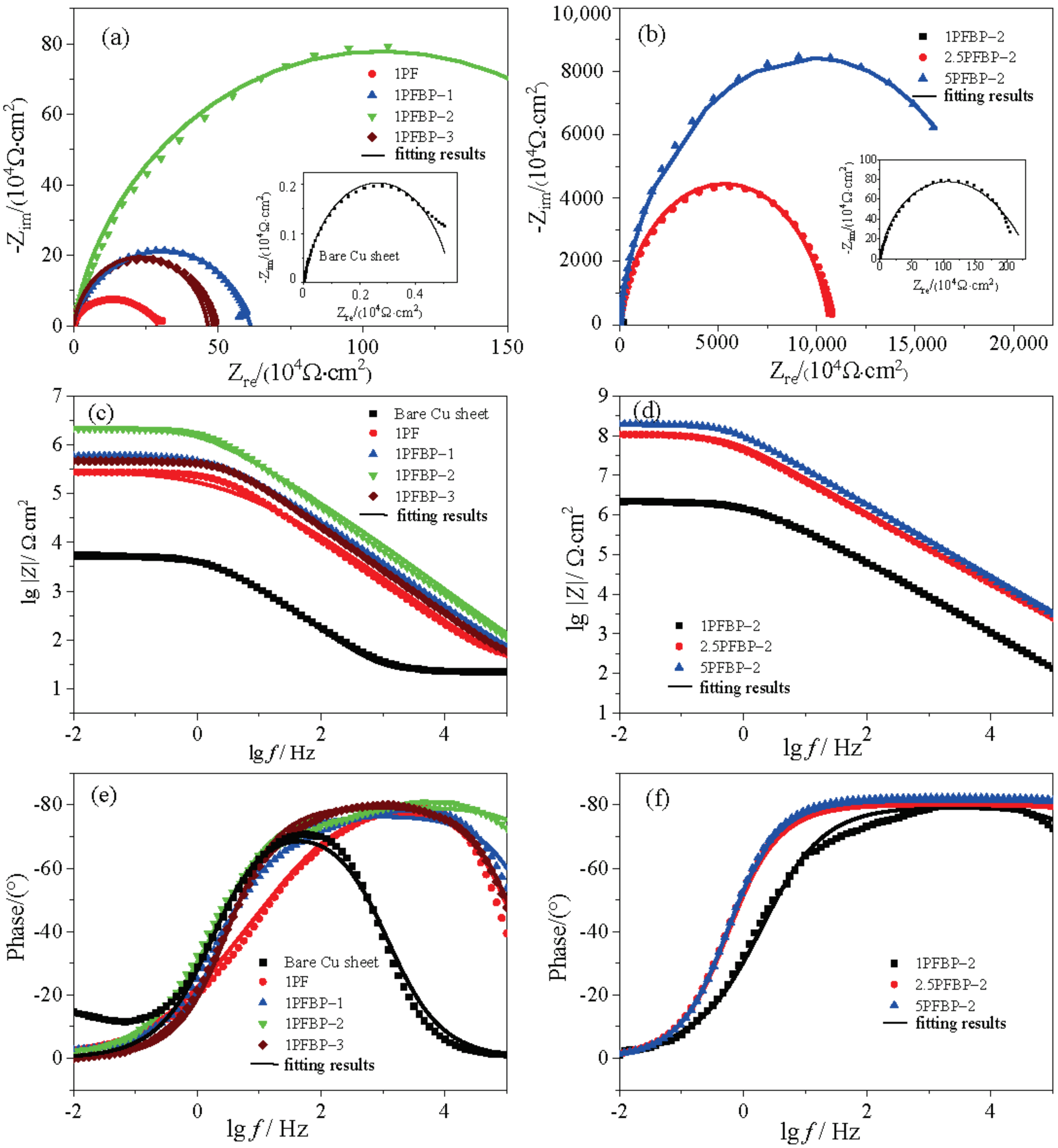

Figure 6. Nyquist (**a**,**b**) and Bode (**c**–**f**) plots of the different coatings in 3.5 wt.% NaCl aqueous solution.

Table 2. Fitting data of electrochemical AC impedance curve of PFBP coatings.

Sample	1PF	1PFBP-1	1PFBP-2	1PFBP-3	2.5PFBP-2	5PFBP-2
$R_c/(\Omega{\cdot}cm^2){\cdot}10^4$	25.06	55.77	209.44	48.00	14,480.00	15,590.00
$Z_{f=0.01\ HZ}/(\Omega{\cdot}cm^2)$	3.07×10^5	5.74×10^5	2.16×10^6	4.84×10^5	1.06×10^8	1.95×10^8

3.5. Surface Salt Fog Corrosion Test

Salt fog test was conducted to investigate the corrosion behaviors in intensified conditions. Q235 carbon steel is conventionally used as the substrate [36–39]. From the photographs, the appearance of the Q235 sheet shows no change after coating with PFBP. The evolution of the salt fog corrosion is illustrated in Figure 7. Corrosion easily happens on the bare substrate. By contrast, when the carbon steel sheets were coated with PFBP coatings, the corrosion was inhibited. The large area rust changes to be corrosion dots. Close inspection of three samples of 1PFBP-1, 1PFBP-2, 1PFBP-3 after 24 h of salt fog corrosion indicates that the Q235 sheet coated with 1PFBP-2 displays fewer corrosion dots. The 1PFBP-2 coating shows the best protective performance among the three coatings with different BN contents. For the 5PFBP-2 coating prepared with increased concentration of 5 wt.%, corrosion can be hardly observed even after 24 h of salt fog test, indicating the good corrosion resistance of the PFBP coating.

The morphology of the substrate after the salt fog tests was monitored by SEM technique. As shown in Figure 8, the Q235 carbon steel exhibits a flat surface with some orientation streaks. The orientation streaks can still be observed on the PFBP-coated Q235, suggesting the coating is very thin. After enduring a salt fog test for 18 h, severe corrosion occurs for the bare Q235 carbon steel. Many pits appear on the surface, indicating the pitting corrosion happens in the salt fog. By contrast, no change is observed for the PFBP-coated carbon steel, suggesting the good corrosion resistance of the PFBP coating.

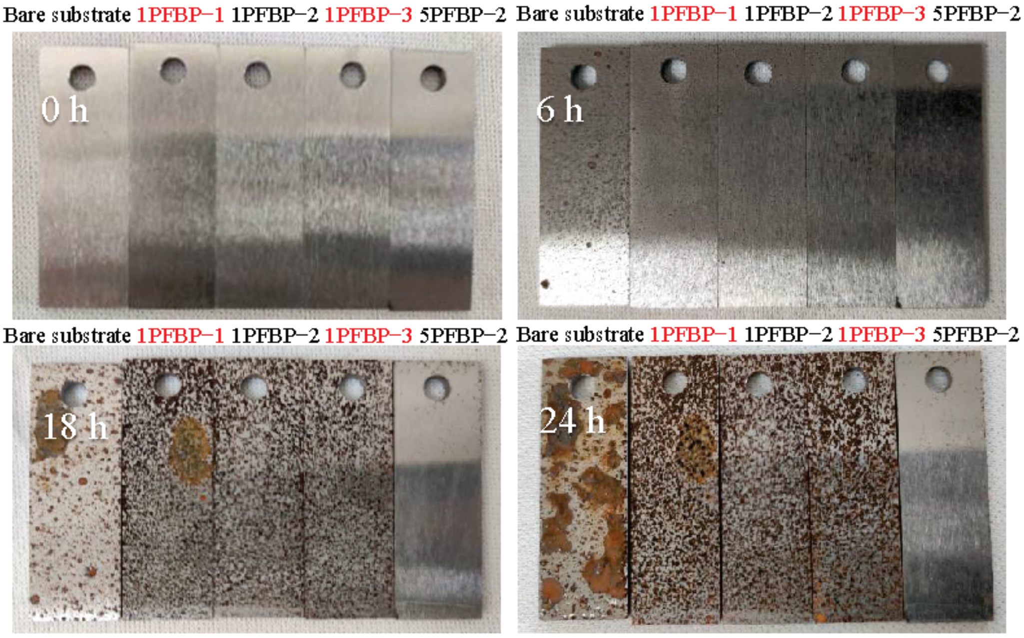

Figure 7. Photographs of Q235 carbon steel sheets coated with PFBP polymers after salt fog corrosion for different periods. From left to right: bare, 1PFBP-1, 1PFBP-2, 1PFBP-3 and 5PFBP-2.

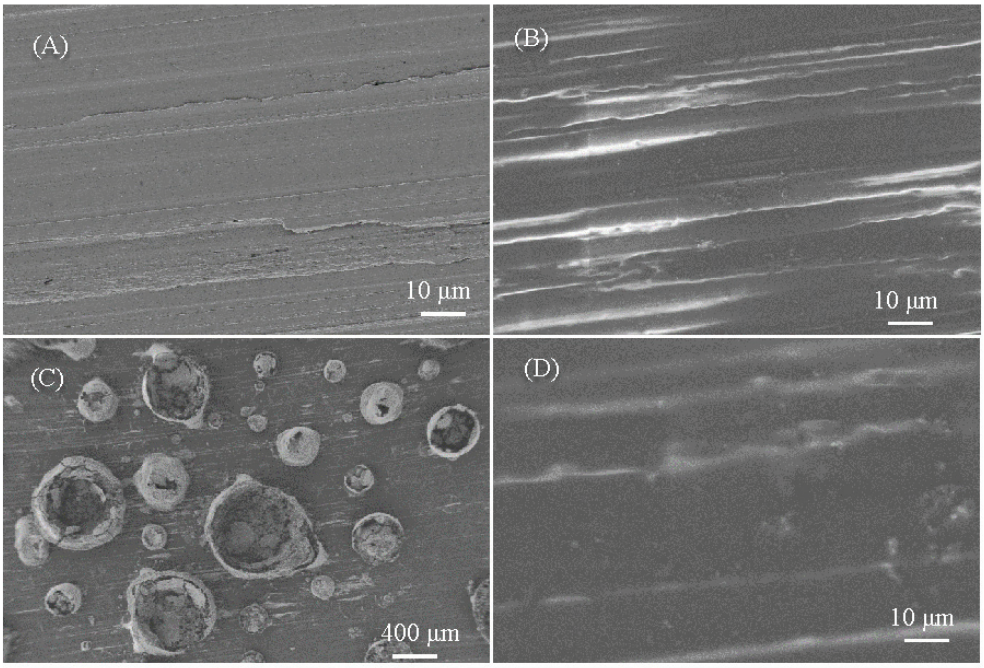

Figure 8. SEM images of bare Q235 carbon steel (**A**), Q235 carbon steel coated with PFBP-2 (**B**), bare Q235 carbon steel after salt fog test (**C**) and PFBP-2 coated Q235 carbon steel after salt fog test (**D**).

3.6. Adhesion Test

Adhesion test was performed on two different substrates coated with three coatings of 1PFBP-1, 1PFBP-2 and 1PFBP-3, respectively. The micrographs of coatings after hundred cell tests are shown in Figure 9. It can be seen that the scratch edges of the cut are smooth and no shedding is observed, which can be classified to be 5B grade according to ASTM 3359 [28]. This indicates that the PFBP coatings show good adhesion property. The fluorous coating solution features very low surface tension and can achieve good wetting of the substrate. The C=O bond linked to the C–C main chain of the acrylate polymer intensifies the adsorption forces due to the Keesom’s dipole effect, Debye’s induced dipole effect and London’s dispersion effect [40]. By virtue of the good adhesion of the acrylate polymer matrix, the PFBP coatings show excellent adhesion properties.

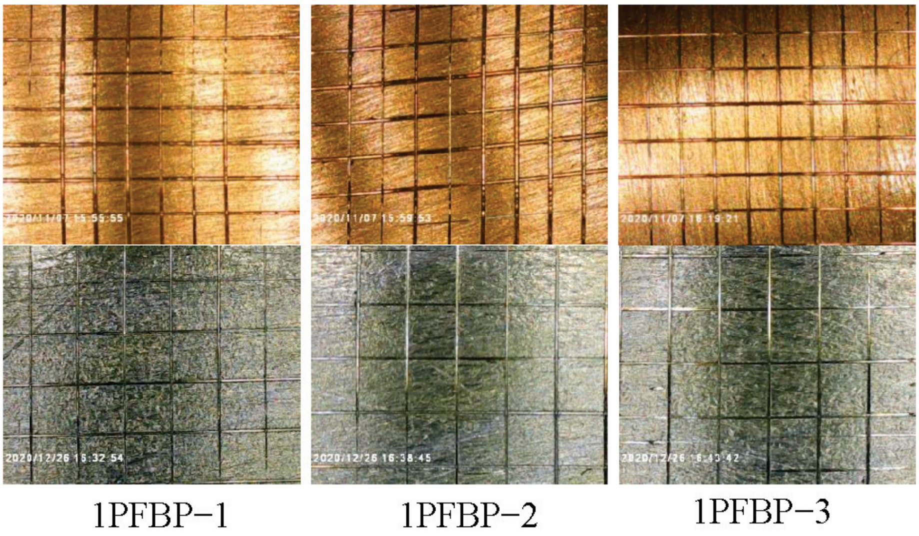

Figure 9. Micrographs of coatings on copper sheet (upper) and Q235 steel sheet (below) after hundred cell tests.

3.7. Abrasion Test of Coating

The abrasion resistance of the PFBP coating was studied through recording the water contact angle and Tafel curves after abrasion for hundreds of cycles. The Tafel curve and water contact angle of PFBP-2 coating after 400 cycles of abrasion exhibits a small change, compared to the one without abrasion (Figure S2). The corrosion potential and the corrosion current vary slightly, the corrosion rate only decays from 2.10 to 4.33 mm·year^{-1} (Table S3). The evidences suggest that the PFBP coating features excellent abrasion resistance, which is plausibly attributed that the well-dispersed BN flakes are linked with the fluorinated poly methacrylate and reinforce the polymer chains.

As illustrated in Scheme 2, the coating solution containing well-dispersed BN-fluorinated poly methacrylate composites can be facilely coated on substrate. After evaporation of the solvent, dense film forms which consists of BN flakes in the polymer matrix. In the case of bare substrate, electrochemical corrosion easily happens when the corrosion media directly contacts the substrate. The hydrophobic fluorinated poly methacrylate could separate the corrosion media from the substrate and thus delays the corrosion. For the coating of BN-fluorinated poly methacrylate composite, the combination of acrylated BN flakes and fluorinated acrylate through the in situ copolymerization, on one hand, improves the dispersion of BN flakes in the coating solution; on the other hand, it eliminates the voids between BN flakes and the polymer matrix. As a result, the penetration of the corrosion media from the coating film is greatly reduced and the labyrinth effect is intensified, compared to the composite coatings prepared by the physical incorporation of BN flakes [41].

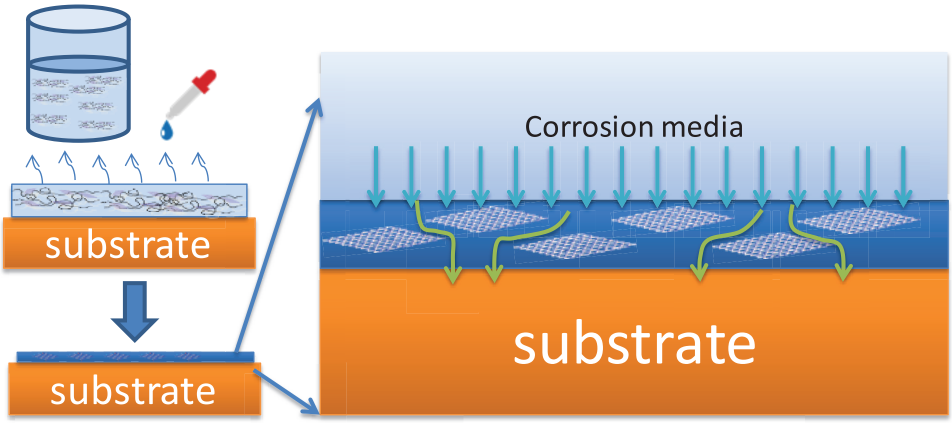

Scheme 2. The formation of PFBP coatings and the corrosion resistance principle.

4. Conclusions

BN flakes, which were successfully prepared by wet-balling BN powder with NaOH solution, were modified with a silane coupling agent (KH570) to obtain acrylated BN flakes. The acrylated BN flakes were in situ copolymerized with 2-(perfluorohexyl)ethyl methacrylate to prepare BN-fluorinated poly methacrylate (PFBP) composites, which were well dissolved in a fluorous solvent. Beneficial from the chemical linkage between the BN flakes and the polymer chains, sedimentation seldom happens in the formed coating solution and BN flakes are well dispersed in the coating film. Electrochemical corrosion tests indicated that the corrosion resistance of the sample coated PFBP is greatly improved compared to the fluorinated polymethacrylate coating. The self-corrosion current density (I_{corr}) fitted from Tafel curves and the charge transfer resistance (R_c) derived from EIS of the PFBP-2 coating containing 2.5 wt.% BN are 0.018 μA·cm^{-2} and 2.09 × 10^6 Ω·cm^2, respectively. When increasing the concentration of PFBP-2, thicker coatings were prepared. The PFBP coating with 726 nm in thickness on Cu sheet displays Icorr and corrosion rate of as low as 4 × 10^{-10} A·cm^{-2} and 5 × 10^{-6} mm·year^{-1}, respectively. Additionally, the PFBP coatings exhibit good adhesion to substrate and abrasion resistance, confirmed by adhesion and abrasion tests. The BN flakes dispersed in the fluorinated polymer act as barriers for the penetration of corrosion media, improving the corrosion resistance of the coated samples. The prepared PFBP coating would find good applications in the corrosion protection of electronic devices through forming thin coating film.

Supplementary Materials: The following are available online at https://www.mdpi.com/2079-6412/11/12/1518/s1, Figure S1: Pore resistance of the coating (Rc) for the specimen coated with 5PFBP-2 coating at different im-mersion time in 3.5 wt.% NaCl solution, Figure S2: Surface wettability (a) of 1PFBP-2 coating after numbers of friction and Tafel curves (b) of 1PFBP-2 coating after 400 cycles of abrasion, Table S1: Absorbance and calculated sedimentation rate of the coating solutions, Table S2: EIS fitting parameters of 5PFBP-2 coatings in various immersion times, Table S3: Electrochemical corrosion data from Tafel curves of 1PFBP-2 coating before and after friction for 400 cycles.

Author Contributions: Conceptualization, X.M. and Q.X.; methodology, Q.X.; software, Q.H.; validation, A.L.; formal analysis, Q.H. and A.L.; investigation, Q.H. and Y.W.; resources, Y.M.; data curation, Y.M. and H.Z.; writing—original draft preparation, Q.H.; writing—review and editing, H.Z. and Q.X.; visualization, Q.H. and Y.M.; supervision, Q.X.; funding acquisition, Q.X. All authors have read and agreed to the published version of the manuscript.

Funding: This research received no external funding.

Institutional Review Board Statement: Not applicable.

Informed Consent Statement: Not applicable.

Data Availability Statement: Not applicable.

Acknowledgments: Financial support by the Beijing Thinvec conjoint project is gratefully acknowledged.

Conflicts of Interest: The authors declare that they have no known competing financial interest or personal relationship that could have appeared to influence the work reported in this paper.

References

1. Hu, G.R.; Zhang, S.; Bu, F.J.; Lin, J.C.; Song, L.G. Recent progress in corrosion protection of magnesium alloys by organic coatings. *Prog. Org. Coat.* **2012**, *73*, 129–141. [CrossRef]
2. Vazirinasab, E.; Jafari, R.; Momen, G. Application of superhydrophobic coatings as a corrosion barrier: A review. *Surf. Coat. Technol.* **2018**, *341*, 40–56. [CrossRef]
3. James, G.R.; John, B.D. Fluorinated naval coatings. *Ind. Eng. Chem. Prod. Res. Dev.* **1978**, *17*, 8–9. [CrossRef]
4. Yin, X.; Song, Z.Y.; Liang, Y.Z.; Zhang, B.; Fang, F.L.; Zhu, P.L.; Zhu, K.B. Synthesis of sulfonyl fluorinated macro emulsifier for low surface energy emulsion polymerization application. *J. Appl. Polym. Sci.* **2017**, *134*, 44921. [CrossRef]
5. Imae, T. Fluorinated polymers. *Curr. Opin. Colloid Interface Sci.* **2003**, *8*, 307–314. [CrossRef]
6. Honda, K.; Morita, M.; Otsuka, H.; Takahara, A. Molecular aggregation structure and surface properties of poly (fluoroalkyl acrylate) thin films. *Macromolecules* **2005**, *38*, 5699–5705. [CrossRef]
7. Weng, J.C.; Peng, W.C.; Chang, C.H.; Chang, H.Y.; Yeh, M.J. Corrosion resistance conferred by superhydrophobic fluorinated polyacrylate-silica composite coatings on cold-rolled steel. *J. Appl. Polym. Sci.* **2012**, *126*, E48–E55. [CrossRef]
8. Liang, L.X.; Liu, H.C.; Mi, X.; Zhu, D.W.; Zhou, Q.; Xiao, Q. Preparation and corrosion resistance of SiO_2 or TiO_2 nano particles/fluorinated polyacrylate polymer composite coatings. *J. Compos. Mater.* **2019**, *37*, 1832–1840. [CrossRef]
9. Maria, S.; William, R.; Will, G.J.; Anna, Z.M.; Michael, C.F.; Alex, Z. Graphene as a long-term metal oxidation barrier worse than nothing. *ACS Nano* **2013**, *7*, 5763–5768. [CrossRef]
10. Kalendová, A.; Sapurina, I.; Stejskal, J.; Veselý, D. Anticorrosion properties of polyaniline-coated pigments in organic coatings. *Corros. Sci.* **2008**, *50*, 3549–3560. [CrossRef]
11. Liu, D.; Zhao, J.W.; Liu, S.; Cen, H.Q.; Xue, J.Q. Comparative tribological and corrosion resistance properties of epoxy composite coatings reinforced with functionalized fullerene C60 and graphene. *Surf. Coat. Technol.* **2016**, *286*, 354–364. [CrossRef]
12. Mo, T.M.; Zhao, J.W.; Chen, F.Z.; Yu, Y.Q.; Zeng, X.Z.; Wu, D.X.; Xue, J.Q. Excellent tribological and anti-corrosion performance of polyurethane composite coatings reinforced with functionalized graphene and graphene oxide nanosheets. *RSC Adv.* **2015**, *5*, 56486–56497. [CrossRef]
13. Zhang, R.X.; Ma, N.R.; Du, A.; Liu, Q.; Fan, Y.Z.; Zhao, X.; Wu, J.J.; Cao, M.X. Corrosion resistance of organic coating based on polyhedral oligomeric silsesquioxane-functionalized graphene oxide. *Appl. Surf. Sci.* **2019**, *484*, 814–824. [CrossRef]
14. Shen, T.L.; Zhao, D.Y.; Wang, Y.; Song, B.R.; Yao, Q.; Chen, S.S.; Chai, Y. A long-term corrosion barrier with an insulating boron nitride monolayer. *J. Mater. Chem. A* **2016**, *4*, 5044–5050. [CrossRef]
15. Eichler, J.; Lesniak, C. Boron nitride (BN) and BN composites for high-temperature applications. *J. Eur. Ceram. Soc.* **2008**, *28*, 1105–1109. [CrossRef]
16. Jiang, B.H.; Ma, T.L.; Yang, Q.; Tang, J.Z.; Song, F.X.; Zeng, B.H.; Zhi, Y.C. Three-dimensional porous boron nitride foam for effective CO_2 adsorption. *Solid State Commun.* **2019**, *294*, 1–5. [CrossRef]
17. Lin, Y.; Connell, W.J. Advances in 2D boron nitride nanostructures: Nanosheets, nanoribbons, nanomeshes, and hybrids with graphene. *Nanoscale* **2012**, *4*, 6908–6939. [CrossRef]

18. Lee, H.G.; Yu, J.Y.; Lee, C.; Dean, C.; Shepard, L.K.; Kim, P.; James, H. Electron tunneling through atomically flat and ultrathin hexagonal boron nitride. *Appl. Phys. Lett.* **2011**, *99*, 243114. [CrossRef]
19. Jiang, H.; Wang, Z.; Ma, L.; Yang, Q.; Tang, Z.; Song, X.; Zeng, H.; Zhi, C. Boron ink assisted in situ boron nitride coatings for anti-oxidation and anti-corrosion applications. *Nanotechnology* **2019**, *30*, 335704. [CrossRef]
20. Husain, E.; Narayanan, N.T.; Taha-Tijerina, J.J.; Vinod, S.; Vajtai, R.; Ajayan, M.P. Marine corrosion protective coatings of hexagonal boron nitride thin films on stainless steel. *ACS Appl. Mater. Interfaces* **2013**, *5*, 4129–4135. [CrossRef]
21. Huang, P.Z.; Zhao, J.W.; Zhao, C.W.; Ci, J.X.; Li, T.W. Tribological and anti-corrosion performance of epoxy resin composite coatings reinforced with differently sized cubic boron nitride (CBN) particles. *Friction* **2021**, *9*, 104–118. [CrossRef]
22. Cui, J.M.; Ren, M.S.; Chen, J.; Liu, S.; Zhang, G.G.; Zhao, C.H.; Wang, P.L.; Xue, J.Q. Anticorrosive performance of waterborne epoxy coatings containing water-dispersible hexagonal boron nitride (h-BN) nanosheets. *Appl. Surf. Sci.* **2017**, *397*, 77–86. [CrossRef]
23. Cui, J.M.; Ren, M.S.; Qin, L.S.; Xue, J.Q.; Zhao, C.H.; Wang, P.L. Non-covalent functionalized hexagonal boron nitride nanoplatelets to improve corrosion and wear resistance of epoxy coatings. *RSC Adv.* **2017**, *7*, 44043–44053. [CrossRef]
24. Pan, D.; Zhang, D.X.; Yang, G.; Shang, Y.; Su, M.F.; Hu, Q.; Patil, R.R.; Liu, H.; Liu, T.C.; Guo, H.Z. Thermally conductive anticorrosive epoxy nanocomposites with tannic acid-modified boron nitride nanosheets. *Ind. Eng. Chem. Res.* **2020**, *59*, 20371–20381. [CrossRef]
25. Oh, H.; Kim, J. Fabrication of polymethyl methacrylate composites with silanized boron nitride by in-situ polymerization for high thermal conductivity. *Compos. Sci. Technol.* **2019**, *172*, 153–162. [CrossRef]
26. He, Z.; Zhao, J.; Li, F.; Zhang, D.; Guo, F.; Guo, H.; Wang, X.; Hu, H. In Situ synthesis of polymer-modified boron nitride nanosheets via anionic polymerization. *Appl. Surf. Sci.* **2021**, *537*, 147966. [CrossRef]
27. Lee, D.; Lee, B.; Park, H.K.; Ryu, J.H.; Jeon, S.; Hong, H.S. Scalable exfoliation process for highly soluble boron nitride nanoplatelets by hydroxide-assisted ball milling. *Nano Lett.* **2015**, *15*, 1238–1244. [CrossRef] [PubMed]
28. American Society for Testing of Materials (ASTM). *ASTM D3359–02: Standard Test Methods for Measuring Adhesion by Tape Test*; ASTM: West Conshohocken, PA, USA, 2005.
29. American Society for Testing of Materials (ASTM). *ASTM B117-09: Standard Practice for Operating Salt Spray (Fog) Apparatus*; ASTM: West Conshohocken, PA, USA, 2009.
30. Tuckerman, B.L. On the intensity of light reflected from or transmitted through a pile of plates. *J. Opt. Soc. Am.* **1947**, *37*, 818–825. [CrossRef] [PubMed]
31. Zhao, Y.L.; Wei, Y.M.; Nie, J.; He, Y. Cationic UV-curable fluorine-containing polyacrylic epoxy prepolymer with good compatibility. *Prog. Org. Coat.* **2016**, *100*, 70–75. [CrossRef]
32. Conradi, M.; Kocijan, A.; Kek-Merl, D.; Zorko, M.; Verpoest, I. Mechanical and anticorrosion properties of nanosilica-filled epoxy-resin composite coatings. *Appl. Surf. Sci.* **2014**, *292*, 432–437. [CrossRef]
33. Sun, W.; Wang, D.L.; Wu, T.T.; Pan, Q.Y.; Liu, C.G. Synthesis of low-electrical-conductivity graphene/pernigraniline composites and their application in corrosion protection. *Carbon* **2014**, *79*, 605–614. [CrossRef]
34. Ye, H.X.; Lin, Z.; Zhang, J.H.; Zhu, W.H.; Liu, Z.; Zhong, L.M. Protecting carbon steel from corrosion by laser in situ grown graphene films. *Carbon* **2015**, *94*, 326–334. [CrossRef]
35. Liu, T.; Zhao, C.H.; Li, Y.J.; Zhang, W.D.; Zheng, R.W.; Wang, P.L. POSS-tetraaniline based giant molecule: Synthesis, self-assembly, and active corrosion protection of epoxy-based organic coatings. *Corros. Sci.* **2020**, *168*, 108555. [CrossRef]
36. Wu, Y.; Guo, L.; Tan, B.; Li, W.; Zhang, F.; Zheng, X. 5-Mercapto-1-phenyltetrazole as a high-efficiency corrosion inhibitor for Q235 steel in acidic environment. *J. Mol. Liq.* **2021**, *325*, 115132. [CrossRef]
37. Wang, J.; Liu, J.; Liu, Q.; Chong, Y. The inhibition performance of heterocyclic compounds on Q235 steel in methanol/formic acid medium: Experimental and theory. *J. Mol. Liq.* **2021**, *343*, 117663. [CrossRef]
38. Njoku, I.D.; Njoku, N.C.; Lgaz, H.; Okafor, C.P.; Oguzie, E.E.; Li, Y. Corrosion protection of Q235 steel in acidic-chloride media using seed extracts of Piper guineense. *J. Mol. Liq.* **2021**, *330*, 115619. [CrossRef]
39. Zhang, W.; Nie, B.; Wang, M.; Shi, S.; Gong, L.; Gong, W.; Pang, H.; Liu, X.; Li, B.; Feng, Y.; et al. Chemically modified resveratrol as green corrosion inhibitor for Q235 steel: Electrochemical, SEM, UV and DFT studies. *J. Mol. Liq.* **2021**, *343*, 117672. [CrossRef]
40. Poth, U.; Schwalm, R.; Schwartz, M.; Baumstark, R. *Acrylic Resins*; Vincentz Network: Hanover, Germany, 2011.
41. Cui, J.M.; Ren, M.S.; Qin, L.S.; Xue, J.Q.; Zhao, C.H.; Wang, P.L. Processable poly(2-butylaniline)/hexagonal boron nitride nanohybrids for synergetic anticorrosive reinforcement of epoxy coating. *Corros. Sci.* **2018**, *131*, 187–198. [CrossRef]

coatings

Article

Numerical Analysis of High-Velocity Oxygen Fuel Thermal-Spray Process for Fe-Based Amorphous Coatings

Jianxing Yu [1,2], Xin Liu [1,2,*], Yang Yu [1,2], Haoda Li [1,2], Pengfei Liu [1,2], Ruoke Sun [1,2], Limin Wang [3] and Pengfei Li [4,*]

[1] State Key Laboratory of Hydraulic Engineering Simulation and Safety, Tianjin University, Tianjin 300072, China; yjx2000@tju.edu.cn (J.Y.); yangyu@tju.edu.cn (Y.Y.); lihaoda@tju.edu.cn (H.L.); m13920367969@163.com (P.L.); srk_@tju.edu.cn (R.S.)
[2] Tianjin Key Laboratory of Port and Ocean Engineering, Tianjin University, Tianjin 300072, China
[3] State Key Laboratory of Metastable Materials Science and Technology, School of Materials Science and Engineering, YanShan University Qinhuangdao, Qinhuangdao 066004, China; LiminWang@ysu.edu.cn
[4] School of Resources and Materials, Northeastern University at Qinhuangdao, Qinhuangdao 066004, China
* Correspondence: lx_2020@tju.edu.cn (X.L.); lipengfei@neuq.edu.cn (P.L.)

Abstract: High-velocity oxygen fuel (HVOF)-sprayed amorphous alloy coatings usually have advantages of a dense structure that improve their resistance to corrosion, wear, and fatigue in the substrate. The flame flow characteristics and particle behaviors during the spray process have a significant influence on the amorphous coating structure and properties. In this study, a computational fluid dynamics model is enforced to analyze the flame flow and Fe-based amorphous alloy particle behavior in an HVOF spray process. The flame flow temperature, velocity characteristics, and the $Fe_{48}Cr_{15}Mo_{14}C_{15}B_6Y_2$ Fe-based amorphous alloy particles' velocities, temperatures, flight trajectories, and mass concentration distribution characteristics are simulated. Moreover, the effects of the oxygen/fuel ratio, particle morphology parameter, particle-injection rate, and angle on the particle behavior are also investigated. Judging from the simulation results, the optimum amorphous alloy particle size varies between 20 and 30 μm, the shape factor is within the range of 0.9–1, the optimum O/F ratio is 3.4, the optimum injection angle is 45°, and the optimum injection rate is 10 m/s. With these conditions, most of the particles settled toward the centerline of the spray gun and are in a semisolid or solid state before affecting the substrate, giving the materials optimal coating structure and performance.

Keywords: HVOF; Fe-based amorphous coating; flame flow characteristics; particle dynamics

1. Introduction

Corrosion and wear of as well as fractures on materials' surfaces and interfaces are major issues in engineering environments, which not only lead to significant economic losses but also to enormous personal harm caused by these material failures. In China alone, the cost of corrosion of materials within engineering components amounts to billions of dollars or approximately 3.34% of the country's Gross Domestic Product (GDP) according to Hou et al.'s statistics [1]. Many researchers have studied surface engineering to explore superior coatings deposited onto metallic materials to overcome deterioration, among which amorphous alloys exhibit the excellent advantages of corrosion resistance, superior wear resistance, high mechanical strength, and high hardness, ensuing from their special disordered atomic structure [2–5]. In the past decade, a large number of bulk metallic glasses with a high glass-forming ability (GFA) have been developed in Pd-, Mg-, Zr-, and Fe-based systems using various rapid solidifying techniques [6–9]. Nevertheless, these bulk metallic glasses typically exhibit no work hardening or plastic deformation during room temperature deformation that considerably limits their applications as structural materials. To avoid this situation and simultaneously give play to their unique anticorrosion and wear-resistant properties, these materials are made into coatings.

Coatings **2021**, *11*, 1533. https://doi.org/10.3390/coatings11121533

Thermal spray technologies provide sufficient rapid cooling rates that inhibit long-range diffusion and avoid crystallization, existing as an alternate approach to beat scale disadvantages and increase the industrial applications of amorphous alloys. Many studies have attempted to manufacture Fe-based amorphous alloy coatings using various spraying methods, e.g., high-velocity oxygen fuel (HVOF) spraying [10,11], plasma spraying [12,13], laser cladding [14], and kinetic spraying [15]. Among these methods, HVOF spraying has attracted additional attention because of its benefits of low temperature and high velocity, which are conducive to manufacturing dense or low-porosity amorphous alloy coatings [16]. The complexity of HVOF thermal spraying in terms of its complex physics and multiscale interactions of variables makes it difficult to determine production parameters directly [17]. In the past decade, many amorphous alloy coatings have been prepared experimentally. Many experimental procedures in previous studies aimed to correlate the manufacturing parameters against coatings microstructure and properties [18,19]. However, to obtain high-quality Fe-based amorphous alloy coatings with homogeneous structure and high amorphous content, several trial-and-error attempts are needed, which consumes plenty of time and leads to high experimental costs. Simultaneously, it is troublesome to reveal the transient rule of gas and the particle flight history in HVOF spraying through experimental methods. Therefore, in addition to intuitive experimental exploration, it is necessary to gain a deeper understanding of the spraying mechanism [20]. Some simulations of the HVOF spraying process have been carried out [21–24]; however, these were mainly focused on WC–12Co and Ni–Cr materials, whereas, to our knowledge, studies on amorphous alloy coatings are relatively lacking. However, the excellent performance of amorphous coatings cannot be ignored by researchers, and a variety of amorphous alloy coatings have been applied in industry. Therefore, through computer simulations of HVOF spraying, the momentum and heat transfer between the flame flow and amorphous alloy particles can be analyzed in detail, which provides theoretical guidance for improving the properties of Fe-based amorphous coatings [25,26].

In the HVOF spraying process, the coating performance mainly depends on the behavior of particles close to the substrate surface [21,27,28], which is affected by the physical and chemical state at the moment of particle impact. With the increase in the impact velocity, the degree of flattening of the amorphous alloy particles increases, and the contact area between the particles and the substrate becomes larger, which improves the bonding strength and compactness of the coating and forms a high-performance coating. During the spraying process, the high temperature will cause the molten amorphous alloy particles to stick to the inner wall of the gun barrel, affecting the normal spraying process. In addition, the high temperature can also lead to partial oxidation of the amorphous alloy powder and increase the porosity of the coating. When the particles are in a molten or semimolten state, they form denser coatings with better corrosion resistance. Obviously, the particle velocity, particle temperature, and melting state have significant influence on the coating performance [17]. Therefore, the temperature, trajectory, and velocity of those amorphous alloy particles should be controlled to manufacture repeatable coatings.

To better analyze the HVOF spraying process and manufacture the corrosion- and wear-resistant Fe-based amorphous alloy coatings, the $Fe_{48}Cr_{15}Mo_{14}C_{15}B_6Y_2$ (SAM1651) amorphous alloy is chosen as the spray material owing to its excellent corrosion resistance and glass forming ability (GFA). The alloy features a nominal critical cooling rate of 80 K/s, suggesting that it can be cooled to an entirely glass state. In this study, the JP-5220 spray gun (Praxair, Danbury, CT, USA) is the object of analysis, and the gas flow and particle motion models for HVOF spraying are established based on computational fluid dynamics (CFD). The transient rules of the composition changes, flame characteristics, and particle distribution in the HVOF spray process are analyzed.

2. Models and Methods

Figure 1 shows a model diagram of the HVOF thermal spraying, including the kerosene and oxygen inlet, the combustion chamber, the Laval spray nozzle, and the spray barrel. Figure 1a shows the two-dimensional (2D) model of the spray gun, and the detailed model parameters are annotated in figure and shown in Table 1. In this study, the three-dimensional (3D) calculation model shown in Figure 1b is used; that is, the 2D model is rotated 360°.

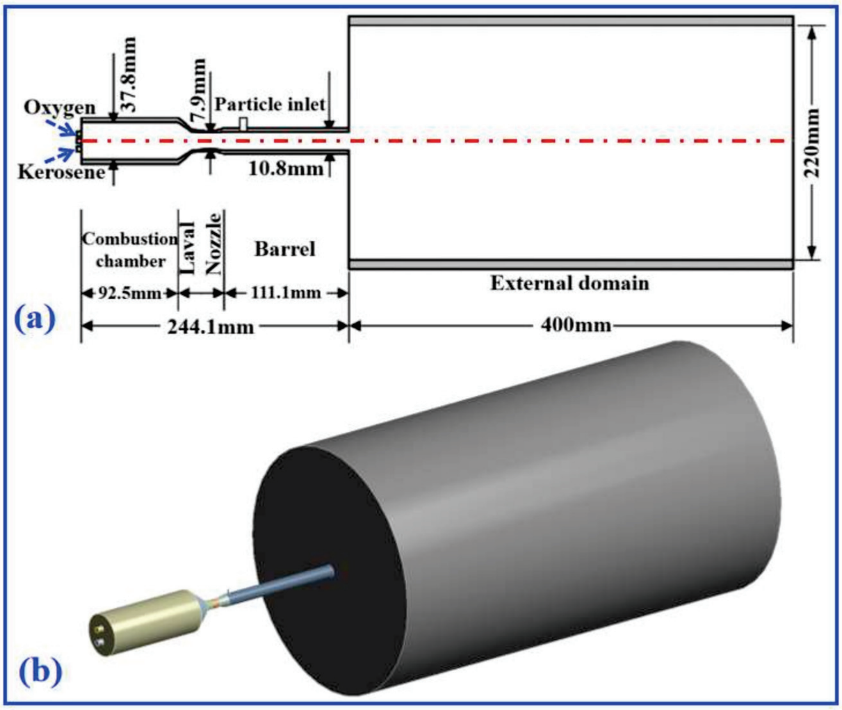

Figure 1. High-velocity oxygen fuel (HVOF) spray gun (**a**) two-dimensional (2D) model, and (**b**) three-dimensional (3D) model.

Table 1. High-velocity oxygen fuel (HVOF) spray model parameter.

Model Parameter	Values
The length of combustion chamber	92.5 mm
The width of the combustion chamber	37.8 mm
The length of the spray barrel	111.1 mm
The width of the spray barrel	10.8 mm
The length of external field cylindrical domain	400 mm
The width of external field cylindrical domain	220 mm

Figure 2a shows the computational mesh of the spraying model. The ICEM software (Fluent 19.0) is used to mesh the calculation domain. There are 1,282,729 elements and 1,243,608 nodes in the entire domain, and the elements sizes are in the range of 0.2–2 mm. The mean quality of elements is 0.897. To ensure the accuracy of the calculation, a hexahedral element is selected for depicting the combustion chamber and external region, as shown in Figure 2b,d, and a tetrahedral element is used for depicting the barrel part, as shown in Figure 2c. In addition, the external region is divided into two parts and uses a transitional grid, whereas the internal grid is refined. The refinement of the external region is conducive to accurately obtaining the flame flow characteristics and particle trajectories. Oxygen and kerosene are injected into the spray gun at flow rates of 0.02163 and 0.007 kg/s, respectively. Table 2 presents the property parameters of the SAM1651 amorphous alloy, where the material's density is 7310 kg/m^3 and the C_p is 460 J/(kg K).

By adjusting the nitrogen gas flow, the particle injection rate varies from 5 to 20 m/s. It is assumed that the wall temperature of the HVOF spray gun is 300 K. The pressure far field and pressure outlet boundary are applied at the external domain, and the atmospheric pressure is 1.01 KPa.

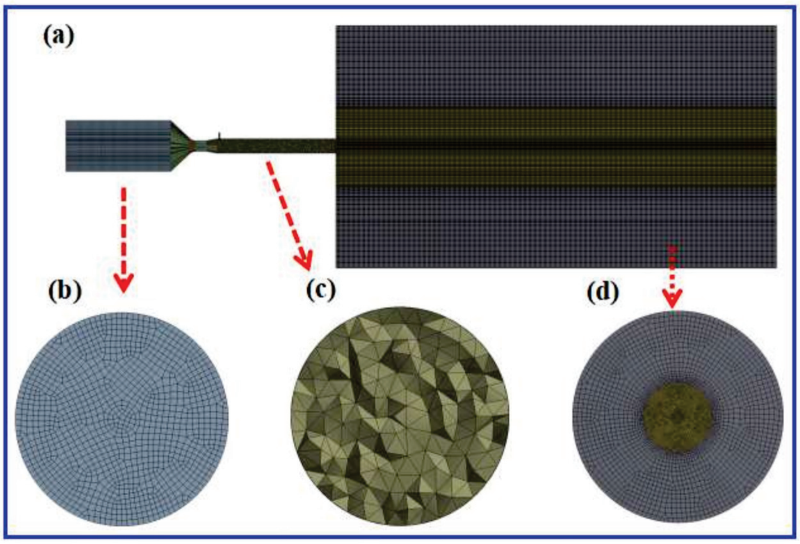

Figure 2. (**a**) Computational mesh of the model, (**b**) combustion chamber mesh, (**c**) barrel mesh, and (**d**) external region mesh.

Table 2. Powder properties of SAM1651 [29].

Powder Properties	Values
Density	7310 kg/m^3
Melting temperature	1394 K
Specific heat capacity	460 J/(kg K)
Thermal conductivity	22.5 W/(m K)
Latent heat of fusion	3.25·10^5 J/kg

A realizable k–ε model is used, and within the Cartesian tensor, the governing equations of the 3D model are defined as follows [16,30]:

Mass conservation equation:

$$\frac{\partial \rho}{\partial t} + \frac{\partial}{\partial x_i}(\rho u_i) = 0 \tag{1}$$

Momentum conservation:

$$\frac{\partial}{\partial t}(\rho u_i) + \frac{\partial}{\partial x_j}(\rho u_i u_j) = -\frac{\partial p}{\partial x_i} + \frac{\partial}{\partial x_j}(\tau_{ij})_{eff} + \frac{\partial}{\partial x_j}\left(-\rho u_i' \overrightarrow{u_j'}\right) \tag{2}$$

Energy transport equation:

$$\frac{\partial}{\partial t}(\rho E) + \frac{\partial}{\partial x_i}(u_i(\rho E + p)) = \frac{\partial}{\partial x_j}\left(k_{eff}\frac{\partial T}{\partial x_j} + u_i(\tau_{ij})_{eff}\right) + S_h \tag{3}$$

The deviatoric stress tensor is

$$(\tau_{ij})_{eff} = \mu_{eff}\left(\frac{\partial u_j}{\partial x_i} + \frac{\partial u_i}{\partial x_j}\right) - \frac{2}{3}\mu_{eff}\frac{\partial u_i}{\partial x_i}\delta_{ij} \tag{4}$$

The effective thermal conductivity is

$$k_{eff} = k + \frac{c_p \mu_t}{\sigma_t} \tag{5}$$

Mass fraction conservation equation was added to the transport equations, and species transport model was customized to simulate the combustion reaction. The convection sources, diffusion sources, and reaction sources of the transport equation are described in [31]:

$$\frac{\partial}{\partial x_i}(\rho Y_\alpha u_i) = -\frac{\partial J_{\alpha,i}}{\partial x_i} + R_\alpha + S_\alpha,\ \alpha = 1,\ 2,\ \ldots,\ N-1 \tag{6}$$

In this study, the eddy dissipation model is used [32], which assumes that the combustion rate is decided by the blending rate of fuel and oxidants. The consumption rate of fuel is given by [33]:

$$R_F = -\frac{\rho\varepsilon}{k} A \min\left(mF, \frac{m_0}{s_0}, B\frac{m_P}{S_P}\right) \tag{7}$$

where

$$S_o \equiv \frac{n_o M_o}{n_F M_F} \tag{8}$$

$$S_P \equiv \frac{n_P M_o}{n_F M_F} \tag{9}$$

The empirical constants A and B are 4 and 0.5, respectively.

In practice, kerosene fuel is a mixture of alkanes with carbon content ranging from 9 to 17. Therefore, there is no precise chemical formula for kerosene. In the simulation, $C_{12}H_{23}$ is used as the representative average of the individual component of the kerosene. Because the combustion chamber's temperature exceeds 2300 K, H_2O and CO_2 break down into several lightweight mass substances, not solely to H_2 and CO flammable gases, however, additionally to O, H, OH, and other atomic gases [16]. The combustion dynamics is described by a global reaction [31] that accounts for intermediate and dissociation reactions.

$$\begin{gathered} C_{12}H_{23} + 17.286\ O_2 \rightarrow 7.397\ CO + 4.603\ CO_2 + 7.955\ H_2O \\ +1.613\ H_2 + 1.204\ H + 2.66O\ H + 1.154\ O + 3.1O_2 \end{gathered} \tag{10}$$

In solving the Navier–Stokes equation, gases are treated as continuous phases, dispersed particle phases are solved by tracking large droplets, and there is no interaction between the particles. The trajectories of these discrete phases and the thermal transfer are calculated.

In Cartesian coordinates, the equations of particle motion in x direction can be written as a force balance, equating droplet inertia with forces acting on the particle; the basic particle equation is as follows.

$$\frac{du_p}{dt} = F_D\left(\mu - \mu_p\right) + F_x = \frac{18\mu}{\rho_p d_p^2}\frac{C_D Re}{24}\left(\mu - \mu_p + F_x\right) \tag{11}$$

A single-particle energy equation that ignores radiation heat transfer is shown below:

$$m_p c_p \frac{dT_p}{dt} = h_c Ap\left(T_g - T_p\right) \tag{12}$$

The CFD commercial software (Fluent 19.0) is used, and the calculation is run on a GTS2-RIS208Q workstation. First, a 3D model for the JP5220 gun is established. Second, the boundary conditions, combustion reaction model, and gas flow model are established. To avoid simulation calculation divergence, all equations use the second-order upwind discretization method. Third, according to the convergence criterion to determine whether the calculation results converge; if convergence has been reached, then we end the calculation.

3. Results and Discussion

3.1. Flame Flow Characteristics

Figure 3 shows the simulation results of the flame flow characteristics (gas velocity, gas pressure, and gas temperature as well as the Mach number). The calculation shows that the flow characteristics of the flame change with the axial distance in the spraying process. The velocity, pressure, and temperature distribution have symmetrical distributions above and below the centerline of the gun body. As can be seen from Figure 3a, due to the large inlet oxygen flow rate, the gas behavior in the combustion chamber is streamlined along the symmetry axis. The overall gas velocity distribution in the combustion chamber is uniform but relatively low at 130 m/s. As the flame flows through the Laval nozzle, the velocity quickly exceeds 2000 m/s. Figure 3b illustrates the changes in the flame flow pressure during spraying, and the gas pressure is approximately 0.9 MPa in the combustion chamber. Due to the convergence of the spray nozzle, the pressure drops sharply to 0.18 MPa after passing through the nozzle and then exhibits overall stable distribution and slight local fluctuations. On the right side of the barrel outlet, the pressure profile alternates between light and dark conditions. The pressure value oscillations decrease and then stabilize at a fixed distribution of 0.1 MPa.

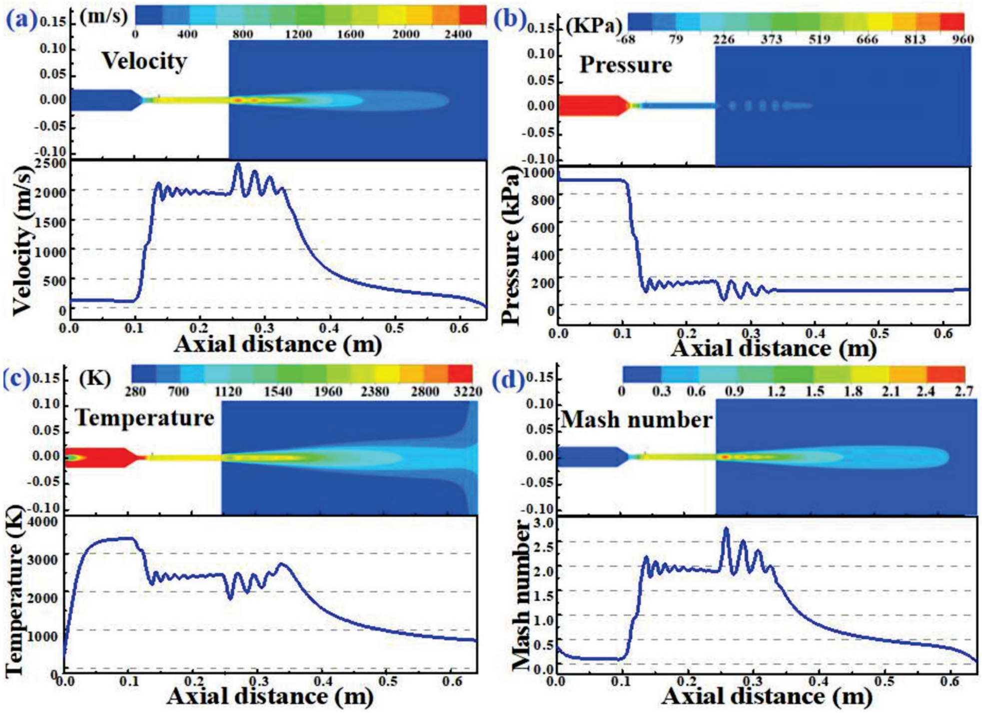

Figure 3. Contours of the flame flow and gas characteristics along the centerline for (**a**) gas velocity, (**b**) gas pressure, (**c**) gas temperature, and (**d**) Mach number.

As seen in Figure 3c, the initial temperature is relatively low because the kerosene and oxygen are not mixed sufficiently. With the combustion intensifies, the combustion chamber flame flow temperature peaks at 3400 K. When the flame flows through the spray nozzle, the temperature drops significantly and then fluctuates slightly toward a constant of 2400 K. The contour shows that when the flame flows into the cold air, the axial temperature continues to decrease after periodic fluctuations. Eventually, the temperature drops to 650 K at the substrate position. This whole process reflects the attenuation process of kerosene combustion energy. Figure 3d represents the changes in the Mach number, which are similar in trend to the flame flow velocity.

3.2. The Mass Fraction of Gas Components

In order to reveal the reaction mechanism of kerosene–oxygen combustion, the variation contours and curves of the mass fraction of various combustion components are shown in Figure 4. Red lines show the mass fraction of each component distributed along the centerline, with the horizontal and vertical axes in units of m. At the gun inlet, the mass fractions are only kerosene and oxygen. The temperature rises rapidly as the combustion reaction occurs. Concurrently, the temperature increase also promotes the diffusion of kerosene and oxygen, which intensifies the combustion reaction, and the mass fractions of the kerosene and oxygen decrease rapidly, whereas the mass fractions of the other combustion products increase rapidly [34]. The calculation results show that the concentration of kerosene flight into the combustion chamber is comparatively high in the axial direction. When mixture intensifies and burns completely, kerosene is consumed rapidly until its mass fraction decreases to zero in the combustion chamber. Simultaneously, oxygen acts as a flammable agent with relatively large inlet concentrations and oxygen declines rapidly in combustion chamber. In addition, oxygen increases in external region due to the presence of oxygen in the air. The concentrations of the combustion products H_2O, CO_2, and CO are relatively high, i.e., more than 0.2, and the concentrations of other gases are comparatively low.

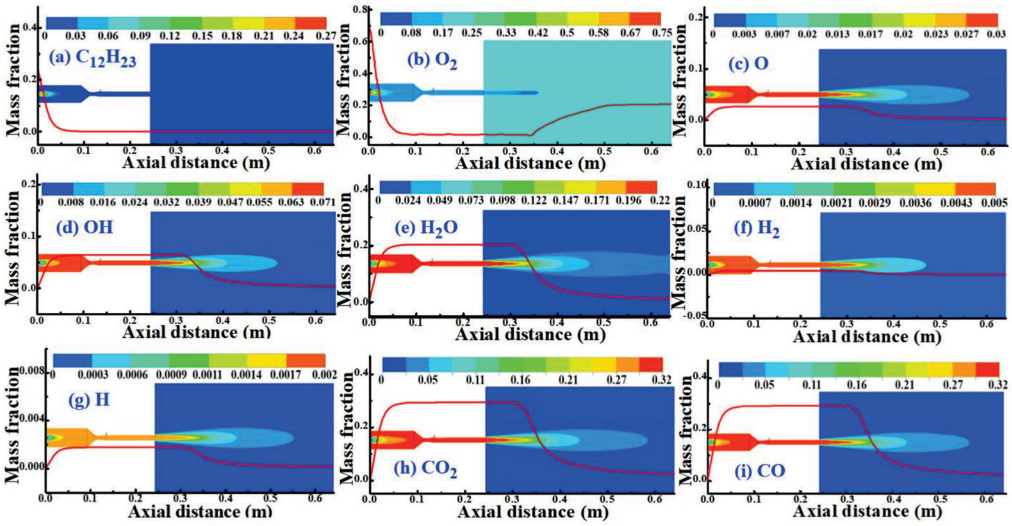

Figure 4. Contours and curves of the mass fraction of various components; (**a**) $C_{12}H_{23}$ (**b**) O_2 (**c**) O (**d**) OH € H_2O (**f**) H_2 (**g**) H (**h**) CO_2, and (**i**) CO.

3.3. Effect of the Oxygen/Fuel Ratio on Flame Flow

The O/F ratio is a pivotal variable for regulating the flame flow characteristics during the HVOF process [22,27]. According to the kerosene–oxygen combustion reaction formula (Equation (10)), the ideal conditions for full combustion of 1 L kerosene requires a mass ratio of oxygen 3.09 times that of kerosene. To further explore the influence of oxygen and kerosene on HVOF spraying, this study sets 11 comparative conditions to analyze the influence of different O/F ratios and the same O/F ratio but different total fuel oxygen amounts on the pressure, temperature, and velocity of the flame flow. The specific O/F ratio conditions are shown in Table 3 and Figure 5.

The characteristic curves for different O/F ratios are simulated and plotted, as shown in Figure 6. Through comparison, the pressure differences in the spray gun are mainly observed in the combustion chamber. The pressure in the platform region of the combustion chamber is compared, as shown in Figure 6d, and the pressure increases with the increasing O/F ratio. However, when the O/F ratio is 3.4, the pressure reaches the maximum and then decreases. Interestingly, the maximum pressure does not occur at the ideal O/F ratio of 3.09. At the barrel outlet, all curves exhibit low-amplitude fluctuations. Comparing condition 4 with conditions 8–11, the changes in the pressure observed when adjusting the total amount of kerosene and oxygen under the condition of a fixed O/F ratio are analyzed. The combustion chamber pressure increases as the total fuel increases.

Table 3. Details of oxygen/fuel ratio conditions.

Condition	Kerosene (kg/s)	Oxygen (kg/s)	O/F Ratio
Condition 1	0.0077	0.01694	2.2
Condition 2	0.0077	0.01925	2.5
Condition 3	0.0077	0.02156	2.8
Condition 4	0.0077	0.02379	3.09
Condition 5	0.0077	0.02618	3.4
Condition 6	0.0077	0.02849	3.7
Condition 7	0.0077	0.0308	4
Condition 8	0.00847	0.02617	3.09
Condition 9	0.00924	0.02855	3.09
Condition 10	0.00693	0.02141	3.09
Condition 11	0.00616	0.01903	3.09

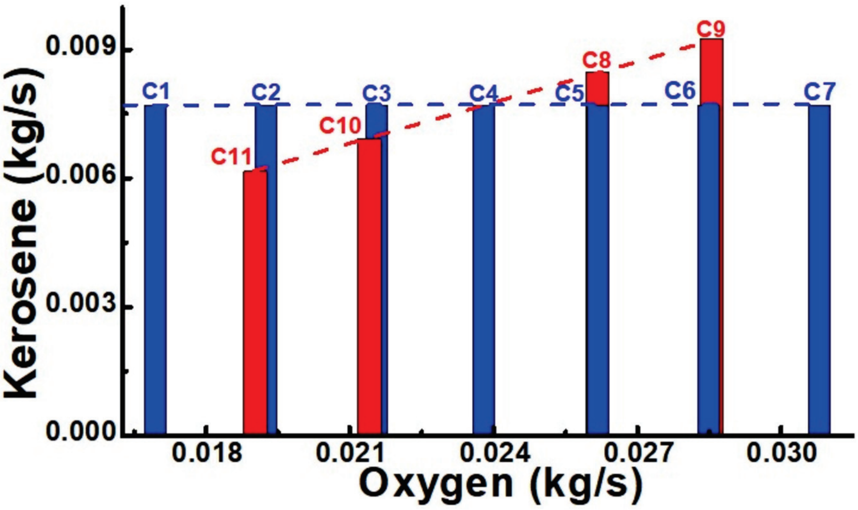

Figure 5. Details of oxygen/fuel ratio conditions.

According to the temperature analysis curves in Figure 6b,e, the O/F ratio has a certain influence on the heating rate of the combustion chamber. The higher the O/F ratio is, the higher is the slope of the curve in Figure 6b is. When the O/F ratio is fixed at 3.09, the slope of the temperature increase is the same. However, the maximum temperature does not monotonically increase with the increasing of O/F ratio, which is the same as in the case of pressure. The maximum temperature appears when the O/F is 3.4; then, the temperature decreases. The flame flow temperature does not increase significantly when the fuel mass increases by 10% or 20%, and the flame flow temperature does not decrease significantly when the fuel mass decreases by 10%. However, the temperature decreases significantly when the fuel mass is reduced by 20%, indicating that the total fuel quantity has no significant effect on the temperature within a certain fluctuation range. The final flame flow temperature decreases because of the effect of the cold air outside the spray gun on the flame flow. Due to the heat transfer between the air and the flame flow, the higher the temperature at the nozzle outlet, the faster the cooling rate. As shown in Figure 6c,f, the O/F ratio has an effect similar to that of the pressure and temperature on the velocity of the flame flow. As can be seen from the momentum equation, the higher the flame pressure, the faster the flame velocity. However, the variation trends of velocity and pressure are not the same. The maximum velocity appears when the O/F ratio is 3.7.

Adjustments of the total fuel amount have a significant effects on speed with the fixed O/F ratio of 3.09, which changes in the same way as pressure.

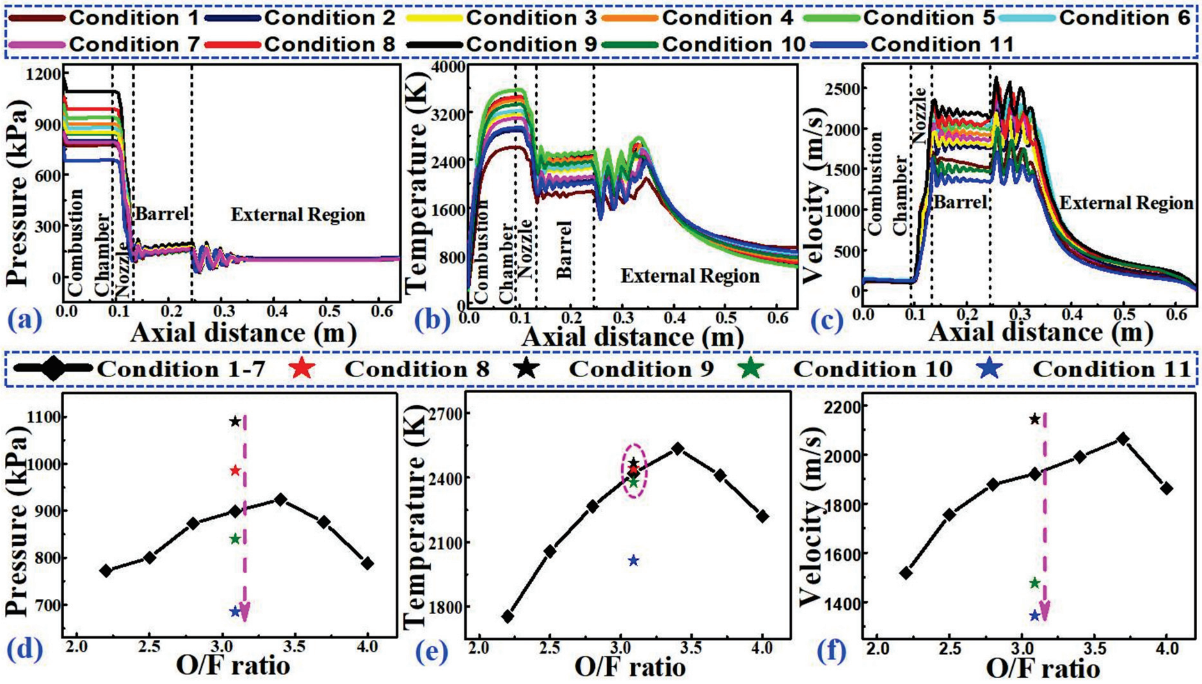

Figure 6. Predicted (**a**,**d**) gas pressure, (**b**,**e**) gas temperature, and (**c**,**f**) gas velocity curves with different O/F ratios.

At values higher than the ideal O/F ratio 3.09, an oxidizing environment forms, resulting in excessive oxidation of molten powder particles and an increase in the oxide content of the coating. If the ratio is less than 3.09, a large amount kerosene in the mixture will produce a flame with low temperature and poor oxygen content, and the number of unmelted particles and holes in the coating will increase. In fact, the ideal combustion conditions do not exist; to induce the full combustion of kerosene, usually, values higher than the ideal ratio are chosen for this spraying parameter. Combined with our work, it is intuitive that when the O/F quantitative relation is 3.4, the kerosene and oxygen can be totally combusted and the temperature and velocity of the flame flow are also optimal.

3.4. Effect of the Particle Size on Particle Behavior

Particle size is one of the most important factors affecting particle behavior. Particles of different sizes have different dynamic behaviors due to differences in their momentum. We selected six different particle sizes, fixed the O/F ratio at 3.4, and fixed the particle flow and nitrogen flow at 30 g/min and 10 m/s, respectively. The particles temperature and velocity curves with different sizes are simulated, as shown in Figure 7.

As can be seen from Figure 7a, small-sized particles are can be heated more than large particles; furthermore, their thermal inertia is smaller than that of large particles, so the temperature decreases faster. The liquid temperature T_l and solid temperature T_S of SAM1651 amorphous alloy are shown. The results show that 5–10 μm particles endure melting and solidifying throughout flight. The 20 and 30 μm particles remain melted; however, particles greater than 40 μm in size may not melt before they reach the substrate. With the increase in the particle size, the dynamic and thermal response of particles becomes slower than that of smaller particles, but the insulation capacity of large particles is stronger than that of smaller particles. Small particles are susceptible to heat but have a weaker ability to keep warm [24,35]. The melting behavior of the amorphous alloy powder is closely related to the amorphous phase content of the coating. The more fully melted the powder is, the more amorphous are the phases formed in the coating. When the particles hit the substrate in a molten or semimolten state, the splash thickness decreases, resulting in faster cooling and optimum corrosion resistance [36]. However, the amorphous phase content is low in the unmelted particles due to the presence of the crystal phase. Figure 7b shows that the small particles are susceptible to gas flow due to higher heating rates. However, due to their relatively large resistance, the reduction is greater as the distance increases from the outlet of the spray gun. Although the speed of large particles increases slowly, they tend to maintain axial velocity given their greater inertia.

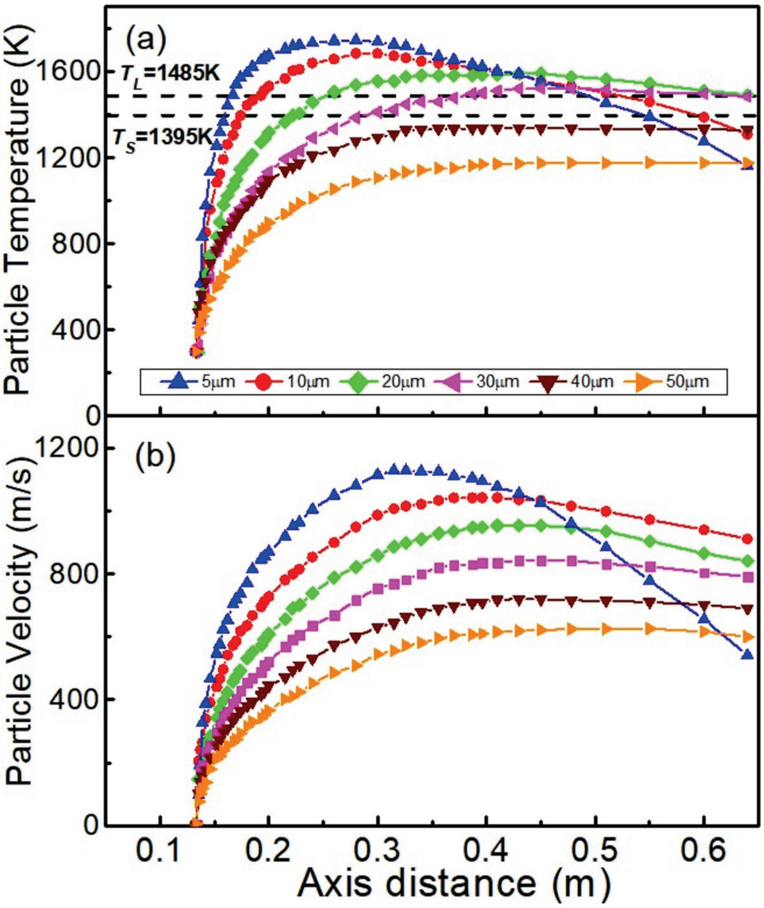

Figure 7. Effect of the particle size on the particle behavior for (**a**) particle temperature and (**b**) velocity.

To better analyze the effect of different particle sizes on coating properties, the particle trajectories under six conditions and the distribution of particles on X65 steel substrate are compared 0.04 s after the spraying process reaches the steady state. Figure 8 shows the particle flight behavior for various particle sizes with an injection rate of 10 m/s. As shown in Figure 8a, the small 5 μm particles move along the edge of the barrel. When the particles affect the substrate, they are concentrated in the upper half of the substrate and the local thickness of the coating is large. As the particle size increases, the radial motion distance of the particle increases. Large particles exhibit greater inertia than that of smaller; therefore, they maintain a radial motion and move a greater distance from the spray gun. Although 10 μm particles do not travel along the upper barrel, they are still mainly distributed in the upper half of the substrate. As shown in Figure 8c,d, the 20 and 30 μm particles move closer to the centerline of the external region and are evenly distributed on the substrate. Concurrently, the mass concentration of the coating with 30 μm particles is higher, indicating that the coating thickness and deposition efficiency are higher than those of the 20 μm particles. Figure 8f shows that when the particle size is large, the axial motion of the particle is close to the lower edge of the barrel and the particle distribution is concentrated in the lower part of the substrate, and a similar result was also observed in a past study [7].

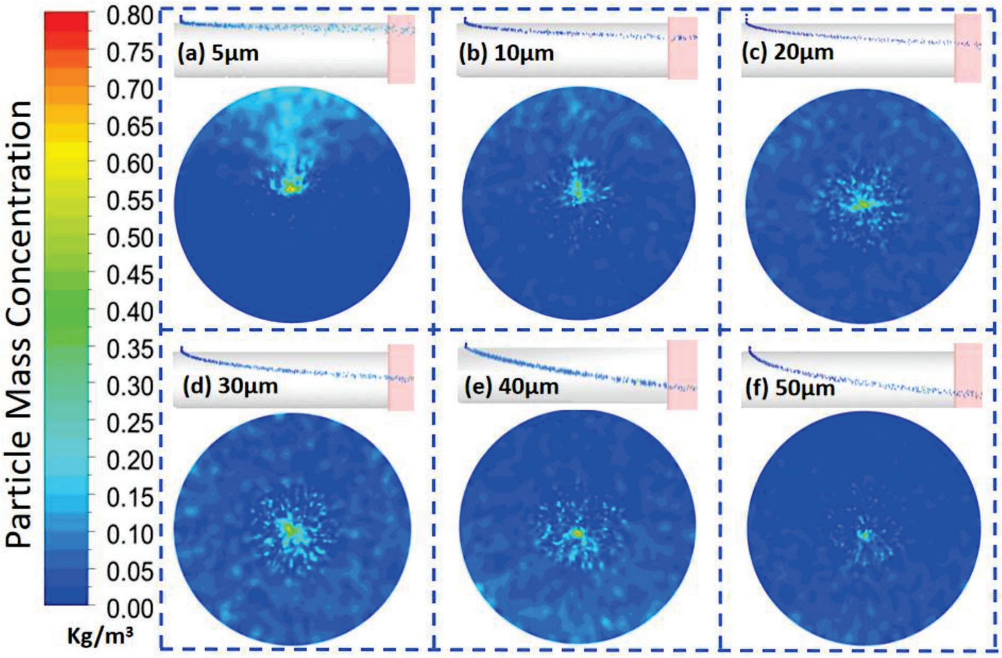

Figure 8. Effect of the particle size on particle trajectory and distribution.

According to the particle temperature and velocity curves, the particle size has an important influence in determining the particle temperature and velocity. In addition, according to the experiment, when the particle diameter is too small (less than 15 μm), the powder and nozzle exhibit a serious adhesion phenomenon, affecting the coating deposition rate. The degree of heating reduces greatly with particle diameters larger than 50 μm, which affects the deposition rate and surface quality of the coating. Compared with the small particles, when the particle size increases, the unmelted particles increase in number and the coating porosity increases. However, the amorphous alloy coating passive film prepared with large size powder particles is more stable than that of prepared with small particles [37]. The smaller the particle size, the larger is the surface area, and the higher the degree of oxidation is during spraying. As discussed above, the melting state is best when the particle size of the amorphous alloy powder is 20–30 μm and the prepared coating has a more uniform structure and excellent corrosion resistance.

3.5. Effect of Particle Shape on Particle Behavior

In this study, gas phase atomization is used to prepare an Fe-based amorphous alloy powder, a large number of nonspherical amorphous alloy particles inevitably exist. Previous studies have shown that the particle shape is related to particle motion resistance. With the increase in the particle sphericity, the drag decreases [38,39]. Figure 9 shows the temperature and velocity behavior of amorphous particles with different shapes when the particle size is 30 μm and the injection velocity is 10 m/s. As shown in Figure 9a, the particle temperature curves demonstrate that the temperatures of nonspherical powder particles are lower than those of spherical particles. Only when the sphericity is 1 or 0.9 does the particle temperature reach the molten or semimolten state. From Figure 9b, it can be seen that the nonspherical particles have a higher velocity. When the shape factor is reduced from 1 to 0.6, the nonspherical particles attain greater velocity and shorter times in the flame flow, which in turn brings their temperature down. Kamnis and Gu found similar results in particle spheres [40]. The flight behavior of the nonspherical WC–Co powder in an HVOF spray gun was simulated. Kamnis and Gu found that the nonspherical particles had a higher axial velocity and a lower temperature than spherical particles and were closer to the centerline of the torch. When the particle size decreases, the spherical degree has little effect on particle behavior.

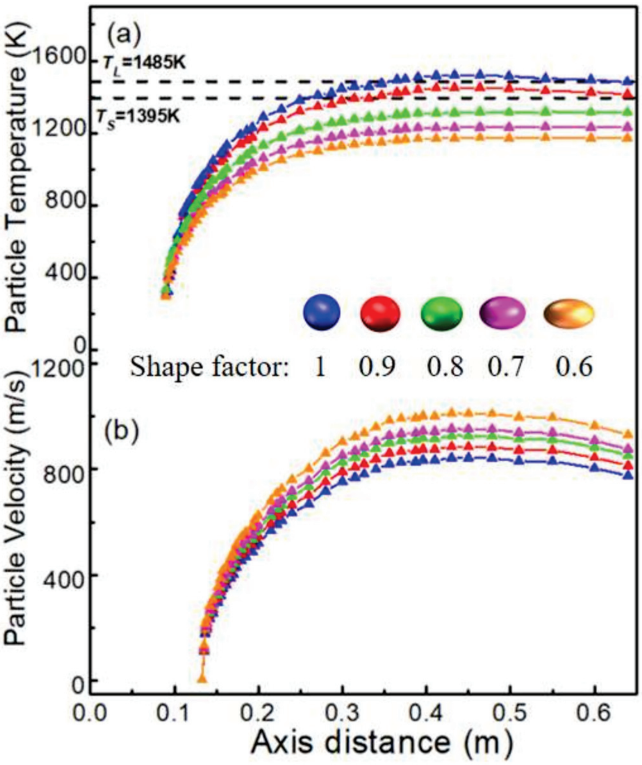

Figure 9. Effect of the particle shape on particle characteristics for (**a**) temperature and (**b**) velocity.

3.6. Effect of the Nitrogen Flow Rate and Particle Injection Rate on Particle Dynamics

The effect of the nitrogen injection rate and particle injection rate on amorphous particle dynamics has been studied in the literature [41–45]. In general, because nitrogen is inert and does not participate in combustion reactions, increasing the flow of nitrogen reduces its flow temperature and velocity [46]. The effect of different nitrogen flow and amorphous particle injection rates on HVOF-sprayed amorphous alloy coatings are compared and analyzed when the O/F ratio and particle size are fixed. In Figure 10a,b,d, it can be seen that when the nitrogen flow rate is 10 m/s, the particles move along the centerline of the spray gun and are evenly distributed on the substrate. When the nitrogen flow is 5 m/s, the particles move along the upper part of the gun and are concentrated in the upper part of the substrate. When the nitrogen flow rate is 20 m/s, the particles rebound after colliding with the inner wall of the spray barrel, changing the original trajectory and increasing the likelihood that the particles will adhere to the wall of the cylinder. At the same time, particle attachments lower the diameter of the spray gun barrel, further undermining the stability of the flame flow.

In addition, Figure 10b,c compare the fixed nitrogen flow at 10 m/s with different particle injection rates. The results show that the particle injection rate has no effect on the particle trajectory. However, the thickness of the coating (particle mass concentration) increases with the increasing particle injection rate. In HVOF spraying, the coating is deposited layer by layer. At the time the first layer formed, the temperature difference between the substrate and amorphous particles was large and the cooling rate of the amorphous alloy powder was the largest, approximately 10^6 K/s. In general, amorphous alloys display a lower heat conductivity [47–49], so the coating forms a temperature gradient along the depth of the coating [50,51]. The amorphous phase content of the coating decreases with the increase in the thickness.

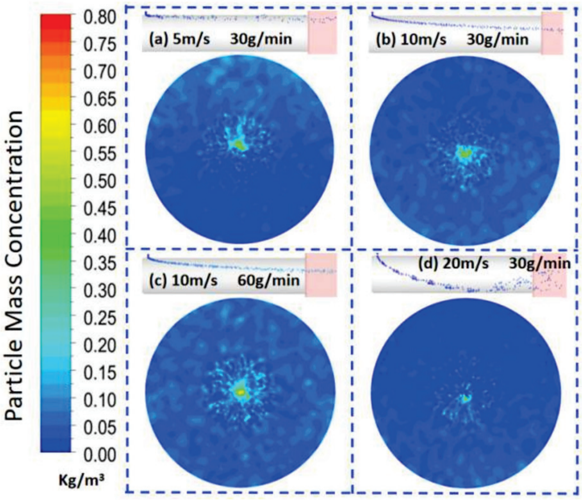

Figure 10. Effect of the nitrogen flow rate and particle injection rate on particle dynamics.

3.7. Effect of the Injection Angle of the Particle

We injected 30 μm particles at a nitrogen flow rate of 10 m/s. The trajectories of particles with injection angles of −45°, −30°, 0°, 30°, and 45° are simulated, as shown in Figure 11. As can be seen from Figure 11a, when the injection angle is in the opposite direction to the flame flow, the particle temperature is higher than that of the vertical injection particles. Because particles encounter high-temperature flame flow, more heat is generated. In contrast, when particles are shot in the direction of the flame, the temperature of the particles is lower than the temperature of the vertical injection particles. In addition, except for the particles at the −45° injection angle, the temperature differences between the other four angles are not large and the particles can melt well. Figure 11b shows the particle velocity during flight. The particles have the maximum velocity when the injection angle is 0°, and the velocity at the other four angles decreases slightly. Similar to the temperature behavior, the particles at −45° have the lowest velocity. Referring to the particle movement trajectories in Figure 11c, it is found that when the injection angle is −45°, the particles move along the upper gun wall and deviate from the flame flow's centerline. The best injection angle to obtain high temperature and low velocity is 45°. The precise selection of an injection angle not only ensures that the particles obtain reasonable temperature and velocity but also helps control the particles deposition position.

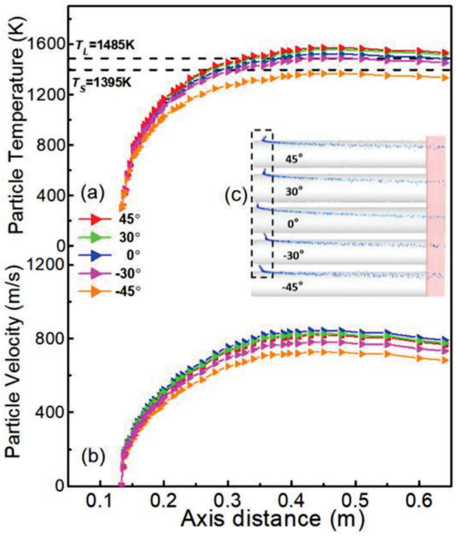

Figure 11. Effect of the particle injection angle on the particle behavior for (**a**) particle temperature, (**b**) velocity, and (**c**) trajectories.

4. Conclusions

A 3D CFD model is established using the Fluent software to study flame flow and amorphous alloy particle behavior in the HVOF spray process. The gas pressure, temperature, velocity, gas component, and amorphous alloy particle morphology and deposition patterns were examined in the HVOF spray process. Based on the results of numerical simulation, the following three conclusions can be obtained.

1. During the HVOF spraying process, the temperature, velocity, and pressure of flame flow appear the maximum value near O/F ratio of 3.4. When the O/F ratio is fixed, the flame flow pressure and velocity increases monotonically with the increases in the total fuel flow rate, but the total fuel flow rate has no significant effect on flame flow temperature.
2. Particle size and shape have an important influence on particle melting state and movement behavior. When the particle size of the amorphous alloy powder is 20–30 μm, the particles are evenly distributed on the substrate with high mass concentration. When the particle sphericity is 1 or 0.9, the particle reaches the molten or semimolten state. The prepared coating has a more uniform structure and low porosity.
3. Nitrogen flow rate, particle injection rate, and angle have a great influence on HVOF spraying amorphous alloy coating. When the nitrogen flow rate is 10 m/s, the particles move along the centerline of the spray gun and are evenly distributed on the substrate. The increase in the particle injection rate can increase the coating thickness (particle mass concentration) but has no effect on particle trajectory. The best incident angle is 45°, which not only ensures that the particles obtain reasonable temperature and velocity but also helps control the particle deposition.

This study is helpful to understand the process of preparing Fe-based amorphous alloy coatings by HVOF spraying, deepen the understanding of flame flow and particle behavior, and provide theoretical guidance for the improvement of HVOF spraying equipment and selection of manufacturing parameters.

Author Contributions: Conceptualization, X.L. and P.L. (Pengfei Liu); Data curation, P.L. (Pengfei Liu); Formal analysis, X.L.; Funding acquisition, J.Y. and Y.Y.; Investigation, X.L. and H.L.; Project administration, X.L. and Y.Y.; Resources, J.Y.; Software, X.L. and R.S.; Validation, H.L.; Writing—original draft, X.L., L.W. and P.L. (Pengfei Li); Writing—review & editing, X.L. and P.L. (Pengfei Li). All authors have read and agreed to the published version of the manuscript.

Funding: This project is supported by the National Natural Science Foundation of China (Grant No. 52071234), National Natural Science Foundation of China (Grant No. 51879189), and the National Natural Science Foundation of China for Innovative Research Groups (Grant No. 51321065).

Institutional Review Board Statement: Not applicable.

Informed Consent Statement: Not applicable.

Data Availability Statement: Data sharing is not applicable to this article.

Conflicts of Interest: There are no conflicts of interest to declare.

Abbreviations

Nomenclature

C_p	specific heat, J/(kg·K)
E	enthalpy value
K_{eff}	kinetic energy in turbulent and nonturbulent flow
u_{eff}	the addition of nonturbulent viscosity
k	thermal conductivity
R_a	net productivity
S_a	productivity
S_h	reaction source energy

x_i	coordinate in the i direction
J_a	mass diffusion flux
δ	Kronecker delta
σ_t	turbulent Prandtl number
T	temperature
T_g	glass transition temperature
T_l	liquid temperature
T_s	solid temperature
τ	deviatoric stress tensor
T	turbulent environment
p	pressure, Pa
ρ	density, kg/m^3
u_i	velocity in the i direction
μ_t	turbulent viscosity
Y_a	mass fraction of product a

References

1. Hou, B.; Li, X.; Ma, X.; Du, C.; Zhang, D.; Zheng, M.; Ma, F. The cost of corrosion in China. *J. NPJ Mater. Degrad.* **2017**, *1*, 4. [CrossRef]
2. Shen, J.; Chen, Q.; Sun, J.; Fan, H.; Wang, G. Exceptionally high glass-forming ability of an FeCoCrMoCBY alloy. *J. Appl. Phys. Lett.* **2005**, *86*, 279. [CrossRef]
3. Xu, D.; Duan, G.; Johnson, W.L. Unusual Glass-Forming Ability of Bulk Amorphous Alloys Based on Ordinary Metal Copper. *J. Phys. Rev. Lett.* **2004**, *92*, 245504. [CrossRef] [PubMed]
4. Amjad, I.; Sumera, S.; Moazam, M.; Muhammad, Y. Comparative analysis on the structure and properties of iron-based amorphous coating sprayed with the thermal spraying techniques. *Coatings* **2020**, *10*, 1003.
5. Wei, H.W. Roles of minor additions in formation and properties of bulk metallic glasses. *J. Prog. Mater. Sci.* **2007**, *52*, 540–596.
6. Ramya, M.; Karthika, M.; Selvakumar, R.; Raj, B.; Ravi, K.R. A facile and efficient single step ball milling process for synthesis of partially amorphous Mg-Zn-Ca alloy powders for dye degradation. *J. Alloy. Compd.* **2017**, *696*, 185–192. [CrossRef]
7. Lan, S.; Ren, Y.; Wei, X.; Wang, B.; Gilbert, E.P.; Shibayama, T. Hidden amorphous phase and reentrant supercooled liquid in Pd-Ni-P metallic glasses. *Nat. Commun.* **2017**, *8*, 14679. [CrossRef]
8. Li, X.; Roberts, M.; O'Keeffe, S.; Sercombe, T. Selective laser melting of Zr-based bulk metallic glasses: Processing, microstructure and mechanical properties. *Mater. Des.* **2016**, *112*, 217–226. [CrossRef]
9. Tului, M.; Bartuli, C.; Bezzon, A.; Marino, A.L.; Marra, F.; Matera, S.; Pulci, G. Amorphous steel coatings deposited by cold-gas spraying. *Metals* **2019**, *9*, 678. [CrossRef]
10. Lin, T.-J.; Sheu, H.-H.; Lee, C.-Y.; Lee, H.-B. The study of mechanical properties and corrosion behavior of the Fe-based amorphous alloy coatings using high velocity oxygen fuel spraying. *J. Alloy. Compd.* **2021**, *867*, 159132. [CrossRef]
11. Jadidi, M.; Moghtadernejad, S.; Dolatabadi, A. A comprehensive review on fluid dynamics and transport of suspension/liquid droplets and particles in High-velocity oxygen fuel (HVOF) thermal spray. *Coatings* **2015**, *5*, 576–645. [CrossRef]
12. Zhu, Y.Y.; Li, Z.G.; Li, R.F.; Li, M.; Feng, K.; Wu, Y.X.; Kato, H. High power diode laser cladding of Fe-Co-B-Si-C-Nb amorphous coating: Layered microstructure and properties. *J. Surf. Coat. Technol.* **2013**, *235*, 699–705. [CrossRef]
13. Li, G.; Gan, Y.; Liu, C.; Shi, Y.; Zhao, Y.; Kou, S. Corrosion And Wear Resistance of Fe-Based Amorphous Coatings. *Coatings* **2020**, *10*, 73. [CrossRef]
14. Zhou, Z.; Han, F.X.; Yao, H.H.; Li, Y.Z.; Yang, Y.G.; Guo, X.Y.; Wang, L. Novel Fe-Based Amorphous composite coating with a unique interfacial layer improving thermal barrier application. *J. ACS Appl. Mater. Interfaces* **2021**, *13*, 23057–23066. [CrossRef] [PubMed]
15. Yoon, S.; Lee, C.; Choi, H.; Jo, H. Kinetic spraying deposition behavior of bulk amorphous NiTiZrSiSn feedstock. *J. Mater. Sci. Eng. A* **2005**, *415*, 45–52. [CrossRef]
16. Kamnis, S.; Gu, S. Numerical modelling of propane combustion in a high velocity oxygen–fuel thermal spray gun. *Chem. Eng. Process.* **2006**, *45*, 246–253. [CrossRef]
17. Li, M.; Christofides, P.D. Modelling and control of high-velocity oxygen-fuel (HVOF) thermal spray: A tutorial review. *J. Therm. Spray Technol.* **2009**, *18*, 753–768. [CrossRef]
18. Oksa, M.; Turunen, E.; Suhonen, T.; Varis, T.; Hannula, S.-P. Optimization and characterization of high velocity oxy-fuel sprayed coatings: Techniques, Materials, and applications. *J. Therm. Spray Coat.* **2011**, *1*, 17–52. [CrossRef]
19. Li, M.; Christofides, P.D. Modelling and analysis of HVOF thermal spray process accounting for powder size distribution. *Chem. Eng. Sci.* **2003**, *58*, 849–857. [CrossRef]
20. Tabbara, H.; Gu, S. Computational Simulation of Liquid-Fuelled HVOF Thermal Spraying. *Surf. Coat. Technol.* **2009**, *204*, 676–684. [CrossRef]

21. Oberkampf, W.L.; Talpallikar, M. Analysis of High-Velocity Oxygen-Fuel (HVOF) Thermal Spray Torch Part 1: Numerical Formulation. *J. Therm. Spray Technol.* **1996**, *5*, 53–68. [CrossRef]
22. Gu, S.; Eastwick, C.N.; Sirnmons, K.A.; McCartney, D.G. Computational Fluid Dynamic Modeling of Gas Flow Characteristics in a High-Velocity Oxy-Fuel Thermal Spray System. *J. Therm. Spray Technol.* **2001**, *10*, 461–469.
23. Sakaki, K.; Shimizu, Y. Effect of the Increase in the Entrance Convergent Section Length of the Gun Nozzle on the High-Velocity Oxygen Fuel and Cold Spray Process. *J. Therm. Spray Technol.* **2001**, *10*, 487–496. [CrossRef]
24. Yang, X.; Eidelman, S. Numerical Analysis of a High-Velocity OxygenFuel Thermal Spray System. *J. Therm. Spray Technol.* **1996**, *5*, 175–184. [CrossRef]
25. Dongmo, E.; Wenzelburger, M.; Gadow, R. Analysis and optimization of the HVOF process by combined experimental and numerical approaches. *Surf. Coat. Technol.* **2008**, *202*, 4470–4478. [CrossRef]
26. Liu, S.L.; Zheng, X.P.; Geng, G.Q. Influence of nano-WC-12Co powder addition in WC-10Co-4Cr AC-HVAF sprayed coatings on wear and erosion behavior. *Wear* **2010**, *269*, 362–367. [CrossRef]
27. Li, M.; Shi, D.; Christofides, P.D. Diamond Jet Hybrid HVOF Thermal Spray: Gas-Phase and Particle Behavior Modeling and Feedback Control Design. *Ind. Eng. Chem. Res.* **2004**, *43*, 3632–3652. [CrossRef]
28. Jadidi, M.; Yeganeh, A.Z.; Dolatabadi, A. Numerical Study of Suspension HVOF Spray and Particle Behavior Near Flat and Cylindrical Substrates. *J. Therm. Spray Technol.* **2018**, *27*, 59–72. [CrossRef]
29. Ajdelsztajn, L.; Dannenberg, J.; Lopez, J.; Yang, N.; Farmer, J.; Lavernia, E.J. High-velocity oxygen fuel thermal spray of Fe-based amorphous alloy: A numerical and experimental study. *Metall. Mater. Trans. A* **2009**, *40*, 2231–2240. [CrossRef]
30. Khan, M.N.; Shamim, T. Investigation of a dual-stage high velocity oxygen fuel thermal spray system. *Appl. Energy* **2014**, *130*, 853–862. [CrossRef]
31. Pan, J.; Hu, S.; Yang, L.; Ding, K.; Ma, B. Numerical analysis of flame and particle behavior in an HVOF thermal spray process. *Mater. Des.* **2016**, *96*, 370–376. [CrossRef]
32. Magnussen, B.F.; Hjertager, B.H.J.S.O.C. On Mathematical Modeling of Turbulent Combustion with Special Emphasis on Soot Formation and Combustion. *Symp. Int. Combust. Proc.* **1977**, *16*, 719–729. [CrossRef]
33. Emami, H.; Mahmoudi, Y. Effects of Combustion Model and Chemical Kinetics in Numerical Modeling of Hydrogen-Fueled Dual-Stage HVOF System. *J. Therm. Spray Technol.* **2019**, *28*, 333–345. [CrossRef]
34. Li, C.; Gao, X.; Zhang, D.; Gao, H.; Han, X.; Zhang, B. Numerical Investigation on the Flame Characteristics and Particle Behaviors in a HVOF Spray Process Using Kerosene as Fuel. *J. Therm. Spray Technol.* **2021**, *30*, 725–738. [CrossRef]
35. Pawlowski, L. *The Science and Engineering of Thermal Spray Coating*; John Wiley & Sons Ltd.: New York City, NY, USA, 2008; Volume 2.
36. Planche, M.P.; Liao, H.; Normand, B.; Coddet, C. Relationships between NiCrBSi particle characteristics and corresponding coating properties using diferent thermal spraying processes. *Surf. Coat. Technol.* **2005**, *200*, 2465. [CrossRef]
37. Farmer, J.C.; Haslam, J.J.; Day, S.D.; Lian, T.; Saw, C.K.; Hailey, P.D.; Aprigliano, L.F. Corrosion resistance of thermally sprayed high-boron iron-based amorphous-metal coatings: $Fe_{49.7}Cr_{17.7}Mn_{1.9}Mo_{7.4}W_{1.6}B_{15.2}C_{3.8}Si_{2.4}$. *J. Mater. Res.* **2007**, *22*, 2297. [CrossRef]
38. Cheng, D.; Xu, Q.; Trapaga, G.; Lavernia, E.J. The effect of particle size and morphology on the in-flflight behaviour of particles during high-velocity oxyfuel thermal spraying. *Metall. Mater. Trans. B* **2001**, *32*, 525–535. [CrossRef]
39. Ganser, G. A rotational approach to drag prediction of spherical and nonspherical particles. *Powder Technol.* **1993**, *77*, 143–152. [CrossRef]
40. Gu, S.; Kamnis, S. Numerical modelling of in-flight particle dynamics of non-spherical powder. *Surf. Coat. Technol.* **2009**, *203*, 3485–3490. [CrossRef]
41. Gu, S.; McCartney, D.G.; Eastwick, C.N.; Simmons, K. Numerical modelling of in-flight characteristics of inconel 625 particles during High-Velocity Oxy-Fuel thermal spraying of nanocrystalline materials: An overview. *Model. Simul. Mater. Sci. Eng.* **2002**, *11*, 1.
42. Li, M.; Christofides, P.D. Multi-scale modeling and analysis of an industrial HVOF thermal spray process. *Chem. Eng. Sci.* **2005**, *60*, 3649–3669. [CrossRef]
43. Hossainpour, S.; Binesh, A.R. A CFD study of sensitive parameter effects on the combustion in a High Velocity Oxygen Fuel thermal spray gun. *Proc. World Acad. Sci. Eng. Technol.* **2018**, *31*, 213–220.
44. Kamali, R.; Binesh, A.R. The importance of sensitive parameters effect on the combustion in a High Velocity Oxygen-Fuel spray system. *Int. Commun. Heat Mass Transf.* **2009**, *36*, 978–983. [CrossRef]
45. Chang, C.H.; Moore, R.L. Numerical simulation of gas and particle flow in a high velocity oxygen fuel (HVOF) torch. *J. Therm. Spray Technol.* **1995**, *4*, 358–366. [CrossRef]
46. Li, M.; Christofides, P.D. Computational study of particle in-flight behaviour in the HVOF thermal spray process. *Chem. Eng. Sci.* **2006**, *61*, 6540–6552. [CrossRef]
47. Shin, D.I.; Gitzhofer, F.; Moreau, C. Properties of induction plasma sprayed iron based nanostructured alloy coatings for metal based thermal barrier coatings. *J. Therm. Spray Technol.* **2007**, *16*, 118. [CrossRef]
48. Lee, K.; Euh, K.; Nam, D.H.; Lee, S.; Kim, N.J. Wear resistance and thermal conductivity for zr-base amorphous alloy/metal surface composites fabricated by high-energy electron beam irradiation. *Mater. Sci. Eng. A* **2007**, *449*, 937. [CrossRef]

49. Kim, J.; Lee, C.; Choi, H.; Jo, H.; Kim, H. Ni-Ti-Zr-Si-Sn bulk metallic glass particle deposition and coating formation vacuum plasma spraying. *Mater. Sci. Eng. A* **2007**, *449*, 858. [CrossRef]
50. Vardelle, A.; Moreau, C.; Fauchais, P. The dynamics of deposit formation in thermal-spray processes. *MRS Bull.* **2000**, *25*, 32. [CrossRef]
51. Sampath, S.; Herman, H. Rapid solidification and microstructure development during plasma spray deposition. *J. Therm. Spary. Technol.* **1996**, *5*, 445–456. [CrossRef]

coatings

MDPI

Article

Impact of Engineering Surface Treatment on Surface Properties of Biomedical TC4 Alloys under a Simulated Human Environment

Hongyun Deng [1], Kuixue Xu [1], Shuguang Liu [1,2,*], Chaofeng Zhang [1], Xiongwei Zhu [1], Haoran Zhou [1], Chaoqun Xia [3] and Chunbao Shi [1]

[1] Beijing Chunlizhengda Medical Instrucments Co., Ltd., Beijing 101100, China; denghongyun@clzd.com (H.D.); xukuixue@clzd.com (K.X.); zhangchaofeng@clzd.com (C.Z.); zhuxiongwei@clzd.com (X.Z.); zhouhaoran@clzd.com (H.Z.); shichunbao@clzd.com (C.S.)

[2] School of Materials Science and Engineering, University of Science and Technology Beijing, Beijing 100083, China

[3] School of Materials Science and Engineering, Research Institute for Energy Equipment Materials, Hebei University of Technology, Tianjin 300130, China; chaoqunxia@hebut.edu.cn

* Correspondence: lsg_lsglsg@hotmail.com

Abstract: The impact of sandblasting, anodic oxidation, and anodic oxidation after sandblasting on the surface structure and properties of titanium alloys was investigated. It was found that the surface treatments had a significant influence on the surface roughness values, contact angle values, Vickers hardness, wear resistance, and corrosion resistance of titanium alloys. The surface roughness of titanium alloys with sandblasting treatment was increased by 67% compared to untreated specimen. The Vickers hardness of titanium alloys treated with anodic oxidation after sandblasting was found to increase from 380.8 HV to 408.5 HV, which was increased by 7.3%. The surface treatments in this work improved the wear resistance of the titanium alloys to some extent, and it can be found that the wear scar width is reduced by up to 18.6%. The corrosion resistance of the titanium alloys was found to improve on anodic oxidation. Sandblasting was found to increase surface roughness and promote the formation of a porous layer during the anodization process, resulting in a slight decrease in corrosion resistance. The corrosion current density was increased by 21% compared to the untreated specimen. The corrosion current density of the titanium alloy treated with anodic oxidation decreased to 7.01×10^{-8} A/cm^2. The corrosion current density was decreased by 24% compared to the untreated specimen. The corrosion current density of the titanium alloys treated with anodic oxidation after sandblasting decreased to 7.63×10^{-8} A/cm^2. The corrosion current density was decreased by 8.8% compared to the specimen with anodic oxidation. The anodic oxidation provided a hydrophilic property for the surface of Ti alloys, which could show a better osseointegration characteristic than that of sandblasting. The impact of the surface treatments on surface structure and properties of titanium alloys was studied.

Keywords: Ti alloys; anodic oxidation; wear; corrosion resistance; surface properties

1. Introduction

Nowadays, titanium (Ti) and Ti alloys are applied in many key areas, such as ocean and aerospace engineering and the medical industry, due to their excellent combination of mechanical properties, strong corrosion resistance, and low density [1–4]. As a medical material, specifically, the TC4 alloy exhibits good processability and mechanical properties; therefore, it is applied widely in artificial joints, oral applications, and as a skull modification Ti mesh [5–7]. The formation of oxide films of Ti alloys can hinder the contact of the medium and the substrates of Ti alloys, which improve the corrosion resistance of Ti alloys [8,9]. However, Ti alloys oxide films naturally generated are relatively thin, and do not make a significant contribution towards corrosion resistance of Ti alloys. Moreover, as a biomedical metal implant material, after Ti alloys are implanted in the human body, they may undergo corrosion due to body fluids within the human environment, and suffer abrasion from human bone or other implants. The occurrence of wear can reduce the mechanical properties of the metal material, and cause the failure of the implant [10–13], eventually leading to increased patient suffering. It has been reported that the wear debris generated due to poor wear resistance of Ti alloys can lead to osteolysis [14,15]. Therefore, improving the surface properties of medical implants using Ti alloys is urgent.

Surface modification technologies are very important methods to improve the surface properties of lightweight alloys [16–18]. Various surface modification technologies, including magnetron sputtering, sandblasting, electroless plating, anodizing, and laser surface treatment, have been applied to improve the surface properties of Ti alloys [19–23]. In actual production and processing, sandblasting and anodic oxidation are mature technologies for surface modification of Ti alloys. However, in the case of artificial joint prostheses, there are very few studies on the performance of Ti alloys after sandblasting and anodizing.

In this study, different surface treatments were carried out on the surface of the Ti alloys, including sandblasting, anodizing, and anodizing after sandblasting. The microstructures, surface roughness values, Vickers hardness, wear resistance, corrosion resistance, and contact angle value of Ti alloys were investigated. The influence of surface treatments on the microstructures and properties of the Ti alloys was carefully studied, and the related mechanism was also discussed.

2. Materials and Methods

2.1. Materials

The biomedical Ti alloys used in the present work is Ti-6Al-4V which has lower content interstitial elements C, N, and O and impurity element, Fe (material designation is TC4 ELI), compared to that of the common TC4 alloy. The elements content of Al, V, C, N, O, Fe, and H are 6%, 4%, 0.03%, 0.01%, 0.1%, 0.1%, and 0.003%, respectively. The balance is Ti. Specimens of 3 mm thickness and 14 mm diameter were cut from a bar. Then, the surfaces of the specimens were treated by finish turning (specimen A). The specimens were fine turned and washed ultrasonically in acetone and ethanol [24,25]. Finally, the surfaces of the Ti alloys were treated by different surface treatments, i.e., sandblasting (specimen B), anodic oxidation (specimen C), and anodic oxidation after sandblasting (specimen D).

2.2. Experimental Procedure

2.2.1. Sandblasting

The specimens were placed on the sample table. A sandblasting machine (Jichuan Machinery Technology Co., Ltd., Shanghai, China) was used to treat the surface of the Ti alloys. Emery with 16 mesh was used for the sandblasting. The distance between the spray gun and specimen was 50 mm, and the treatment lasted 10–30 s. After the surfaces of the Ti alloys were treated, the specimens were cleaned and dried carefully.

2.2.2. Anodic Oxidation

Before anodic oxidation, the specimens were pre-treated for 1–25 min. The specimens were anodized using an anodizing equipment for 20 min. A voltage of 30 V was applied to the specimens. The electrolyte for anodic oxidation consisted of NaOH (7.5 M/L), $Na_2C_4H_4O_6$ (0.05 M/L), Na_2SiO_3 (0.33 M/L), and EDTA (0.07 M/L); it was heated to 25 °C and was agitated during anodizing. After the surfaces of the Ti alloys were treated, the specimens were cleaned and dried carefully.

2.2.3. Anodic Oxidation after Sandblasting

In the first part of the process, the specimens were treated by sandblasting. The conditions of sandblasting treatment were identical to those listed in Section 2.2.1. In the second part of the process, the sandblasted specimens were anodized, according to the steps mentioned in Section 2.2.2.

2.2.4. Analysis Methods

The surface morphology of the specimens was observed by scanning electron microscopy (SEM, JSM-7100, JEOL, Ltd., Tokyo, Japan) and atomic force microscopy (AFM, Agilent 5500, Agilent Technologies Co., Ltd., Santa Clara, CA, USA). The phase compositions of untreated and surface-treated specimens were confirmed by conventional X-ray diffraction (XRD) and Cu Kα radiation (D/ max-2500/PC), and the diffraction angle range was 20–100 degrees (step size 0.02 degrees). The microhardness of the specimens before and after surface treatment was tested by the microhardness tester (HMV-2T, Shimadzu Corp., Tokyo, Japan) with a load of 200 gf and a testing duration of 15 s. The penetration depth of the indentation tip was about 1 µm. The wear resistance was evaluated by a Bruker UMT-5 friction and wear tester (Beijing Asia Science&Tech technology Co., Ltd., Beijing, China) with a load of 2N and a testing time of 1600s at 25 °C. Grinding ball was a Cr15 ball with 6 mm. The surface roughness values were measured by a roughometer (SRA-2, Shangguang Instruments Co., Ltd., Beijing, China) with a testing range of 1–3 µm and testing speed of 0.5 mm/s. The CHI660E electrochemical workstation (Shanghai Chenhua Instrument Co., Ltd., Shanghai, China) and the three-electrode electrochemical cell system were used for electrochemical studies in a simulated body fluid (SBF) solution at 37 °C. The electrochemical impedance spectroscopy (EIS) of specimens were tested after the specimens were soaked for 30 min. A Pt foil electrode and saturated calomel electrode (SCE) were used as counter electrode and reference electrode, respectively. The contact angles of water on the surface of specimens were tested using a contact angle measuring instrument (DCAT21, DataPhysics Instruments, Filderstadt, Germany) equipped with a digital camera (DataPhysics Instruments, Filderstadt, Germany) at 20 °C.

3. Results

This section may be divided by subheadings. It should provide a concise and precise description of the experimental results, their interpretation, as well as the experimental conclusions that can be drawn.

3.1. Morphologies and Structures

Figure 1 shows the macroscopic morphology of each specimen. This shows that sandblasting could significantly increase the surface roughness of the Ti alloys. In addition, black films appeared on the Ti alloys after anodizing.

Figure 2 shows the surface morphologies of the Ti alloys with different surface treatments by SEM. Grain boundaries were found on the surface of specimen A (Figure 2a). However, the grain boundaries disappeared when the Ti alloys were anodized. Moreover, some cracks and islands were found on the surface of the specimen C (Figure 2c). In addition, surface deformation was generated and grain boundaries disappeared on sandblasted for specimen B. Furthermore, some boundaries were generated on the surface of specimen B (Figure 2b). More islands were found on specimen D. However, the boundaries resulting from the sandblasting treatment were significantly reduced (Figure 2d). In addition, EDS showed O and Ti on the surface of specimens C and D (Figure 2e,f). This indicates that oxidation films of Ti alloys were formed, which is consistent with optical microscopy images (Figure 1c,d).

Figure 3 shows the AFM morphology of Ti alloys with different surface treatments. The surface of specimen A was found to be smooth (Figure 3a) and treated surfaces were rougher. Moreover, a larger number of small bumps were found on the specimen D (Figure 3d).

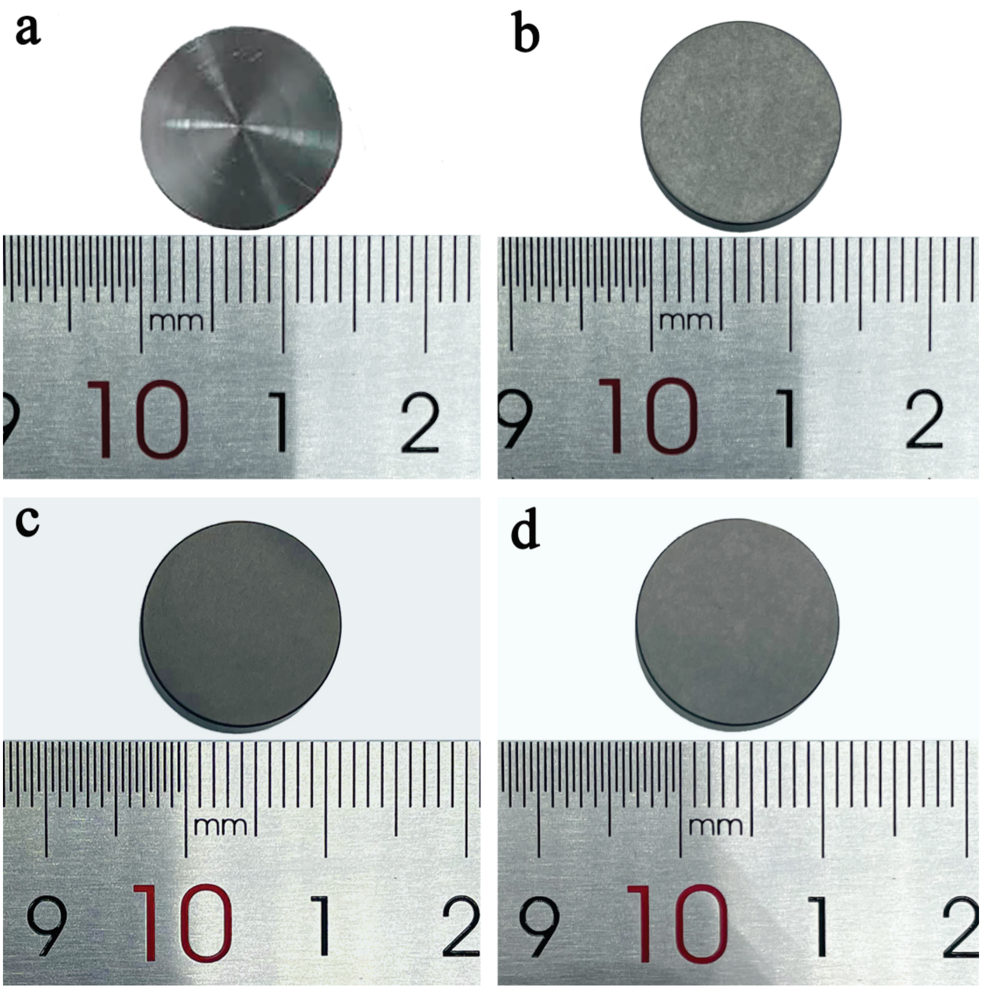

Figure 1. The appearance of Ti alloys with different surface treatments. (**a**) specimen A, (**b**) specimen B, (**c**) specimen C, and (**d**) specimen D.

Figure 4 shows the XRD results of the Ti alloys with different surface treatments. Three diffraction peaks with higher diffraction intensity were all substrates of Ti alloys. Moreover, the peak of titanium oxide was not found on the specimens C and D. However, the minute changes of XRD patterns can still be observed through the partial enlarged view with 2θ from 35 to 42 degrees. The XRD peak of the sample after processing of sandblasting shifted slightly towards a high angle orientation compared to the untreated sample. According to Bragg's Law ($2d\sin\theta = n\lambda$), the micro residual stress produced by severe deformation within a certain depth of the surface in the process of sandblasting changed lattice parameter. The crystal plane spacing perpendicular to the surface direction is decreased. After the following anodic oxidation treatment, the stress was released by the synergistic effect of the electrolyte corrosion and oxide film growth. Therefore, the XRD peaks of sample C and D returned to normal position again. Moreover, for specimen C, it could be seen that the α(101) peak shifted to the higher angles indicating a compressive strain out-of-plane[1,2] compared to specimen D. In addition, the width of the diffraction peaks slightly broadened apart from the untreated sample, which indicate that the grains were refined in the condition of identical composition after surface deformation strengthening and anodic oxidation treatment.

Figure 5 shows surface roughness values of Ti alloys with different surface treatments. It could be found that the surface roughness values of specimen C had a little change compared to that of specimen A. In addition, the surface roughness values of specimen B were increased by 67% obviously compared to that of specimen A. Moreover, the surface roughness values of specimen D were increased by 100% compared to that of specimen A.

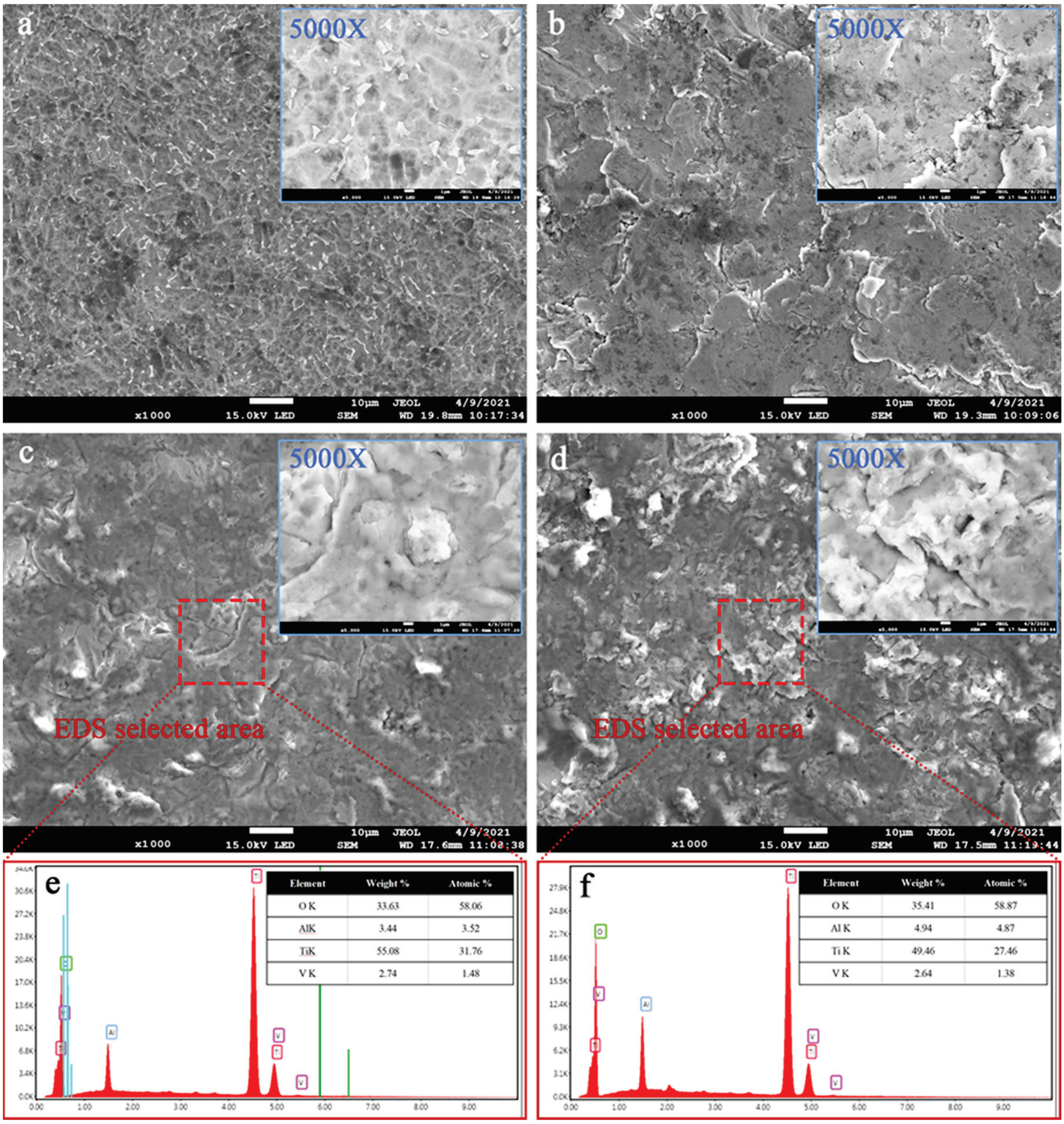

Element	Weight %	Atomic %
O K	33.63	58.06
AlK	3.44	3.52
TiK	55.08	31.76
V K	2.74	1.48

Element	Weight %	Atomic %
O K	35.41	58.87
Al K	4.94	4.87
Ti K	49.46	27.46
V K	2.64	1.38

Figure 2. Surface morphologies of Ti alloys with different surface treatments. (**a**) specimen A, (**b**) specimen B, (**c**) specimen C, and (**d**) specimen D, (**e**) the EDS results of specimen C, (**f**) the EDS results of specimen D.

3.2. Mechanical Properties

Figure 6 shows the Vickers hardness of Ti alloys with different surface treatments. It could be found that the Vickers hardness of specimen C was increased to 393.4 HV, which was increased by 2.5% compared to specimen A. Moreover, the Vickers hardness of specimen B was increased to 390.7 HV, which was increased by 3.3% compared to specimen A. It also could be found that the Vickers hardness of specimen D was increased to 408.5 HV, which was increased by 7.3% compared to specimen A. Therefore, the increase in Vickers hardness of Ti alloys with various surface treatments was not significant in this work.

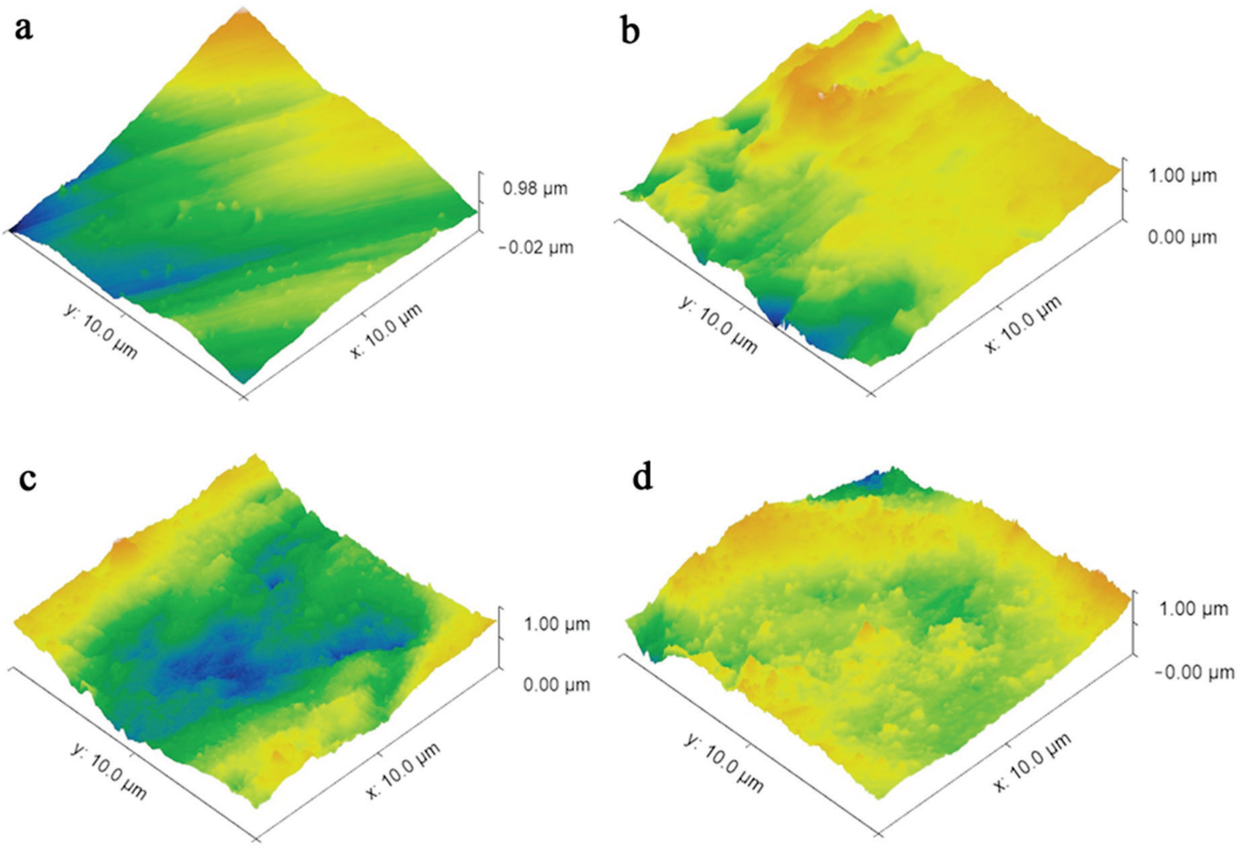

Figure 3. Atomic force microscopy morphology of Ti alloys with different surface treatments. (**a**) specimen A, (**b**) specimen B, (**c**) specimen C, and (**d**) specimen D.

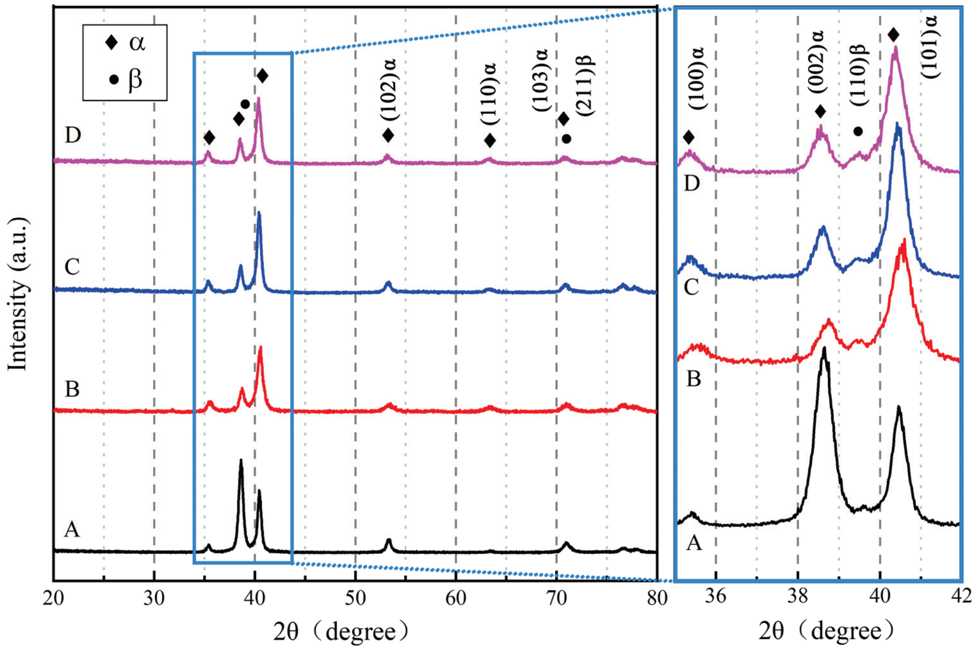

Figure 4. The XRD results of Ti alloys with different surface treatments. (**A**) specimen A, (**B**) specimen B, (**C**) specimen C, and (**D**) specimen D.

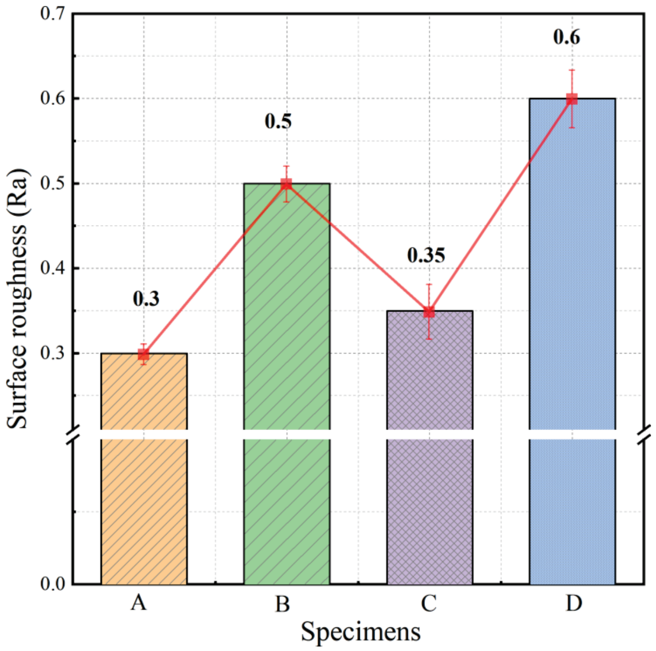

Figure 5. Surface roughness values of Ti alloys with different surface treatments.

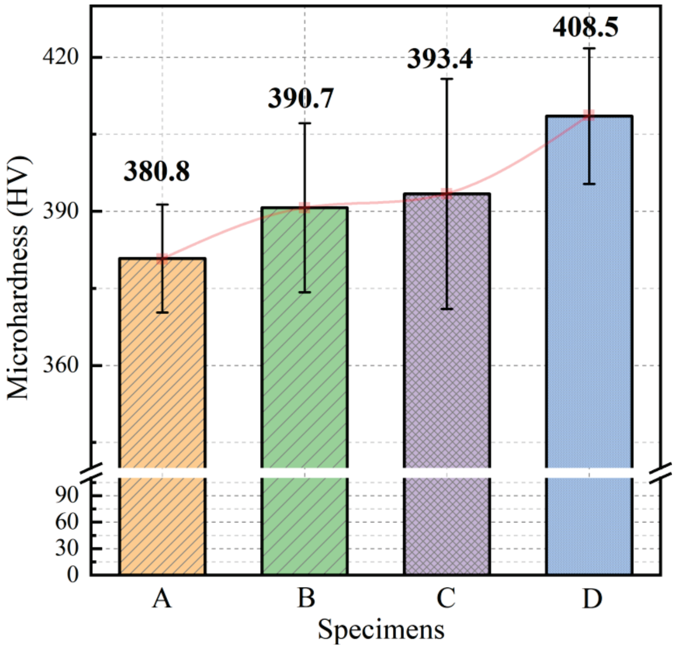

Figure 6. The Vickers hardness of Ti alloys with different surface treatments.

Figure 7 shows the variations of friction coefficients of Ti alloys with wear time. Figure 8 shows the wear morphologies of Ti alloys with different surface treatments. It could be found that friction coefficients of Ti alloys with different surface treatments had a little change in the stable stage of wear. However, it also could be found that the friction coefficients of specimens C and D were increased gradually from very low values in the initial stage of wear (Figure 7). Moreover, there are some differences in the optical images of wear morphology of Ti alloys with different surface treatments (Figure 8). The wear scar width of 980.2 μm was found on the surface of Ti alloys without surface treatment. However, the wear marks of specimens B, C, and D were narrower, reaching wear scar width of 823.1 μm, 798.3 μm, and 818.2 μm, which was decreased by 16%, 18.6%, and 16.5% compared to specimen A.

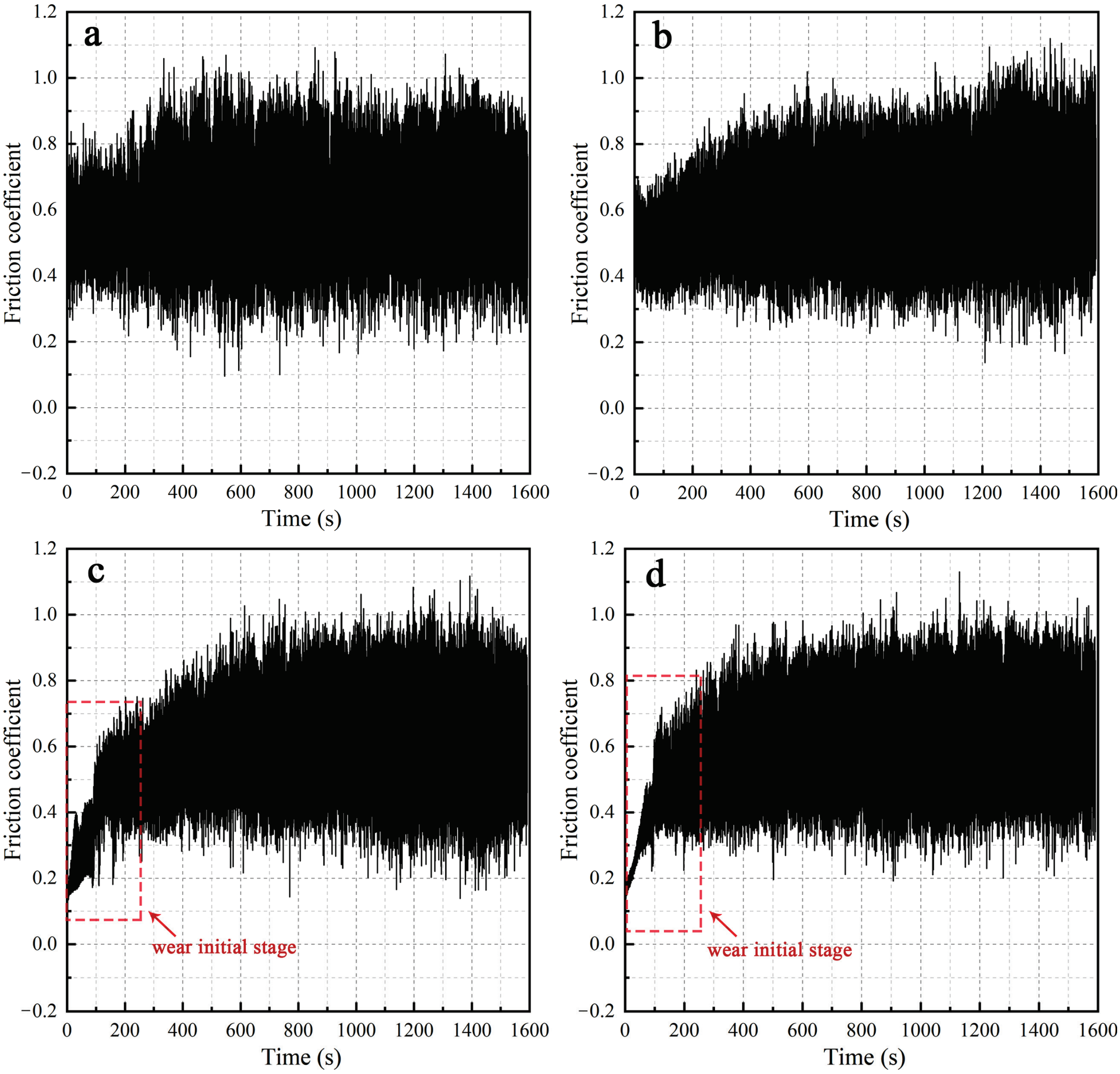

Figure 7. Variations of friction coefficients of Ti alloys with wear time. (**a**) specimen A, (**b**) specimen B, (**c**) specimen C, and (**d**) specimen D.

3.3. Corrosion Resistance

Figure 9 shows the potentiodynamic polarization curves of Ti alloys with different surface treatments in the SBF solution. The corrosion current density of specimen A was 9.17×10^{-8} A/cm^2. The corrosion current density of specimen C was decreased to 7.01×10^{-8} A/cm^2. The corrosion current density of specimen C was decreased by 24% compared to the specimen A. This was indicated that the corrosion resistance of Ti alloys was improved by anodic oxidation. However, the corrosion current density of specimen B was increased to 1.11×10^{-7} A/cm^2. The corrosion current density of specimen B was increased by 21% compared to the specimen A. The corrosion current density of specimen D was decreased to 7.63×10^{-7} A/cm^2. It was also found that corrosion current density of specimen D was increased to 8.8% compared to it of specimen C. Therefore, there was no significant difference in the corrosion current density between the specimens treated by anodic oxidation and those treated by anodic oxidation after sandblasting.

Figure 10 shows the EIS of Ti alloys with different surface treatments. It can be found that the phase angles of specimens C and D were close to −90 degrees in the high frequency region. However, the phase angles of specimens A and B were close to −90 degrees in the low frequency region (Figure 10a). This was indicated that the treatment of anodic oxidation on Ti alloys changed the corrosion process of Ti alloys. Moreover, the peak width of specimen A was wider than that of specimen B. It was indicated that the corrosion resistance of specimen A was better than that of specimen B. In addition, the values of impedance modulus of specimens C and D were larger than that of specimens A and B (Figure 10b). This was indicated that the treatment of anodic oxidation improved the corrosion resistance of Ti alloys. The corrosion resistance of specimen C was found to be better than that of specimen D. This was consistent with the results of the potentiodynamic polarization curves.

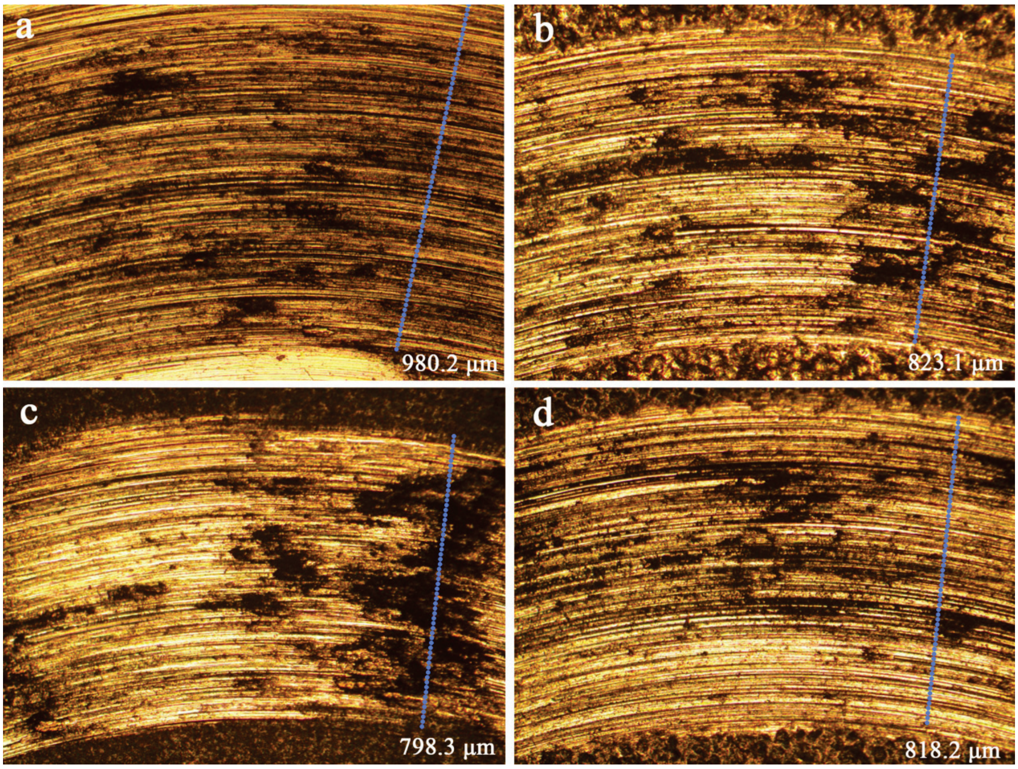

Figure 8. Optical images of wear morphologies of Ti alloys with different surface treatments. (**a**) specimen A, (**b**) specimen B, (**c**) specimen C, and (**d**) specimen D.

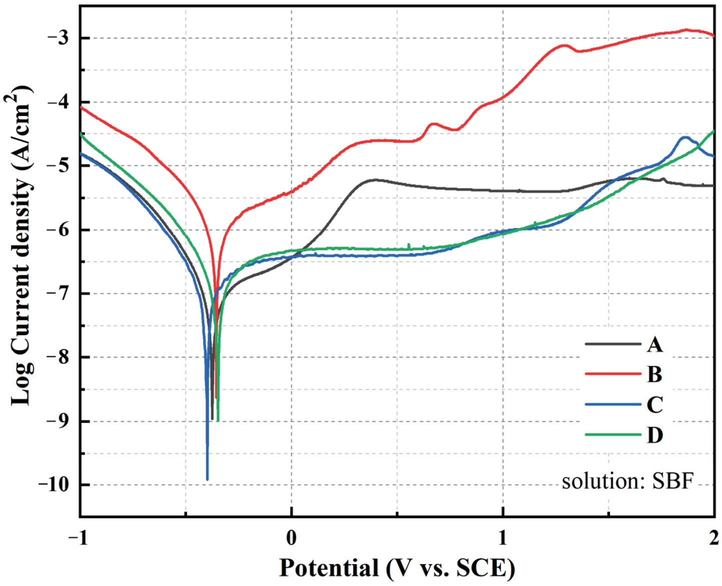

Figure 9. The potentiodynamic polarization curves of Ti alloys with different surface treatments.

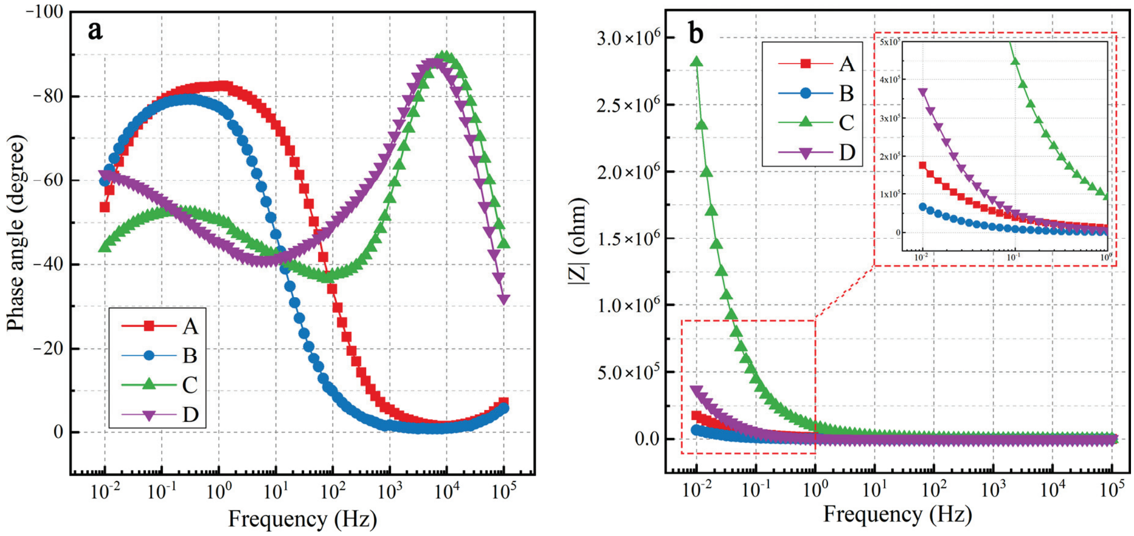

Figure 10. EIS of Ti alloys with different surface treatments. (**a**) the phase angle diagram of different specimens, (**b**) impedance modulus of different specimens.

3.4. Contact Angles

Figure 11 shows the contact angles of water on the surface of Ti alloys with different surface treatments. The contact angles of Ti alloys had a significant change. The contact angles of specimen A were 56.3 degrees. It was found that the contact angles of specimen C increased to 88.2 degrees. Moreover, the contact angles of specimen B were increased to 101.5 degrees. However, the contact angle value of specimen D decreased to 77.2 degrees compared to that of specimen B.

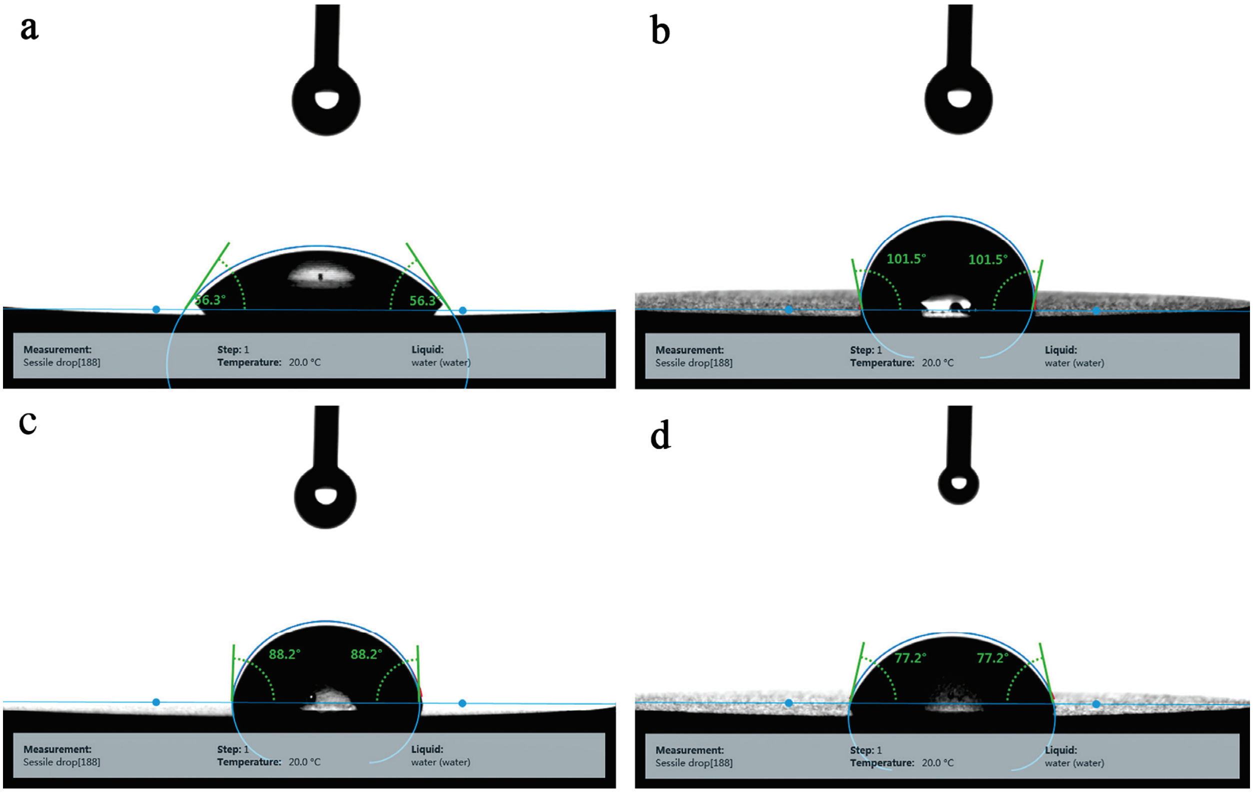

Figure 11. The contact angles of Ti alloys with different surface treatments. (**a**) specimen A, (**b**) specimen B, (**c**) specimen C, and (**d**) specimen D.

4. Discussion

The results of morphologies of Ti alloys (Figures 1 and 2) showed that oxidation films were formed on the Ti alloys. However, the peaks of titanium oxide were not found for specimens C and D (Figure 4). The diffraction peaks are shown in Figure 4, and specimens only showed peaks for α or β phases, with no other intermetallic phases. In other words, only nanoscale depth from the surface was affected by the anodic oxidation treatment; the phase compositions of substrate alloy and XRD detection results were insusceptible. In addition, the analyses of results (Figures 5–10) suggest that Ti alloys with different surface treatments had different mechanical properties, wear resistance, corrosion resistance, and contact angles.

Different surface roughness values were found on the Ti alloys with different surface treatments from Figure 5. It is generally accepted that the surface roughness of Ti alloys increased on sandblasting [24]. Moreover, it can be found that the surface roughness value of Ti alloys increased with anodic oxidation after sandblasting. Thus, anodic oxidation could improve the surface roughness values, which is consistent with literature reports [25,26]. The increase of roughness can be attributed to the growth of oxidation films. Dense oxidation films were formed on the Ti alloys at the beginning of anodization. The electrolyte diffusion rate of the position in depression of the rough-surface was slow, so the generated Joule heat was more difficult to diffuse. Therefore, the dissolution rate of the layer in the concave of rough surface was increased, resulting in a decrease in membrane resistance and an increase in current and current density. This resulted in a large amount of heat, which intensified the dissolution of the films in the concave of rough surface. The Ti alloys with sandblasting were rougher; therefore, the dissolution of layers in concave of rough surface increased significantly. Moreover, the dissolution of layers would also occur where the oxidation layer was uneven. Therefore, the surface roughness value of specimen D was higher.

The surface treatments were found to improve the Vickers hardness of the Ti alloys in this study. However, the increase in the Vickers hardness resulting from surface treatment was not very significant. It is generally accepted that a certain degree of plastic deformation occurs on the surface of metal due to sandblasting, causing the lattice distortion to become larger [27]. The surface of Ti alloys was strengthened to a certain extent. Therefore, the sandblasting improved the surface hardness of the Ti alloys. Moreover, it was generally also accepted that the oxidation films of Ti alloys have a higher hardness [28]. However, surface treatments of sandblasting and anodic oxidation in this study did not significantly improve the hardness of the Ti alloys. This may be because the strengthened layer or the oxidation films prepared were thin, and were easily destroyed in the Vickers hardness test. Therefore, the Vickers hardness measured was the composite hardness of the strengthened layer/oxidation films and the substrate, resulting in an inconspicuous increase in the Vickers hardness of Ti alloys.

The friction coefficients of Ti alloys with different surface treatments had a little change in the stable stage of wear. Moreover, obvious wear marks were found on the Ti alloys with different surface treatments. It was indicated that the different surface treatments had no effective protection on Ti alloys substrate in this work. For specimens A and B, Ti alloy and grinding ball were contacted directly in wear test. There was adhesion between metals during wearing, so the friction coefficient of specimens A and B was larger. It could be found the initial friction coefficients were about 0.2 for specimens C and D. The oxidation films were generated for specimens C and D during anodizing, which hindered to Ti alloy contact with grinding ball, thereby reducing adhesion between the specimens and grinding ball in wear. Therefore, the initial friction coefficients were smaller for specimens C and D. The oxidation films were broken as the extension of wear time. The formation of wear debris increased the friction coefficients. Therefore, the friction coefficients increased gradually with the extension of wear time. The friction coefficients of specimens C and D were approached to that of specimens A and B in the stable stage of wear, indicating that substrates of specimens C and D were contacted by a grinding ball in the stable stage of wear. In addition, narrower wear marks were found on the surface of Ti alloys with surface treatment. This indicates that the surface treatment could reduce the wear rate of the Ti alloys. It is generally also accepted that the wear resistance of materials is influenced by the hardness. The hardness of Ti alloys with surface treatments had a slight increase compared to that of Ti alloys without surface treatment. The resistance to deformation of specimens C and D was stronger during wear. Therefore, the surface treatment improved the wear resistance of Ti alloys to some extent.

The corrosion current density of specimen C was decreased by 24% compared to the specimen A, indicating improved corrosion resistance. This can be attributed to the anodic oxidation layer on the Ti, which prevents the SBF solution from contacting the Ti alloy substrates. The corrosion current density of specimen B was increased by 21% compared to the specimen A, suggesting decreased corrosion resistance. It is generally observed that sandblasting can improve the roughness value of specimens. Therefore, the corrosion area of Ti alloys increased after sandblasting, resulting in increased corrosion current density. The corrosion current density of specimen D was 7.63×10^{-8} A/cm^2, which was increased by 8.8% compared to the specimen C. This can be attributed to a further increase in the surface roughness of the Ti alloy, leading to an increase in the corrosion area of the specimens. Therefore, corrosion current density of specimen D was increased slightly. Moreover, it was reported that the corrosion resistance of the Ti alloys was influenced by the formation of a barrier layer and porous layer [9].

To further analyze the corrosion behavior of the Ti alloys with different surface treatments, the equivalent circuits of specimens were established. Figure 12 shows the equivalent circuits which are used for modelling the EIS results, and the extracted parameters according to the model are presented in Table 1.

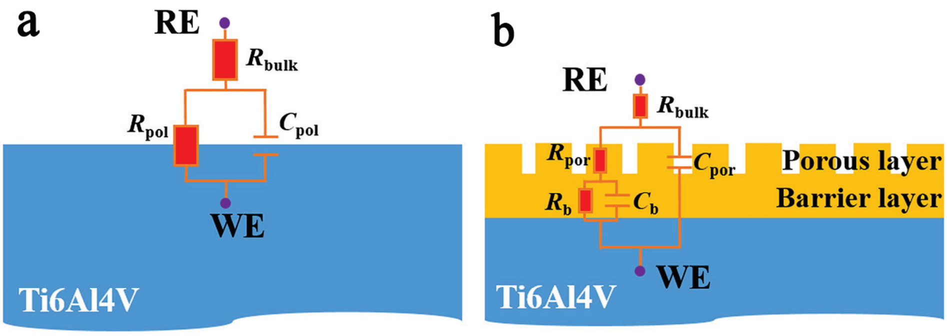

Figure 12. The equivalent circuits which are used for modelling the EIS results. (**a**) the equivalent circuit of specimens A and B; (**b**) the equivalent circuit of specimens C and D.

Table 1. Extracted parameters of different specimens according to the equivalent circuits.

Specimens	R_{bulk} ($\Omega \cdot cm^2$)	R_{pol} ($\Omega \cdot cm^2$)	C_d ($F \cdot cm^{-2}$)	R_{por} ($\Omega \cdot cm^2$)	C_{por} ($F \cdot cm^{-2}$)	R_b ($\Omega \cdot cm^2$)	C_b ($F \cdot cm^{-2}$)
A	119	7.4×10^5	3×10^{-5}	-	-	-	-
B	104	1.8×10^3	1.6×10^{-4}	-	-	-	-
C	110	-	-	4.5×10^3	1.6×10^{-7}	7.5×10^6	2.8×10^{-6}
D	105	-	-	2.4×10^3	1.6×10^{-6}	9.7×10^5	3.2×10^{-5}

The equivalent circuit used to simulate the electrode process of specimens A and B is shown in Figure 12a, where C_d is the double-layer capacitance of the substrate, R_{pol} is the polarization resistance of substrate, and R_{bulk} is the bulk resistance of the solution. The phase angle diagram shows that there are two peaks in specimens C and D, so there are two corrosion processes for specimens C and D. The equivalent circuit used to simulate the electrode process of specimens C and D is shown in Figure 12b, where C_{por} is the capacitance of the porous layer, R_{por} is the ohmic resistance of the porous layer, C_b is the capacitance of the barrier layer, R_b is the ohmic resistance of the barrier layer, and R_{bulk} is the bulk resistance of the solution. Table 1 shows that R_{por} and R_b of specimen C were 4.5×10^3 Ω·cm^2 and 7.5×10^6 Ω·cm^2, respectively. However, R_{por} and R_b of specimen D increased to 2.4×10^3 Ω·cm^2 and 9.7×10^5 Ω·cm^2, respectively. Thus, anodic oxidation films of specimen C could provide better corrosion resistance. It is generally accepted that the formation of a porous layer can decrease the corrosion resistance of the anodic oxidation film. The formation and dissolution of the film occur simultaneously during anodic oxidation. However, significant heat is generated in the cavities on the films, which may not be released during anodization, resulting in the dissolution of films in the cavities. Therefore, the formation of the porous layer was accelerated. The surface roughness of Ti alloys without sandblasting was found to be low. Therefore, a small number of cavities were generated during anodization. After sandblasting, Ti alloys had higher roughness on the surface. This allowed the Ti alloys to have more cavities during anodization, resulting in the promotion of the formation of porous layers and the dissolution of barrier layers. This resulted in a decrease in the R_{por} and R_b of specimen D.

Through the above analysis, the anodic oxidation diagram of specimens before and after sandblasting was given (Figure 13). The surface of the specimen was relatively smooth for the unsandblasted specimen, so the porous layer formed was relatively thin and had fewer voids in anodizing. However, after sandblasting, the surface roughness increased, promoting the formation of the porous layer and an increase in thickness of the porous layer during the anodization process.

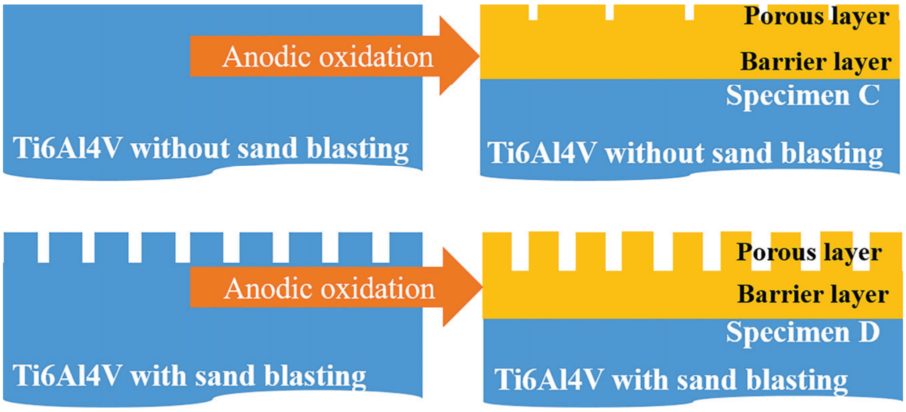

Figure 13. Anodic oxidation diagram of specimens before and after sandblasting.

Hydrophilicity is an important property for biomaterials [29,30]. The hydrophilic property is mainly related to the contact angles [31]. According to the relations between wetting tension and the wetting of a solid, the macroscopic result shows the high wettability (i.e., hydrophilicity) when the contact angles are between 0 and 90 degrees, and the low wettability (i.e., hydrophobicity) when the contact angles is between 90 and 180 degrees [32]. Gittens et al. [31] reported that the hydrophilic surface interacts closely with biological fluids, allowing normal protein adsorption to the surface and subsequent interactions with cell receptors. However, the hydrophobic surfaces are prone to hydrocarbon contamination, leading to entrapment of air bubbles that can interfere with protein adsorption and cell receptor adhesion/activation. In this study, the contact angle of the Ti alloy without treatments was 56.3 degrees, which showed a good hydrophilic property. After sandblasting, the contact angles of specimen B increased to 101.5 degrees showing the hydrophobicity which was not conducive to the adsorption of osteoblast cells. The contact angles of the specimens C and D, which were treated by anodic oxidation, were found to be 88.2 degrees and 77.2 degrees, respectively, revealing a similar hydrophilic level. In actual production and processing, the surface treatment of Ti-alloy implants is the sandblasting rather than stopping at the finish turning. Therefore, only the surface treatment of sandblasting and surface anodic oxidation could be applied to the implant prosthesis products. In conclusion, the anodic oxidation provided a hydrophilic property for the surface of Ti alloys, which could show a better osseointegration characteristic than that of sandblasting.

5. Conclusions

The influence of the different surface treatments on the microstructure and surface properties of the Ti alloys was investigated. The following conclusions could be drawn based on the present results.

The different surface treatments improved the Vickers hardness of Ti alloys slightly. The Vickers hardness of Ti alloys treated by anodic oxidation after sandblasting was increased from 380.8 HV to 408.5 HV, which was increased by 7.3%. In addition, the surface treatments by anodic oxidtion decreased wear scar widths by 18.6% compared to the untreated specimen, which improved the wear resistance of the Ti alloys.

The treatment of anodic oxidation improves the corrosion resistance of Ti alloys, which was found to be decreased by 24% in corrosion current density compared to the untreated specimen. Sandblasting increased the roughness and promoted the formation of the porous layer during the anodization process, resulting in a decrease in corrosion resistance of Ti alloys, which was increased by 8.8% in corrosion current density compared to the specimen with anodic oxidation.

The contact angle of Ti alloys after anodizing was 88.2 degrees. The contact angle of Ti alloys treated by anodic oxidation after sandblasting was 77.2 degrees. The anodic oxidation provided a hydrophilic property for the surface of Ti alloys, which could show a better osseointegration characteristic than that of sandblasting.

Author Contributions: Conceptualization and funding acquisition, S.L.; writing and formal analysis, H.D.; project administration, K.X.; resources, C.Z.; methodology and investigation, X.Z., H.Z.; review and editing, S.L., H.D.; data curation and validation, C.X.; supervision, C.S. All authors have read and agreed to the published version of the manuscript.

Funding: This work was supported by the National Key Research and Development Program of China (Grant No. 2020YFC1107502), the China Postdoctoral Science Foundation (Grant No. 2021M700490), and the Beijing Postdoctoral Research Foundation (Grant No. 2021-ZZ-075).

Institutional Review Board Statement: Not applicable.

Informed Consent Statement: Not applicable.

Data Availability Statement: The raw/processed data required to reproduce these findings cannot be shared at this time as the data also form part of an ongoing study.

Acknowledgments: Special thanks go to Pengfei Ji and Tianshuo Song for experimental assistance.

Conflicts of Interest: The authors declare no conflict of interest.

References

1. Liu, S.G.; Xia, C.Q.; Feng, Z.H.; Zhang, X.; Chen, B.H.; Xie, C.L.; Zhou, Y.K.; Zhang, X.Y.; Ma, M.Z.; Liu, R.P. Influence of phase composition and microstructure on mechanical properties of hot-rolled Ti-χZr-4Al-0.005B alloys. *J. Alloys Compd.* **2018**, *751*, 247–256. [CrossRef]
2. Yang, J.L.; Wang, G.F.; Zhang, W.C.; Chen, W.Z.; Jiao, X.Y.; Zhang, K.F. Microstructure evolution and mechanical properties of P/M Ti-22Al-25Nb alloy during hot extrusion. *Mater. Sci. Eng. A.* **2017**, *699*, 210–216. [CrossRef]
3. Li, X.X.; Yang, C.; Lu, H.Z.; Luo, X.; Lvasisshin, O.M. Correlation between atomic diffusivity and densification mechanism during spark plasma sintering of titanium alloy powders. *J. Alloys Compd.* **2019**, *787*, 112–122. [CrossRef]
4. Qiu, K.J.; Liu, Y.; Zhou, F.Y.; Wang, B.L.; Li, L.; Zheng, Y.F.; Liu, Y.H. Microstructure, mechanical properties, castability and in vitro biocompatibility of Ti-Bi alloys developed for dental applications. *Acta Biomater.* **2015**, *15*, 254–265. [CrossRef]
5. Ellis, E.; Tan, Y.H. Assessment of internal orbital reconstructions for pure blowout fractures: Cranial bone grafts versus titanium mesh. *J. Oral Maxillofac. Surg.* **2003**, *61*, 442–453. [CrossRef] [PubMed]
6. Liu, X.Y.; Chu, P.K.; Ding, C.X. Surface modification of titanium, titanium alloys, and related materials for biomedical applications. *Mater. Sci. Eng. R* **2004**, *47*, 49–121. [CrossRef]
7. Dikova, T.; Milkov, M. Application of Ti and Ti alloys in dental implantology. *Int. J. Tuberc. Lung Dis.* **2013**, *17*, 48–50.
8. Marbacher, S.; Andres, R.H.; Fathi, A.-R.; Fandino, J. Primary reconstruction of open depressed skull fractures with titanium mesh. *J. Craniofacial Surg.* **2008**, *19*, 490–495. [CrossRef]

9. Assis, S.; Wolynec, S.; Costa, I. Corrosion characterization of titanium alloys by electrochemical techniques. *Electrochim. Acta* **2006**, *51*, 1815–1819. [CrossRef]
10. González, J.E.G.; Mirza-Rosca, J.C. Study of the corrosion behavior of titanium of its alloys for biomedical and dental implant applications. *J. Electroanal. Chem.* **1999**, *471*, 109–115. [CrossRef]
11. Sathish, S.; Geetha, M.; Pandey, N.D.; Richard, C.; Asokamani, R. Studies on the corrosion and wear behavior of the laser nitrided biomedical titanium and its alloys. *Mater. Sci. Eng. C* **2010**, *30*, 376–382. [CrossRef]
12. Vadiraj, A.; Kamaraj, M.; Gnanamoorthy, R. Fretting wear studies on uncoated, plasma nitrided and laser nitrided biomedical titanium alloys. *Mater. Sci. Eng. A* **2007**, *445*, 446–453. [CrossRef]
13. Engh Jr, C.A.; Moore, K.D.; Vinh, T.N.; Engh, G.A. Titanium prosthetic wear debris in remote bone marrow. A report of two cases. *J. Bone Jt. Surg.* **1997**, *79*, 1721–1725. [CrossRef] [PubMed]
14. Buly, R.L.; Huo, M.H.; Salvati, E.; Brien, W.; Bansal, M. Titanium wear debris in failed cemented total hip arthroplasty. An analysis of 71 cases. *J. Arthroplast.* **1992**, *7*, 315–323. [CrossRef]
15. Buchanan, R.A.; Rigney Jr, E.D.; Williams, J.M. Ion implantation of surgical Ti-6Al-4V for improved resistance to wear-accelerated corrosion. *J. Biomed. Mater. Res. Part A* **1987**, *21*, 55–366. [CrossRef] [PubMed]
16. Zhang, L.C.; Chen, L.Y.; Wang, L.Q. Surface Modification of Titanium and Titanium Alloys: Technologies, Developments, and Future Interests. *Adv. Eng. Mater.* **2019**, *22*, 1901258. [CrossRef]
17. Deng, H.Y.; Chen, D.X.; Wang, Y.N.; Zhou, Y.W.; Gao, P. Effects of silicon on microstructure and corrosion resistance of diamond-like-carbon film prepared on 2024 aluminum alloy by plasma-enhanced chemical vapor deposition. *Diam. Relat. Mater.* **2020**, *110*, 108144. [CrossRef]
18. Hiraga, H.; Inoue, T.; Kojima, Y.; Kamado, S.; Watanabe, S. Surface modification by dispersion of hard particles on magnesium alloy with laser. *Mater. Sci. Forum* **2000**, *350–351*, 253–260. [CrossRef]
19. Qi, J.W.; Yang, Y.M.; Zhou, M.M.; Chen, Z.B.; Chen, K. Effect of transition layer on the performance of hydroxyapatite/titanium nitride coating developed on Ti-6Al-4V alloy by magnetron sputtering. *Ceram. Int.* **2019**, *45*, 4863–4869. [CrossRef]
20. Li, D.H.; Liu, B.L.; Han, Y.; Xu, K.W. Effects of a Modified sandblasting surface treatment on topographic and chemical properties of titanium surface. *Implant. Dent.* **2001**, *10*, 59–64. [CrossRef]
21. Tang, E.J.; Liu, Z.; Zhao, Y.Q. A Study of electroless Ni-P plating on titanium alloy. *Electroplat. Pollut. Control* **2003**, *23*, 21–22.
22. Song, H.J.; Kim, M.K.; Jung, G.C.; Vang, M.S.; Park, Y.J. The effects of spark anodizing treatment of pure titanium metals and titanium alloys on corrosion characteristics. *Surf. Coat. Technol.* **2007**, *201*, 8738–8745. [CrossRef]
23. Tian, Y.S.; Chen, C.Z.; Li, S.T.; Huo, Q.H. Research progress on laser surface modification of titanium alloys. *Appl. Surf. Sci.* **2005**, *242*, 177–184. [CrossRef]
24. Khanlou, H.M.; Ang, B.C.; Barzani, M.M.; Silakhori, M.; Talebian, S. Prediction and characterization of surface roughness using sandblasting and acid etching process on new non-toxic titanium biomaterial: Adaptive-network-based fuzzy inference System. *Neural Comput. Appl.* **2015**, *26*, 1751–1761. [CrossRef]
25. Wu, L.; Liu, J.H.; Wu, G.L.; Li, S.M.; Yu, M. Growth behaviour of anodic oxide film on titanium alloy. *Surf. Eng.* **2015**, *33*, 841–848. [CrossRef]
26. Li, B.; Li, J.; Liang, C.; Li, H.; Liu, S.; Wang, H. Surface Roughness and hydrophilicity of titanium after anodic oxidation. *Rare Met. Mater. Eng.* **2016**, *45*, 858–862. [CrossRef]
27. Arifvianto, B.; Suyitno, S.; Mahardika, M. Effect of sandblasting and surface mechanical attrition treatment on surface roughness, wettability, and microhardness distribution of aisi 316l. *Key Eng. Mater.* **2011**, *462–463*, 738–743. [CrossRef]
28. Pang, M.; Eakins, D.E.; Norton, M.G.; Bahr, D.F. Structural and mechanical characteristics of anodic oxide films on titanium. *Corrosion* **2001**, *57*, 523–531. [CrossRef]
29. Schwarz, F.; Wieland, M.; Schwartz, Z.; Zhao, G.; Rupp, F.; Geis-Gerstorfer, J.; Schedle, A.; Broggini, N.; Bornstein, M.M.; Buser, D.; et al. Potential of chemically modifified hydrophilic surface characteristics to support tissue integration of titanium dental implants. *Biomed. Mater. Res. B* **2009**, *88*, 544–557. [CrossRef]
30. Rupp, F.; Scheideler, L.; Eichler, M.; Geis-Gerstorfer, J. Wetting behavior of dental implants. *Int. J. Oral Maxillofac. Implant.* **2011**, *26*, 1256–1266.
31. Gittens, R.A.; Scheideler, L.; Rupp, F.; Hyzy, S.L.; Geis-Gerstorfer, J.; Schwartz, Z.; Boyan, B.D. A review on the wettability of dental implant surfaces II: Biological and clinical aspects. *Acta Biomater.* **2014**, *10*, 2907–2918. [CrossRef] [PubMed]
32. Rupp, F.; Gittens, R.A.; Scheideler, L.; Marmur, A.; Boyan, B.D.; Schwartz, Z.; Geis-Gerstorfer, J. A review on the wettability of dental implant surfaces I: Theoretical and experimental aspects. *Acta Biomater.* **2014**, *10*, 2894–2906. [CrossRef] [PubMed]

coatings

MDPI

Article

Asynchronous Synergistic Damage Effect of Atomic Oxygen and Space Micro Debris on Kapton Film

Peiyi Tong [1], **Qiang Wei** [2,3,*], **Ning Hu** [2,3] **and Xueguang Chen** [1,*]

[1] School of Materials Science and Engineering, Hebei University of Technology, Tianjin 300401, China; tongpeiyi@126.com
[2] School of Mechanical Engineering, Hebei University of Technology, Tianjin 300401, China; ninghu@hebut.edu.cn
[3] State Key Laboratory of Reliability and Intelligence Electrical Equipment, Hebei University of Technology, Tianjin 300130, China
* Correspondence: weiqiang@hebut.edu.cn (Q.W.); cxg@hebut.edu.cn (X.C.)

Abstract: In the low earth orbit environment, many environmental factors lead to the degradation of material properties. The synergistic effect of long-term atomic oxygen (AO) irradiation and instantaneous impact of micro debris (MD) on long-term and transient space environmental factors has attracted more and more attention. In this paper, the performance evolution of Kapton films under the conditions of MD, AO single factor load spectrum and MD + AO, AO + MD asynchronous synergistic load spectrum were studied by laser driven flyer and microwave atomic oxygen technology. The macro morphology, optical properties and quality changes of Kapton films before and after each load spectrum were compared, and the mechanism of micro morphology and structure changes was explored. The results show that compared with MD + AO loading spectrum, the surface holes of Kapton films are larger under AO + MD load spectrum condition, the residual aluminum particles formed by reverse sputtering of Al particles during impact are less, the average transmittance of the film decreases slightly, and the weight loss of Kapton film is slightly more under the same atomic oxygen exposure time. Under the condition of MD + AO load spectrum, plastic tearing cracks, craters and holes are formed on the surface of Kapton film; the edge of the hole formed under the condition of AO + MD load spectrum is straight, without obvious depression and tear characteristics. Under the condition of MD + AO load spectrum, due to the adhesion of Al after the impact of micro debris, the subsequent atomic oxygen erosion of the film is reduced, so the C-C bond is not seriously damaged, and a considerable part of the residual aluminum flyer is oxidized to alumina by atomic oxygen; The AO + MD loading spectrum test makes the film first eroded by atomic oxygen, resulting in the reduction in C–O bond and C–C bond. The fracture of C–N bond is caused by the hypervelocity impact of micro debris. Hypervelocity impact leads to the thermal decomposition of the material, destroys the C–N bond in the imide ring and generates an N–H bond. This study will provide a method reference and a reference for the multi-factor ground collaborative simulation of space environment of spacecraft materials.

Keywords: atomic oxygen; micro debris; asynchronous synergistic; Kapton film

1. Introduction

During the operation of a spacecraft in orbit, it will be affected by many environmental factors, such as micro debris (MD), atomic oxygen (AO), ultraviolet, charged particles, high vacuum and so on [1–3]. The data of material performance degradation in single factor ground simulation test is often inconsistent with the data of space in orbit test, so the synergistic effect caused by various environmental factors has gradually attracted attention [4,5]. According to the different duration of environmental factors, on the one hand, it can be manifested as the long-term effect of continuous degradation of spacecraft surface materials until failure and termination of service, including atomic oxygen erosion, ultraviolet irradiation, charged particle irradiation, etc.; On the other hand, it can be expressed as the instantaneous effect of sudden damage to spacecraft surface materials leading to failure, including micro debris impact, single particle effect and so on [6–8].

In recent years, the long-term synergistic damage mechanism of aerospace materials, such as the synergistic effect of atomic oxygen and vacuum ultraviolet [9–11], and the synergistic effect of atomic oxygen and electron irradiation [12], has been widely studied. In view of the dynamic changes of long-term and instantaneous synergistic effects in time and space, there are complex sequential and coupling relationships [13], so far, there are few relevant studies. The physical impact and chemical erosion of long-term atomic oxygen will degrade the mechanical properties. The weight loss of polymer materials will also reduce the thermal, optical and mechanical properties [14]. The impact of instantaneous effect small debris will lead to holes and cracks in polymer materials, reduce the performance of spacecraft surface materials and reduce the service time of spacecraft surface polymers [15]. The long-term irradiation of atomic oxygen and the transient impact of small debris are typical synergistic effects of long-term and instantaneous space environmental factors. Previous studies have shown that the accelerated corrosion of polyimide materials is mainly manifested in the generation of new radial holes induced by AO. Due to the residual stress on the material surface caused by high-speed impact, the local free volume of the polymer increases, which promotes the diffusion of oxygen atoms into the polymer, thus accelerating the local degradation process [16]. The synergistic effect of atomic oxygen and micro debris will greatly aggravate the erosion speed of space materials. It is pointed out that the synergistic effect with space debris must be given when considering the erosion effect of atomic oxygen [17,18]. However, these studies focus on the damage behavior of polymer materials first impacted by debris and then eroded by atomic oxygen, and the damage mechanism of materials in the case of different action sequences of AO and MD has not been studied clearly. For the damage of materials caused by the synergistic effect of the two effects and the different damage on materials under the action of a single factor, this also needs to be further studied.

Polymers are often used as spacecraft surface materials for service [19]. For example, polyimide is widely used in the fire compartment of spacecraft and the flexible substrate of a solar panel, and silicone rubber is used as the condenser lens or binder of a spacecraft solar cell array [20,21]. Therefore, it is necessary to conduct ground simulation evaluation for polymers applied on the spacecraft surface. In this paper, the synergistic effect of atomic oxygen and micro debris is studied on Kapton film, which has excellent mechanical properties, insulation properties and thermal stability. The damage mechanism of Kapton film caused by the asynchronous synergistic effect of atomic oxygen and micro debris with different load spectra was explored. At the same time, the damage behavior of Kapton film under the separate action of two environmental factors was also compared. This study will provide a method reference and a reference for multi factor ground collaborative simulation of space environment of spacecraft materials.

2. Experiment

2.1. Materials

The material used in this work is diphenylamine oxide pyromellitic dianhydride (ODA-PMDA) polyimide (produced by DuPont, Wilmington, DE, USA), and the molecular formula of ODA-PMDA polyimide is shown in Figure 1. The test sample was 25 μm thick and cut to 20 mm × 20 mm rectangle. Before use, the sample was washed with absolute ethanol through an ultrasonic cleaner for ten minutes, and then dried naturally.

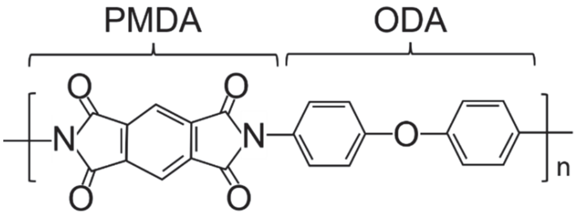

Figure 1. Molecular formula of ODA-PMDA polyimide.

2.2. Ground Simulation Method of Atomic Oxygen and Micro Debris

The laser driven flyer (LDF) method was used to carry out the hypervelocity impact test of space micro debris. The equipment diagram is shown in Figure 2a. The aluminum film with thickness of 20 μm (1060 Al with purity of 99.5%, Shanghai Yuanbao metal materials Co., Ltd., Shanghai, China) was cut into 40 mm in diameter. Using 9307 ultraviolet light curing adhesive as binder, Al film was pasted on quartz glass (Jiangsu Chengtai quartz Co., Ltd., Lianyungang, China) with thickness of 1.5 mm and diameter of 40 mm as flyer target. Quartz glass and Al film can be pasted and fixed by irradiation with 380 nm ultraviolet for 3 min. Nimma 900 (Nd: YAG, Beijing LeiBao company, Beijing, China) was used as the laser source. The single pulse energy of the laser was set to 826 mJ, the frequency was 1 Hz and the pulse width was 7 ns. The peak power of the laser was 1.18×10^8 w. The laser beam was focused into a spot of about 1 mm by the focusing lens and irradiated on the flyer target placed in the vacuum chamber with vacuum degree of 1×10^{-3} Pa. Laser ablation of flyer target resulted in rapid expansion of plasma with extremely high pressure and temperature, resulting in tensile stress along the vertical direction of aluminum film. When the tensile stress exceeds the tensile strength of the aluminum film, the micro aluminum flyer was formed, and with the plasma expansion, the flyer accelerated to a speed of about 2 km/s in a short distance and stroked the Kapton film material. In this paper, the average velocity of flyer was measured by piezoelectric method [22].

The atomic oxygen exposure test of Kapton film was carried out by using the ground simulation device of microwave plasma source. The equipment diagram is shown in Figure 2b. During the operation of the equipment, oxygen entered the atomic oxygen cavity. At the same time, the microwave generated by the microwave source entered the atomic oxygen cavity after being selected by the circulator. The gas was ionized by microwave discharge to form plasma. Under the action of magnetic field, the plasma accelerated to impact the metal target with negative bias, which made the plasma neutralize and reduce to obtain the neutral atomic oxygen beam [23]. The metal molybdenum sheet (Baoji Jiajun metal material Co., Ltd., Beijing, China) was used as the neutralization target with a diameter of 12 cm. The negative bias voltage on the target was provided by a 36 V direct current regulated power supply. The average energy of atomic oxygen was about 5 eV. The equivalent flux at the sample location was 8.2×10^{15} O-atoms $\text{cm}^{-2} \cdot \text{s}^{-1}$.

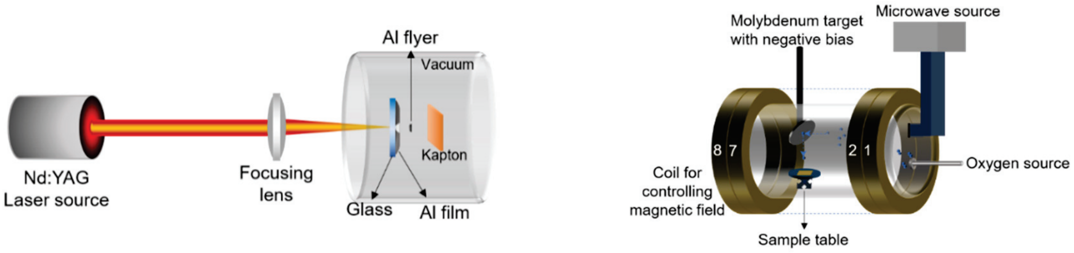

(**a**) (**b**)

Figure 2. Schematic diagram of ground environment simulation test: (**a**) Laser driven flyer; (**b**) Atomic oxygen erosion.

2.3. Development of Load Spectra

In order to facilitate the description of the types and sequence of atomic oxygen and micro debris in the test scheme, the load spectrum method was used in this paper. Four groups of different load spectrum tests of atomic oxygen and micro debris were carried out. The test method is shown in Figure 3. Single factor load spectrum: (a) MD load spectrum: micro debris hypervelocity impact test was carried out on Kapton film; (b) AO load spectrum: atomic oxygen corrosion test was carried out on Kapton film, and the samples were exposed to atomic oxygen for 5, 10, 15, 20 and 25 h, respectively. Asynchronous cooperative load spectrum; (c) MD + AO load spectrum: five samples were subjected to micro debris hypervelocity impact test, and then atomic oxygen exposure test for 5, 10, 15, 20 and 25 h, respectively; (d) AO + MD load spectrum: Kapton films were exposed to atomic oxygen for 5, 10, 15, 20 and 25 h, respectively, and then each sample was subjected to micro debris hypervelocity impact test.

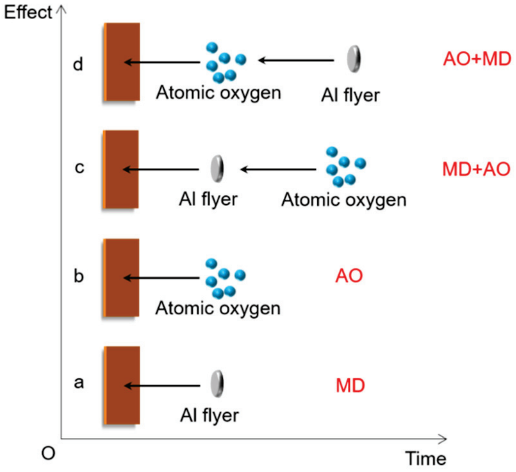

Figure 3. Schematic diagram of four load spectrum tests.

2.4. Material Performance Test and Characterization

The mass loss of Kapton film was measured by analytical balance (x-56, accuracy 0.1 mg, Mettler Toledo, Zurich, Switzerland). The atomic oxygen reaction coefficient of the corresponding sample was calculated according to the following formula [24]:

$$\mathrm{Re} = \frac{\Delta \mathrm{m}}{\varphi} \cdot \frac{1}{\rho \cdot \mathrm{A}} \tag{1}$$

where Δm is the mass change of the sample before and after atomic oxygen exposure, g; φ is the atomic oxygen flux, atoms/cm^2; ρ is the sample density, 1.4 g/cm^2; A is the exposed area of the sample, 4 cm^2.

The optical properties of Kapton films were characterized by the average transmittance in the range of Φ20 mm in diameter. The optical property was characterized by ultraviolet, visible near infrared spectrophotometer (Lambda 1050, PerkinElmer, Waltham, MA, USA). The test wavelength ranged from 250 to 800 nm and the resolution was 0.5 nm. The surface morphology of Kapton film after erosion and impact was observed by high resolution field emission scanning electron microscope (SEM, JSM-7610F, JEOL, Tokyo, Japan) equipped with an energy dispersive spectrometer (EDS). It had an acceleration voltage of 10 kV. The sample surface was plated with gold (palladium alloy, particle size about 20 nm) before observation. Fourier transform infrared spectrometer (vertex80v, Bruker, Karlsruhe, Germany) was used for infrared spectrum test, and the spectral range was 2000–400 cm^{-1}. X-ray photoelectron spectrometer (Escalab 250xi, Thermo Fisher, Waltham, MA, USA) was used to analyze the chemical bond states. The excitation source is Al Kα radial. All elements were corrected with C1s (about 284.8 eV) as a reference.

3. Results and Discussion

3.1. Optical Performance Analysis

The macro comparison of the original Kapton film, after MD + AO load spectrum and AO + MD load spectrum test Kapton film is shown in Figure 4. The atomic oxygen erosion time of the sample in Figure 4b,d,e was 25 h. It can be seen from the Figure 4a, the surface of the original Kapton film had luster. The film after atomic oxygen single factor loading spectrum test is shown in Figure 4b, and the surface lost gloss. In Figure 4c, after MD single factor load spectrum, there were many holes and cracks on the film surface, as well as Al particles. The film still had luster outside the impact area. Compared with MD + AO load spectrum, the surface holes of Kapton film under AO + MD load spectrum were larger and the residual aluminum particles were less.

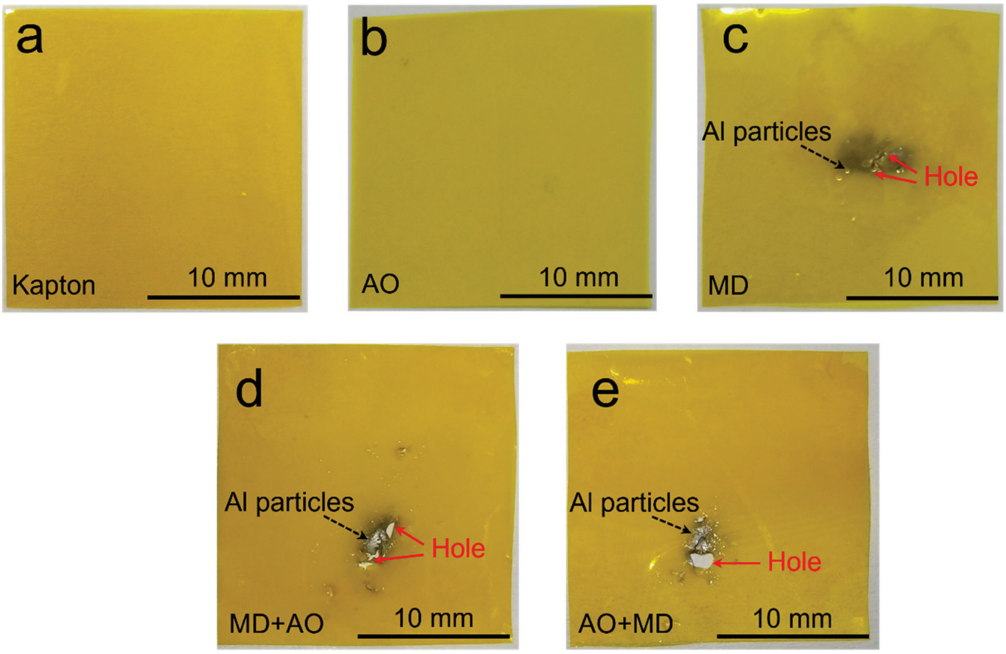

Figure 4. Macro images of Kapton film: (**a**, ×2) original film; (**b**, ×2) film after AO load spectrum test; (**c**, ×2) film after MD load spectrum; (**d**, ×2) film after MD + AO load spectrum test; (**e**, ×2) film after AO + MD load spectrum test.

The optical transmittance of Kapton film and the film after each load spectrum test is shown in Figure 5. In the load spectrum involving atomic oxygen the Figure 5, the exposure time of samples in atomic oxygen was 25 h. It can be seen from the figure that the transmittance trend of the film under the original and various load spectrum test conditions was the same as that in the literature [25–27]. In the ultraviolet region below 400 nm, the optical transmittance was about 5%. In the wavelength range of 470–800 nm, the optical transmittance of the film increased with the increase in wavelength. The transmittance increased rapidly in the wavelength range of 500–550 nm. In the 550–650 nm band, the increase in transmittance slowed down. The transmittance of 650–750 nm band increased obviously, and tends to be flat again when the wavelength was close to 800 nm.

The original Kapton film had the highest transmittance as a whole. Under the condition of MD single factor loading spectrum, the transmittance of Kapton film decreased by about 2% in the wavelength range of 600–800 nm. This can be attributed to the decrease in transmittance caused by the residual Al particle pollution on the surface of Kapton film after impact. After MD + AO loading spectrum test, the transmittance of the film was the lowest, which was about 10% lower than that of the original film in the wavelength range of 600–800 nm. The reason being, in addition to the Al particle pollution effect, the entire

Kapton film surface was eroded by atomic oxygen, resulting in a significant decrease in film transmittance.

After AO single factor load spectrum test and AO + MD load spectrum test, the transmittance of the film was almost the same, which was about 8% lower than that of the original film. This can be attributed to the larger holes on the surface of Kapton film and less residual aluminum particles under the condition of AO + MD load spectrum, which increased the transmittance of the film to a certain extent. This is also consistent with the observation results of macro photo morphology in Figure 4.

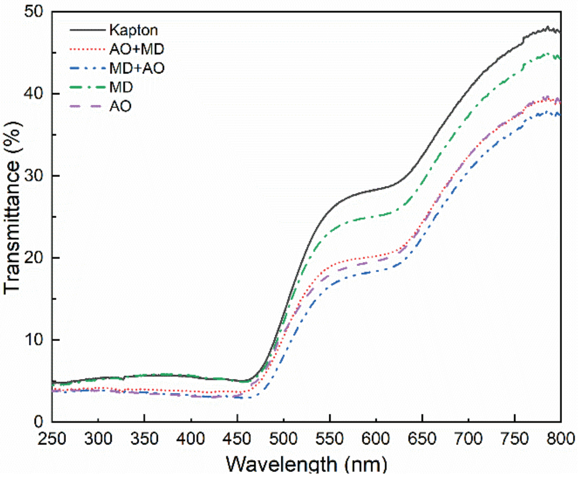

Figure 5. Optical transmittance of Kapton film before and after different load spectrum tests.

3.2. Quality Change of Kapton Film

The weight loss curve of Kapton film with atomic oxygen etching time after different load spectrum tests is shown in Figure 6. It can be seen from Figure 6 that in the three load spectrum conditions, the weight loss of Kapton film increased with the extension of atomic oxygen exposure time. The three weight loss curves shown in the figure are approximately parallel and linear, and the fitting slope is about -0.197, which shows that the weight loss rate of Kapton film was almost the same under three different load spectrum test conditions. The mass loss law of Kapton film in AO single factor load spectrum is consistent with that in the literature [28,29].

It can be seen from the figure that under the same atomic oxygen exposure time, the test conditions of weight loss of Kapton material from large to small are AO single factor, AO + MD load spectrum and MD + AO load spectrum test. The average atomic oxygen reaction coefficient of Kapton materials can be calculated according to Formula (1) as 2.12×10^{-24}, 1.70×10^{-24} and 0.99×10^{-24} cm^3/atom, respectively. The atomic oxygen reaction coefficient of Kapton film under AO single factor condition is close to 3.0×10^{-24} cm^3/atom reported in the literature [30], while the atomic oxygen reaction coefficient decreased to a certain extent under the conditions of AO + MD load spectrum and MD + AO load spectrum.

Under the three loading spectrum conditions, the difference in atomic oxygen erosion weight loss of Kapton films was mainly due to the impact of small Al flyers and the action sequence. The process mechanism of Al flyer impacting Kapton film at high speed is shown in Figure 7. When the Al flyer strikes the Kapton film, the integrity of the film is destroyed and shock waves S_1 and S_2 are generated. They propagate in the flyer and film, respectively, and sparse waves R_1 and R_2 propagate inward from the side. Under strong compression, the strength of the flyer target decreases, and then it breaks under the action of sparse wave, and some fragments splash back. When the incident shock wave reaches the free surface of Kapton film, a sparse wave R_3 is generated. When the tensile stress amplitude exceeds the dynamic fracture strength of the material, the region where the film is impacted breaks [31]. It can be seen that in addition to the cracks and holes formed by the impact of

Al flyer through Kapton film, a certain amount of Al contaminated particles will remain on the surface of Kapton film due to the reverse sputtering and redeposition of Al particles formed during the impact process. This is the reason for the difference of atomic oxygen erosion weight loss of Kapton film under three load spectrum test conditions. Without the influence of residual Al particles, the weight loss of Kapton film was the most obvious under the condition of AO single factor load spectrum. Compared with the MD + AO load spectrum test condition, the weight loss of Kapton film under AO+ MD load spectrum conditions was slightly more, which may be attributed to the reduction in material erosion and aging strength of Kapton film after atomic oxygen erosion. Therefore, the reverse sputtering and redeposition of Al particles formed during impact are relatively small.

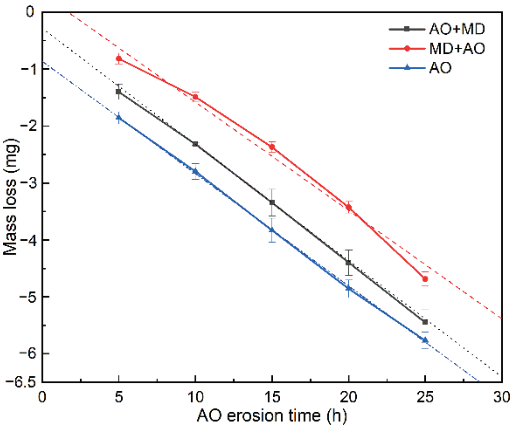

Figure 6. Weight loss curve of Kapton film before and after different load spectrum tests.

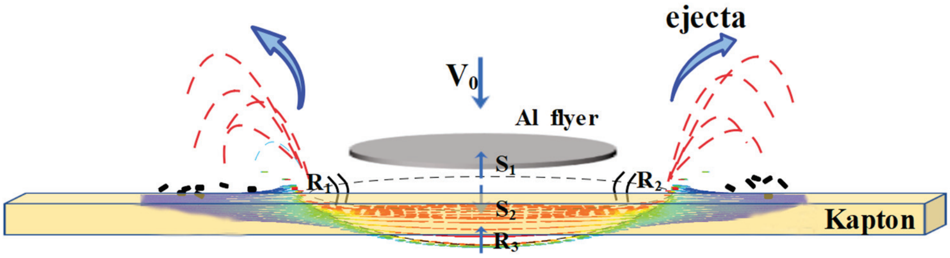

Figure 7. Schematic diagram of debris cloud formation process.

3.3. Microstructure Characterization

Figure 8a shows the SEM observation of the surface microstructure of Kapton film. In the load spectrum involving atomic oxygen in Figure 8, the exposure time of samples in atomic oxygen was 25 h. It can be seen that the original Kapton surface was smooth and flat. The surface morphology of Kapton after AO single factor load spectrum test is shown in Figure 8b. Due to the erosion of atomic oxygen, the film surface presented a classic rough carpet shape with high roughness, which is consistent with the literature report [28,32,33]. The surface morphology of Kapton after MD single factor load spectrum test is shown in Figure 8c. After aluminum flyer impacts Kapton film, pits, even cracks and holes appear on the surface. Further observation shows that there were granular substances in the pits, which are mainly aluminum by EDS energy spectrum analysis. This indicated that the integrity of Al flyer was destroyed and a debris cloud was formed during the impact. The formation of a debris cloud is an obvious feature of a hypervelocity collision [34]. When the splashed secondary fragments fall back to the film surface, the momentum was small, and then impact the film surface again to form pits and deposit.

After MD + AO load spectrum test, the surface microstructure of Kapton film is shown in Figure 8d–f. Similar to the MD single factor load spectrum test results, pits, holes and cracks on the film surface were clearly shown in Figure 8d. Figure 8e,f show the local enlargement of the crack area in Figure 8d. The crack showed a tearing state and belongs to the characteristics of plastic deformation. After atomic oxygen erosion, the surface near the crack was rough.

The surface microstructure of Kapton film after AO + MD load spectrum test is shown in Figure 8g–i. In Figure 8g, it can be observed that the central area was an impact hole with a diameter of 1.4 mm. The hole size was significantly larger than the hole size of 0.69 mm in Figure 8d, and the hole edge was straight without obvious depression and tear characteristics. Kapton film was first eroded by atomic oxygen, and a rough carpet shape was formed on the material surface, which became the crack source of subsequent flyer impacts. At the same time, the atomic oxygen corrosion aging of the surface material reduced the fracture strength, and the flyer showed brittle fracture when impacted at high speed, forming holes with a larger diameter. It is worth noting that in Figure 8h,i, the thin film away from the crack area was eroded by atomic oxygen to form a carpet shape, and the morphology near the crack showed a certain directivity. The dilution wave and shock heat effect produced in the hypervelocity impact of small debris make the original carpet shape into an "impact like plain".

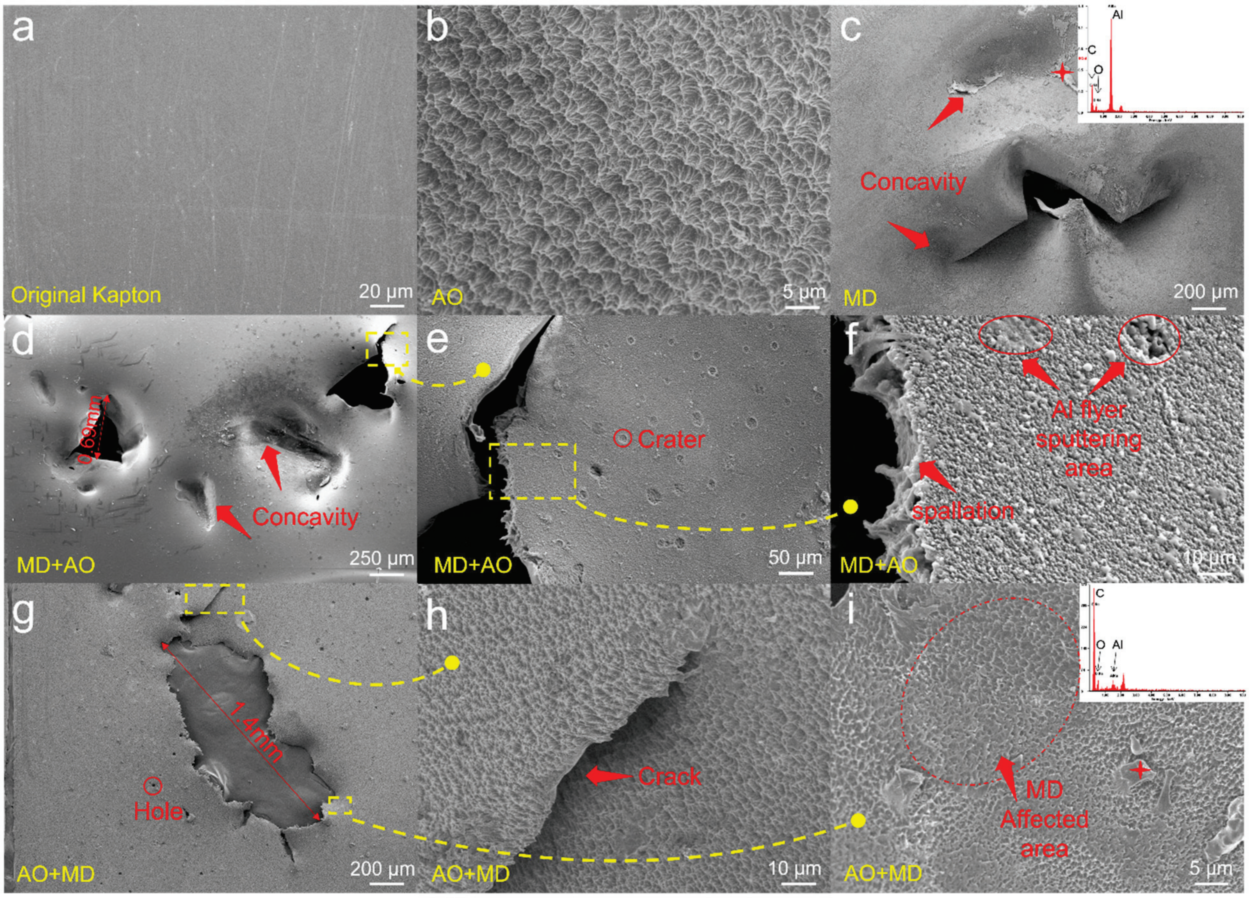

Figure 8. SEM surface morphology of Kapton film after different load spectrum tests: (**a**, ×500) original Kapton film; (**b**, ×2000) film after AO single factor load spectrum test; (**c**, ×50) film after MD single factor load spectrum test; (**d**, ×30); (**e**, ×200); (**f**, ×1000) film after MD + AO load spectrum test; (**g**, ×50); (**h**, ×1000); (**i**, ×2000) film after AO + MD load spectrum test.

3.4. Infrared Spectrum Analysis

In order to study the changes of functional groups on the surface of Kapton films before and after each load spectrum test, the test samples were analyzed by infrared spectroscopy. Figure 9 is the infrared spectrum of each sample, in which the positions of functional groups are given. In the load spectrum involving atomic oxygen in Figure 9, the exposure time of samples in atomic oxygen was 25 h. According to the infrared spectrum of the original Kapton film, 1774 and 1704 cm^{-1} absorption bands appear in the range of 1800–1680 cm^{-1}, corresponding to imide I band and II band, respectively, representing the symmetrical and asymmetric stretching vibration of two carbonyls (C=O) on the five membered imine ring. Absorption bands of 1366 and 719 cm^{-1} correspond to imide III and IV bands, respectively, which are C–N stretching vibration and C=O symmetric stretching vibration in polyimide. These are the four amide bands of a typical Kapton film [35]. Absorption bands of 1596 and 1502 cm^{-1} are the stretching vibration of benzene ring carbon skeleton in aryl ether. An absorption band of 1232 cm^{-1} is the stretching vibration of C–O in aryl ether, and shows wide and strong absorption. The 1163 cm^{-1} and 1111 cm^{-1} absorption bands can be attributed to the variable angle vibration in the =C–H plane on the substituted benzene ring. The 1012 cm^{-1} absorption band is the in-plane rocking vibration of para substituted phenyl hydrogen atoms. The 880 and 813 cm^{-1} absorption bands are out of plane deformation vibrations of isolated hydrogen atoms and ortho hydrogen atoms of benzene ring, respectively [36,37]. These are the characteristic peaks of Kapton films.

The infrared spectrum is shown in Figure 8. It can be observed that the position and shape of the infrared absorption peak of the original Kapton were basically unchanged compared with the samples after the MD single factor load spectrum test. There were few functional groups affected, which was attributed to the area affected by micro debris accounts for a small proportion. For the three samples eroded by atomic oxygen, it can be seen that although the position of the absorption peak does not change significantly, the strong absorption peaks were weakened. The obvious changes were 1704 cm^{-1} imide II band, 1596, 1502 and 1232 cm^{-1} absorption band. This showed that atomic oxygen will erode C=O on the five membered imine ring and C–C and C–O of the benzene ring carbon skeleton in the aryl ether.

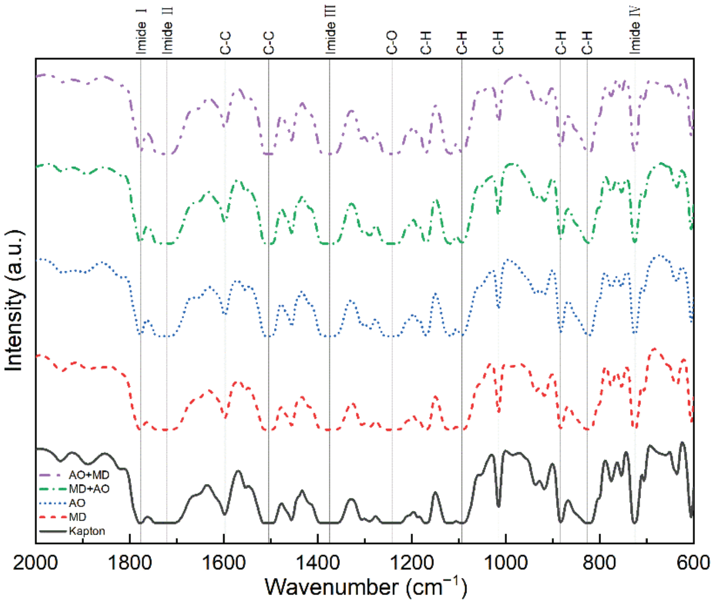

Figure 9. Infrared spectra of Kapton film before and after different load spectrum tests.

3.5. XPS Analysis

Kapton could produce a series of changes such as mass loss and surface morphology after MD + AO and AO + MD load spectrum tests. In order to further analyze the damage mechanism of Kapton induced in the test, the changes of surface elements and valence bonds of the sample were analyzed by X-ray photoelectron spectroscopy to explain the interaction mechanism of atomic oxygen and micro debris. In MD + AO and AO + MD load spectrum tests, the atomic oxygen erosion time is 25 h. The XPS full scan energy spectrum is shown in Figure 10, and the surface composition of the sample is shown in Table 1. As shown in Figure 10, Kapton thin film is composed of three elements C, O and N, while it is composed of four elements C, O, N and Al after atomic oxygen and micro debris impact test, which is caused by the sputtering deposition of aluminum flyers on the film during hypervelocity impact. It can be seen from Table 1 that the C element in Kapton film was greatly reduced after MD + AO and AO + MD load spectrum tests. This may be attributed to atomic oxygen that has a strong oxidation ability and has reacted with the polyimide film, so that the surface C element was oxidized to CO_2 and CO volatilization [33,38]. The increase in the proportion of O indicates that atomic oxygen was adsorbed on the surface of the film and reacts with the film. The decrease in N indicates that it participates in the chemical reaction. The reaction mechanism is further investigated by High-resolution XPS spectra, as shown in Figure 11. And the reaction mechanism diagram of Kapton film MD + AO and AO + MD load spectrum is shown in Figure 12.

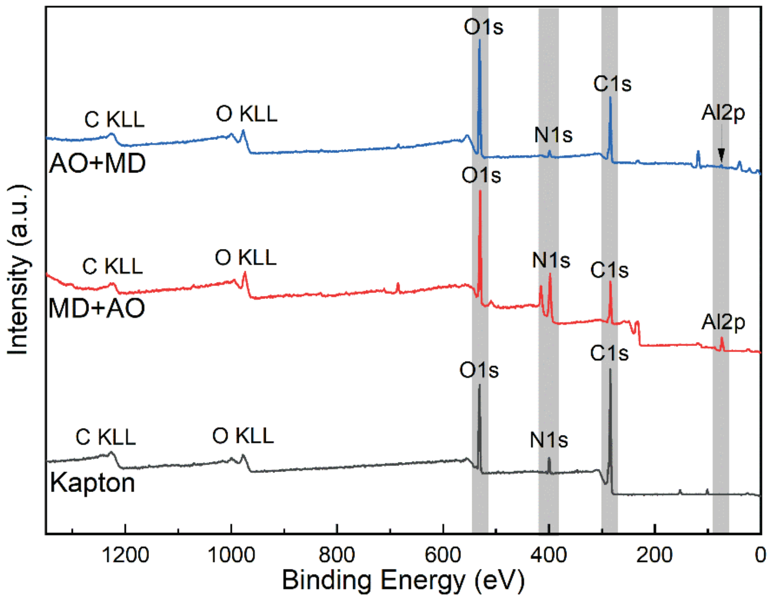

Figure 10. XPS full scan energy spectrum of original Kapton film and film after MD + AO and AO + MD load spectrum test.

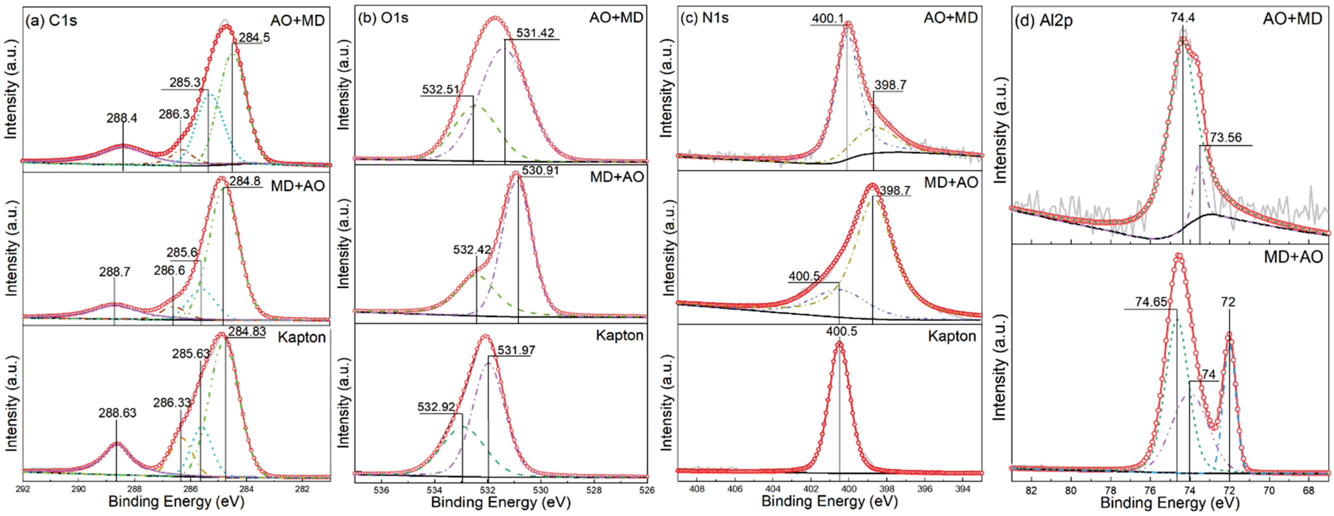

Figure 11. High-resolution XPS spectra of: (**a**) C1s, (**b**) O1s, (**c**) N1s, (**d**) Al2p on Kapton film before and after MD + AO, AO + MD load spectrum.

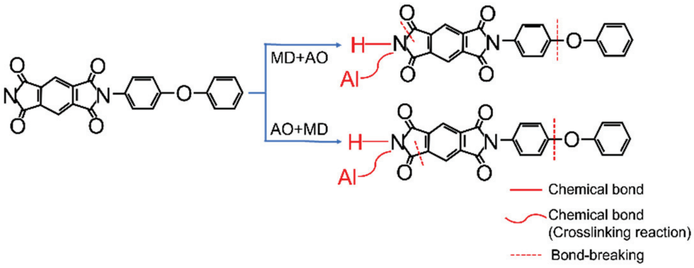

Figure 12. Reaction mechanism diagram of Kapton film MD + AO and AO + MD load spectrum.

Table 1. Relative content of surface elements after original Kapton film and MD + AO, AO + MD load spectrum test.

Material	**Surface Composition (%)**			
	C	**O**	**N**	**Al**
Original Kapton	75.18	19.18	5.64	-
MD + AO Kapton	45.66	32.58	3.62	18.15
AO + MD Kapton	47.32	48.95	0.15	3.58

According to the C1s high-resolution spectrum shown in Figure 11a, there are four states of C atoms in Kapton films. According to the peak fitting curve of XPSPEAK software (version 4.1), the four carbon atoms of the original Kapton film are located at the binding energy of 284.83 eV (corresponding to C–C bond in ODA benzene ring), 285.63 eV (corresponding to C=C bond in PMDA benzene ring), 286.33 eV (C–O bond) and 288.63 eV (C=O bond). After MD + AO load spectrum test, the four peaks are located at the binding energies of 284.8, 285.6, 286.6 and 288.7 eV, respectively. Compared to the original Kapton film, the most obvious reduction in relative peak area is the C–O bond corresponding to 286.6 eV, indicating that this load spectrum made the C–O bond break. The fitting peak area after AO + MD load spectrum test decreased significantly, including the C–O bond corresponding to 286.3 eV and the C–C bond corresponding to 284.5 eV. AO + MD load spectrum made the C–O bond and C–C fracture. It can be seen that in the MD + AO test, due to the adhesion of Al after the impact of small debris, the subsequent atomic oxygen erosion of the film was reduced, so the C–C bond was not seriously damaged. However, after the AO + MD load spectrum test, the film was first eroded by atomic oxygen, resulting in the reduction in the C–O bond and the C–C bond.

According to Figure 11b, the oxygen element energy spectrum of the original Kapton film can be fitted to two peaks of 532.92 and 531.97 eV, with peak areas of 36.6% and 63.4%, respectively, corresponding to the C–O bond and the C=O bond [39]. After MD + AO load spectrum test, the peak positions were 532.42 eV (C–O) and 530.91 eV (C=O), the peak areas were 33.2% and 66.8%, respectively, and the peak area of the C–O bond decreased slightly. After AO + MD load spectrum test, the relative peak area of the C–O bond corresponded to 532.51 eV is 30.17%, which was 6.43% lower than that of the original film and indicated that the C–O bond was seriously damaged by this load spectrum test. The results are the same as those of C1′s fine spectrum analysis, which is attributed to the fact that the deposited Al particles on the MD + AO load spectrum test film delayed the erosion of atomic oxygen, and the atomic oxygen in the AO + MD load spectrum could directly destroy the C–O bond.

It can be seen from Figure 11c, that the original Kapton film has only one characteristic peak with binding energy of 400.5 eV, which is the C–N bond [40]. After the MD + AO load spectrum test, the N–H bond corresponding to the characteristic peak with a binding energy of 398.7 eV appeared in the sample [41]. Compared with the two characteristic peaks in the sample after the AO + MD load spectrum test, it can be seen that micro debris had a great impact on the C–N bond. Hypervelocity impact led to thermal decomposition of the material, destruction of the C-N bond in the imide ring and the generation of the N–H bond. After the AO + MD load spectrum test, the film also has two characteristic peaks in Figure 11c, although only a small amount of N–H bond, which showed that atomic oxygen has little effect on the C–N bond, and the fracture of the C–N bond was caused by high-temperature pyrolysis of materials caused by hypervelocity impact [42].

After the MD + AO load spectrum test, the peak fitting of Al element on the sample surface is shown in Figure 11d. The three peaks are located at 74.65, 74 and 72 eV, respectively, corresponding to Al–O bond, Al–N bond and Al-Al bond [43,44]. The relative peak area of Al–O bond is 46.2%, indicating that after hypervelocity impact, a considerable part of the residual aluminum flyer on the sample was oxidized to alumina by atomic oxygen. The relative peak area of the Al–N bond is 34.5%, which may be due to the cross-linking between Al debris and N in the sample. A small amount of Al has not been oxidized and reacted. The peak fitting of the sample after AO + MD load spectrum test is shown in Figure 11d. Only two peaks are located at 74.4 and 73.56 eV, respectively, corresponding to the Al–O bond and Al-N bond, respectively. It can be seen from Figure 10 AO + MD that the intensity of Al peak was very low, and the Al element content on the sample surface in Table 1 was also very small. This is because the mechanical strength and impact resistance of the sample were reduced after being corroded by atomic oxygen. The impact of aluminum flyers on the film caused perforation and reduced residual al fragments. After the AO + MD loading spectrum test, the Al element on the sample surface was oxidized, and a small part was crosslinked with n to form an Al-N bond.

4. Conclusions

In this paper, the damage effects of a single factor of atomic oxygen (AO) and micro debris (MD), and the asynchronous synergy of MD + AO and AO + MD load spectra on Kapton films were studied. The results show that:

- After the asynchronous synergistic action of atomic oxygen and small debris, the Kapton film changed from brown yellow to light yellow; the gloss disappeared, and the transmittance decreased in the wavelength range of 600–800 nm. Under the condition of AO + MD load spectrum, the surface hole of Kapton film was larger than that under the MD + AO load spectrum, the residual aluminum particles formed by the reverse sputtering of Al particles produced during the impact process were less, the average transmittance of the film decreased slightly, and the weight loss of Kapton film was slightly more under the same atomic oxygen exposure time;
- Under the condition of MD + AO load spectrum, plastic tearing cracks, pits and holes appeared on the surface of Kapton film; under the condition of AO + MD load spectrum, the hole edge on the surface of Kapton film was straight, without obvious depression and tear characteristics. This is attributed to the fact that the film was eroded by atomic oxygen first, and the rough carpet shape was formed on the material surface, and the subsequent flyer impact became the crack source; at the same time, the atomic oxygen corrosion aging fracture strength of the surface material decreases.
- Under the condition of MD + AO load spectrum, due to the adhesion of Al after the impact of micro debris, the subsequent atomic oxygen erosion of the film was reduced, so the C–C bond was not seriously damaged, and a considerable part of the residual aluminum flyer was oxidized to alumina by atomic oxygen. While the AO + MD loading spectrum test made the film first eroded by atomic oxygen, resulting in the reduction in the C–O bond and the C–C bond. The impact of micro debris had a great impact on the C–N bond. Hypervelocity impact leads to the thermal decomposition of the material, destroyed the C–N bond in the imide ring and generated N–H bond.

Author Contributions: Conceptualization, Q.W., methodology, Q.W.; investigation, Q.W. and P.T., writing—original draft preparation, P.T., writing—review and editing, Q.W. and P.T., supervision, X.C. and N.H., project administration, Q.W. and N.H., funding acquisition, Q.W. and N.H. All authors have read and agreed to the published version of the manuscript.

Funding: This research was funded by the National Natural Science Foundation of China (Grant No. 51873146), the Fund for Innovative Research Groups of Natural Science Foundation of Hebei

Province (Grant No. A2020202002), and Natural Science Foundation of Hebei Province (Grant No. E2019202106).

Institutional Review Board Statement: Not applicable.

Informed Consent Statement: Not applicable.

Data Availability Statement: Data sharing is not applicable to this article.

Conflicts of Interest: The authors declare no conflict of interest.

References

1. Yeritsyan, H.N.; Sahakyan, A.A.; Grigoryan, N.E.; Harutyunyan, V.V.; Arzumanyan, V.V.; Tsakanov, V.M.; Grigoryan, B.A.; Davtyan, H.D.; Dekhtiarov, V.S.; Rhodes, C.J.; et al. Space low earth orbit environment simulator for ground testing materials and devices. *Acta Astronaut.* **2021**, *181*, 594–601. [CrossRef]
2. Shivakumar, R.; Bolker, A.; Tsang, S.H.; Atar, N.; Verker, R.; Gouzman, I.; Hala, M.; Moshe, N.; Jones, A.; Grossman, E.; et al. POSS Enhanced 3D Graphene–Polyimide Film for Atomic Oxygen Endurance in Low Earth Orbit Space Environment. *Polymer* **2020**, *191*, 122270. [CrossRef]
3. Shimamura, H.; Nakamura, T. Investigation of degradation mechanisms in mechanical properties of polyimide films exposed to a low earth orbit environment. *Polym. Degrad. Stab.* **2010**, *95*, 21–33. [CrossRef]
4. Shimamura, H.; Nakamura, T. Mechanical properties degradation of polyimide films irradiated by atomic oxygen. *Polym. Degrad. Stab.* **2009**, *94*, 1389–1396. [CrossRef]
5. Qiu, J.W.; Shen, Z.C.; Xiao, L. Study on Synergistic Effect of Space Environments on Spacecraft. *Spacecr. Eng.* **2013**, *22*, 15–20. [CrossRef]
6. Lu, Y.F.; Shao, Q.; Yue, H.H.; Yang, F. A Review of the Space Environment Effects on Spacecraft in Different Orbits. *IEEE Access* **2019**, *7*, 93473–93488. [CrossRef]
7. Han, J.-H.; Kim, C.-G. Low earth orbit space environment simulation and its effects on graphite/epoxy composites. *Compos. Struct.* **2006**, *72*, 218–226. [CrossRef]
8. He, S.Y.; Yang, D.Z.; Jiao, Z.K. *Space Materials Manual–Physical State of Space Environment*, 1st ed.; Aerospace Press: Beijing, China, 2012; Volume 1, pp. III–IV.
9. Chen, R.M.; Zhang, L.; Yan, C.W. Synergic Effect of Atomic Oxygen and Vacuum Ultraviolet on Organic Coatings Degradation. *J. Aeronaut. Mater.* **2007**, *27*, 41–45. [CrossRef]
10. Yokota, K.; Ohmae, N.; Tagawa, M. Effect of Relative Intensity of 5 eV Atomic Oxygen and 172 nm Vacuum Ultraviolet in the Synergism of Polyimide Erosion. *High Perform. Polym.* **2004**, *16*, 221–234. [CrossRef]
11. Shimamura, H.; Miyazaki, E. Investigations into Synergistic Effects of Atomic Oxygen and Vacuum Ultraviolet. *J. Spacecr. Rockets* **2009**, *469*, 241–247. [CrossRef]
12. Zhai, R.Q.; Ren, G.H.; Tian, D.B.; Li, Y.; Yang, Y.B.; Liu, C. Advances in research on low-orbit ultraviolet, charged particles, thermal cycling and atomic oxygen synergistic effects. *Vacuum* **2019**, *56*, 72–76.
13. Sun, P.W.; Song, L.M.; Wang, Z.H. A Study on Process Management and Control Technology of Asynchronous Coliaborative Simulation. *J. Inn. Mong. Univ. Technol.* **2007**, *26*, 65–70. [CrossRef]
14. Tagawa, M.; Yokota, K. Atomic oxygen-induced polymer degradation phenomena in simulated LEO space environments: How do polymers react in a complicated space environment? *Acta Astronaut.* **2008**, *62*, 30203–30211. [CrossRef]
15. Liu, T.; Qiu, X.M.; Zhang, X.H.; Cao, Y.; Liu, Y.F.; Yang, J.H. Experimental investigation on the hypervelocity impact damage behavior of polyimide film. *Int. J. Impact Eng.* **2020**, *141*, 103538. [CrossRef]
16. Verker, R.; Grossman, E.; Gouzman, I.; Laikhtman, A.; Katz, S.; Freankel, M.; Maman, S.; Lempert, G.; Eliaz, N. Synergistic effect of simulated hypervelocity space debris and atomic oxygen on durability of POSS-polyimide nanocomposite. In Proceedings of the 10th Int. Symp. on Materials in Space Environment & the 8th Int. Conf. on Protection of Materials and Structures in a Space Environment—ISMSE/ICPMSE 2006, Collioure, France, 19–23 June 2006.
17. Li, H.W.; Cai, M.H.; Han, J.W.; Huang, J.G.; Li, X.Y.; Yu, J.X.; Gao, Z.X.; Liu, D.Q. Research of Combined Effect of Small Space Debris and Atomic Oxygen. *Chin. J. Space Sci.* **2011**, *31*, 503–508.
18. Jiang, H.F.; Cao, Y.; Li, Y.; Chai, L.H. The combined effect of space micro-debris and atomic oxygen on ITO/Kapton/Al film. *Spacecr. Environ. Eng.* **2016**, *33*, 530–533. [CrossRef]
19. Gouzman, I.; Grossman, E.; Verker, R.; Atar, N.; Bolker, A.; Eliaz, N. Advances in Polyimide-Based Materials for Space Applications. *Adv. Mater.* **2019**, *31*, 1807738. [CrossRef]
20. Zhang, L.; Yan, C.W.; Qu, Q.; Li, M.S.; Cao, C.N. Effect of Atomic Oxygen on Spacecraft Materials and Its Protection II. Protection of Atomic Oxygen-Susceptible Materials. *Mater. Rev.* **2002**, *16*, 7–8. [CrossRef]
21. Shit, S.C.; Shah, P.M. A Review on Silicone Rubber. *Natl. Acad. Sci. Lett.* **2013**, *36*, 355–365. [CrossRef]
22. Man, Y.R.; Li, Z.H.; Shu, M.; Liu, K.; Liu, H.T.; Gao, Y. Surface treatment of 25-μm Kapton film by ammonia for improvement of TiO_2 SiO_2 coating's adhesion. *Surf. Interface Anal.* **2017**, *49*, 843–849. [CrossRef]
23. Song, L.H.; Wei, Q.; Bai, Y.; Wang, Z.H. Review on the Laser Technology Application in Space Environment Ground Simulation. *Optoelectron. Technol.* **2016**, *33*, 96–102. [CrossRef]

24. Duo, S.W.; Li, M.S.; Zhang, Y.M. A Simulator for Producing of High Flux Atomic Oxygen Beam by Using ECR Plasma Source. *J. Mater. Sci. Technol.* **2004**, *20*, 759–762. [CrossRef]
25. Liu, K.; Mu, H.; Shu, M.; Li, Z.; Gao, Y. Improved adhesion between SnO_2/SiO_2 coating and polyimide film and its applications to atomic oxygen protection. *Colloids Surf. A Physicochem. Eng. Asp.* **2017**, *529*, 356–362. [CrossRef]
26. Lian, R.H.; Lei, X.F.; Xue, S.Y.; Chen, Y.H.; Zhang, Q.Y. Janus polyimide films with outstanding AO resistance, good optical transparency and high mechanical strength. *Appl. Surf. Sci.* **2021**, *535*, 147654. [CrossRef]
27. Li, Y.; Fu, S.-Y.; Li, Y.-Q.; Pan, Q.-Y.; Xu, G.S.; Yue, C.-Y. Improvements in transmittance, mechanical properties and thermal stability of silica–polyimide composite films by a novel sol–gel route. *Compos. Sci. Technol.* **2007**, *67*, 2408–2416. [CrossRef]
28. Wang, H.D.; Ma, G.Z.; Xu, B.S.; Xing, Z.G.; Li, G.L.; Zhang, S. The Erosion Effect of Kapton Film in a Groundbased Atomic Oxygen Irradiation Simulator. *J. Wuhan Univ. Technol. Mater. Sci. Ed.* **2014**, *29*, 1277–1282. [CrossRef]
29. Buczala, D.M.; Brunsvold, A.L.; Minton, T.K. Erosion of Kapton® H by Hyperthermal Atomic Oxygen. *J. Spacecr. Rockets* **2006**, *43*, 421–425. [CrossRef]
30. Reddy, M.R. Effect of low earth orbit atomic oxygen on spacecraft materials. *J. Mater. Sci.* **1995**, *30*, 281–307. [CrossRef]
31. Maiden, C.J.; Mcmillan, A.R. An Investigation of the Protection Afforded a Spacecraft by a Thin Shield. *Aerosp. Sci. Meet.* **1964**, *2*, 1992–1998. [CrossRef]
32. Huang, Y.X.; Tian, X.B.; Yang, S.Q.; Chu, P.K. A ground-based radio frequency inductively coupled plasma apparatus for atomic oxygen simulation in low Earth orbit. *Rev. Sci. Instrum.* **2007**, *78*, 103301. [CrossRef]
33. Wei, Z.; Weiping, L.; Huicong, L.; Liqun, Z. Erosion of a Polyimide Material Exposed to Simulated Atomic Oxygen Environment. *Chin. J. Aeronaut.* **2010**, *23*, 268–273. [CrossRef]
34. Cui, W.F.; Zeng, X.W. Simulation investigations on debris cloud impact damage potential. *Explos. Shock. Waves* **2009**, *29*, 434–438. [CrossRef]
35. Yang, Y.; Yin, D.; Xiong, R.; Shi, J.; Tian, F.Q.; Wang, X.; Lei, Q.Q. FTIR and Dielectric Studies of Electrical Aging in Polyimide under AC Voltage. *IEEE Trans. Dielectr. Electr. Insul.* **2012**, *19*, 574–581. [CrossRef]
36. Naddaf, M.; Balasubramanian, C.; Alegaonkar, P.S.; Bhoraskar, V.N.; Mandle, A.B.; Ganeshan, V.; Bhoraskar, S.V. Surface interaction of polyimide with oxygen ECR plasma. *Nucl. Instrum. Methods Phys. Res. Sect. B Beam Interact. Mater. At.* **2004**, *222*, 135–144. [CrossRef]
37. Wang, W.; Li, C.X.; Zhang, G.B.; Sheng, L.S. Synthesis and Studies of Polyimide. *Mater. Rev.* **2008**, *22*, 119–128. [CrossRef]
38. Duo, S.W.; Li, M.S.; Zhou, Y.C.; Tong, J.Y.; Sun, G. Investigation of Surface Reaction and Degradation Mechanism of Kapton during Atomic Oxygen Exposure. *J. Mater. Sci. Technol.* **2003**, *19*, 535–539. [CrossRef]
39. Jiang, D.H.; Wang, D.; Liu, G.; Wei, Q. Atomic Oxygen Adaptability of Flexible Kapton/Al2O3 Composite Thin Films Prepared by Ion Exchange Method. *Coatings* **2019**, *9*, 624. [CrossRef]
40. Shen, Z.C.; Ma, Z.L.; Dai, W.; Mu, Y.Q.; Bai, Y.; Ding, Y.G. Evolution Mechanism for Mechanical Property of Polyimide Film by Far Ultraviolet Irradiation. *Surf. Technol.* **2018**, *47*, 22–26. [CrossRef]
41. Xin, J.J.; Shen, S.C.; Wang, J.B. X-ray Photoelectron Spectroscopy Study of Polyimide Film by Ar Ion Bombardment. *Adv. Sci. Technol.* **2015**, *29*, 1–3. [CrossRef]
42. Lu, X.; Han, S.; Li, Q.M.; Huang, X.Y.; Wang, X.L.; Wang, G.Y. Reactive Molecular Dynamics Simulation of Polyimide Pyrolysis Mechanism at High Temperature. *Trans. China Electrotech. Soc.* **2016**, *31*, 14–23. [CrossRef]
43. Rosenberger, L.; Baird, R.; McCullen, E.; Auner, G.; Shreve, G. XPS analysis of aluminum nitride films deposited by plasma source molecular beam epitaxy. *Surf. Interface Anal.* **2008**, *40*, 1254–1261. [CrossRef]
44. Motamedi, P.; Cadien, K. XPS analysis of AlN thin films deposited by plasma enhanced atomic layer deposition. *Appl. Surf. Sci.* **2014**, *315*, 104–109. [CrossRef]

coatings

MDPI

Article

Combination of Electron Beam Surface Structuring and Plasma Electrolytic Oxidation for Advanced Surface Modification of Ti6Al4V Alloy

Hugo Mora-Sanchez [1,2,*], Florian Pixner [3], Ricardo Buzolin [3,4], Marta Mohedano [1], Raúl Arrabal [1], Fernando Warchomicka [3] and Endzhe Matykina [1]

[1] Departamento de Ingeniería Química y de Materiales, Facultad de Ciencias Químicas, Universidad Complutense de Madrid, 28040 Madrid, Spain
[2] CIDETEC, Basque Research and Technology Alliance (BRTA), Po. Miramón 196, 20014 Donostia-San Sebastián, Spain
[3] Institute of Materials Science, Joining and Forming, Graz University of Technology, Kopernikusgasse 24/I, 8010 Graz, Austria
[4] Christian Doppler Laboratory for Design of High-Performance Alloys by Thermomechanical Processing, Kopernikusgasse 24/I, 8010 Graz, Austria
* Correspondence: hmora@cidetec.es

Abstract: The objective of this work is to study for the first time the combination of electron beam (EB) surface structuring and plasma electrolytic oxidation (PEO) with the aim of providing a multiscale topography and bioactive surface to the Ti6Al4V alloy for biomedical applications. Ca and P-containing coatings were produced via 45 s PEO treatments over multi-scale EB surface topographies. The coatings morphology and composition were characterized by a means of scanning electron microscopy (SEM) and energy dispersive X-ray spectroscopy (EDS). The effect on the previous EB topography was evaluated by means of a 3D optical profilometry and electrochemical response via potentiodynamic polarization tests. In general, the PEO process, morphology, composition and growth rate of the coatings were almost identical, irrespective of the topography treated. Minimal local differences were found in terms of morphology, and the growth rate were related to specific topographical features. Nevertheless, all the PEO-coated substrates presented essentially the same corrosion resistance. Electrochemical tests revealed a localized crevice corrosion susceptibility of all the bare EB topographies, which was successfully prevented after the PEO treatment.

Keywords: electron beam surface structuring; electron beam processing; plasma electrolytic oxidation; flash-PEO; titanium; crevice; corrosion

1. Introduction

The long-term success of orthodontic and orthopedic metallic devices depends upon minimizing implant and host bone degradation as well as providing rapid osseointegration. Titanium and its alloys offer a low toxicity, an excellent corrosion resistance in physiological media (i.e., a low ion release rate due to the natural formation of a highly stable TiO_2 layer) [1] and, in comparison to stainless steels and Co–Cr alloys (~200 GPa), an elastic modulus (E ~ 110 GPa) that is closer to that of the cortical bone (10 ÷ 40 GPa). Although Ti alloys are known for osseointegration [2], their surface morphology and chemistry can be tailored to promote further initial cellular interactions towards ultimately rapid osseointegration [3].

Mechanical and chemical surface-roughening approaches (i.e., sandblasting and chemical etching) have been shown to promote early cell-to-surface interactions such as adhesion, proliferation and the metabolic activity of osteoblastic cells [4]. Further, it has been shown that linear surface features such as microgrooves can further improve cell proliferation, differentiation and alignment [5]. This approach also provides an improved biomedical interlocking with the host bone [6–9].

Electron beam (EB) surface structuring is capable of producing linear and complex microscale topographies (i.e., hexagonal or circular) that are free from cracks, pores and impurities, with a high degree of repeatability and control [10]. EB surface structuring is based on the fast melting and solidification of the metallic surface by the action of a high-speed, high-power focused electron beam. The focused EB leads to local melting and evaporation. inducing the so-called "keyhole" effect where the high vapor pressure displaces the molten material away from the center of the beam. A fast and precise deflection of the EB causes a material transport behind the beam and a subsequent fast solidification, leading to the formation of microscale features. This technique was firstly reported by Dance et al. [11] with the name Surfi-Sculpt® for a wide range of applications. Ramskogler et al. [10] used this technology to produce 2 mm wide hexagonal structures with a multiscale topography consisting of radial canal shapes 1.3–9 μm deep and 68.6–119.7 μm wide and, depending on the beam travel direction, either a central pin up to a 305 μm height or a 452 μm deep depression. The authors showed that all the structures improved the MC3T3-E1 pre-osteoblast cells spreading area with respect to the unstructured Ti6Al4V alloy for up to 24 h. Based on the same technique, microgrooves were performed successfully in different titanium alloys to favor a contact guidance for fibroblast cells and prevent a bacterial contamination at the material's surface [12]. Grooves with a width of 10 μm and a roughness (Ra) close to 0.2 μm showed the ability to align the fibroblast cells. An additional nano structuring provoked during the structuring reduces the bacterial adhesion in the first 48 h without using active agents.

Other surface modification approaches to improve the osseointegration of Ti implants rely on the formation of osteoconductive coatings by techniques such as plasma electrolytic oxidation (PEO), which has shown clinical success in immediate loading orthodontic procedures [13]. The PEO is an advanced high voltage anodizing technique that allows the fabrication of porous and rough ceramic coatings with the aid of short-lived plasma micro-discharges favoring the incorporation of the bioactive elements (i.e., Ca, P, Zn and Mg) [14–16]. Compared with traditional anodizing, PEO coatings improve the corrosion resistance and surface mechanical properties (i.e., the hardness and adhesion). Moreover, the combination of the surface topography, microstructure and composition of PEO coatings promotes early cell-to-surface interactions [17]. In the last few years, with the aim being to reduce treatment costs and minimize the impact on the mechanical properties of the substrate (i.e., fatigue), short PEO treatments (<120 s), termed flash-PEO, have been developed [18].

Henceforth, the PEO treatment of a multiscale EB-structured Ti surface would combine the composition (Ca- and P-containing), roughness ($S_a \approx 0.3$–0.6 μm), porosity (pore size 0.5 up to 4 μm) and corrosion protection of the PEO coating with micro-canals (width: 10–200 μm and depth: 1–20 μm) and sub-millimeter structures (lateral and vertical dimensions between 100 and 500 μm). This combination is believed to be a powerful synergy to enhance the osteoconductive, antibacterial, corrosion resistance and biomechanical interlocking of the Ti6Al4V alloy. To the best knowledge of the authors, there is no study regarding the PEO treatment of multiscale EB structures. Specifically, it is unknown what role different structure scales might play during PEO, i.e., micro-meter and sub-millimeter scales. Therefore, the present work aims to study the PEO treatment of multiscale EB structures on Ti6Al4V, together with their electrochemical behavior in a physiological media. For this, it was decided to follow a bottom-to-top approach, treating the characteristic flat surface separately after the EB, linear EB micro-grooves and linear multiscale EB.

2. Materials and Methods

2.1. Material and Electron Beam Surface Structuring

The material selected for this investigation was the α + β alloy Ti6Al4V provided in a rectangular sheet shape with dimensions 200 × 100 × 2 mm. Prior to the EB processing, the surface contaminations were removed mechanically, generating a surface roughness (S_a) of approximately 4 µm, and the surface was subsequently cleaned with isopropanol.

The surface structuring was performed using an electron beam machine (EB) model Probeam EBG 45 ÷ 150 K14 (Probeam GmbH & Co. KGaA, Gilching, Germany), with a maximum acceleration voltage and power of 150 kV and 45 kW, respectively. The structuring of a surface is driven by the melting of the material and its displacement as the electron beam scans the surface. The melting is dependent on the energy input per the unit of length (E, [J/m]), which is ultimately dependent on the acceleration voltage (U, [V]), beam current (I, [A]) and deflection velocity (v, [m/s]): $E = \frac{U \cdot I}{v}$. Due to the “keyhole” effect, the molten material is displaced behind the beam and subsequently solidifies. It implies that controlling the deflection of the beam determines the accumulation of the material and, ultimately, the surface structuring.

Since electrons serve as the energy source, the negatively charged subatomic particles can be easily deflected by the magnetic lenses in the beam gun column to form geometric patterns called beam figures. These beam figures can be designed independently and implemented in the process, which then defines the trajectory of the electron beam. In the present study, the beam figures were designed using MATLAB R2017a software (MathWorks, Natick, MA, USA). In addition to the geometric dimensions (x and y coordinates), each beam figure consists of a number of coordinates/elements.

In order to proceed with the electrochemical characterization and PEO treatment, it was required that the beam figures/specimens had a square 20 × 20 mm area covered by EB structures. Henceforth, the EB structure height was fixed at 20 mm. The following EB structures/beam figures were designed to study the effect of the microstructure (i.e., martensitic α′ Ti) separately, multiple topography scales on the PEO treatment and electrochemical corrosion behavior:

The plain EB surface (designated M): molten and solidified surface with α′ martensitic microstructure, to form an identical microstructure compared to ii and iii (Figure 1).

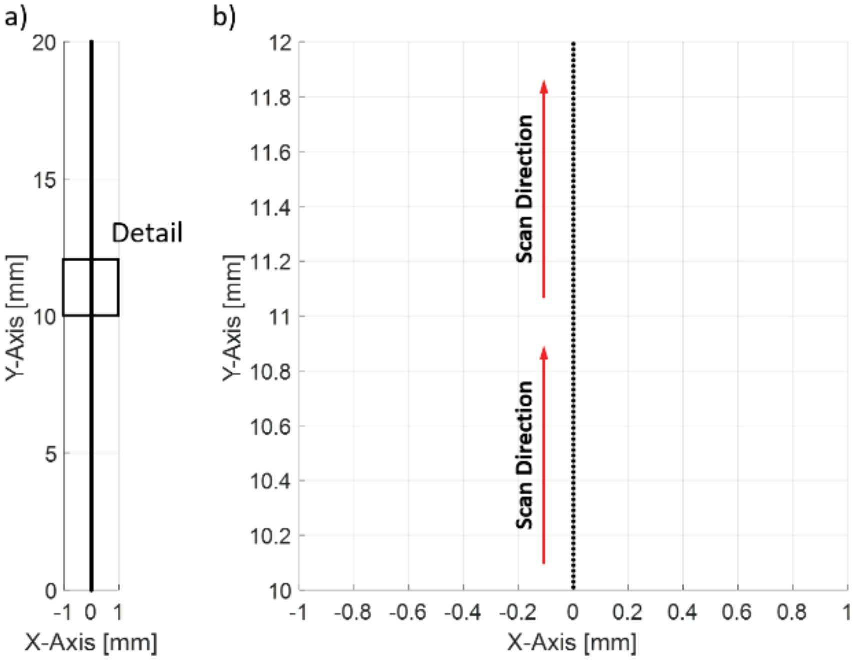

Figure 1. (**a**) Electron beam scan strategy followed to produce the molten surface (M). (**b**) detailed view of (**a**).

The micro-grooves (designated G): 50 ÷ 200 µm groove/hatch spacing, 2 ÷ 15 µm deep and dimension (height × width) of 20 mm × 20 mm (Figure 2).

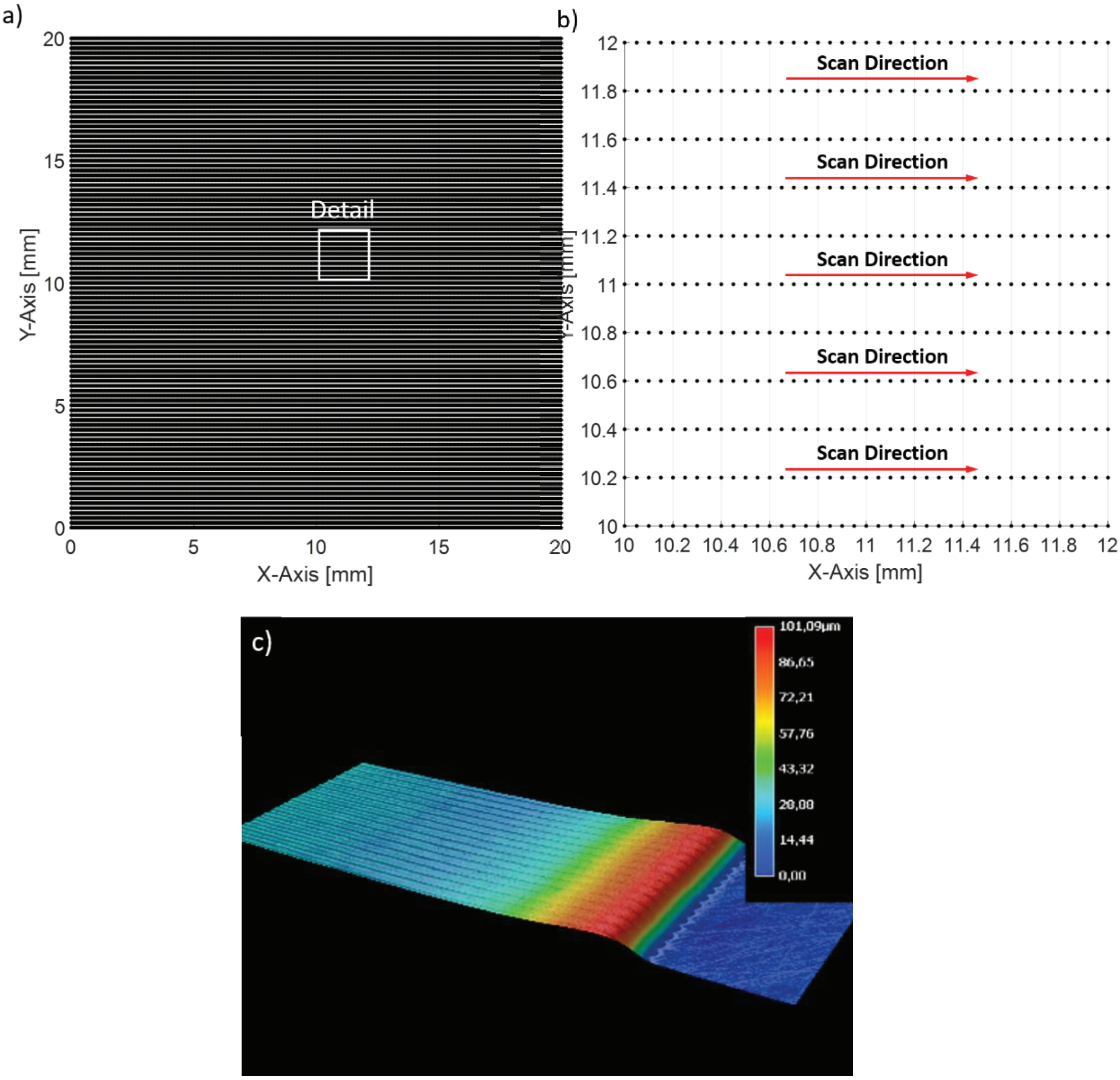

Figure 2. (**a**) Electron beam scan strategy followed to produce the micro-grooves (G) over 20 mm × 20 mm area. (**b**) detail view of (**a**). (**c**) 3D reconstruction of beam figure.

The linear macrostructures in the center, termed "Bridge", has perpendicular micro-grooves (designated B): 50 ÷ 200 µm groove/hatch spacing, approx. a 800 µm center height and a dimension (height × width) of 20 mm × 5 mm (Figure 3). To achieve the required dimensions (20 mm × 20 mm), four such unit cells (20 mm × 5 mm, Figure 3a) are lined up (Figure 3c).

Figure 1 shows the designed beam figure for the melting of the surface without any surface structuring. The beam figure consisted of 1000 elements, i.e., coordinates, arranged in a vertical alignment over a length of 20 mm. In contrast to the surface structuring of ii and iii, the machine table was not held stationary but moved in the x-direction at a travelling speed of 5 mm/s, while the beam figure was traversed at 1000 Hz (i.e., 1000 times per second). The required power/energy input was determined based on the preliminary studies, and for the present study, the surface was melted locally with a power input of 600 W. The parameters are summarized in Table 1.

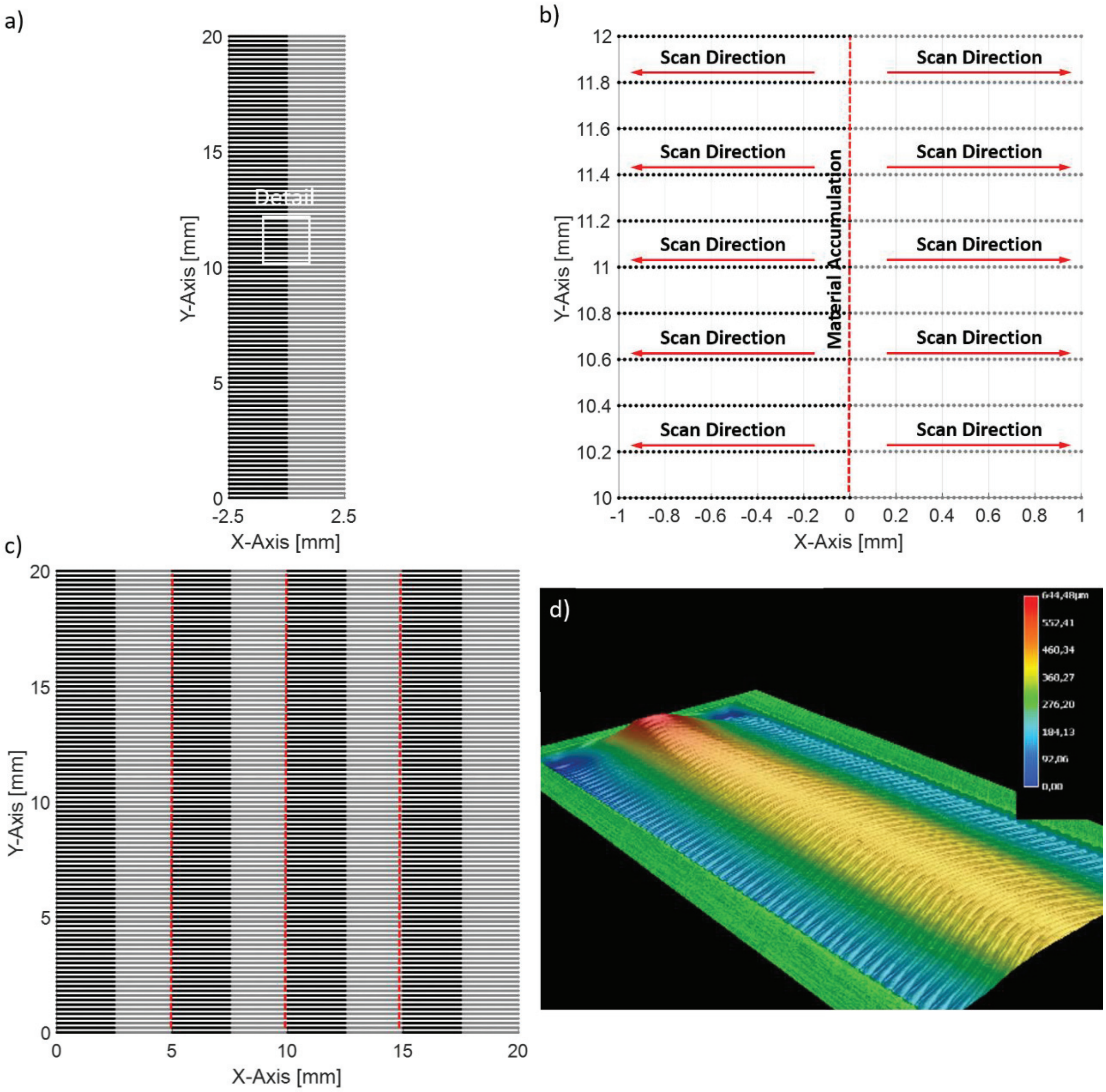

Figure 3. (**a**) Electron Beam scan strategy followed to produce the bridge structures (B). (**b**) detail view of (**a**). (**c**) arrangement of four bridge structures covering a 20 mm × 20 mm area. (**d**) 3D reconstruction of the single Bridge beam figure (**a**).

Table 1. Summary of input and beam oscillation parameters to achieve: M, plain EB molten and solidified surface with α' martensitic microstructure; G1/G2, micro-grooves; B1/B2, bridge macrostructures.

Attribute		M	G1/G2	B1/B2	Unit
Acceleration Voltage	U_{acc}	120	120	120	kV
Beam Current	I_{beam}	5	2	2	mA
Power	P_{beam}	600	240	240	W
Welding Speed	V_{trav}	5	-	-	mm/s
Beam Figure		Figure 1	Figure 2	Figure 3	
Focal Position		Surface	Surface	Surface	
Dimension (bop)		20 × 20	20 × 20	20 × 5	mm
Hatch Spacing (bop)	d	-	100/200	100/200	µm
Elements (bop)	e	1000	80,000/40,000	40,000/20,000	
Frequency (bop)	f	1000	20/10	20/10	kHz
Welding Time	t_{weld}		8	4	s
Number of Passes		1	2	2	
Scan Speed (bop)	v_{scan}	20,000	1000/500	500/250	mm/s
Energy Input	E		240/480	480/960	J/m

Figures 2 and 3 show the designed beam figures for the surface structuring to produce (i) micro-grooves and (ii) bridge linear macrostructures, respectively. For the surface structuring, the beam only was deflected, and the machine table was kept stationary. For both beam figures, the scan was line-by-line with predefined hatch spacings (i.e., vertical spacing between the beam trajectories, Figure 2b). While for the micro-grooves the beam trajectory was unidirectional from one side to the other, the beam trajectory for the linear macrostructures with perpendicular micro-grooves was multidirectional. Consequently, in addition to the micro-grooves, the multidirectional beam trajectory leads to a high linear macrostructure in the center (Figure 3d).

To determine the suitable process and beam oscillation parameters, preliminary studies were performed and the parameters varied were: (1) the beam current (0.5–2 mA), (2) hatch spacing (50–200 μm), (3) frequency (10–40 kHz) and (4) weld time, i.e., the number of passes (1–4). The final parameters were selected based on the defect-free surfaces with regular patterns and the desired feature dimensions. The selection of the specimens to be PEO treated was carried out using a digital microscope (Keyence VHX-5000, Keyence, Mechelen, Belgium), 3D analysis and scanning electron microscopy (SEM) observations (TESCAN Mira 3, Tescan, Brno, Czech Republic).

The final parameters for the further characterization of the microgrooves and linear macrostructure with perpendicular micro-grooves are listed in Table 1, respectively. A final power input of 240 W (i.e., beam current 2 mA), hatch spacing of 100 and 200 μm, frequency of 10 and 20 kHz and two passes for each beam figure were applied. The EB surface structured micro-grooves with a hatch-spacing of 100 and 200 μm are designated as G1 and G2, and the linear macrostructure with perpendicular micro-grooves with a hatch-spacing of 100 and 200 μm are designated as B1 and B2, respectively.

2.2. Flash Plasma Electrolytic Oxidation

The EB-structured samples were cleaned in ethanol in an ultrasonic bath for 5 min for both the PEO treatment and the electrochemical corrosion tests. They were subsequently attached to a copper wire as an electrical contact and electrically insulated with a commercial stopping-off resin (Lacquer 45, MacDermid plc), maintaining an unmasked 1 or 3 cm^2 working area (depending on the specimen size).

The electrolyte was a Ca and P-containing aqueous solution with the following composition: 0.05 M $C_6H_{10}CaO\ 5H_2O$; 0.055 M $NaH_2PO_4\ 2H_2O$; 0.025 M NaOH; and 0.15 M $Na_2(EDTA)\ 2H_2O$. The PEO treatment was carried out in a double-wall electrochemical cell with agitation and maintaining the temperature of the bath at ~23 °C. An AC square voltage signal with a 490 V positive pulse and a 30 V negative pulse (V_{RMS} = 347 V) at 300 Hz and a 50% duty cycle was used for the treatment. The initial rise of the voltage was controlled using a 60 s ramp. The current density was limited to a maximum of 300 $mA \cdot cm^{-2}$. The total treatment time was 45 s to obtain thin PEO coatings (~2 ÷ 4 μm) in agreement with the flash-PEO philosophy.

2.3. Surface Metrology and Microstructural Characterization

The surfaces of the non-treated and PEO-treated samples were studied with high-resolution 3D optical metrology (InfiniteFocusSL, Bruker, Alicona). A 3D reconstruction of the surfaces provided quantitative information on the surface features. The surface and cross-section morphology and composition of the PEO coatings were studied by SEM and energy dispersive X-ray spectroscopy (EDS, Oxford X-Max 20, Gatan, Pleasanton, CA, USA) in a JEOL JSM-6400 system at 20 kV and a working distance of 15 mm. The cross-section of the specimens was prepared following the traditional metallographic preparation. The thickness of the PEO coatings was measured from the SEM cross-section images using ImageJ software.

2.4. Electrochemical Characterization

The physiological medium selected for the present work was a modified α-MEM solution containing only inorganic compounds: 6.8 g/L NaCl; 0.2 g/L $CaCl_2$; 0.098 g/L $MgSO_4$; 0.4 g/L KCl; 2.2 g/L $NaHCO_3$; and 0.122 g/L Na_2HPO_4 (diluted in deionized water). The pH was adjusted to 7.4 ÷ 7.6 using HCl. The electrochemical tests were carried out using a Gamry Interface 1010E Potentiostat/Galvanostat/ZRA (Gamry Instruments, Warminster, PA, USA) and an Ag/AgCl reference electrode and graphite as a counter electrode. A double-wall cell connected to a water thermostat was used to maintain the electrolyte temperature at ~37 °C during the experiments. Two specimens of each condition with a working area of ~2 cm^2 were tested to ensure the repeatability. The specimens were immersed in the medium and the open circuit potential (OCP) was continuously measured for 1 h. It was followed by potentiodynamic polarization tests (PDP) in the voltage range between −0.5 V and 3.5 V, with respect to the OCP, with a scan rate of 0.5 mV/s. The electrochemical tests were set up, controlled and recorded using the Gamry Instruments Framework software (Gamry Instruments, USA). The Gamry Echem Analyst and OriginPro 8 (version 8.1) were used to analyze and plot the OCP and PDP resulting curves. The corrosion potential and current densities were obtained from the Tafel extrapolation of the cathodic branch. The corrosion rates were calculated with the following formula:

$$CR\ (\mu m/year) = \frac{3.272 \cdot i \cdot MW_{Ti}}{Val_{Ti} \cdot d_{Ti}} \tag{1}$$

where MW_{Ti} stands for the molecular weight of *Ti* (47.87 g/mol), Val_{Ti} for the valence (4), d_{Ti} for the density of *Ti* (4.51 g/cm^3) and *i* for the corrosion current density in mA/cm^2. The polarization resistance values were obtained from the linear region of the polarization curves located within ±10 mV from the E_{corr}.

3. Results and Discussion

3.1. EB Modified Surface Topography and Microstructure

Figure 4a,b show the 3D topographic images and profile analysis of the micro-grooves (G; G1 hatch spacing 100 μm, G2 hatch spacing 200 μm) and the lined up unit cells of the bridge structures (B; B1 hatch spacing 100 μm, B2 hatch spacing 200 μm), respectively. Notice that the longitudinal, transversal and vertical directions were labelled (LD, TD and VD, respectively), the LD direction being the main direction of the structures: parallel to the micro-grooves in G1 and G2; and parallel to the central line of the bridges in B1 and B2. The TD profiles taken for the G1 and G2 specimens (Figure 4a) are shown in Figure 4c. It can be seen in both cases the 100 and 200 μm spacing between the micro-grooves in agreement with the design. A peak profile was found for the G1 specimen, while it had an asymmetric wave-like shape in the G2 specimen with a total height of almost half of that of the G1 profile. According to the literature [19–21], the main influence on the total height of the protrusion is the beam current, i.e., an increase in the beam current directly leads to an increase in the height of the protrusion, although the scan frequency also has an influence. While Tändl and Enzinger [21] observed that a decrease in the scan frequency leads to an increase in the height, Wang et al. [19] found that such a decrease does not necessarily lead to an increase in the height and that there is a more complex relationship to the formation of protrusions; i.e., if the parameter combination is chosen such that the liquid metal reaches a certain high temperature with a low viscosity, the interaction of the surface tension and vapor pressure no longer contributes much to the formation of the protrusions. This may be the case in the present study because, although the scan frequency was lower in G2 compared with G1, the local energy input (heat input) was twice as high. As a result of the greater heat input, the molten metal downstream of the beam remained at a relatively high temperature for an extended period of time, so that it did not have a sufficient amount of time to cool and had not effectively piled up. The protrusions were wider rather than taller as the increase in the heat input resulted in a wider single bead width, which is also consistent with the literature [20]. Additionally, the lateral dimensions of the single-bead lines in G2 were larger than the spacing between the subsequent lines, thus displacing the material from the previous lines, while the G1 strategy allowed for the accumulation of the material more effectively, despite the lower input energy (Figure 4c).

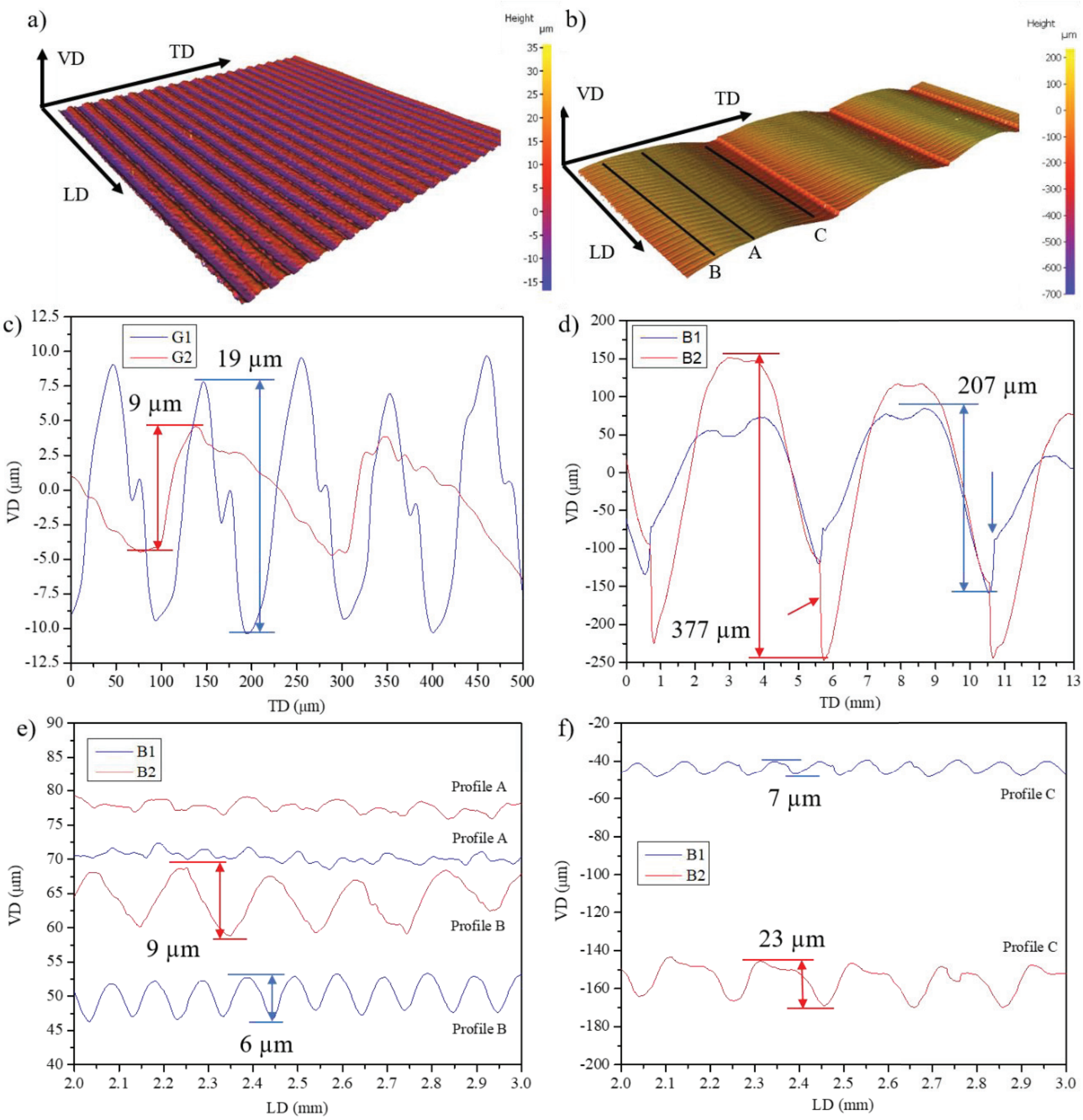

Figure 4. (**a**,**b**): 3D reconstruction of micro-canals and bridge structures. LD: longitudinal direction along the main direction of the structures. TD: transversal direction perpendicular to the main direction of the structures. VD: vertical direction. (**c**): TD profiles of G1 and G2 specimens. (**d**): TD profiles of B1 and B2 samples. (**e**): LD profiles A and B of B1 and B2 samples. (**f**): LD profiles C of B1 and B2 samples.

The surface descriptors obtained from the 3D optical metrology of the representative areas for each structure are presented in Table 2. The G1 structure produced a rougher surface than the G2 structure, with a larger S10z in correlation with the profiles shown in Figure 4. The effective area of the G1 specimen was increased by 14%, while one of the G2 surfaces was increased by only 2.2%. The S_{ku} parameter indicated the roundness of both surfaces ($S_{ku} < 3$). On the other hand, the S_{sk} parameter indicated that the G1 surface had an even distribution of the peaks and valleys (S_{sk} near 0) while the valleys dominated the G2 surface, related to shape ($S_{sk} < 0$). It could be concluded that the G1 surface structuring was optimal in terms of the line spacing and input energy to produce a regular micro-groove topography with evenly distributed rounded peaks and valleys.

Table 2. Surface descriptors of the bare EB structures obtained by 3D metrology. S_a: average surface roughness. S_q: square root average surface roughness. S_{10z}: ten-point average height. S_{sk}: skewness parameter. S_{ku}: kurtosis parameter. Areas analyzed: G1 and G2 4.2 mm^2. B1: (5.8 × 13) 75.4 mm^2. B2: (5.8 × 13) 86.54 mm^2. B1-B, B1-C, B2-B and B2-C stand for the profiles B and C specified in Figure 4b,e,f. *: R_{10z} values.

Specimen	Area Ratio (%)	S_a (μm)	S_q (μm)	S_{10z} (μm)	S_{sk}	S_{ku}
G1	14	5.7	6.43	18 ± 0.5	0.06	1.7
G2	2.2	2.3	3.46	10 ± 1	−0.3	1.9
B1	5.3	58	68	218 ± 17	−0.6	2.2
B2	9.6	99	116	353 ± 23	−0.5	2.2
B1-B	-	-	-	* 5.6 ± 0.5	-	-
B1-C	-	-	-	* 7.4 ± 0.8	-	-
B2-B	-	-	-	* 8.6 ± 1.4	-	-
B2-C	-	-	-	* 23 ± 1.8	-	-

Figure 4b shows the 3D topographic image of the B2 sample. The profile plots in Figure 4d correspond to the TD profiles of both the B1 and B2 specimens. The LD profiles for both B1 and B2 along the lines indicated as A and B in Figure 4d are shown in Figure 4e. The LD profiles along line C in Figure 4e for both B1 and B2 are shown in Figure 4f. It could be seen that both B1 and B2 consisted of a central structure, i.e., a bridge, with a total height of ~220 μm and ~350 μm, respectively. The bridges were spaced by ~5 mm in agreement with the design. It is worth noticing that the structures were not symmetrical in the TD, having a sharp valley at one end of each bridge (indicated with the arrows in Figure 4d). This was due to the overlap of the bridges, i.e., a consecutive bridge removed the material from the previous one. It indicates that a further bridge width and spacing optimization would be necessary.

The LD profiles (Figure 4e,f) revealed that micro-grooves in the TD were formed while maintaining the 100 and 200 μm spacing distances. These were more regular at the sides of the bridges (the B and C profiles) than at the top (the A profiles), where the surface was irregular. It was also observed that their total height increased towards the edges of the bridge (Table 2).

The roughness parameters of the B1 and B2 samples in Table 2 correspond primarily to the bridge structures. There was an increase in the area ratio, S_a, S_q and S_{10z} in the B2 specimen with respect to the B1 sample due to the larger amount of material which accumulated at the top part of the bridge because of the higher input energy (Table 1, Figure 4).

Considering the profiles shown in 4c (grooves) and 4e (bridge–position B), a similar height of the grooves for G2 (scan speed 500 mm/s and energy input 480 J/m), B1 (scan speed 500 mm/s, energy input 480 J/m) and B2 (scan speed 250 mm/s, energy input 960 J/m) can be observed. This confirms previous indications which showed that with a higher energy/heat input, the height of the grooves cannot be further increased. This is unlike the low heat input G1 (scan speed 1000 mm/s, energy input 240 J/m), which has a groove height twice as large. In addition to the formation of the microgrooves, there is also a macroscopic displacement of material: (1) for the grooves from one side to the other (Figure 2c), since the deflection of the beam is unidirectional, and (2) for the bridge in the center (Figure 3d), since the beam travels alternately. The amount of locally melted material can be related to the heat input, i.e., the higher the energy input, the more material which is melted and macroscopically displaced. This is of particular interest for the bridge structure, since the alternating beam travel causes the material in the centerline to be piled up from both sides. Consequently, for the higher energy input B2, a more pronounced macroscopic material displacement can be observed in the center (Figure 4d).

Figure 5 shows the SEM images of the bare EB specimens and cross-sections. Figure 5a,b shows the surface and cross-section of the M sample where a typical α' martensitic microstructure was found within the prior β grains due to the rapid solidification that contrasts, with respect to the initial equiaxed α + β microstructure of the Ti6Al4V alloy (Figure 5c). The relief formed at the surface by the grain boundaries and α′ needles was due to the solidification in a vacuum, as described by Ferraris et al. [12]. Figure 5d,g,j,m demonstrates that the EB structuring was successful in producing reproducible micro-grooves with the hatch distance being set by the design in each case. These figures also shown that while the micro-grooves in G1 and G2 had a linear shape, these were curved in the B1 and B2 due to the different deflection and velocity of the beam. Images 5e, h, k and n show that the relief on the surface observed in image 5a was also replicated in the structured samples. Similarly, the α′ martensitic microstructure was seen in the cross-section of these samples (Figure 5f,i,l,o).

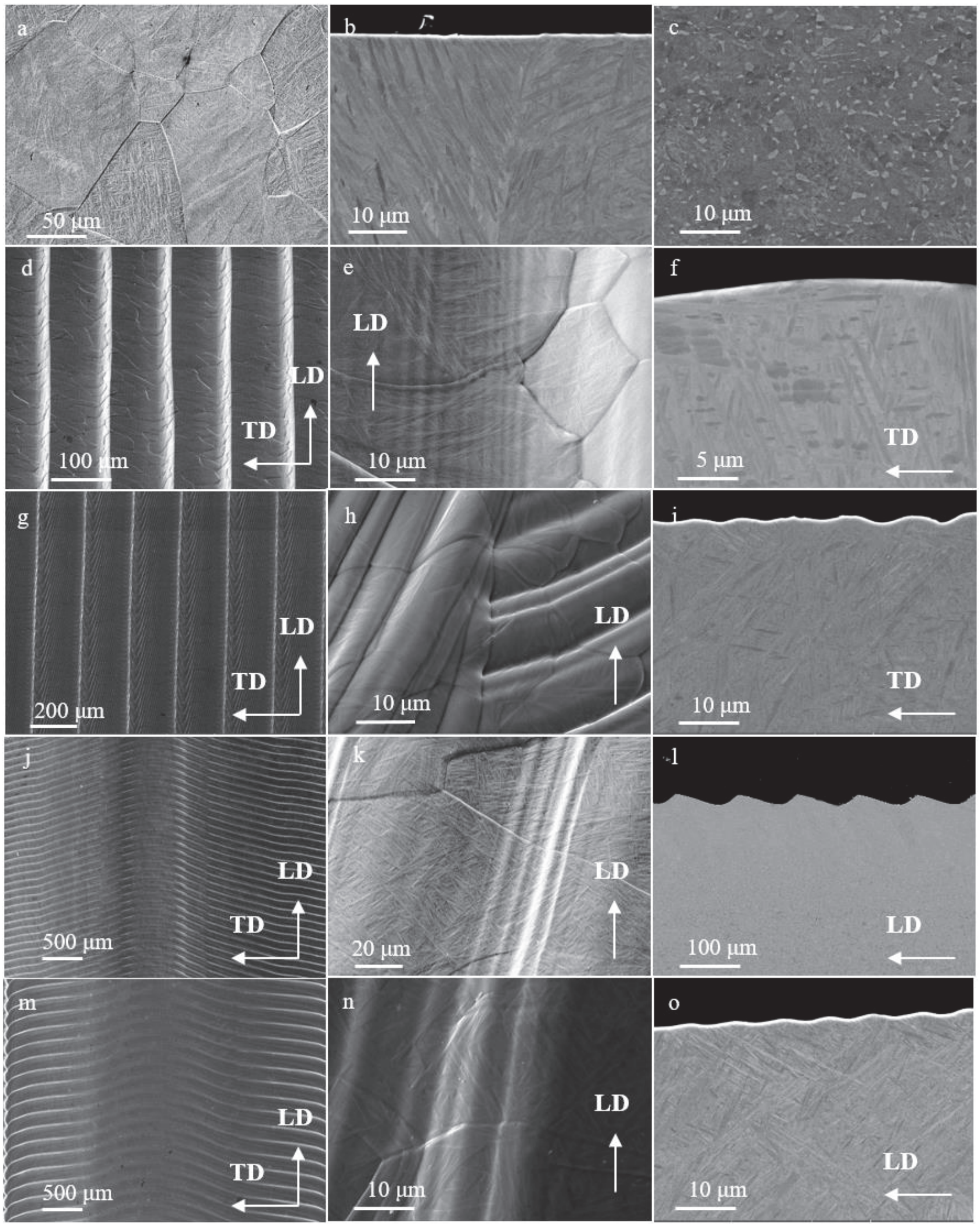

Figure 5. Surface and cross-section SEM images of the bare EB structures: (**a**–**c**), M; (**d**–**f**), G1; (**g**–**i**), G2; (**j**–**l**), B1; and (**m**–**o**), B2. (**d**,**g**,**j**,**m**) correspond to an overview of the structures. (**e**,**h**,**k**,**n**) correspond to detail images of the EB surfaces. (**f**,**i**) TD cross-section of G1 and G2. (**l**,**o**) LD cross-section of B1 and B2 showing the cross-section of the micro-grooves.

3.2. Flash-PEO Coatings Fabrication

Figure 6 presents the RMS current density and voltage (i_{RMS} and V_{RMS}, respectively) during the 45 s PEO treatment for all of the specimens. The initial stage of the process (<15 s) consists of the growth of a TiO_2 anodic film on the surface of the samples at a near-constant i_{RMS} (~50 mA·cm^{-2}) while the V_{RMS} increases at a constant ratio. Beyond 15 s of the process, the i_{RMS} increases rapidly up to 300 mA·cm^{-2} (maximum limit set). The first visible sparks accompanied the current rise on the surface of the specimens. The current surge's initiation was the only significant difference between the molten material and the structured samples. The i_{RMS} of the G1 specimen followed a nearly identical trend to the M sample. The current rising was delayed by ~3 s for the G2 and B1 specimens and around 5 s for the B2 surface, showing a slower rise. Nevertheless, the current density reached the maximum in all of the samples for the same treatment time, and the process continued without any other difference.

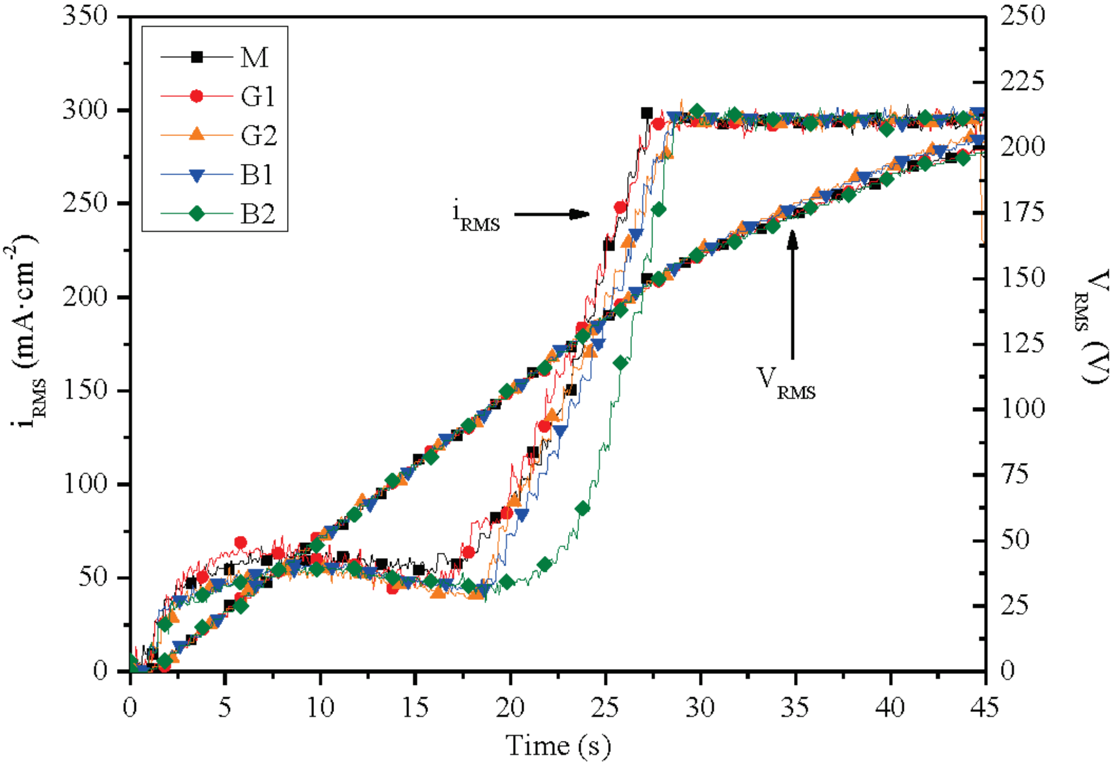

Figure 6. Evolution of the RMS current density and voltage (i_{RMS} and V_{RMS}, respectively) during the PEO treatments.

3.3. Microstructural Characterization of Flash-PEO Coatings

3.3.1. Flash-PEO Coatings on Flat Molten Surface

The PEO-treated molten material (herein M-PEO) showed the characteristic of a rough and porous surface of this type of Ca- and P-containing PEO coatings (Figure 7a) and a thickness of 3.2 ± 0.8 µm [22,23]. The image analysis carried out on 3 areas (10,000 µm^2 each) of the surface revealed that the M-PEO coating had a mean pore size of ~0.6 µm and a surface porosity of about 5% (Table 3). The cross-section of the coating (Figure 7b) presented a sub-micrometer inner nanoporous layer in intimate contact with the substrate (black arrow in Figure 7b) and a compact outer layer that accounted for most of the coating thickness. The porosity within the film was also found to be consisting of micro-cavities and trapped gas bubbles (white arrows in Figure 7b).

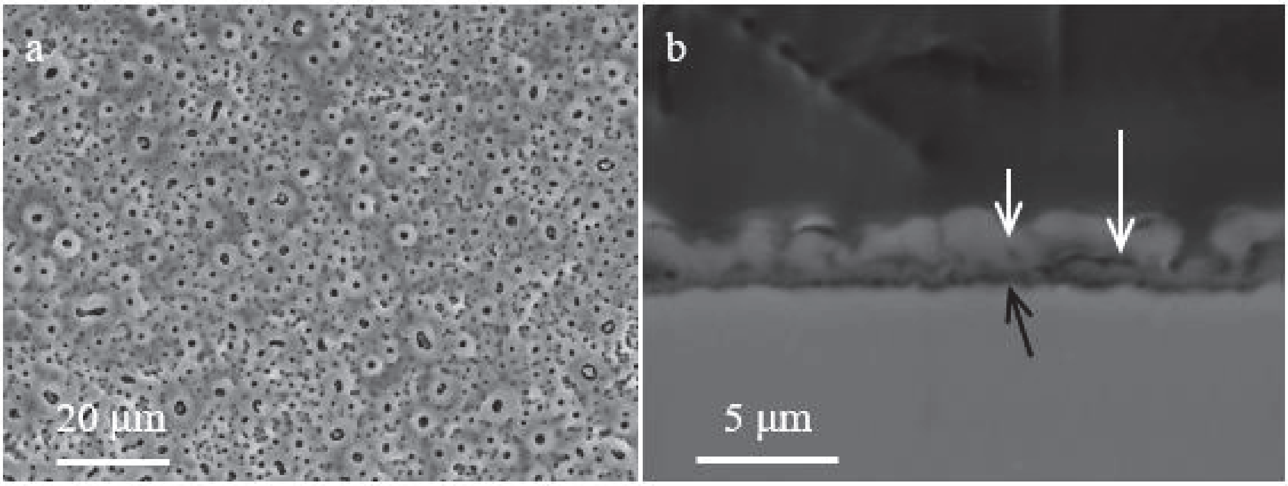

Figure 7. (**a**,**b**): SEM of the M-PEO specimen surface and cross-section, respectively. White and black arrows indicate porosity remarks discussed in the text.

Table 3. Porosity values obtained by image analysis for the flash-PEO coatings on the EB-structured samples. * G1-PEO-R1 and 2013R2 correspond to image analysis in regions marked in Figure 9a.

Specimen	Population/1000 µm^2	Mean Size (µm)	Max Size (µm)	Porosity (%)
M-PEO	148 ± 26	0.64 ± 0.42	4.0	5
G1-PEO	238 ± 13	0.63 ± 0.41	4.6	6
G1-PEO-R1 *	239	0.67 ± 0.43	4.1	6
G1-PEO-R2 *	250	0.75 ± 0.53	5.1	7
G2-PEO	168 ± 23	0.74 ± 0.50	5.0	5

A compositional analysis of the surface (Table 4) revealed the main presence of O and Ti corresponding to the formation of TiO_2. The substrate elements Al and V were also found in a small amount (<2 at.%), indicating their incorporation in the coating. The incorporation of the electrolyte-derived elements P and Ca was also confirmed, P being predominant over Ca and with a Ca to P atomic ratio of 0.7.

Table 4. Energy dispersive X-ray spectroscopy (EDS) of PEO-treated specimens. Values given in at.%.

Specimen	O	Na	Al	P	Ca	Ti	V	Ca/P
M-PEO	64.3	0.6	1.7	7.6	5.5	19.6	0.6	0.7
G1-PEO	67.0	0.4	1.5	6.8	5.3	18.3	0.7	0.8
G2-PEO	65.8	0.7	1.8	7.5	5.7	17.8	0.7	0.8
B1-PEO	66.3	0.5	1.7	7.1	5.5	18.3	0.6	0.8
B2-PEO	68.1	0.6	2.4	6.7	5.2	16.5	0.6	0.8

3.3.2. Flash-PEO of EB Surface Structures

The TD profiles obtained from the 3D topographic images of the G1-PEO and G2-PEO specimens are shown in Figure 8. It was found that the periodicity, shape and vertical and lateral sizes of the micro-grooves (Figure 4c) were not altered during the flash-PEO treatment. The surface descriptors presented in Table 5 were similar to those of the bare structured samples (Table 2). These results indicated that the flash-PEO coatings did not modify the EB structures which were produced.

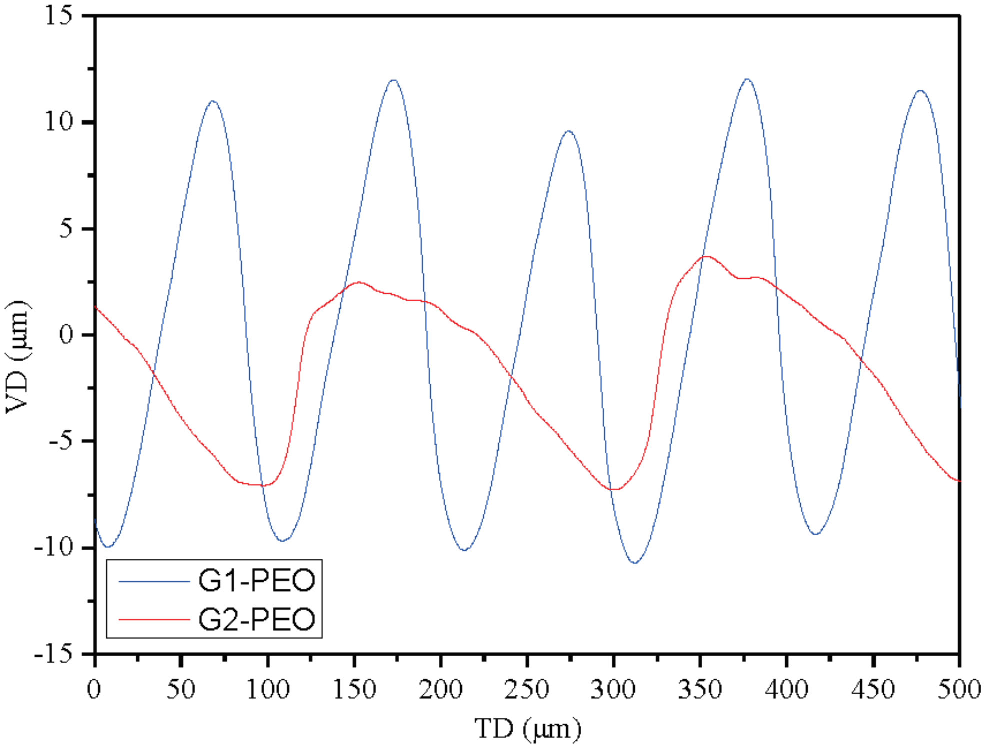

Figure 8. TD profiles of G1-PEO and G2-PEO specimens.

Table 5. Surface descriptors of the flash-PEO-treated specimens obtained via 3D metrology. S_a: average surface roughness. S_q: square root average surface roughness. S10z: ten-point average height. S_{sk}: skewness parameter. S_{ku}: kurtosis parameter.

Specimen	Area Ratio (%)	S_a (µm)	S_q (µm)	S_{10z} (µm)	S_{sk}	S_{ku}
G1-PEO	11	6.8	7.6	25 ± 0.5	0.1	1.6
G2-PEO	1.2	3.2	3.7	15 ± 1.0	−0.4	1.9
B1-PEO	2.6	66	74	204 ± 14	−0.7	2.2
B2-PEO	9.7	107	123	347 ± 21	−0.4	2.0

Flash-PEO Coatings on the Micro-Grooves Structures

The SEM images of the G1-PEO and G2-PEO coatings are shown in Figure 9. Figure 9a,c were taken over the top part of the micro-canals, which was seen as a brighter line in the image. The adjacent areas descended to the valleys of the beam figure (regions R1 and R2). Both the G1-PEO and G-PEO samples presented a comparable surface morphology to the one of the M-PEO (Figure 9b,d). Nevertheless, the surface of the G1-PEO coating seemed to have a larger number of fine pores at the bottom of the micro-canals. The image analysis carried out on the G2-PEO coating (Figure 9d) revealed porosity values similar to those of the M-PEO coating (Table 3). The image analysis of the G1-PEO was carried out over the side surfaces and (Figure 9b) valleys (regions R1 and R2 in Figure 9a). These three analyses revealed that the mean and maximum pore sizes were close to the M-PEO coating, but there were a higher pore population and a slightly higher porosity (Table 3).

The EDS area measurements (Table 4) of the G1-PEO and G2-PEO specimens show the Ca and P contents in agreement with those of the M-PEO coating. Figure 10 presents the cross-section of the G1-PEO and G2-PEO specimens, which revealed a similar morphology and thickness (Table 6) to the M-PEO coating.

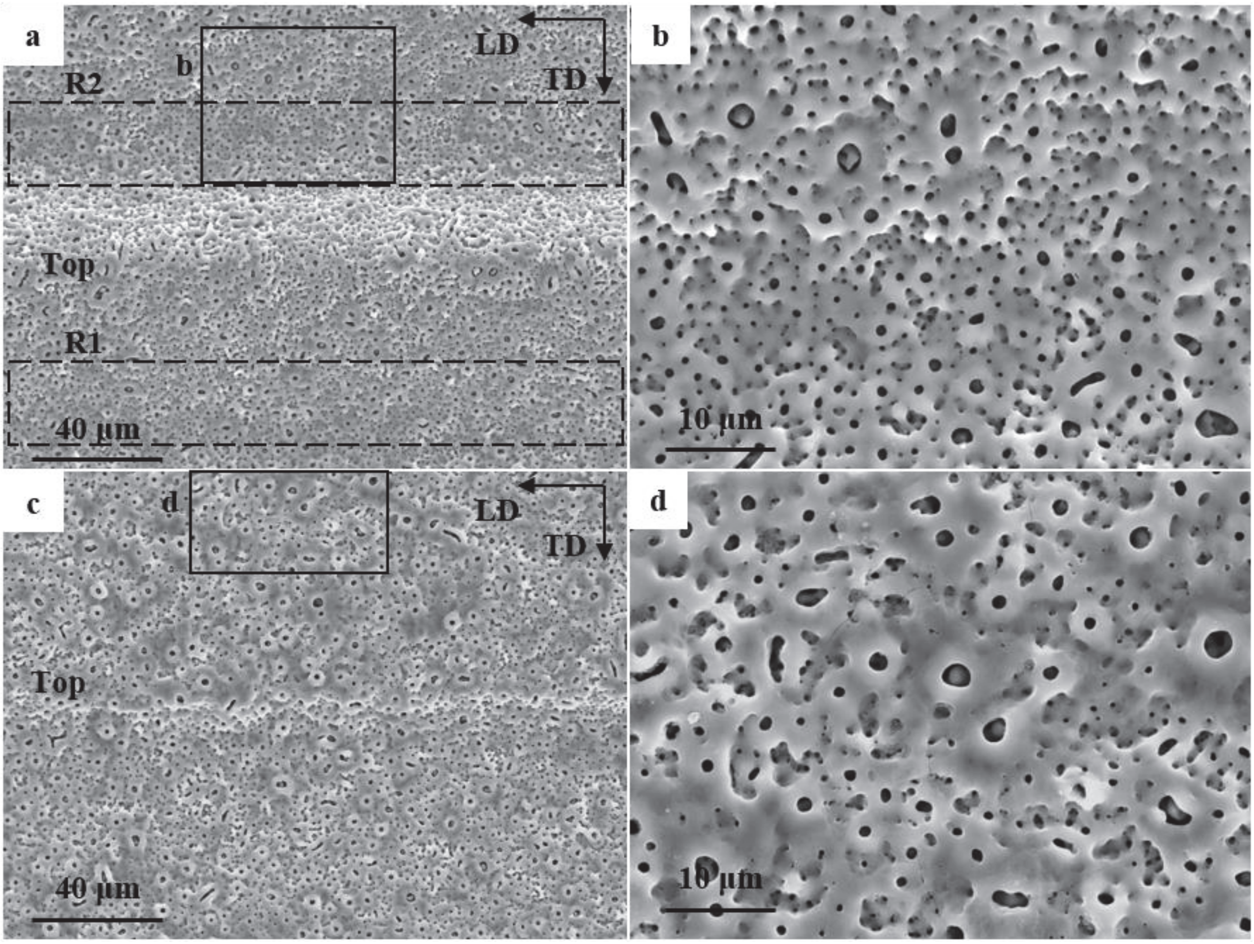

Figure 9. SEM surface of G1-PEO (**a**,**b**) and G2-PEO (**c**,**d**) samples. Dashed regions R1 and R2 in image a mark the regions analyzed for porosity in Table 3.

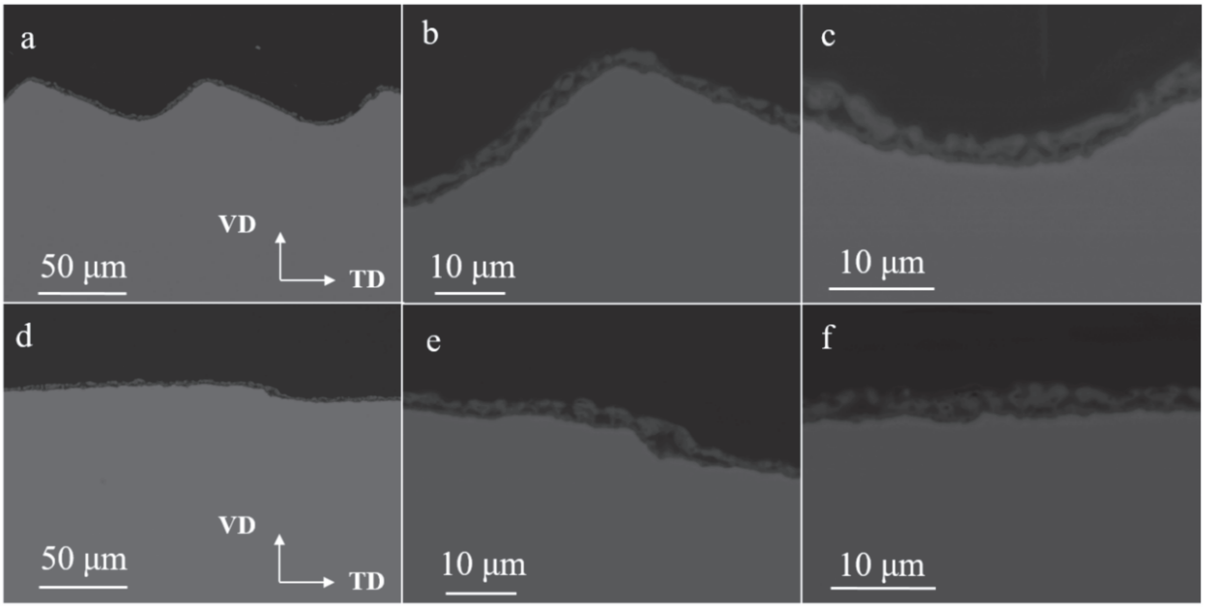

Figure 10. Cross-section SEM of G1-PEO (**a**–**c**) and G2-PEO (**d**–**f**) coatings. Notice that cross-sections corresponded to the VD-TD plane across the micro-grooves.

Table 6. Thickness measurements of the flash-PEO coatings on the EB-structured samples. Values obtained from cross-section images in Figure 7, Figure 10 and Figure 12, respectively.

Specimens	Location	Thickness (μm)
M-PEO	-	3.2 ± 0.8
G1-PEO	-	2.9 ± 0.6
	Top—Figure 10b	2.7 ± 0.4
	Bottom—Figure 10c	3.1 ± 0.8
G2-PEO	-	2.8 ± 0.8
B1-PEO–TD	Overlap—Figure 12a	3.2 ± 0.6
B1-PEO–LD	Profile B—Figure 12c	3.5 ± 0.9
B2-PEO–TD	Overlap—Figure 12a	3.3 ± 0.6
	Overlap—Figure 12a	2.3 ± 0.6
	Overlap—Figure 12a	4.5 ± 0.9
B2-PEO–LD	Profile B—Figure 12f	3.1 ± 0.7

To summarize, the most remarkable finding was the greater pore population of the G1-PEO. The agreement in pore size, thickness and composition between the three samples indicated a similar PEO growth rate. Henceforth, it is suggested that the higher pore density in G1-PEO was related to a greater heat diffusion during the PEO, steaming from a larger surface area, promoting a faster solidification of molten oxide and preventing finer pores from clogging [24]. On the other hand, a lower heat diffusion allowed for the flow of molten oxide in M-PEO and G2-PEO, producing a smoother surface near the larger pores.

Flash-PEO Coatings on the Bridge Structures

Figure 11 shows the SEM images of the B1-PEO (a–d) and B2-PEO (e–h) specimens. Figure 11a,b,e,f were taken where the bridges overlap. Figure 11c,g shows the top part of the bridges (profile A in Figure 4b), while d and h correspond to the areas over the micro-canals formed on these structures (approximately profile B in Figure 4b). It could be seen that the coating grew over the sharp edges and perpendicular surfaces of both structures without any apparent discontinuities, and it maintained the morphology observed for the rest of the samples (Figure 11a,b,e,f). The coating formed at the top part of the structures and over the micro-canals also showed the same morphology and no defects whatsoever. The EDS area measurements of these samples (Table 4) were taken over the bridge overlaps since it was expected that any deviations from the M-PEO were most likely to appear in this region. Nevertheless, no changes in composition were observed.

Figure 12 present the cross-section of the B1-PEO (a–c) and B2-PEO (d–f). Figure 12a,b,d,e corresponds to the cross-sections in the VD-TD plane at the bridges overlap. Figure 12c,f corresponds to the cross-sections in the VD-LD plane along Profile B, indicated in Figure 4, approximately. In general, the cross-section morphology of these samples was similar to that of the PEO on the molten surface. The thickness measurements revealed no significant difference with respect to the M-PEO specimen (Table 6), except at the overlap area in the B2-PEO specimen (Figure 12d,e). It is evident that the coating at the bottom of the overlap area (Figure 12e) was noticeably thinner than the coating at the adjacent region: 2.3 μm and 3.3 μm, respectively. Additionally, at the top part of the overlap, the coating thickened significantly (4.5 μm).

This suggested a lower growth rate at the bottom part of the bridge overlap, which could be linked to the delay in the current density surge of the B2-PEO specimen, as observed in Figure 6. It is believed that a lower current density passed through this region due to a poor orientation, with respect to the cathode. It may be also considered that the gas bubbles arising from the process were not easily detached, further shielding the region.

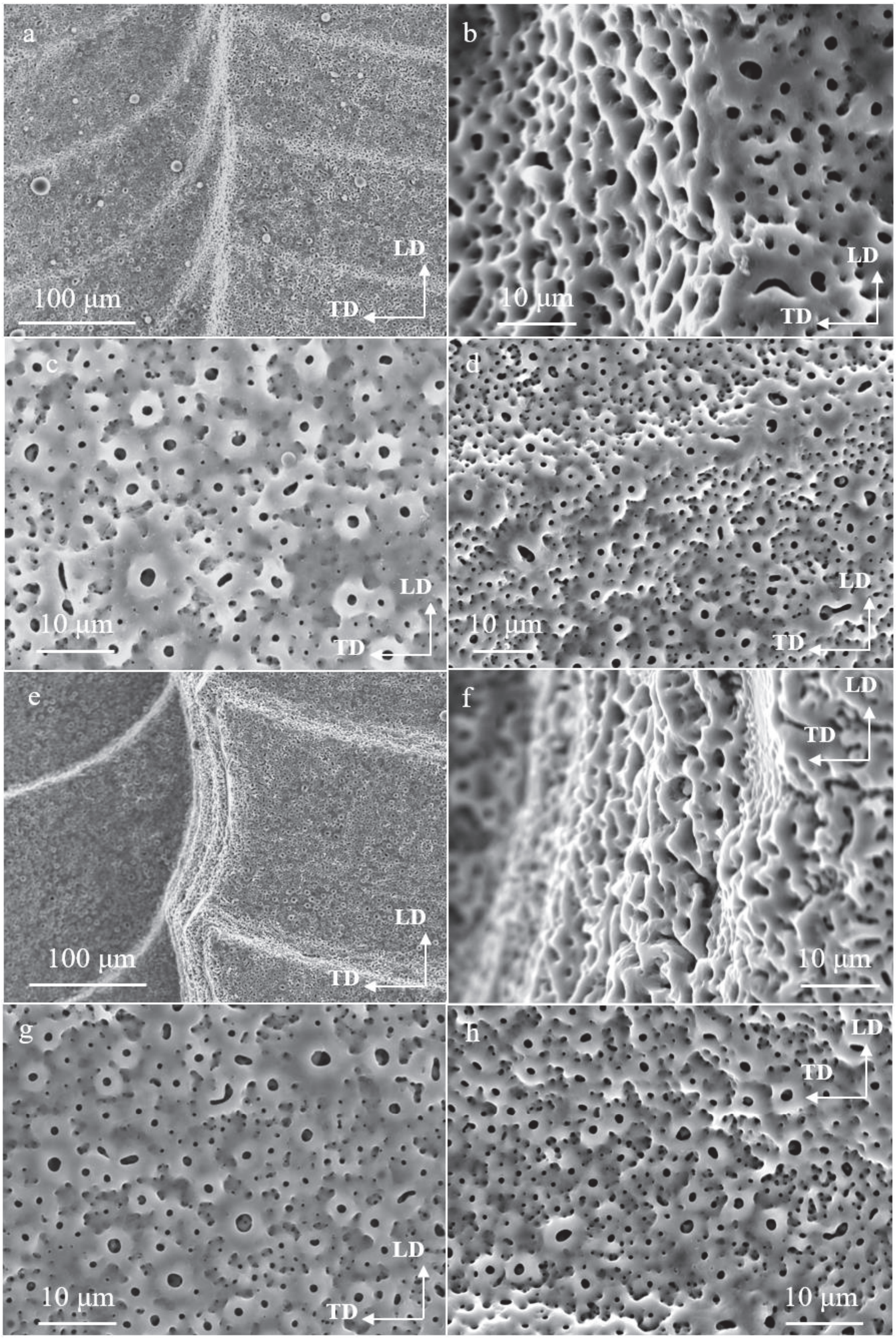

Figure 11. SEM of B1-PEO (**a**–**d**) and B2-PEO (**e**–**h**) specimens: (**a**,**b**,**e**,**f**) were taken at the overlapping area; (**c**,**g**) at the top part of the bridges; and (**d**,**h**) at over micro-canals formed.

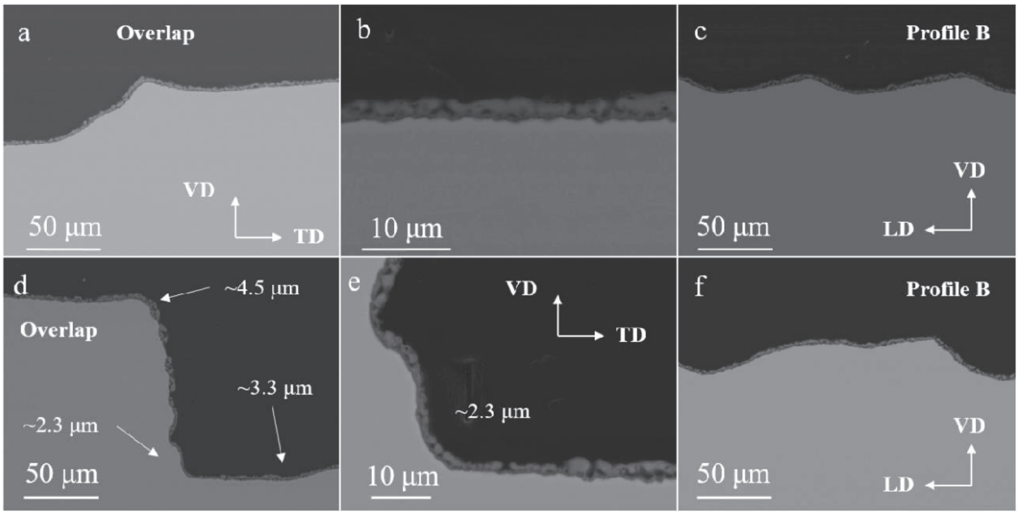

Figure 12. Cross-section SEM of B1-PEO (**a**–**c**) and B2-PEO (**d**–**f**) coatings. Images (**a**,**b**,**d**,**e**) correspond to the VD-TD plane (across the bridge macrostructure) at the bridge overlap region. Images (**c**,**f**) correspond to the VD-LD plane across the micro-grooves of the macrostructures along the profile B (marked in Figure 4) approximately.

The PEO coatings at the micro-canals on the outer part of the bridge structures (Figure 12c,f, approximately the B profiles) were also similar in thickness to the coatings on the G1 and G2 structures and the molten surface, indicating that these surfaces did not produce a significant loss of efficiency during the process. Henceforth, these results suggested that beyond a 50 µm depth, careful consideration should be taken during the design of EB surface structures to avoid the electrical occlusion of the material.

3.4. Electrochemical Response

Figure 13 presents the OCP evolution during 1 h of immersion time before the potentiodynamic polarization of the non-treated and PEO-treated specimens. The non-treated samples had negative OCP values, while the PEO-treated samples showed higher values. Among the non-treated specimens, the EB-structured surfaces presented more negative OCPs.

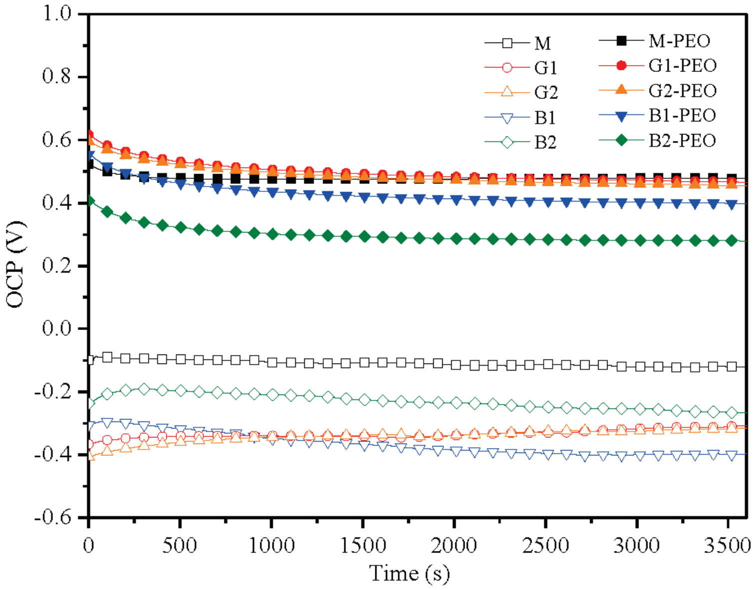

Figure 13. Evolution of the open circuit potential (OCP) over 1 h of immersion in modified α-MEM solution.

Figure 14 presents the polarization curves of the non-treated and PEO-treated specimens. The corrosion potentials and current densities (E_{corr} and i_{corr}, respectively, obtained by Tafel extrapolation) as well as the initial potentials and currents of the passive segments (E_{pass} and i_{pass}) are given in Table 7. The non-treated specimens showed a negative E_{corr} close to those shown during the OCP measurements, making the M specimen the noblest. The i_{corr} was one order of magnitude higher in the structured samples, with respect to the molten surface. In turn, the corrosion rates of the bare structured specimens were found to be one order of magnitude higher (1.1–3.4 µm/year), with respect to the molten surface (0.1 µm/year). At the same time, the polarization resistance decreased one order of magnitude for the groove and bridge structures. I_{corr} and CR were greater and the R_p was lower for the bare bridge structures than for the groove structures, indicating a correlation with larger surface features. These effects may be assigned to defects within the natural passive oxide layer. It may be assumed that this layer was homogeneous and compact on the flat molten surface while it became more defective due to tensile stresses at the top of the convex features, such as peaks in the grooves' specimens and the top and the sharp edges of the bridge structures. Nevertheless, it is worth recalling that all the specimens presented a passive behavior.

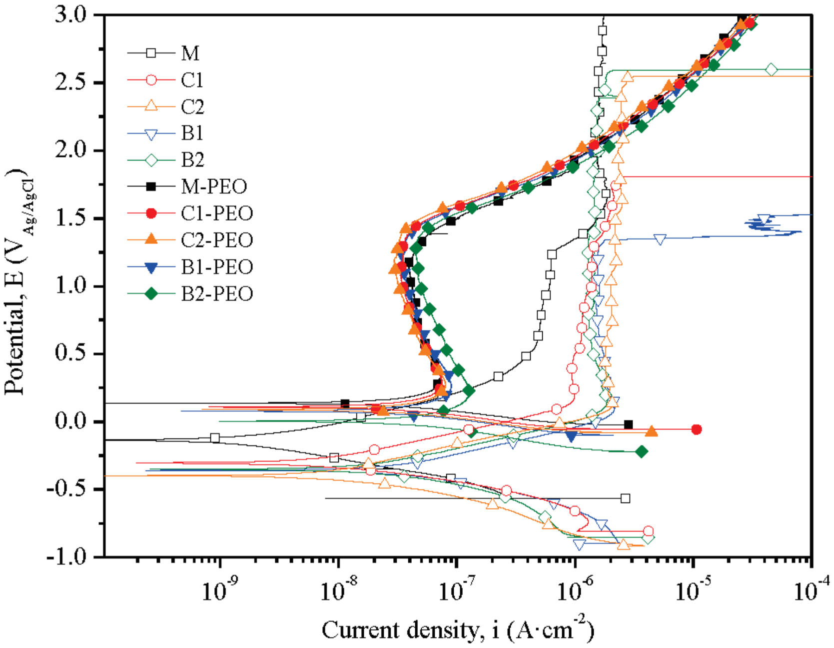

Figure 14. Potential vs. current density (E and i, respectively) during potentiodynamic polarization experiments of bare and PEO-treated samples in modified α-MEM solution.

Table 7. Electrochemical parameters of non-treated and PEO-treated specimens. CR stands for corrosion rate and Rp for polarization resistance. * i_{pass} values correspond to the density current at E_{pass}.

Specimen	OCP (V)	E_{corr} (V)	i_{corr} ($A \cdot cm^{-2}$)	CR (µm/year)	Rp ($\Omega \cdot cm^2$)	E_{pass} (V)	i_{pass} ($A \cdot cm^{-2}$) *	E_O (V)
M	−0.12	−0.13	1.34×10^{-9}	0.1	4.69×10^{7}	0.60	4.81×10^{-7}	>3
G1	−0.31	−0.30	1.23×10^{-8}	1.1	4.95×10^{6}	0.18	1.06×10^{-6}	-
G2	−0.32	−0.40	1.29×10^{-8}	1.1	5.39×10^{6}	0.13	2.05×10^{-6}	-
B1	−0.4	−0.36	3.88×10^{-8}	3.4	2.13×10^{6}	0.09	2.16×10^{-6}	-
B2	−0.27	−0.35	2.57×10^{-8}	2.2	3.05×10^{6}	0.14	1.85×10^{-6}	-
M-PEO	0.48	0.13	3.18×10^{-8}	2.8	1.37×10^{6}	0.25	8.83×10^{-8}	1.31
G1-PEO	0.47	0.11	2.48×10^{-8}	2.2	1.75×10^{6}	0.25	8.83×10^{-8}	1.31
G2-PEO	0.46	0.09	2.46×10^{-8}	2.1	2.16×10^{6}	0.25	8.83×10^{-8}	1.31
B1-PEO	0.4	0.08	3.02×10^{-8}	2.6	1.87×10^{6}	0.25	8.83×10^{-8}	1.31
B2-PEO	0.28	0.003	4.25×10^{-8}	3.7	1.53×10^{6}	0.25	1.5×10^{-7}	1.31

The molten surface presented a passive region at 4.81 × 10^{-7} A·cm^{-2} above 0.6 V. A second passivation region beyond 1.3 V at about 1.5 × 10^{-6} A·cm^{-2} was observed, which extended above 3 V. The bare structured specimens had similar passivation regions (1 ÷ 2 × 10^{-6} A·cm^{-2}) above ~0.1 V. All the EB-structured samples presented a sudden increase in current density beyond 10^{-5} A·cm^{-2}, which was related to localized crevice corrosion, as demonstrated by the post-mortem analysis of the tested samples.

The 3D optical topographic images of the micro-canal specimens presented in Figure 15 show that the initiation of the localized crevice corrosion started under the resin mask and spread laterally underneath it, reaching the nearby canals and advancing along the micro-canals (Figure 15a, image taken on a sample right after the initiation of the current density increase). For longer immersion times, the corrosion region spread laterally to several micro-canals at the initiation point and at the exposed surface near the resin (Figure 15b). At the same time, the corrosion advanced further along the micro-canals (Figure 15c). In the case of the bridge structures (Figure 16), crevice corrosion initiated at the overlapping areas beneath the resin. In this case, the corrosion spread laterally towards the outer parts of the bridge only at the initiation point (Figure 16a), while within the exposed area of the surface, the corrosion advanced exclusively along the overlapping area (Figure 16b). The formation of a loosely adherent light-brown gel on the surface accompanied the crevice corrosion.

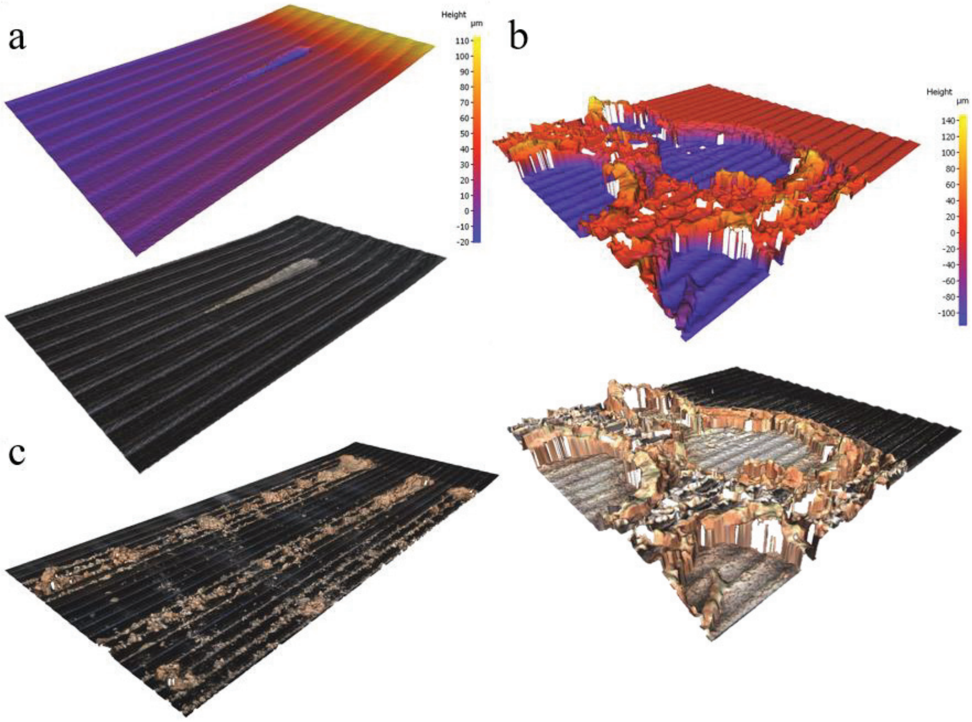

Figure 15. Representative 3D reconstructions of localized crevice corrosion on samples G2 (**a**,**c**) and G1 (**b**). Image (**a**) shows the initiation of crevice corrosion on sample G2. Image (**b**) shows the corrosion pits at the initiation point of corrosion at the end of the test of sample G1. Image (**c**) corresponds to the whole area of G2 samples after the completion of the PDP tests.

The crevice corrosion takes place within the restricted volumes where oxidizing species, such as dissolved O_2, are consumed faster than what is replenished from the bulk solution, preventing the formation of new oxide. This situation also involves low pH levels with the hydrolysis of titanium chlorides that form hydrochloric acid and Ti hydroxides ($Ti(OH)_x^{(4-x)}$), among other products [25–27], and the generation of an electrochemical microcell between the crevice becomes the anode and the outer exposed surface becomes the cathode.

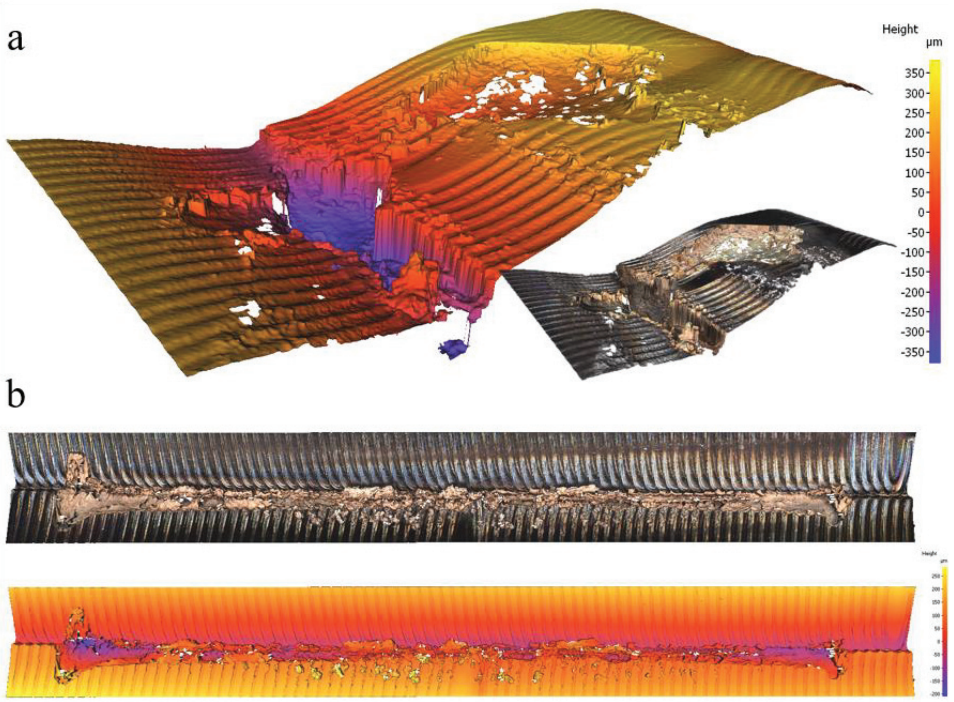

Figure 16. Representative 3D reconstructions of localized crevice corrosion on sample B2 after the PDP test: (**a**) initiation point; and (**b**) whole surface.

Such a localized corrosion has been reported previously in the literature which dealt with the electrochemical behavior of the DMLS Ti6Al4V pins, where the crevice corrosion appeared at the superficial porosity and imperfections [25]. The Ti6Al4V alloys manufactured by laser-based powder bed fusion are characterized by an α'/α martensitic microstructure similar to the one formed in EB structures. Additionally, the formation of a light-brown gel was also reported and assigned to $TiO_2 \cdot H_2O$ and $TiO_3 \cdot H_2O$, which presents a higher solubility and a worse adherence than TiO_2. The remnants of these oxides were observed to be adhered to the specimens shown in Figures 15 and 16. It might be hypothesized that such products and oxides formed within the crevice extended outside the crevice and along the micro-canals and overlapping area, occluding these valleys and leading to under deposit corrosion.

Additional PDP tests were carried out on M specimens at the pH values of 7.5, 3.6 and 2 (Figure 17). Localized corrosion, or any other type of corrosion whatsoever, was not observed in these specimens. This indicates that the consumption of the oxidizing species (i.e., dissolved O_2) within the restricted volume played a more dominant role in the localized crevice corrosion of EB-treated specimens than low pH levels.

Finally, a crevice appeared between 1 and 2 V for the G1 and B1 specimens and between 2.5 and 3 V for the G2 and B2 samples, indicating a correlation between the crevice potential and the hatch spacing. It is believed that is related to a greater number of possible crevice locations in G1 and B1, hence increasing the chances for localized corrosion.

All the PEO-treated specimens presented an identical electrochemical behavior with positive E_{corr} (~0.1 V) values, slightly lower than those of the OCP recorded. This shift is commonly observed for titanium and is related to the charging process of the electrode/solution interface capacitance. Despite the relatively slow scan rate used in this study (0.5 mV/s), which is a well-known strategy for minimizing this artefact [28], PEO-treated specimens, unlike bare substrates, showed a sufficiently high charging current to shift the E_{corr} to significantly lower values than the OCP. The icorr values were found in the range between 2.5 and 4.5 × 10^{-8} A·cm^{-2}, which are in agreement with the values reported for the PEO coatings on the AM Ti6A4V alloys in the biological media [29]. The i_{corr} of the PEO-treated specimens was one order of magnitude higher than that of the bare molten surface and of the same order in comparison to the groove and bridge structures. This can be assigned to the microstructure of the inner barrier-like layer of the PEO coatings that is in intimate contact with the substrate. Such a layer is known to contain nano-pores that might explain the higher icorr and CR and lower Rp with respect to the molten surface. Nevertheless, these specimens presented a strong passive behavior and passive current densities lower than those of the un-treated specimens. All the samples reached a passive region at about 0.25 V (E_{pass}) and a passive current (i_{pass}) of ~8.83 × 10^{-8} A·cm^{-2}. Up to 1.3 V, the current density decreased to 3.18 × 10^{-8} A·cm^{-2}. Finally, the current density of the PEO-treated specimens increased rapidly beyond 1.5 V due to the oxygen evolution.

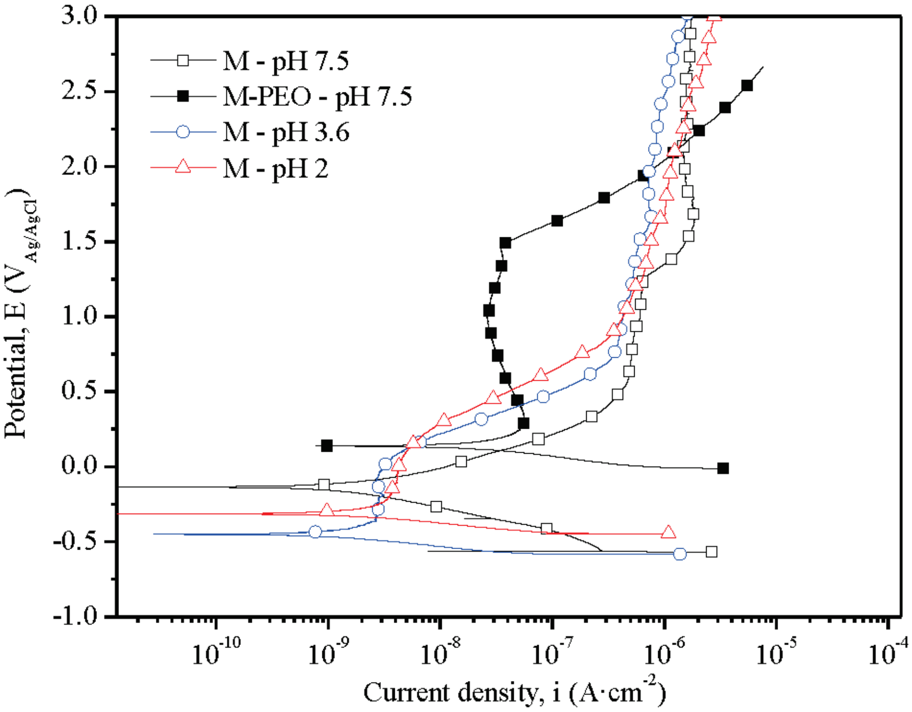

Figure 17. Potential vs. current density (E and i, respectively) during potentiodynamic polarization experiments of bare molten surface at pH 7.5, 3.6 and 2. PDP curve of M-PEO at pH 7.5 is also given for comparison.

As a concluding remark, unlike the untreated structured surfaces, the PEO-treated samples did not reveal any sign of crevice corrosion. It would therefore be recommended that EB-structured Ti surfaces were treated via PEO to avoid this issue while enhancing the osteoconductivity of the surface.

4. Conclusions

The PEO treatment of EB surface structures was carried out successfully with only minimal differences at the onset of sparking. The coating morphology, thickness, composition and electrochemical properties were identical for all of the coatings. At the same time the EB structures were unchanged by the PEO process. The following remarks were drawn as the conclusions from this study:

+ The coating could reproduce the topography carried out with the EB process. The submicrometer topographical features were only affected by the flash process.
+ The PEO coatings provided a surface with a sub-micrometric roughness and a maximum thickness of ~3 μm, containing biocompatible elements in the composition (Ca/P atomic ratio of 0.8). The pore density was estimated to contain about 150 ÷ 240 pores/1000 μm^2 and with a pore mean size of ~0.7 μm.
+ For the groove structures, a higher pore density of the fine pores was found at the bottom of the valleys in the G1 EB structure which was assigned to a higher cooling

rate of the topography, leading to a faster solidification of the molten oxide, preventing the clogging of the pores.

+ For the bridge structures, structures with a hatch-spacing of 200 μm (B2) lead to a slightly less efficient process, delaying the onset of sparking by about 5 s. The only morphological difference was found at the bottom of the overlapping areas where the coating was thinner.
+ The topography of the PEO-coating did not incur in any significant differences in the electrochemical behavior, showing a passive behavior with passive current densities at approximately 9×10^{-8} A/cm^{-2}.
+ The PEO-coatings prevented, effectively, the crevice corrosion in the structured surfaces. In future, it is recommended that titanium implants in contact with other surfaces or with a designed topography are subjected to PEO treatments to prevent a localized crevice corrosion.
+ From the point of view of the EB structuring design and fabrication, the results on this work showed that deep topographies might hinder the PEO efficiency and growth, compromising the functionality and electrochemical performance of the coating.

The combination of both techniques may be of great interest for orthodontic and orthopedic applications. For that, further investigations may need to address, to improve the functionalization of the surface, (a) the bonding strength between the PEO-treated EB surface structures and the bone, (b) a higher Ca/P ratio closer to the hydroxyapatite keeping the topography of the substrate and (c) the application of PEO treatments to finer EB structures.

Author Contributions: Conceptualization, H.M.-S., F.P., R.B., E.M. and F.W.; methodology, H.M.-S., F.P., R.B., E.M. and F.W.; formal analysis, H.M.-S., F.P., E.M. and F.W.; investigation, H.M.-S., F.P., R.B., E.M. and F.W.; resources, H.M.-S., F.P., R.B., E.M. and F.W.; writing—original draft preparation, H.M.-S., F.P. and R.B.; writing—review and editing, R.A., M.M., E.M. and F.W.; supervision, E.M. and F.W.; funding acquisition, H.M.-S., M.M., E.M. and F.W. All authors have read and agreed to the published version of the manuscript.

Funding: The authors gratefully acknowledge the support of PID2021-124341OB-C22 (MICINN/AEI/FEDER, UE) and ADITIMAT-CM (S2018/NMT-4411, the Regional Government of Madrid and EU Structural Funds). M.M. is grateful for the support of RYC-2017-21843. H.M.-S. is grateful for the support of PEJD-2019-POST/IND-16119 (the Regional Government of Madrid and EU Structural Funds), FEI-EU-20-05 (UCM) and KMM-VIN for the research fellowship (https://www.kmm-vin.eu/fellowships/) granted to carry out a research stay at the IMAT Institute (TU-Graz, Graz, Austria). R.H.B. acknowledges the Christian Doppler Forschungsgesellschaft; project number: D-1303000107.

Institutional Review Board Statement: Not applicable.

Informed Consent Statement: Not applicable.

Data Availability Statement: Not applicable.

Conflicts of Interest: The authors declare no conflict of interest.

References

1. Yan Guo, C.; Tin Hong Tang, A.; Pekka Matinlinna, J. Insights into surface treatment methods of titanium dental implants. *J. Adhes. Sci. Technol.* **2012**, *26*, 189–205. [CrossRef]
2. Guo, C.Y.; Matinlinna, J.P.; Tang, A.T.H. Effects of surface charges on dental implants: Past, present, and future. *Int. J. Biomater.* **2012**, *2012*, 381535. [CrossRef] [PubMed]
3. Amaral, I.; Cordeiro, A.; Sampaio, P.; Barbosa, M. Attachment, spreading and short-term proliferation of human osteoblastic cells cultured on chitosan films with different degrees of acetylation. *J. Biomater. Sci. Polym. Ed.* **2007**, *18*, 469–485. [CrossRef] [PubMed]
4. Nishimura, N.; Kawai, T. Effect of microstructure of titanium surface on the behaviour of osteogenic cell line MC3T3-E1. *J. Mater. Sci. Mater. Med.* **1998**, *9*, 99–102. [CrossRef]
5. Fu, J.; Hu, Y.; Guo, Z.; Zhang, Y.; Hao, Y.; Li, S. Effect of surface micro-topography of titanium material on the behaviors of rabbit osteoblast in vitro. *Appl. Surf. Sci.* **2008**, *255*, 286–289. [CrossRef]

6. Mattila, R.; Laurila, P.; Rekola, J.; Gunn, J.; Lassila, L.; Mäntylä, T.; Aho, A.; Vallittu, P. Bone attachment to glass-fibre-reinforced composite implant with porous surface. *Acta Biomater.* **2009**, *5*, 1639–1646. [CrossRef]
7. Robertson, D.M.; Pierre, L.S.; Chahal, R. Preliminary observations of bone ingrowth into porous materials. *J. Biomed. Mater. Res.* **1976**, *10*, 335–344. [CrossRef]
8. Hansson, S.; Norton, M. The relation between surface roughness and interfacial shear strength for bone-anchored implants, A mathematical model. *J. Biomech.* **1999**, *32*, 829–836. [CrossRef]
9. Mattila, R.; Puska, M.; Lassila, L.; Vallittu, P. Fibre-reinforced composite implant: In vitro mechanical interlocking with bone model material and residual monomer analysis. *J. Mater. Sci.* **2006**, *41*, 4321–4326. [CrossRef]
10. Ramskogler, C.; Warchomicka, F.; Mostofi, S.; Weinberg, A.; Sommitsch, C. Innovative surface modification of Ti6Al4V alloy by electron beam technique for biomedical application. *Mater. Sci. Eng. C* **2017**, *78*, 105–113. [CrossRef]
11. Dance, B.; Buxton, A. An introduction to surfi-sculpt technology, new opportunities, new challenges. In Proceedings of the 7th International Conference on Beam Technology, Halle, Germany, 17–19 April 2007; pp. 75–84.
12. Ferraris, S.; Warchomicka, F.; Iranshahi, F.; Rimondini, L.; Cochis, A.; Spriano, S. Electron beam structuring of Ti6Al4V: New insights on the metal surface properties influencing the bacterial adhesion. *Materials* **2020**, *13*, 409. [CrossRef]
13. Albrektsson, T.; Wennerberg, A. On osseointegration in relation to implant surfaces. *Clin. Implant. Dent. Relat. Res.* **2019**, *21*, 4–7. [CrossRef]
14. Rafieerad, A.R.; Ashra, M.R.; Mahmoodian, R.; Bushroa, A.R. Surface characterization and corrosion behavior of calcium phosphate-base composite layer on titanium and its alloys via plasma electrolytic oxidation: A review paper. *Mater. Sci. Eng. C. Mater. Biol. Appl.* **2015**, *57*, 397–413. [CrossRef]
15. Lim, S.-G.; Choe, H.-C. Corrosion phenomena of PEO-treated films formed in solution containing Mn, Mg, and Si ions. *Appl. Surf. Sci.* **2019**, *477*, 50–59. [CrossRef]
16. Hwang, I.-J.; Choe, H.-C. Effects of Zn and Si ions on the corrosion behaviors of PEO-treated Ti-6Al-4V alloy. *Appl. Surf. Sci.* **2019**, *477*, 79–90. [CrossRef]
17. Santos-Coquillat, A.; Tenorio, R.G.; Mohedano, M.; Martinez-Campos, E.; Arrabal, R.; Matykina, E. Tailoring of antibacterial and osteogenic properties of Ti6Al4V by plasma electrolytic oxidation. *Appl. Surf. Sci.* **2018**, *454*, 157–172. [CrossRef]
18. del Olmo, R.; Mohedano, M.; Visser, P.; Matykina, E.; Arrabal, R. Flash-PEO coatings loaded with corrosion inhibitors on AA2024. *Surf. Coat. Technol.* **2020**, *402*, 126317. [CrossRef]
19. Wang, X.; Guo, E.; Gong, S.; Li, B. Realization and experimental analysis of electron beam Surfi-Sculpt on Ti-6Al-4V alloy. *Rare Met. Mater. Eng.* **2014**, *43*, 819–822. [CrossRef]
20. Wang, X.; Ahn, J.; Bai, Q.; Lu, W.; Lin, J. Effect of forming parameters on electron beam Surfi-Sculpt protrusion for Ti–6Al–4V. *Mater. Des.* **2015**, *76*, 202–206. [CrossRef]
21. Tändl, J.; Enzinger, N. Electron beam surface structuring of AA6016 aluminum alloy. *Weld. World* **2014**, *58*, 795–803. [CrossRef]
22. van Hengel, I.A.; Riool, M.; Fratila-Apachitei, L.E.; Witte-Bouma, J.; Farrell, E.; Zadpoor, A.A.; Zaat, S.A.; Apachitei, I. Selective laser melting porous metallic implants with immobilized silver nanoparticles kill and prevent biofilm formation by methicillin-resistant Staphylococcus aureus. *Biomaterials* **2017**, *140*, 1–15. [CrossRef]
23. van Hengel, I.A.J.; Putra, N.E.; Tierolf, M.; Minneboo, M.; Fluit, A.C.; Fratila-Apachitei, L.E.; Apachitei, I.; Zadpoor, A.A. Biofunctionalization of selective laser melted porous titanium using silver and zinc nanoparticles to prevent infections by antibiotic-resistant bacteria. *Acta Biomater.* **2020**, *107*, 325–337. [CrossRef]
24. Daavari, M.; Atapour, M.; Mohedano, M.; Arrabal, R.; Matykina, E.; Taherizadeh, A. Biotribology and biocorrosion of MWCNTs-reinforced PEO coating on AZ31B Mg alloy. *Surf. Interfaces* **2021**, *22*, 13. [CrossRef]
25. de Damborenea, J.J.; Arenas, M.A.; Larosa, M.A.; Jardini, A.L.; Zavaglia, C.A.D.; Conde, A. Corrosion of Ti6Al4V pins produced by direct metal laser sintering. *Appl. Surf. Sci.* **2017**, *393*, 340–347. [CrossRef]
26. Pariona, M.; Müller, I. An electrochemical study of the crevice corrosion of titanium. *J. Braz. Chem. Soc.* **1997**, *8*, 137–142. [CrossRef]
27. Bhola, R.; Bhola, S.M.; Mishra, B.; Olson, D.L. Corrosion in titanium dental implants/prostheses—A review. *Trends Biomater. Artif. Organs* **2011**, *25*, 34–46.
28. Zhang, X.; Jiang, Z.H.; Yao, Z.P.; Song, Y.; Wu, Z.D. Effects of scan rate on the potentiodynamic polarization curve obtained to determine the Tafel slopes and corrosion current density. *Corros. Sci.* **2009**, *51*, 581–587. [CrossRef]
29. Fazel, M.; Salimijazi, H.; Shamanian, M.; Apachitei, I.; Zadpoor, A. Influence of hydrothermal treatment on the surface characteristics and electrochemical behavior of Ti-6Al-4V bio-functionalized through plasma electrolytic oxidation. *Surf. Coat. Technol.* **2019**, *374*, 222–231. [CrossRef]

coatings

MDPI

Article

Microstructure and Mechanical Properties of Co-Deposited Ti-Ni Films Prepared by Magnetron Sputtering

Xiaolin Zhang [1], Yi Ding [1], Honglu Ma [2], Ruibin Zhao [2], Liangquan Wang [2] and Fanyong Zhang [2,*]

[1] Avic Chengfei Commercial Aircraft Co., Ltd., Chengdu 610092, China
[2] Tianjin Key Laboratory of Materials Laminating Fabrication and Interface Control Technology, School of Material Science and Engineering, Hebei University of Technology, Tianjin 300130, China
* Correspondence: zhangfanyong@hebut.edu.cn

Abstract: Ti-Ni films with various Ni contents (16.5, 22.0, 33.5 at. %) were deposited on Al alloy substrates using DC magnetron co-sputtering. The effects of Ni target power and substrate bias (−10, −70, −110 V) on morphologies, crystallography, nanomechanical properties and scratch behavior of films were studied. All the deposited Ti-Ni films exhibited a BCC structure of β-Ti (Ni). The Ti-Ni films grew with a normal columnar structure with good bonding to substrates. When increasing the Ni target power and substrate bias, the grain size grew larger and the surface became denser. The as-deposited Ti-Ni films significantly improved the hardness (>4 GPa) of the Al alloy substrate. With the increase of bias voltage, the hardness and modulus of the film increased. The hardness and modulus of the Ti-22.0Ni film prepared at −70 V bias were 5.17 GPa and 97.6 GPa, respectively, and it had good adhesion to the substrate.

Keywords: magnetron sputtering; Ti-Ni film; microstructures; mechanical properties

1. Introduction

Titanium and its alloys have excellent properties including low density, high specific strength, and strong corrosion resistance, and are widely used in aerospace, automobile, biomedical applications and other fields [1–6]. Moreover, Ti-based metal films prepared using magnetron sputtering have also attracted interest. Several works have reported the microstructure of pure Ti film (α-Ti, hcp), which is related to the sputtering parameters including target power, bias and deposition temperature [7–12]. In recent years, β-Ti alloys (bcc) have gained increasing attention due to their excellent strength and rigid combinations. Notably, the lower elastic modulus of β-Ti makes it more compatible with bone, showing great prospects in biomedical fields [13–15]. Microstructural features such as morphology, grain size, density and texture strongly affect structural and functional properties of Ti films [16–18]. Thus, it is important to understand the microstructure and performance of β-Ti films for potential applications.

It is known that a solid solution is vital to strengthen the mechanical properties of Ti alloys. The addition of β-stabilizing elements (e.g., Mo, V, Nb, Ni, Cr, Fe, Ta) could shift the β-transition into lower temperatures. The content of alloying elements greatly affects the phase composition and mechanical properties. Both β and $\alpha + \beta$ alloys exhibit excellent biocompatibility and are widely used in medical applications [19]. The addition of β-stabilizing elements such as Zr and Mo to titanium alloys improves their mechanical properties and biocompatibility, resulting in a good combination of ductility, strength, and strain hardening rate. As for casted Ti-Cr and Ti-Mo alloys, only 10 wt% Cr or Mo addition is required to form the β phase [20,21]. In the spark plasma sintered Ti-Mo alloy, the highest hardness (592 $HV_{0.3}$), highest flexural strength (∼2 GPa) and maximum ultimate tensile strength (852 MPa) are achieved for Ti-16Mo, Ti-12Mo and Ti-8Mo alloys (wt.%), respectively [22]. According to Lee et. al., the hcp phase (α) is dominated in Ti-Nb alloys with 15 wt.% or less Nb, while the bcc phase (β) is retained with more than 27.5 wt.% Nb [23]. In view of the powerful β-stabilizing ability of Mo elements, the equivalent percentage of Mo could be established with other betagenic elements [24]. Studies have shown that adding Ni to Ti-based alloys can enhance the stability of the β phase, thereby improving the overall mechanical properties of the material. The addition of Ni can also adjust the phase transition temperature of Ti-Ni alloys, which is crucial for shape memory applications. However, there still exist many unclear issues between β-stabilizing elements and microstructure features of Ti alloys.

In the mass production of β-Ti alloys, a rapid cooling process is often necessary after a high-temperature heating treatment or rapid sintering, as stated in Reference [25]. Nevertheless, magnetron sputtering of Ti-Me films can be easily achieved with a large series of composition just by regulating the power of co-deposited Ti and Me targets. This would be convincing for optimizing the chemical composition of bulk Ti alloys. Photiou et al. [26] revealed the structure–property relationships for magnetron-sputtered Ti-Nb films covering a broad Nb range. The β-Ti phase can be stabilized with Nb content beyond 20 at%. The Ti-15at%Nb film exhibited the lowest elastic modulus of ~85 GPa. In our previous study of Ti-Cr film (Cr, 0~40 at. %) [27], only 10% Cr could stabilize the β phase. Note that the increasing Cr content has little change in the modulus of Ti-Cr films, retaining the values at ~95 GPa. Liu et al. [28] revealed the phase formation and morphology evolution of sputtered Ti-Mo films under different substrate temperatures. The Ti-15Mo film could retain the β phase at 50~100 °C, while the Ti-30Mo film could maintain the β phase at higher temperatures up to 300 °C. Researchers have also explored other Ti alloy films, such as Ti-Al, Ti-Ag and Ti-Cu films, for potential biomedical applications [29–32].

The shape memory effects of Ti-Ni-based alloys or films have been the focus of many studies [33–37], but the structure–property relationship of Ti-Ni alloys in the Ti-rich region (<40 at%) has been rarely reported. In view of the complex processes and cost of cast Ti-Ni bulks, this study employed magnetron sputtering to deposit Ti-Ni films with a series of Ni content by adjusting the Ni target power. The effect of deposition parameters on the phase composition and mechanical properties were also investigated. Through the thin film technique, the Ni composition–structure–property relationships in Ti-Ni alloys are conveniently revealed. This might provide useful guides to tailor compositions in bulk Ti-Ni alloys. The β-phase of Ti-Ni-based alloys is an important research area, and studying the formation mechanism and phase transformation behavior of the β-phase is crucial for understanding β-Ti(Ni) alloys. Considering the need for good bonding between Ti-Ni films and substrate, metallic Al instead of glass or silicon pieces is used as a substrate. The good mutual solubility and property matching between the Ti-Ni film and Al produce good adhesion without flaking. Meanwhile, Ti-Ni films can enhance the surface hardness and corrosion resistance of the relatively soft Al substrate. In addition, post-annealing could stimulate the surface alloying of Ti and Ni on the Al substrate, thus enhancing its surface properties and prolonging the service life of the aluminum alloy.

2. Materials and Methods

Commercial 2024-Al alloy disks (Φ 20 mm × 4 mm) were used as substrate. The substrate was ground with sandpaper and polished into a mirror-like surface, then ultrasonically cleaned with acetone solution for about 30 min.

Using a magnetron sputtering technique with pure Ti and pure Ni targets (Omat Advanced Materials Co., Ltd., Dongguan, China), Ti-Ni alloy films were created on substrates. The parameters are shown in Table 1. Firstly, the bias voltage of the workpiece was first fixed at −70 V. Meanwhile, the Ti target power was fixed at 1.5 kW as basic composition and we changed the Ni target power to 0.1 kW, 0.15 kW and 0.25 kW to obtain different Ni contents. The corresponding Ti-Ni films were denoted as DTN-1, DTN-2 and DTN-3. Consequently, the Ti target power and Ni target power were fixed and we changed the substrate bias at −10 V and −110 V. The corresponding samples were recorded as DTN-4 and DTN-5.

Table 1. Parameters of magnetron sputtering deposition of Ti-Ni films.

Process Parameter	Unit	Value
Background pressure	Pa	4×10^{-3}
Argon flux	sccm	16
Ti target power	kW	1.5
Ni target power	kW	0.1, 0.15, 0.25
Bias voltage	V	−10, −70, −110
Sputtering time	min	120
Sputtering pressure	Pa	0.2–0.3
Target-substrate distance	mm	70

The phase structure of the films was detected using an X-ray diffractometer (XRD) (Rigaku D/max 2500, Tokyo, Japan) with a Cu Kα source (λ = 1.542 Å), The parameters were shown as scanning angle range of 2θ = 10°–90°, and scanning speed of 4° min^{-1}. The morphologies of the films were characterized by scanning electron microscope (JSM7100F, JEOL, Tokyo, Japan) equipped with an energy dispersive spectrometer (EDS). The particle size of the film was measured by Nano Measure software using surface SEM images. The element distribution was determined by JXA-8530 electron probe micro analyzer (EPMA, JEOL, Tokyo, Japan).

A dynamic ultra-micro hardness tester (DUH-211S, SHIMADZU, Kyoto, Japan) was used to evaluate the mechanical properties of Ti-Ni films. The test force was 30 mN, the loading speed was 1 mN/s and dwell time was 10 s. The hardness and Young's modulus were obtained by the obtained load-displacement curves. The scratch test (WS-2005, Lanzhou institute of chemical physics, Lanzhou, China) of the films was carried out using a diamond tip, and the fracture resistance and adhesion strength data of the film were obtained. The maximum load was 80 N, the loading rate was 80 N/min and scratch distance was 2 mm.

3. Results and Discussions

3.1. Phase Analysis of Ti-Ni Films

Figure 1 shows the XRD patterns of the Ti-Ni films deposited at different Ni target powers and different bias pressures. It is apparent that all the Ti-Ni films were crystallized in a β-Ti(Ni) structure with a preferred orientation along the (110) plane. The broad peaks of (110) suggest the presence of nanocrystals in the Ti-Ni films. The XRD peak width between 34~46° becomes broader with the increase of Ni target power, implying the grain refinement in Ti-Ni films. However, the increasing substrate bias results in a slight shrinking of the (110) peak, indicating improved crystallinity. The higher target power generates more Ni atoms with higher energy, facilitating the nucleation of Ti-Ni films. In addition, the higher bias provides more kinetic energy of atoms to bombard the substrate, thus accelerating the surface diffusion of atoms and grain growth. Typically, the β-Ti phase forms at high temperatures. However, during magnetron sputtering, the high kinetic energy of particles dissipates rapidly, creating extremely rapid cooling and freezing conditions for the formation of the β phase. Moreover, the co-sputtering with Ni elements stabilizes the β phase in Ti-Ni films. It is also consistent with the finding that the addition of alloying elements (e.g., Cr, Nb, Mo, etc.) promotes the stabilization of the β-phase in the Ti-based alloy films [26–28]. According to a previous study of Ti-Cr films, with the addition of ~10 at. % Cr, the hcp pure Ti (α-Ti) is converted to a bcc structure (β-Ti) for the Ti-Cr alloy film [27]. In the study of Ti-Nb films, D. Photiou et al. [26] also found that when the Nb content is 20% or more, the stable β phase structure is promoted.

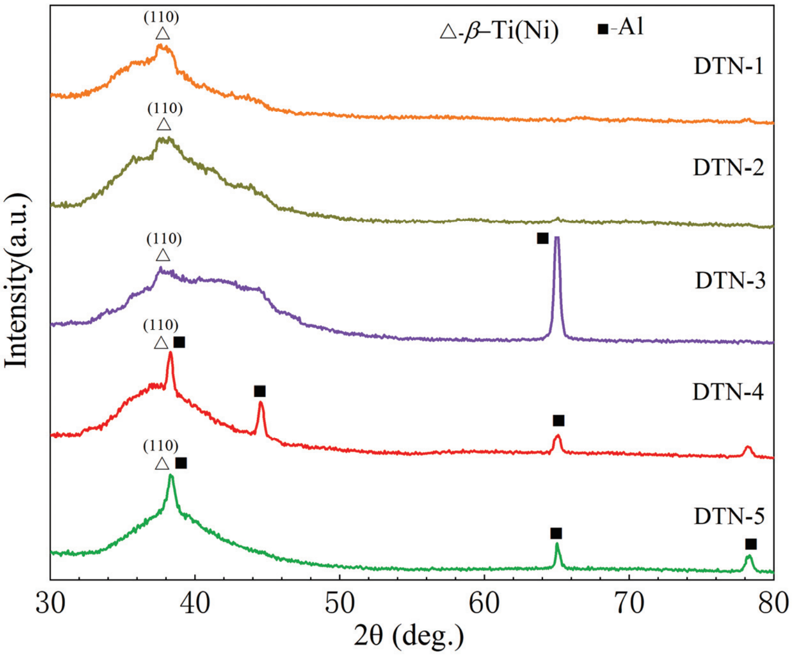

Figure 1. XRD patterns of Ti-Ni film deposited with different Ni target power and bias.

3.2. Surface Morphology and Chemical Composition of Ti-Ni Films

Figure 2 displays the surface morphologies of Ti-Ni films deposited at different Ni target power and substrate bias. The corresponding compositions are summarized in Table 2. The average Ni content of DTN-1, DTN-2 and DTN-3 films were 16.5%, 22.0% and 33.5% (at. %), respectively. Thus, we can refer to the three samples as Ti-16.5Ni, Ti-22Ni, and Ti-33.5Ni films. It should be noted that the substrate bias did not significantly alter the chemical composition of the Ti-16.5Ni film.

Table 2. EDS results of Ti-Ni films deposited at different Ni target power and substrate bias.

Films/Elements	Ti (at. %)	Ni (at. %)
DTN-1	83.5	16.5
DTN-2	78.0	22.0
DTN-3	66.5	33.5
DTN-4	83.4	16.6
DTN-5	83.7	16.3

As seen from Figure 2a–e, all the β-Ti(Ni) films show spherical aggregate morphology with some abnormal large grains. The high magnified images (Figure 2f–j) show that the spherical domains are constituted of nanoscale particles (20~50 nm). However, voids are also visible between adjacent domains. The continuous bombardment of energic particles on the previous films generates more nucleation sites, thus forming fine grains in the domains. As described in Figure 3, the average size of the spherical domains is 269, 311, 327, 231 and 326 nm for DTN-1, DTN-2, DTN-3, DTN-4 and DTN-5 films, respectively. Interestingly, with increasing Ni target power, the size of the spherical particles increases. The surface of domain (Figure 2h) becomes much smoother. However, in the study of D. Photiou et al. [26], the increase in Nb target power resulted in smaller particle size of the films. Higher target power generates more energic atoms, and thus might result in a sputtering-depositing effect on the as-deposited surface. Meanwhile, the surface migration of Ti, Ni atoms is enhanced. These two factors are ascribed to the smooth feature of the Ti-33.5Ni film. As seen from Figure 2f–j, the substrate bias has a slight effect on the growth feature of the Ti-16.5Ni film. However, the film becomes denser and the internal particles grow larger with the increasing bias. As reported in [27], the α-Ti film grows cauliflower-like features with a loose structure, while the β-Ti(Cr) films grow with globular particles. The Nb addition also leads to the formation of a β phase with round particles in Ti-Nb films (20~44 at. %) [26]. These indicate that β-stabilizing elements (Cr, Nb and Ni) generate a similar sphere domain growth in β-Ti films.

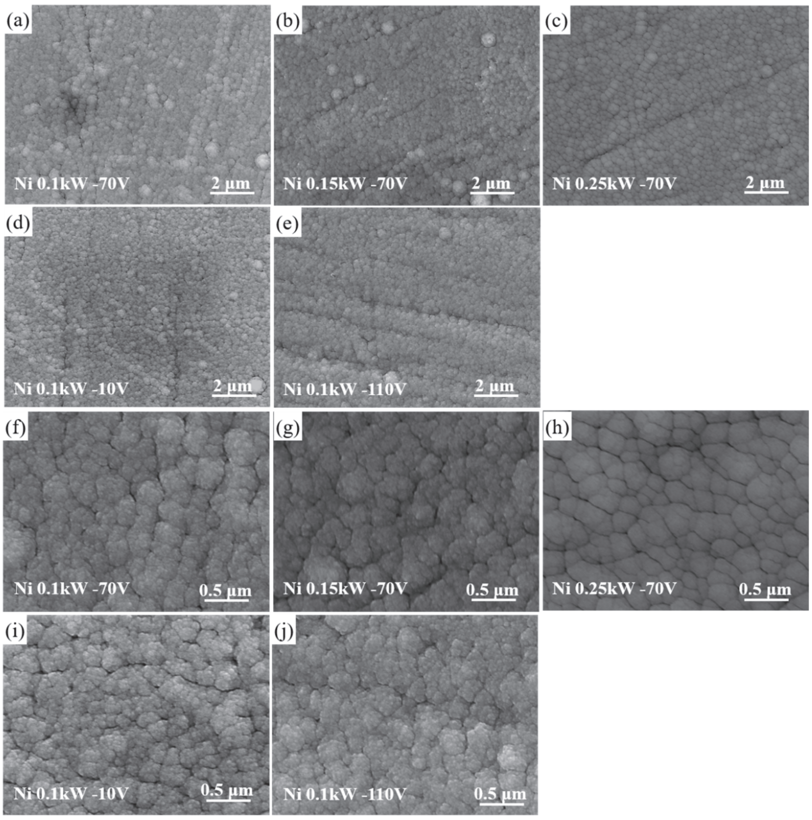

Figure 2. Surface morphology of Ti-Ni films deposited at different Ni target powers and substrate bias. (**a**,**f**) DTN-1; (**b**,**g**) DTN-2; (**c**,**h**) DTN-3; (**d**,**i**) DTN-4; (**e**,**j**) DTN-5.

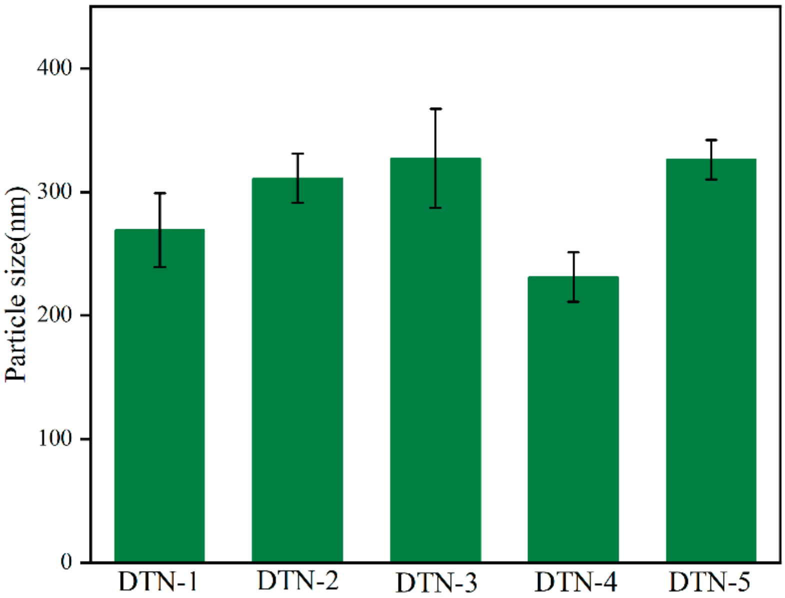

Figure 3. Particle size of Ti-Ni films deposited under different Ni target power and bias.

The elemental distribution of the films was analyzed using EPMA. Figure 4 shows the surface elemental distribution of DTN-1, DTN-3 and DTN-5 films. The Ti and Ni elements are uniformly dispersed without segregation. As the Ni target power increases, the Ni content on the surface of DTN-3 rises more than that on the surface of DTN-1, which is consistent with the results in Table 2. In addition, the Ti and Ni maps hardly change with the increase of substrate bias from −70 V to −110 V. These results imply that co-sputtering is a favorable method to produce homogeneous alloys and as such could provide guidelines for bulk alloy design.

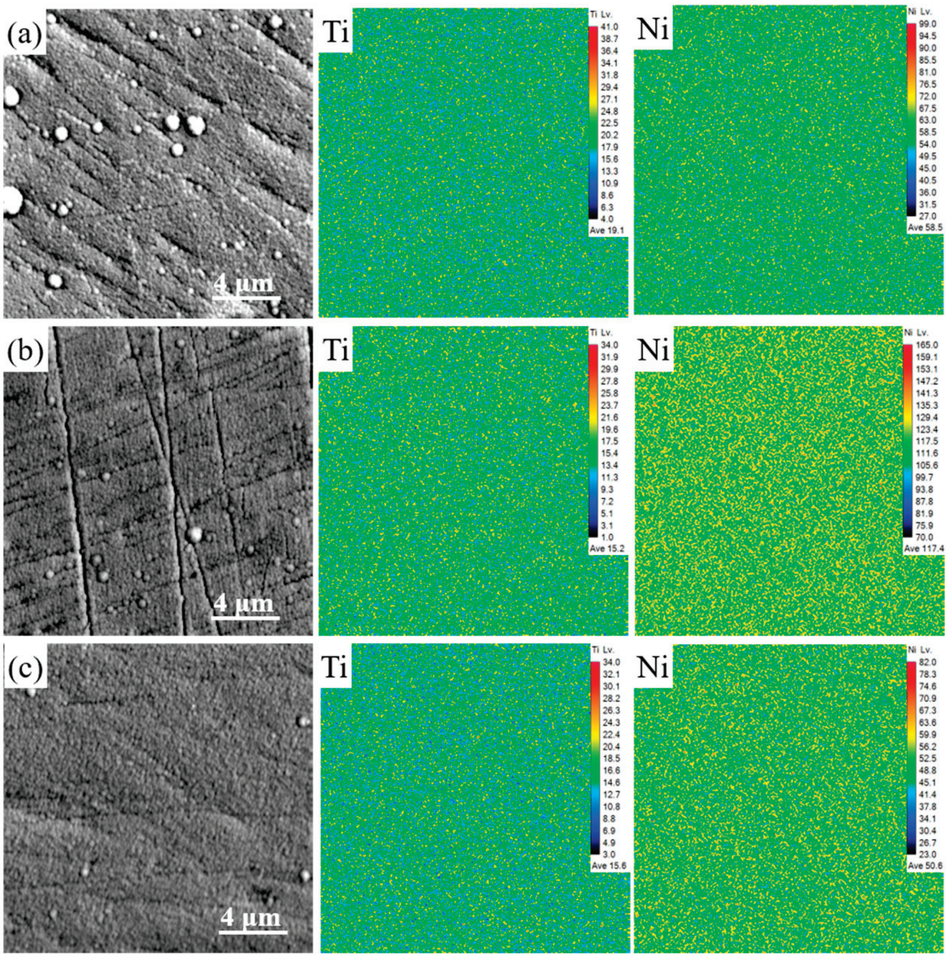

Figure 4. Element distribution of Ti-Ni films deposited at different Ni target power and bias pressures: (**a**) DTN-1, (**b**) DTN-3, (**c**) DTN-5.

3.3. Cross-Sectional and Fracture Morphology of Ti-Ni Films

Figure 5 displays the cross-sectional morphology of the Ti-Ni films. It is clear that there are no voids or cracks at the interface between the Ti-Ni films and the Al substrates, implying good bonding state. The thickness of the Ti-16.5Ni, Ti-22Ni and Ti-33.5Ni films is 3.46, 3.82, and 4.09 μm, respectively. Obviously, the increasing Ni target power leads to thicker films. As seen from Figure 5a,d,e, the thickness of the Ti-16.5Ni film at the bias of −10 V, −70 V and −110 V is 3.47, 3.46 and 3.36 μm, respectively. The decrease in film thickness at high bias pressure was attributed to the back-sputtering effect of Ar ions. The thickness of Ti-Ni films increased with increasing Ni target power at the same Ti target power. Under the same Ni target power condition, the bias has little effect on the film thickness. The results demonstrate that the thickness of Ti-Ni films can be controlled by varying the Ni target power during co-sputtering. These results provide valuable guidance for the design of bulk alloys and demonstrate the potential of co-sputtering for producing homogeneous alloys with controlled thickness.

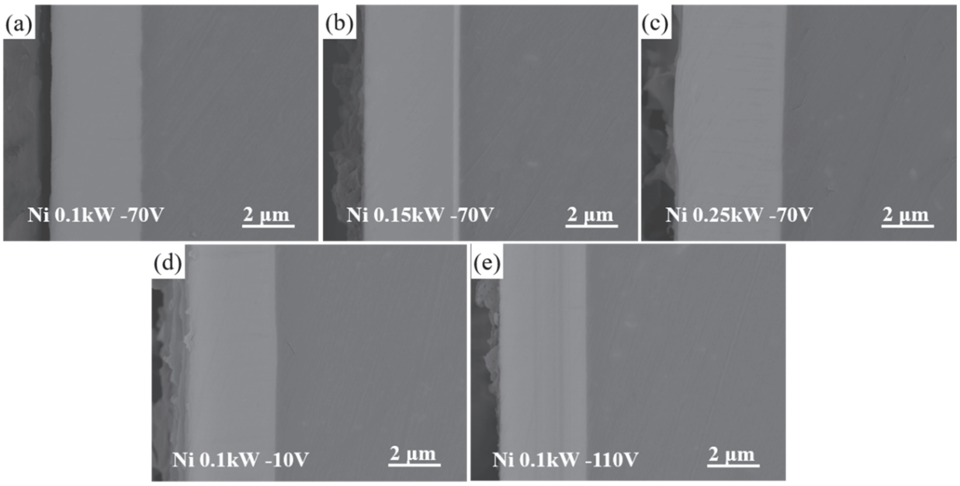

Figure 5. Cross-sectional morphology of Ti-Ni films deposited at different Ni target powers and bias: (**a**) DTN-1; (**b**) DTN-2; (**c**) DTN-3; (**d**) DTN-4; (**e**) DTN-5.

From the fracture morphology in Figure 6, all the Ti-Ni films exhibit a typical columnar structure, which is a typical morphology of the ion sputter-deposited film [7,11]. As the film thickness increases, the columnar clusters become refined at the bottom. Notably, the columnar clusters in the Ti-33.5Ni film show fiber-like characteristics. At lower substrate bias, the columnar structure is coarse and there are large gaps. With the increasing bias, the columnar morphology is not apparent, the gaps decrease, and the film becomes denser. This can be attributed to the fact that an increase in bias results in an increase in the kinetic energy of atoms, thereby enhancing their migration ability in the plane direction, which in turn inhibits the perpendicular growth of columnar crystals.

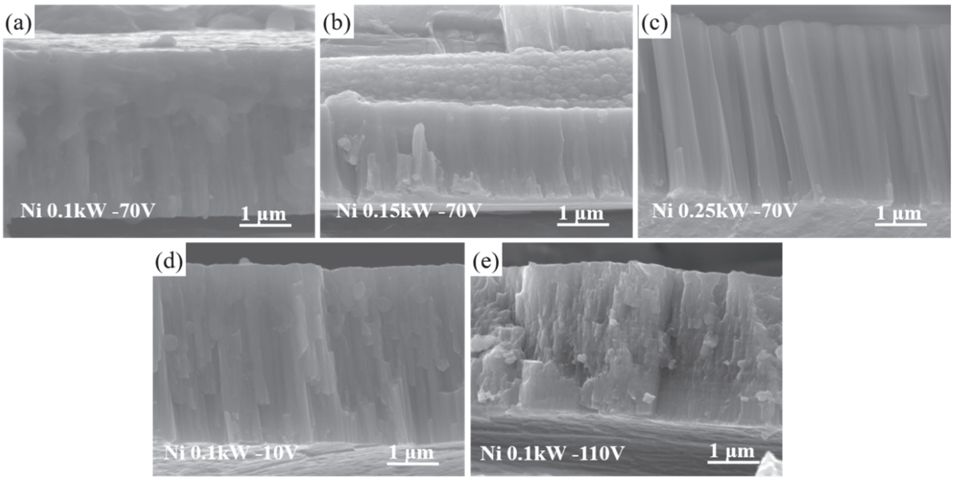

Figure 6. Fracture morphology of Ti-Ni films deposited at different Ni target power and bias: (**a**) DTN-1; (**b**) DTN-2; (**c**) DTN-3; (**d**) DTN-4; (**e**) DTN-5.

3.4. Nano-Indentation Test of Ti-Ni Films

Figure 7 shows the nanoindentation hardness and elastic modulus of Ti-Ni films and the load-displacement curves. The elastic-plastic deformation ability of films is calculated according to the curves, and the corresponding values are summarized in Table 3. The hardness of the Ti-16.5Ni, Ti-22Ni and Ti-33.5Ni films is 4.45, 5.17 and 4.18 GPa. The corresponding modulus is 87, 97.6 and 90.5 Gpa, respectively. As seen from the XRD results in Figure 1, the relatively sharp peak of the (110) plane indicates the better crystallinity of the Ti-22Ni film, which explains its high hardness. The hardness of the Ti-16.5Ni film at −10 V and −110V is 4.71 and 4.89 GPa, and the elastic modulus is 94.5 and 96 GPa, respectively. With the increasing bias, the DTN-5 film also has a sharper (110) peak and denser surface, thus leading to the improved hardness. The modulus of the present Ti-Ni films (87~86 GPa) is close to that of our previous β-Ti(Cr) films (~95 GPa). It has been reported [38] that the hardness of Ti-Ni alloys prepared by selective laser melting (SLM) fluctuates around 255 ± 10 $HV_{0.2}$. The Ti-Ni films deposited in this study show significantly improved hardness compared to that of SLM-TiNi alloys. In addition, the hardness and modulus of the Ti-Ni films are significantly higher than that of the 2024 Al alloy substrate (1.57 and 82 GPa).

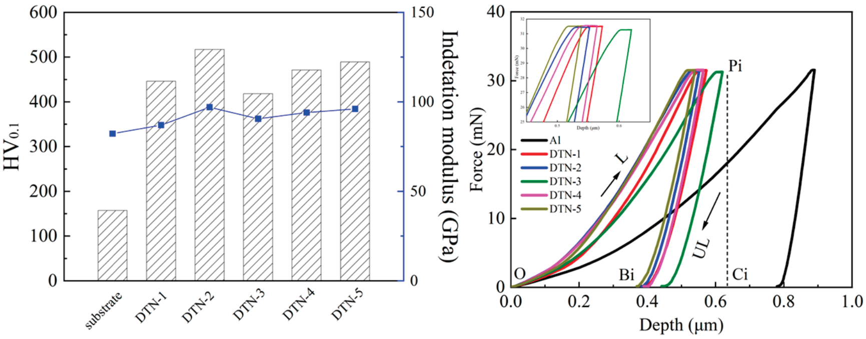

(**a**) (**b**)

Figure 7. Nanoindentation results of Ti-Ni films deposited at different Ni target powers and bias. (**a**) Hardness and modulus, (**b**) load-displacement curves.

Table 3. Calculated nanoindentation results of Ti-Ni films.

Sample	H (GPa)	E (GPa)	H/E ($\times 10^{-2}$)	H^3/E^2 ($\times 10^{-2}$)	W_t (nJ)	W_p (nJ)	η_p
2024Al	1.57	82	1.91	0.05	10.65	9.3	0.87
DTN-1	4.45	87	5.12	1.17	6.17	4.59	0.69
DTN-2	5.17	97.6	5.29	1.14	6.4	5.03	0.79
DTN-3	4.18	90.5	4.62	0.89	7.47	5.59	0.75
DTN-4	4.71	94.5	4.98	1.17	7.09	5.37	0.76
DTN-5	4.89	96	5.10	1.27	6.11	4.69	0.77

In conditions of elastic-plastic behavior, the ability of a material to withstand elastic strain before failure can be described by the ratio of hardness (H) to Young's modulus (E), and materials with a higher H/E usually exhibit lower wear rates; resistance to plastic deformation to failure can be described by H^3/E^2, and materials with high hardness and low modulus have a lower tendency towards plastic deformation [39]. As shown in Table 3, the Ti-22Ni film has the maximum H/E value. However, the H/E value decreases at higher Ni content. As for the Ti-16.5Ni film, the substrate bias has little change in the H/E value. The trend of the effect of different deposition conditions on H^3/E^2 is similar to that of H/E.

Figure 7b displays the load-displacement curves of Ti-Ni alloy films; the total deformation work W_t is defined by the area under the loading curve (A_{OPiCi}) and the plastic deformation work W_p is defined by the area of the closed area of the loading and unloading curves (A_{OPiBi}), both of which are used to assess the elastic and plastic deformation behavior of the material, respectively. The plasticity factor ($\eta_p = W_p/W_t$) is used to assess the material's resistance to plastic deformation, and a larger value indicates a stronger plastic deformation ability of the material. As can be seen from Table 3, the η_p value of the 2024 aluminum alloy is 0.87, indicating its strong plastic deformation ability; the η_p values of DTN-1, DTN-2 and DTN-3 films are 0.69, 0.79 and 0.75, respectively, and the η_p values of DTN-4 and DTN-5 films are 0.76 and 0.77, respectively, showing good plastic deformation ability.

3.5. Scratch Test of Ti-Ni Films

Scratch tests were used to assess the adhesion behavior of Ti-Ni films. The acoustic emission (AE) signal profile can determine the critical normal load (LC). The coating/substrate system's binding strength can be reliably assessed using the critical normal load (LC) [40,41]. The abrupt increase in AE signal typically denotes that the substrate exposure is a factor in coating failure [42,43]. The scratch acoustic signals and critical loads are shown in Figure 8 and Table 4. The results demonstrate that the film adhesion decreases from 26.1 N to 20.5 N as the Ni target power increases. This demonstrates that a lower Ni target power is advantageous for enhancing film-to-substrate adhesion. With the increase of substrate bias, the adhesion force of the film increases from 25.5 N to 26.1 N and then decreases to 14.4 N. The increase of substrate bias generates internal stresses in the film, and the more minor internal stresses are helpful in reducing the number of defects in the films, while the larger internal stress is likely to cause film peeling.

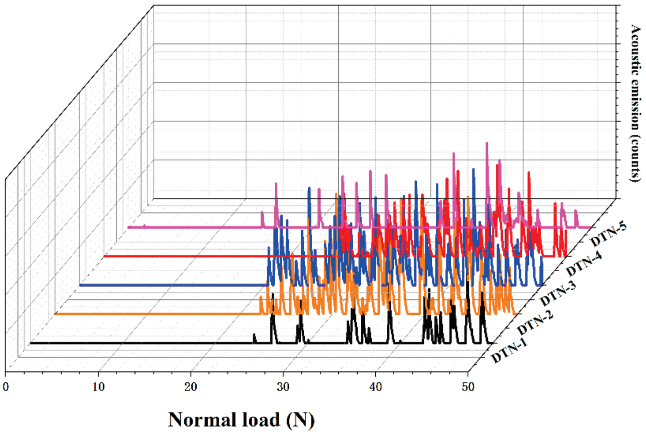

Figure 8. Schematic diagram of the acoustic signals of Ti-Ni films deposited with different Ni target power and bias.

Table 4. Critical loads of Ti-Ni films deposited at different Ni target powers and bias pressures.

Sample	Critical Load (N)
DTN-1	26.1
DTN-2	22.2
DTN-3	20.5
DTN-4	25.5
DTN-5	14.4

Figure 9 shows the SEM morphologies of Ti-Ni alloy films after scratch tests. Specifically, the scratch morphology of the Ti-16.5Ni film is selected for detailed analysis. As seen from Figure 9a–e, the width of the scratch becomes wider with the increase of the load. In the load application process, cracks and "jaggedness" appear on both sides of the scratch at the initial stage. The load continues to increase until the substrate is exposed, the central crack of the scratch becomes dense, and the cracks on both sides become loose. The film at the end of the scratch shows adhesive wear with the direction of indenter movement and the film peels off with the indenter.

As seen in Figure 9a, the DTN-1 film starts to fail furthest from the initial position, indicating the best adhesion between it and the substrate, which is consistent with the data in Table 4. At the middle end of the scratch (Figure 9f,g), dense cracking along the scratch direction can be observed due to increasing load, creating cohesion and slight adhesion breakdown in the film. At the end of the scratch (Figure 9h,i), partial peeling of the film surface occurs due to compressive and radial tensile stresses, producing severe adhesive failure. When the load reaches the upper critical load, a large area of peeling occurs in both the center and edge of the scratch, thus exposing the substrate. This emphasizes the importance of controlling the scratch load in order to avoid catastrophic failure and improve the adhesion strength of Ti-Ni films. Overall, the SEM images provide valuable insights into the failure mechanism of Ti-Ni films during scratch tests and can help guide future film development.

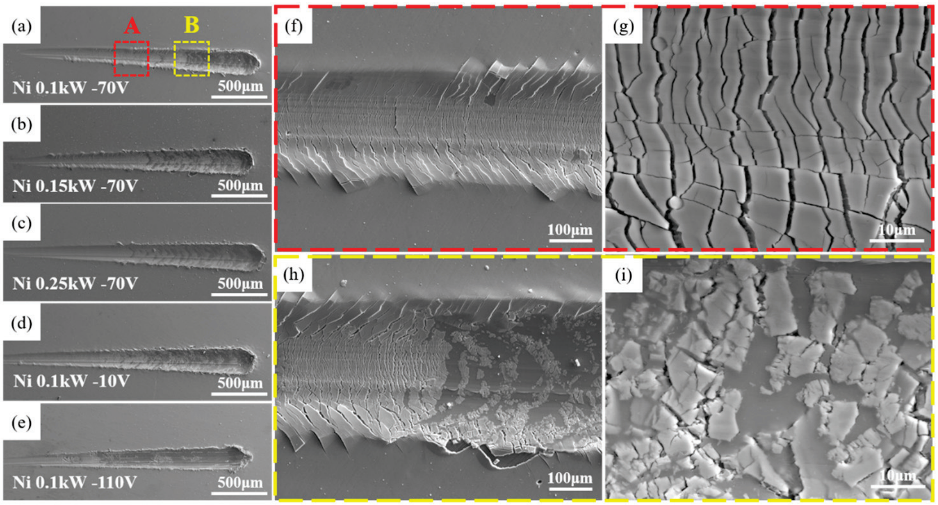

Figure 9. Scratch morphology of Ti-Ni films deposited with different Ni target powers and bias: (**a**) DTN-1, (**b**) DTN-2, (**c**) DTN-3, (**d**) DTN-4, (**e**) DTN-5, (**f**,**g**) DTN-1 mid-scratch, (**h**,**i**) DTN-1 end-scratch.

4. Conclusions

This work deposited a series of Ti-Ni alloy films on the surface of a 2024 Al alloy using magnetron sputtering. Under different deposition conditions, the films all exhibited a stable BCC structure, mainly composed of β-Ti(Ni). The deposited films showed typical cauliflower-like features on the surface and apparent columnar growth morphology in the cross sections. The particle size increased with the increase of Ni content. The thickness of the film increased and became denser and flatter, and the bias had little effect on the phase composition and thickness of the film. With the increase of Ni target power and bias, the ability of the films to resist plastic deformation decreases after the Ni content exceeds 22%, and the Ti-22.0Ni film layer with bias of -70 V has excellent comprehensive mechanical properties with hardness and modulus of 5.76 GPa and 97.6 GPa, respectively. The overall trend of adhesion strength between Ti-Ni film and substrate decreases with increasing Ni target power and decreasing substrate bias.

In conclusion, thin film deposition provides a practical approach to study the composition–structure–property relationship of Ti-Ni alloys. The adjustment of Ni content by magnetron sputtering allows the study of its effect on phase composition and mechanical properties. This work may provide a reference for guiding the composition design of bulk Ti-Ni alloys, exploring more suitable alloys for medical applications. In future, post-annealing could be employed to stimulate the diffusion between Ti-Ni and Al, thus strengthening the surface of Al alloys.

Author Contributions: Conceptualization, F.Z. and X.Z.; methodology, Y.D.; investigation, X.Z., Y.D., F.Z. and H.M.; data curation, R.Z. and L.W.; writing—original draft preparation, Y.D. and H.M.; writing—review and editing, X.Z., H.M. and F.Z.; supervision, F.Z.; funding acquisition, F.Z. All authors have read and agreed to the published version of the manuscript.

Funding: This research was funded by National Natural Science Foundation of China, grant number No. 51701062.

Institutional Review Board Statement: Not applicable.

Informed Consent Statement: Not applicable.

Data Availability Statement: The data presented in this study are available on request from the corresponding author.

Conflicts of Interest: The authors declare no conflict of interest.

References

1. Qi, M.H.; Xu, J.L.; Lai, T.; Huang, J.; Ma, Y.C.; Luo, J.M.; Zheng, Y.F. Novel bioactive Ti-Zn alloys with high strength and low modulus for biomedical applications. *J. Alloys Compd.* **2023**, *931*, 167555. [CrossRef]
2. Romero-Resendiz, L.; Rossi, M.C.; Seguí-Esquembre, C.; Amigó-Borrás, V. Development of a porous Ti-35Nb-5In alloy with low elastic modulus for biomedical implants. *J. Mater. Res. Technol.* **2023**, *22*, 1151–1164. [CrossRef]
3. Wang, W.; Cui, W.; Xiao, Z.; Qin, G. The improved corrosion and wear properties of Ti-Zr based alloys with oxide coating in simulated seawater environment. *Surf. Coat. Technol.* **2022**, *439*, 128415. [CrossRef]
4. Zhang, L.C.; Chen, L.Y. A Review on Biomedical Titanium Alloys: Recent Progress and Prospect. *Adv. Eng. Mater.* **2019**, *21*, 1801215. [CrossRef]
5. Chen, Q.; Thouas, G.A. Metallic Implant biomaterials. *Mater. Sci. Eng. R Rep.* **2015**, *87*, 1–57. [CrossRef]
6. Celesti, C.; Gervasi, T.; Cicero, N.; Giofrè, S.V.; Espro, C.; Piperopoulos, E.; Gabriele, B.; Mancuso, R.; Vecchio, G.L.; Iannazzo, D. Titanium Surface Modification for Implantable Medical Devices with Anti-Bacterial Adhesion Properties. *Materials* **2022**, *15*, 3283. [CrossRef]
7. Chawla, V.; Jayaganthan, R.; Chawla, A.K.; Chandra, R. Morphological study of magnetron sputtered Ti thin films on silicon substrate. *Mater. Chem. Phys.* **2008**, *111*, 414–418. [CrossRef]
8. Jin, Y.; Wu, W.; Li, L.; Chen, J.; Zhang, J.; Zuo, Y.; Fu, J. Effect of sputtering power on surface topography of dc magnetron sputtered Ti thin films observed by AFM. *Appl. Sur. Sci.* **2009**, *255*, 4673–4679.
9. Liu, Y.L.; Fang, L.I.U.; Qian, W.U.; Chen, A.Y.; Xiang, L.I.; Deng, P.A.N. Effect of bias voltage on microstructure and nanomechanical properties of Ti films. *Trans. Nonferrous Met. Soc. China* **2014**, *24*, 2870–2876. [CrossRef]
10. Godfroid, T.; Gouttebaron, R.; Dauchot, J.P.; Leclere, P.; Lazzaroni, R.; Hecq, M. Growth of ultrathin Ti films deposited on SnO_2 by magnetron sputtering. *Thin Solid Film.* **2003**, *437*, 57–62. [CrossRef]
11. Chawla, V.; Jayaganthan, R.; Chawla, A.K.; Chandra, R. Microstructural characterizations of magnetron sputtered Ti films on glass substrate. *J. Mater. Process. Technol.* **2009**, *209*, 3444–3451. [CrossRef]
12. Moskovkin, P.; Maszl, C.; Schierholz, R.; Breilmann, W.; Petersen, J.; Pflug, A.; Muller, J.; Raza, M.; Konstantinidis, S.; von Keudell, A.; et al. Link between plasma properties with morphological, structural and mechanical properties of thin Ti films deposited by high power impulse magnetron sputtering. *Surf. Coat. Technol.* **2021**, *418*, 127235. [CrossRef]
13. Duan, R.; Li, S.; Cai, B.; Zhu, W.; Ren, F.; Attallah, M.M. A high strength and low modulus metastable β Ti-12Mo-6Zr-2Fe alloy fabricated by laser powder bed fusion in-situ alloying. *Addit. Manuf.* **2021**, *48*, 101708. [CrossRef]
14. Prakash, C.; Singh, S.; Ramakrishna, S.; Królczyk, G.; Le, C.H. Microwave sintering of porous Ti–Nb-HA composite with high strength and enhanced bioactivity for implant applications. *J. Alloys Compd.* **2020**, *824*, 153774. [CrossRef]
15. Markhoff, J.; Weinmann, M.; Schulze, C.; Bader, R. Influence of different grained powders and pellets made of Niobium and Ti-42Nb on human cell viability. *Mater. Sci. Eng. C* **2017**, *73*, 756–766. [CrossRef]
16. Liu, L.; Li, W.; Sun, H.; Wang, G. Effects of Ti Target Purity and Microstructure on Deposition Rate, Microstructure and Properties of Ti Films. *Materials* **2022**, *15*, 2661. [CrossRef]
17. Cai, K.; Müller, M.; Bossert, J.; Rechtenbach, A.; Jandt, K.D. Surface structure and composition of flat titanium thin films as a function of film thickness and evaporation rate. *Appl. Surf. Sci.* **2005**, *250*, 252–267. [CrossRef]
18. Oya, T.; Kusano, E. Effects of radio-frequency plasma on structure and properties in Ti film deposition by dc and pulsed dc magnetron sputtering. *Thin Solid Film.* **2009**, *517*, 5837–5843. [CrossRef]
19. Bălţatu, M.S.; Vizureanu, P.; Goanţă, V.; Ţugui, C.A.; Voiculescu, I. *Mechanical Tests for Ti-Based Alloys as New Medical Materials*; IOP Publishing: Bristol, UK, 2019; Volume 572, p. 012029.
20. Hsu, H.C.; Wu, S.C.; Chiang, T.Y.; Ho, W.F. Structure and grindability of dental Ti-Cr alloys. *J. Alloys Compd.* **2009**, *476*, 817–825. [CrossRef]
21. Xu, W.; Chen, M.; Lu, X.; Zhang, D.W.; Singh, H.P.; Jian-shu, Y.; Pan, Y.; Qu, X.H.; Liu, C.Z. Effects of Mo content on corrosion and tribocorrosion behaviours of Ti-Mo orthopaedic alloys fabricated by powder metallurgy. *Corros. Sci.* **2020**, *168*, 108557. [CrossRef]
22. Asl, M.S.; Delbari, S.A.; Azadbeh, M.; Namini, A.S.; Mehrabian, M.; Nguyen, V.H.; Van Le, Q.; Shokouhimehr, M.; Mohammadi, M. Nanoindentational and conventional mechanical properties of spark plasma sintered Ti-Mo alloys. *J. Mater. Res. Technol.* **2020**, *9*, 10647–10658.
23. Lee, C.M.; Ju, C.P.; Chern Lin, J.H. Structure-property relationship of cast Ti-Nb alloys. *J. Oral. Rehabil.* **2022**, *29*, 314–322. [CrossRef]
24. Dos Santos, R.F.; Rossi, M.C.; Vidilli, A.L.; Borrás, V.A.; Afonso, C.R.M. Assessment of β stabilizers additions on microstructure and properties of as-cast β Ti–Nb based alloys. *J. Mater. Res. Technol.* **2023**, *22*, 3511–3524. [CrossRef]
25. Fikeni, L.; Annan, K.A.; Mutombo, K.; Machaka, R. Effect of Nb content on the microstructure and mechanical properties of binary Ti-Nb alloys. *Mater. Today* **2021**, *38*, 913–917. [CrossRef]

26. Photiou, D.; Panagiotopoulos, N.T.; Koutsokeras, L.; Evangelakis, G.A.; Constantinides, G. Microstructure and nanomechanical properties of magnetron sputtered Ti-Nb films. *Surf. Coat. Technol.* **2016**, *302*, 310–319. [CrossRef]
27. Zhang, F.; Li, C.; Yan, M.; He, J.; Yang, Y.; Yin, F. Microstructure and nanomechanical properties of co-deposited Ti-Cr films prepared by magnetron sputtering. *Surf. Coat. Technol.* **2017**, *325*, 636–642. [CrossRef]
28. Liu, G.; Yang, Y.; Luo, X.; Huang, B.; Li, P. The phase, morphology and surface characterization of Ti–Mo alloy films prepared by magnetron sputtering. *RSC Adv.* **2017**, *7*, 52595–52603. [CrossRef]
29. Lopes, C.; Vieira, M.; Borges, J.; Fernandes, J.; Rodrigues, M.S.; Alves, E.; Barradas, N.P.; Apreutesei, M.; Steyer, P.; Tavares, C.J.; et al. Multifunctional Ti–Me (Me = Al, Cu) thin film systems for biomedical sensing devices. *Vacuum* **2015**, *122*, 353–359. [CrossRef]
30. Stranak, V.; Wulff, H.; Rebl, H.; Zietz, C.; Arndt, K.; Bogdanowicz, R.; Nebe, B.; Bader, R.; Podbielski, A.; Hubicka, Z.; et al. Deposition of thin titanium–copper films with antimicrobial effect by advanced magnetron sputtering methods. *Mater. Sci. Eng. C* **2011**, *31*, 1512–1519. [CrossRef]
31. Kobata, J.; Miura, K.I.; Amiya, K.; Fukuda, Y.; Saotome, Y. Nanoimprinting of Ti–Cu-based thin-film metallic glasses deposited by unbalanced magnetron sputtering. *J. Alloys Compd.* **2017**, *707*, 132–136. [CrossRef]
32. Wojcieszak, D.; Mazur, M.; Kaczmarek, D.; Mazur, P.; Szponar, B.; Domaradzki, J.; Kepinski, L. Influence of the surface properties on bactericidal and fungicidal activity of magnetron sputtered Ti-Ag and Nb-Ag thin films. *Mater. Sci. Eng. C* **2016**, *62*, 86–95. [CrossRef] [PubMed]
33. Frenzel, J.; Wieczorek, A.; Opahle, I.; Maaß, B.; Drautz, R.; Eggeler, G. On the effect of alloy composition on martensite start temperatures and latent heats in Ni–Ti-based shape memory alloys. *Acta Mater.* **2015**, *90*, 213–231. [CrossRef]
34. Li, B.Y.; Rong, L.J.; Li, Y.Y.; Gjunter, V.E. Electric resistance phenomena in porous Ni-Ti shape-memory alloys produced by SHS. *Scr. Mater.* **2001**, *44*, 823–827. [CrossRef]
35. Yi, X.; Wang, H.; Sun, K.; Sun, B.; Wu, L.; Meng, X.; Gao, Z.; Cai, W. Tailoring of microstructure and martensitic transformation of nanocrystalline Ti–Ni-Hf shape memory thin film. *Prog. Nat. Sci.-Mater.* **2021**, *31*, 288–295. [CrossRef]
36. Li, J.; Sun, K.; Li, X.; Meng, X.; Cai, W. High damping performances over wide temperature range in the B doped Ti-Ni shape memory alloys. *Mater. Lett.* **2023**, *330*, 133245. [CrossRef]
37. Karki, V.; Debnath, A.K.; Kumar, S.; Bhattacharya, D. Synthesis of co-sputter deposited Ni–Ti thin alloy films and their compositional characterization using depth sensitive techniques. *Thin Solid Film.* **2020**, *697*, 137800. [CrossRef]
38. Ren, D.C.; Zhang, H.B.; Liu, Y.J.; Li, S.J.; Jin, W.; Yang, R.; Zhang, L.C. Zhang, Microstructure and properties of equiatomic Ti–Ni alloy fabricated by selective laser melting. *Mater. Sci. Eng. A* **2020**, *771*, 138586. [CrossRef]
39. Macías, H.A.; Yate, L.; Coy, L.E.; Olaya, J.J.; Aperador, W. Effect of nitrogen flow ratio on microstructure, mechanical and tribological properties of $TiWSiN_x$ thin film deposited by magnetron co-sputtering. *Appl. Surf. Sci.* **2018**, *456*, 445–456. [CrossRef]
40. Kabir, M.S.; Munroe, P.; Zhou, Z.; Xie, Z. Study of the structure, properties, scratch resistance and deformation behaviour of graded $Cr\text{-}CrN\text{-}Cr_{(1\text{-}x)}Al_xN$ coatings. *Ceram. Int.* **2018**, *44*, 11364–11373. [CrossRef]
41. Sha, C.; Zhou, Z.; Xie, Z.; Munroe, P. Scratch response and tribological behaviour of CrAlNiN coatings deposited by closed field unbalanced magnetron sputtering system. *Surf. Coat. Technol.* **2019**, *367*, 30–40. [CrossRef]
42. Heinke, W.; Leyland, A.; Matthews, A.; Berg, G.; Friedrich, C.; Broszeit, E. Evaluation of PVD nitride coatings, using impact, scratch and Rockwell-C adhesion tests. *Thin Solid Film.* **1995**, *270*, 431–438. [CrossRef]
43. Kim, H.K.; La, J.H.; Kim, K.S.; Lee, S.Y. The effects of the H/E ratio of various Cr–N interlayers on the adhesion strength of CrZrN coatings on tungsten carbide substrates. *Surf. Coat. Technol.* **2015**, *284*, 230–234. [CrossRef]

coatings

MDPI

Article

Coating Condition Detection and Assessment on the Steel Girder of a Bridge through Hyperspectral Imaging

Pengfei Ma [1], Jiaoli Li [1], Ying Zhuo [1], Pu Jiao [2] and Genda Chen [1],*

[1] Department of Civil, Architectural, and Environmental Engineering, Missouri University of Science and Technology, Rolla, MO 65409, USA; pm7m8@mst.edu (P.M.); jlbbt@mst.edu (J.L.); yingzhuo@mst.edu (Y.Z.)
[2] Department of Computer Science, University of Kentucky, Lexington, KY 40506, USA; pujiao@uky.edu
* Correspondence: gchen@mst.edu

Abstract: The organic coating of bridge steel girders is subjected to physical scratches, corrosion, and aging in natural weathering. The breakdown of the coating may cause serviceability and safety problems if left unnoticed. Conventional coating inspection is time-consuming and lacks information about the coating's chemical integrity. A hyperspectral imaging method is proposed to detect the condition of steel coatings based on coating-responsive features in reflectance spectra. A field test was conducted on the real-world bridge, which shows obvious signs of degradation. The hyperspectral signature enables an assessment of the coating's health and defect severity. The results indicated that the coating scratch can be effectively located in the domain of a hyperspectral image and the scratch depth can be determined by mapping a scratch depth indicator (SDI = R532 nm/R641 nm). Rust sources and products in steel girders can be identified by the unique spectral signatures in the VNIR range, and the rust stains (and thus stain areas) scattered on the coating can be pinpointed at pixel level by the chloride rust (CR) indicators >1.11 (CR = R733 nm/R841 nm). The chemical integrity of a topcoat is demonstrated by the short-wave infrared spectroscopy and the topcoat degradation can be evaluated by the decreased absorption at 8000 cm^{-1} and 5850 cm^{-1}. Hyperspectral imaging enables faster and more reliable coating condition detection by the spectral features and provides an alternative for multi-object coating detection.

Keywords: steel girder; nondestructive inspection; corrosion; coating degradation; spectroscopic analysis; hyperspectral imaging

1. Introduction

Steel has been a candidate in civil engineering, especially bridges, because of its high strength and light weight. There are many uses of steel components in suspension, cable-stay, and girder bridges to overcome the self-weight problem [1,2]. It can also be used as a superstructure for arch bridges to facilitate the construction of the deck and carry loads. For example, the Sydney Harbor Bay bridge [3]. In addition, steel is also widely used for girders in highway bridge networks (>30%) to provide more clearance for traffic [4]. However, steel components that are exposed to the natural weathering environment will be severely impaired by corrosive media, thus introducing safety and serviceability issues [4,5]. According to the Federal Highway Administration (FHWA) [6], statistics show that around 45% of steel bridges are structurally deficient, with 19% being almost structurally obsolete. Corrosion is currently the biggest concern for the structural integrity of steel components because corrosion can significantly (almost 40%) reduce fatigue strength [7–9]. For example, corrosion is illustrated as the reason for the sudden collapse of the I-35W steel deck truss bridge in Minneapolis, USA [10]. The deteriorated coating increased the chances of corrosion on the steel substrate [4]. Therefore, regular inspection is necessitated for coating, and its conditions should be assessed to ensure acceptable serviceability and protect the substrate from direct contact with corrosive factors [9].

Coatings **2023**, *13*, 1008. https://doi.org/10.3390/coatings13061008

Coatings are required to have protection against various degradations, whether physical or chemical [11]. The coating should be able to withstand physical impairments such as scratches and abrasions, as well as some aggressive species such as chlorides, acids, and water [4,11–13]. Coating defects are thus different depending on degradation exposures [13]. Many aspects of the coatings can be monitored to assess their condition, such as delamination, chalking, checking, and rust staining [13,14]. Visual inspection has long been practiced for bridge coating due to its reliable inspection quality. However, this method requires experienced practitioners, and the evaluation of coating condition assessment might be subjected to objective and quantifiable issues. Visual inspection is also time-consuming and labor-intensive, which makes it impossible in terms of regular inspection [15]. The electrochemical impedance spectroscopy (EIS) technique has been studied to detect coating integrity as well as substrate corrosion occurrence. Impedance values can effectively reflect the coating status before the presence of macroscopic degradations, but EIS does not give local information and thus a vague location of the impaired coating spots [16,17]. Spectroscopic techniques, including Fourier transform infrared spectroscopy (FTIR), Raman spectroscopy, and Mossbauer spectroscopy, have been performed to evaluate the coating conditions but are generally limited to lab experiments [11,18–20]. The image-based method has been implemented together with machine learning techniques over the last two decades to achieve fast inspection [21,22]. The pixel-level imagery features in conjunction with the artificial intelligence (AI) algorithm significantly improved efficiency and reliability, which might be a substitute for human inspection [21,23]. However, an apparent drawback is that red, green, and blue (RGB) images are unable to provide information about the coating chemicals, thus preventing a thorough assessment before the occurrence of the obvious defects [24]. In addition, it may confront some confusion in the detection if the defects are dominantly featured by color and the computer vision method is sensitive to the nonuniform illuminations on the detected surfaces [21].

Hyperspectral imaging (HSI) is emerging as a compromised tool for simultaneous spatial and spectral inspection because hyperspectral imaging possesses the RGB information and the surface composition information according to the response at different wavelengths [8,25]. Therefore, both spatial dysconnectivity and compositional inhomogeneity can be plotted in the context of hyperspectral imaging [25]. The technique has been utilized to quantitatively assess the coating thickness of the paint on the steel according to the spectral signature as well as the discrimination of different chemical binders and polymers in the coating composition for automatic coating condition detection [26–28]. Likewise, near-infrared (NIR) spectroscopy was used to evaluate the conversion of white pigment of the acrylate coatings exposed to ultraviolet (UV) radiation [28]. Hyperspectral imaging has also been tested to identify pinholes in the coating by introducing a matching filter at the pixel level [24]. To differentiate the colors from different objects in the girder coatings, Dayakar established a support vector machine (SVM) model, and the color yellow from corrosion rust in different environments, acid or sulfate, can be discriminated against with 94% accuracy [3]. Hyperspectral imaging was also practiced in an arch bridge truss coating assessment. The proposed multi-class SVM can generate highly accurate coating assessment results by integrating information from only 21 bands in the range of the visible spectrum [29]. However, the application of hyperspectral imaging is mainly focused on the characterization of coating degradation in the lab. It is noted that the established method based on HSI for coating defect identification and condition assessment in real structures is not sufficient.

In this study, hyperspectral imaging is proposed to inspect the coatings on the steel girder of a real bridge. Some typical coating defects under natural weathering exposures are preselected for hyperspectral scanning to demonstrate their capability. The hyperspectral results are validated with ground-truth lab characterizations, FTIR, scanning electron microscope (SEM), and energy-dispersive X-ray spectroscopy (EDS), to illustrate the applicability of hyperspectral imaging techniques in coating condition detection and assessment. It is found that the coating scratch profiles can be detected, and the scratch depth is characterized by the spectral signatures of the coating layers and substrate. The chemically degraded coating can be distinguished from the sound coating by hyperspectral reflectance features in short-wave infrared (SWIR). In addition, the rust stains can be identified without color bias by hyperspectral imaging, and the rust medium can be recognized according to the unique spectral signatures of rust products.

2. Materials and Methods

The proposed hyperspectral imaging technique for coating condition detection is demonstrated on a continuous girder bridge on the main road of 10th Street (37.951454, −91.769034), Rolla, Missouri, USA. The bridge is an eight-span steel girder bridge with a span configuration of 15.79 m, 15.54 m, 16.46 m, 18.59 m, 18.89 m, 12.49 m, 16.15 m, and 11.85 m (totaling 125.5 m) from west to east as shown in Figure 1. The steel used in the bridge girder is fabricated structural carbon with a nominal yield strength of 20,000 psi. W30 and W33 steel girders were used for the continuous-span bridge to provide more clearance for the railway.

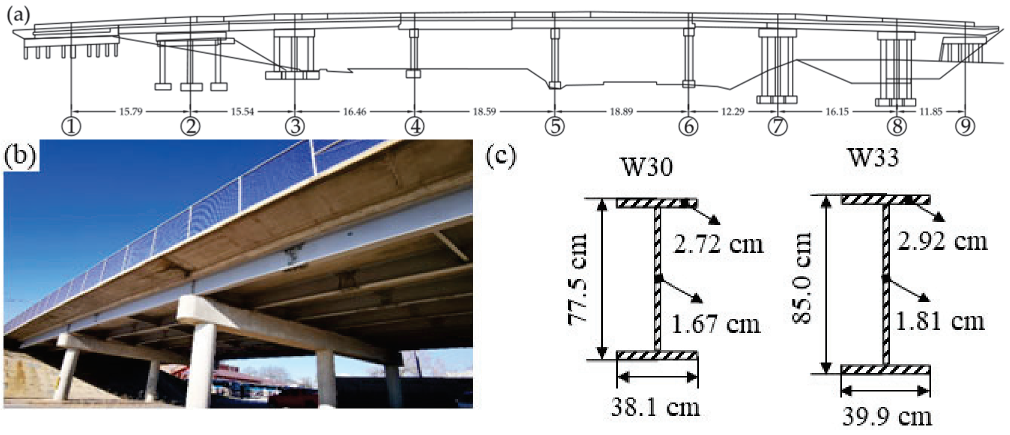

Figure 1. (**a**) the original drawing of the bridge design; (**b**) a view of the real test bridge; (**c**) steel girder dimension.

The bridge was constructed in 1974, and the steel girders were originally coated with brown lead silicochromate. The coating was removed in 2002 due to health concerns in terms of lead and was replaced by the current calcium sulfonate pigmented alkyd coating coupled with epoxy primer, as shown in Figure 2. Calcium sulfonate alkyd paint is designed for replacement due to its significant corrosion-inhabitation effect. The substitution of calcium sulfonate alkyd is due to its continuous release of corrosion inhibitors. Moreover, the multilayer coating system can significantly prevent the ingress of corrosive ions due to the more compact interface between alkyd and epoxy, as demonstrated by the scanning Kelvin probe (SKP) [30]. This bridge was selected as the research object because of the presence of various typical coating detects on the girders. In addition, an alkyd topcoat is also one of the most widely used paints in current bridge protection [4].

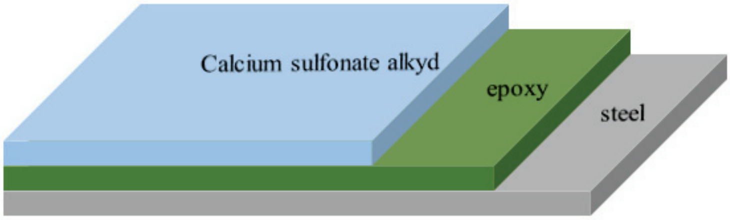

Figure 2. Coating system demonstration for the steel girder.

To characterize the coating defects with hyperspectral imaging, the preselected spots of interest (SOI) on the girder coating were scanned with a Headwall dual-lens hyperspectral (Headwall phonetic, Boston, MA, USA) camera as shown in Figure 3. The camera has a 1.2 m standoff from the SOIs. Under natural light radiation, the exposure time was set to 45 ms accordingly to prevent overexposure in the hyperspectral image. The hyperspectral camera in this study enables the spectral range of visible and near-infrared (VNIR, 400–100 nm) and short-wave infrared (SWIR, 1000–2500 nm) with a spectral resolution of 2.21 nm in VNIR and 6.02 nm in SWIR. Prior to every HSI collection, the dark was captured with the cap on to reduce the internal current noise in the image. Likewise, white reference was also collected for the conversion of the raw digital numbers to radiance and finally reflectance. In this test, the camera was supported by a tripod because the SOIs are accessible; otherwise, the camera can be integrated into an unmanned aerial vehicle for coating inspection.

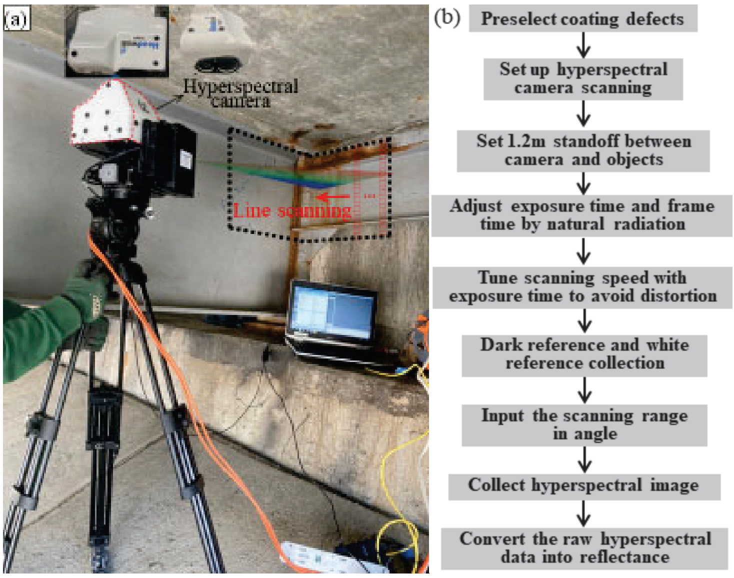

Figure 3. (**a**) Setup for hyperspectral imaging collection in the field; (**b**) data collection configuration.

Hyperspectral imaging is indeed a subset of the spectroscopic technique for polymer characterization in this study. As the hyperspectral imaging in this study enables wavenumbers from 4000 cm^{-1} to 10,000 cm^{-1}, it is characterized by band combinations, coupling, and overtones [28]. Therefore, FTIR is used to validate the hyperspectral results. Some coating samples are retrieved from the bridge for analysis. The FTIR spectra were recorded with a Nicolet™ iS50 FTIR Spectrometer (Thermo Fisher Scientific, Waltham, MA, USA) in the spectral range between 400 cm^{-1} and 4000 cm^{-1} with a resolution of 4 cm^{-1}. For each sample, 16 runs were performed to enhance the spectra and reduce the noise. The FTIR spectra are presented in transmittance for easy comparison in this study. In addition, scanning electron microscopy (SEM) was performed on coating (rust-stained, healthy, and degraded) samples using a Helios Hydra CX (Thermo Fisher Scientific, Waltham, MA, USA) with an accelerating voltage of 15 kV and a beam current of 0.8 nA under high vacuum pressure ($<5.0 \times 10^{-4}$ Pa). The working distance between the lens and the sample was set to 4 mm. To determine the atomic distribution on the topcoat, EDS energy-dispersive X-ray spectroscopy (EDS) was performed with a Thermo Noran Ultra Dry 60 mm^2 detector (Thermo Fisher Scientific, Waltham, MA, USA) by mapping in the Pathfinder X-ray Microanalysis Software-2022 (Thermo Fisher Scientific, Waltham, MA, USA). As the organic coating in this study is nonconductive, all samples were coated with a thin film of gold/palladium (Au/Pd) by sputtering for 45 s to prevent charging.

3. Results and Discussion

3.1. Coating Scratch

Figure 4 presents a view of the coating scratch on the bridge steel girder. It is observed that the scratch depth varies along the trace as the scratch even reaches the undercoat in some areas. The coating thickness is reduced, though the color difference from the original view is not significant. In addition, it is not known whether the substrate steel is exposed due to scratches. A coating is used to protect the steel from corrosive media. Corrosion can initiate at a bare steel spot, and the effect gradually propagates concentrically to the local area, which progressively damages the health coatings. Figure 4b shows the comparison of the spectral signatures in the range of 400–1000 nm (visible and near-infrared, VNIR) from different objects, topcoat (pigmented alkyd), undercoat (epoxy), and girder steel, in the domain of scratches from the hyperspectral imaging. In view of hyperspectral imaging, those three objects are spectrally different, especially for the topcoat and undercoat, though both are organic polymers that are characterized by aromatic rings and side chains. As for the substrate, steel does not yield any absorption features in the range of VNIR because it is composed of metal ions, which do not absorb photons in the current wavelength domain [29].

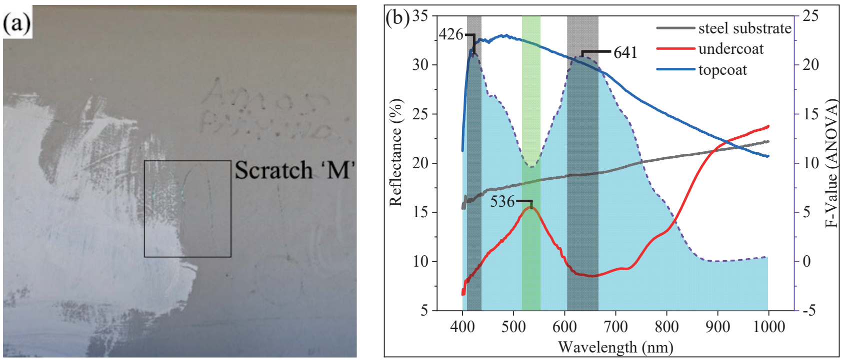

Figure 4. Coating scratch on the steel girder. (**a**) Original view; (**b**) spectral signatures of different coating layers and the corresponding F−values from ANOVA analysis of spectra.

To differentiate different layers of coating, a scratch depth indicator (SDI) is developed by comparing the ratio between two bands, 536 nm and 641 nm. Figure 4b displays the F-value results derived from the one-way ANOVA analysis based on the spectra from the three objects. There are two local maxima at 426 nm and 641 nm and one local minimum at 536 nm. According to the ANOVA F-value, spectra at wavelength 536 nm yield the least variation ($p < 0.05$) in the range of 400–750 nm. For comparison, 426 nm and 641 nm are more sensitive to the differences between different coating layers because higher close F-values are observed, which are around 21 ($p < 0.05$). To establish a robust indicator, 641 nm is selected as the most sensitive band in this study because 426 nm is located at the beginning of the spectrum, which is usually subjected to severe mechanical noises [8]. Figure 5a demonstrates the mapping of SDI (536 nm/641 nm) in hyperspectral imaging. The scratch profile can be easily identified, and the exposed undercoat can be located by the black spots. For the RGB method, the color feature of the scratch is used to identify the scratch profile, and the result is easily subjected to false detection if objects with similar colors are present [31]. In order to assess the scratch condition, different layers of the coating are retrieved from the mapping by thresholds to demonstrate the scratch depth. The corresponding SDI threshold for undercoat and steel is obtained from the distribution of the SDI values, as illustrated in Figure 5c,f. For undercoat epoxy, the critical SDI of 1.33 isolates the exposed undercoat, though some scattered misidentifications can be observed. Most of the misclassifications of the undercoat are located in the shades of the white reference board. This is because the shade can distort the spectra and thus produce incorrect information, which can be eliminated by the additional external light source in real practice [26]. It is noted that several pixels are distinguished from the undercoat in the heart of scratch “M”, which is the substrate steel. As hyperspectral imaging also enables a high spatial resolution of 0.56 mm in this study, the exposed steel can be spotted by the critical SDI of 0.95. The selection of the critical SDI in this study is because 95% of the calculated SDI from the pixels on the steel substrate are between 0.95 and 1.02. There are in total 5 pixels (pixel dimension: 0.56 × 0.56 mm) that can be identified, which makes a 1.57 mm^2 exposure. It is worth noting that hyperspectral imaging can perform a much more accurate inspection by using spectral information compared to RGB inspection because the resolution is not high enough to identify such small defects [21,22].

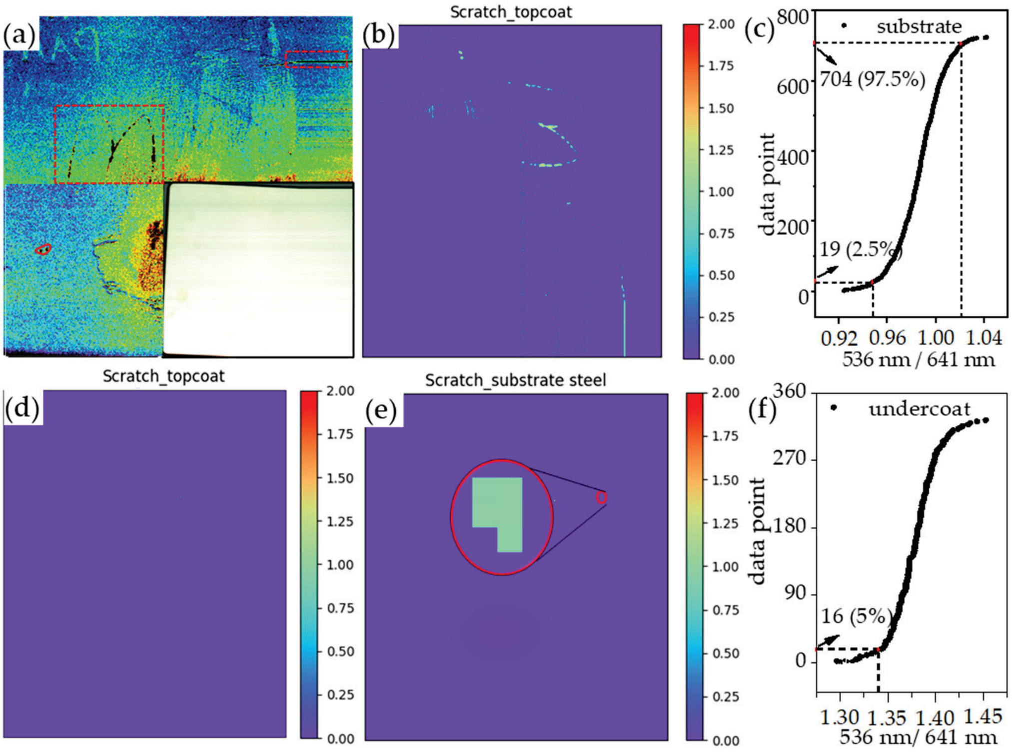

Figure 5. Different layers of the girder coating with scratches. (**a**) Mapping of SDI (536 nm/641 nm) in hyperspectral imaging; (**b**) scratch of undercoat (SDI > 1.33); (**c**) derivation of the critical SDI for undercoat; (**d**) topcoat; (**e**) scratch of substrate steel (0.95 < SDI < 1.02); (**f**) derivation of the critical SDI for steel.

3.2. Steel Rust Stains

The steel rust percentage has been used as an indicator to assess the coating conditions according to ASTM D610-08 for timely remedies [23,31]. Figure 6 presents the coating surface with steel rust stains as well as the corroded steel girder top flange. Many corrosive media cause rust in the atmospheric environment, and the corrosion products may vary. Acidic exposures are prone to producing magnetite (Fe_3O_4), ferrous chloride ($FeCl_2$), and iron oxide-hydroxide (FeOOH) [31]. For chloride salt ions attack, akageneite (β-FeOOH) and goethite (α-FeOOH) are the main corrosion products [31,32]. Two steel plates treated with sodium chloride and water, respectively, are prepared and placed in the scanning view. Figure 6b shows the spectral signatures in the VNIR range derived from corrosion spots on two plates. It is noted that the rust products with different exposures differ spectrally. Rust obtained from sodium chloride solution yields three absorption features at 612 nm, 733 nm, and 841 nm, and water-based corrosion products have features at 708 nm and 950 nm, which are characterized by water [8]. The spectra for the corrosion rust from different sources are consistent with the previous study [33].

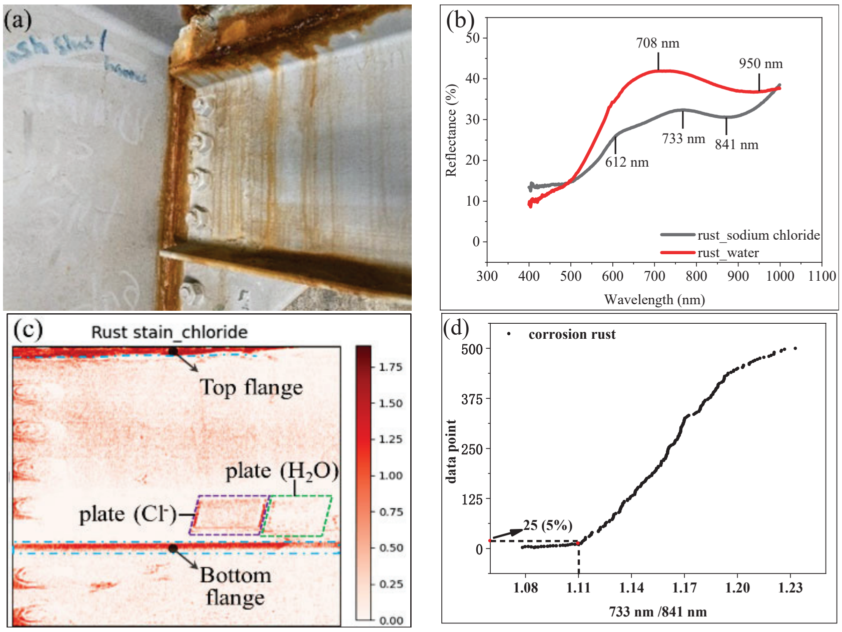

Figure 6. Girder coating with rust stain. (**a**) The view of the rust spot; (**b**) spectral signatures of the different rust products in VNIR; (**c**) rust stain demonstration by CR indicator (>1.11); (**d**) critical CR for rust stain on topcoat.

As chloride corrosion is more aggressive, it is worth emphasizing its corrosion effect before the pervasive attack on both substrate and organic coatings [14]. The chloride rust (CR) indicator, 733 nm/841 nm, is constructed to demonstrate the corrosion products. Figure 6c demonstrates the mapping of CR in the domain of hyperspectral imaging with a threshold of 1.11. This critical CR is obtained from the stain pixels in the diaphragm with the same method as illustrated in SDI. The severely rusted steel flanges can be identified in CR mapping as indicated by the dark red areas. Moreover, the rust stain on the coating in the diaphragm is also detected by the CR, though the CR values are smaller compared to the rust spots. It is because rust products intermingle with the topcoat in the domain of a pixel. The hyperspectral spectrum is representative of the overall composition of the chemicals in that pixel [8]. As for the rust spot inspection, the hyperspectral imaging technique greatly reduced the false detection as opposed to the RGB method [33].

The coating samples with rust stains are analyzed by energy-dispersive X-ray spectroscopy (EDS) as opposed to the normal coating on this girder. Figure 7 shows the comparison of the element mapping results. The EDS spectrum as shown in Figure 7a demonstrates detectable peaks in terms of chloride (Cl) for the rust-stained coating, while the rust-free coating is dominated by the topcoat polymer compositional elements, carbon (C) and oxygen (O). The presence of Cl is also reflected by the element mapping result, as illustrated in Figure 7b. For elements related to steel rust, Fe and Cl show significant differences in distribution. Oxygen (O) is not considered here to distinguish rust because of its massive existence in alkyd resins and thus cannot be easily impacted [34]. As seen from Figure 7b, Fe is more visible on the coating with rust stains, though Fe is also spotted in the rust-free coating samples. For Cl, the contrast is more significant because it almost disappears in rust-free samples. Table 1 shows the element ratio of each detectable element present on the coating surface. C and O occupy, in total, about 90% of the coating topology, and nitrogen (N) is the third prevailing element that makes up around 7.5% of the coating topology. The elemental dominance agrees well with the composition of alkyd. The rust-stained coating has Fe of 1.78%, which is higher than the 0.56% in the rust-free coating. As for Cl, it occupies 0.51% of the total detectable elements for the topcoat with rust stains in comparison with 0% Cl in the stain-free topcoat. Element Cl distinguishes the rust-contaminated coatings from the rust-free sample, which shows negligible presence.

The result is consistent with the hyperspectral imaging result, which shows the rust stain distribution as well as the corrosion source as Cl-related media.

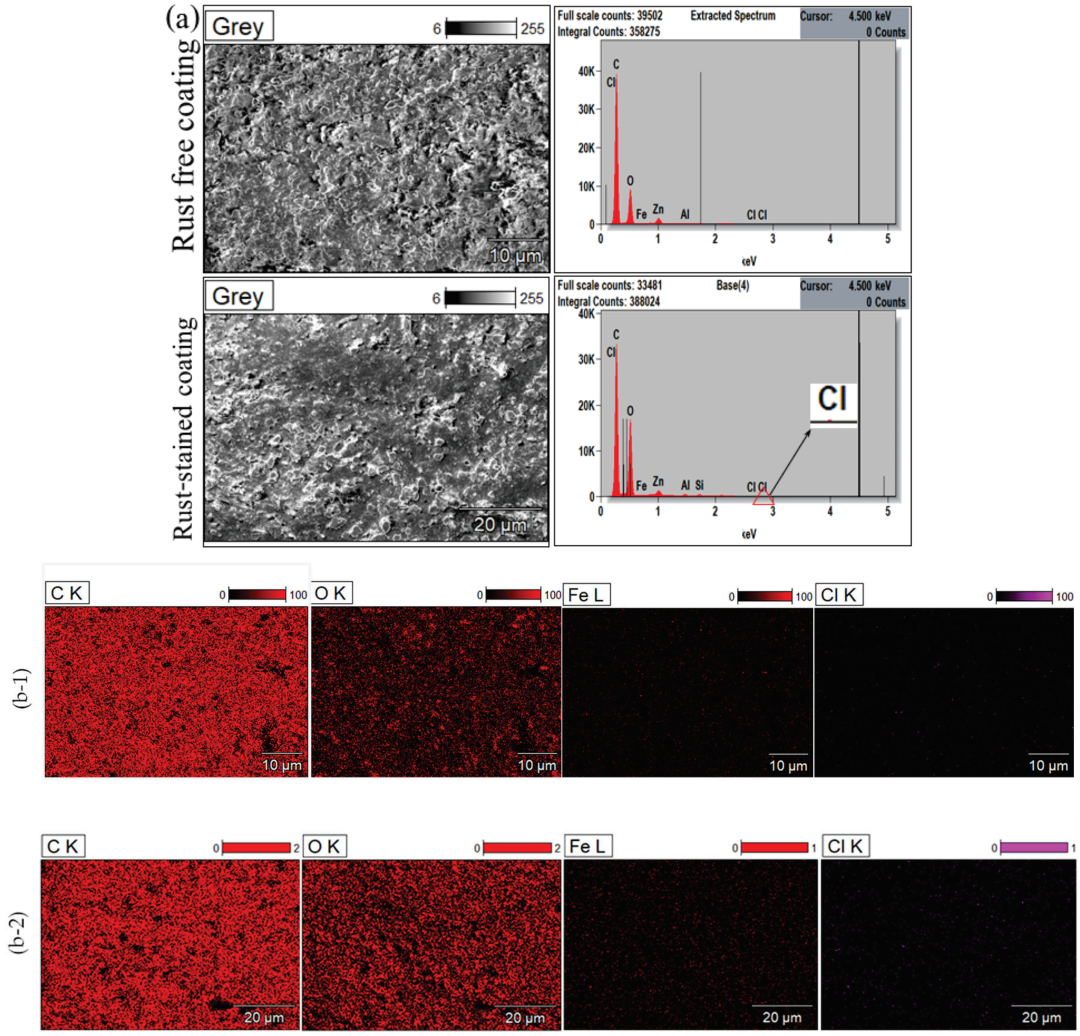

Figure 7. Comparison of the element distribution on the coating with and without rust stains by (**a**) EDS spectra, (**b-1**) element distribution of rust-free topcoat from EDS mapping, (**b-2**) element distribution of rust-stained topcoat from EDS mapping.

Table 1. Percent of the detachable elements on the coating with and without rust stain.

Element	C	O	N	Fe	Cl	Al	Zn
Rust-free coating	54.34	36.00	7.31	0.56	0	0.48	1.31
Rust-stained coating	53.15	34.98	7.43	1.78	0.51	0.38	1.53

3.3. Degraded Topcoat

A degraded topcoat can expose the undercoat and thus increase the corrosion probability of the substrate. Early detection can potentially enhance the serviceability of steel girders. Figure 8 shows the deteriorated topcoat on the bottom flange of the steel girders in the proposed field bridge. Those deteriorated topcoats have lost their cling to the undercoat and thus cannot effectively protect the undercoat and substrate. As the degradation is generally characterized by chain breakage due to oxidation, Figure 9 displays the comparison between healthy and degraded topcoats by both FTIR and SWIR spectroscopy from hyperspectral imaging. FTIR provides complementary information for SWIR spectroscopy to interpret the topcoat degradation in view of the binder’s chemical connections.

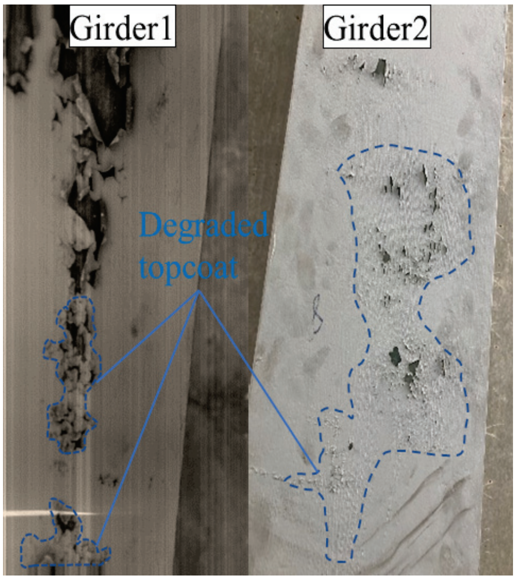

Figure 8. Demonstration of the degraded topcoat on the bottom flange of the steel girder.

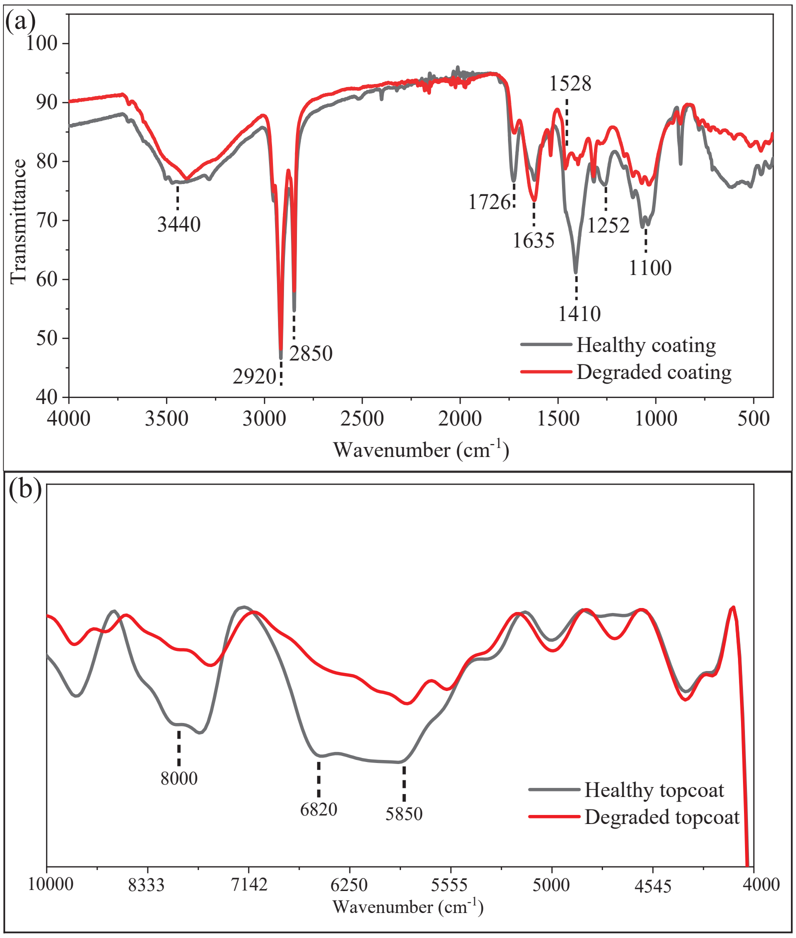

Figure 9. Comparison of the healthy and degraded topcoat in the range of (**a**) 400−4000 cm^{-1} (FTIR), (**b**) 4000–10,000 cm^{-1} (SWIR).

Considering the natural aging and atmospheric exposure effects on the topcoat, the stretching vibrations of the C=O at 1726 cm^{-1} and C–O–C at 1528 cm^{-1} are featured by the bond cleavage in the polyester of the girder topcoat, alkyd resin [35,36]. Table 2 summarizes the band assignment of the alkyd resin. It can be seen that the narrow absorption bands at 1726 cm^{-1} and 1528 cm^{-1} both significantly decrease for the degraded topcoat in comparison to the healthy, which indicates the chains shortening in the polymer [36]. The chain scission in polyester is also observed by the decreasing absorption at 2920 cm^{-1} and 2850 cm^{-1} for degraded topcoat, which illustrates the reduced presence of the side chains [37]. In addition, the O–C–O featured band at 1410 cm^{-1} almost disappears to demonstrate the reduction side chain [38]. On the contrary, it is noted that 1635 cm^{-1} is boosted due to the degradation effect on the topcoat [36,39]. It is because of the autooxidation of the polymer crosslink. In this process, the degraded alkyd resin releases alcohol and carbonyl species, which thus reduces the molecular weight of the original topcoat component [37]. The decreasing weight of alkyd resin can also be implied by the diminished bands at 1100 cm^{-1} and 1252 cm^{-1}. The breakage of C–O–C produces volatile species, for example, phthalic acid due to the Norrish Type I reaction [39]. Figure 10 shows the microstructure of the healthy and deteriorated topcoats by SEM. In comparison, the degraded topcoat yields a messier topology, and the topcoat has been degraded into more pieces. Table 3 illustrates the presence of detectable elements on the topcoat derived from the EDS mapping results. C is significantly reduced from the healthy to the degraded topcoat due to the oxidation effect, which conforms to the FTIR results.

Table 2. Major bands of alkyd resin in FTIR and its band assignment.

Wavenumber (cm^{-1})	Assignment
741–705	Aromatic out-of-plane bending
<1000	Ring vibrations and C–X (with X=Cl or CH_3) coupling
1070	Aromatic in-plane bending
1119	C–O–C stretching
1258	C–O–C stretching
1340–1300	Vibrations involving the aromatic rings
1429	O–C–O bending
1528	C–O–C bending
1590	Aromatic in-plane bending
1650–1500	C=N, C=O
1635	C=C stretching
1726	C=O stretching vibration carboxylic acids and esters
2850	(C–H)-CH_2 symmetric stretching
2921	(C–H)-CH_2 asymmetric stretching
3440/3314	OH stretching

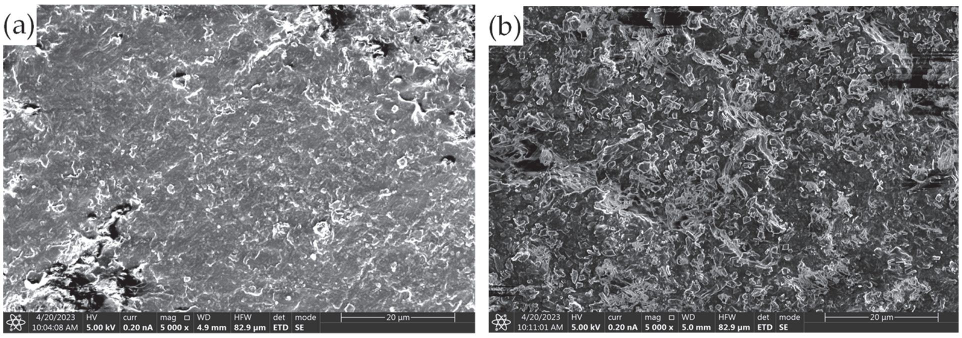

Figure 10. Topology by SEM of (**a**) healthy topcoat; (**b**) degraded topcoat.

Table 3. Percentage of the detachable elements on the coating with and without rust stains.

Element	C	O	N	Fe	Cl	Al	Zn
Healthy topcoat	53.15	37.53	7.43	0.43	0	0.52	1.37
Degraded topcoat	42.19	48.47	7.58	0.25	0	0	1.50

Figure 9b presents the spectra derived from the healthy and the degraded topcoat in the range of 4000–10,000 cm^{-1} after continuum removal processing to facilitate quantitative comparison [28,39]. As illustrated in the FTIR, the main and side chains were greatly shortened due to the degradation effect. The reduction of the C=O in the degraded topcoat can also be detected in SWIR spectroscopy by the carbonyl stretching characterized bands at 5850 cm^{-1} [40]. This band should be the overtones of the fundamental vibration of the carbonyl groups illustrated in 400–2000 cm^{-1}. A similar decreasing trend at 5850 cm^{-1} is also observed on the alkyd resins under ultra-violate exposure [41]. Another significant difference is located around 6820 cm^{-1}, characterized by the second overtone of the hydroxyl group [8,41]. The absorption feature is almost gone due to the deterioration of the topcoat. The deletion of hydroxyl groups is also observed by the absorption at 3440 cm^{-1} [36,37]. However, band 3440 cm^{-1} remains significant, though it has decreased. It is because 3440 is characterized by not only the bending vibration of hydroxyl but also water [8]. The third recognizable spectral zone that differentiates healthy and degraded topcoats is around 8000 cm^{-1}. This absorption intensity of this broadband shrinks due to the degradation of the topcoat, which is attributed to the loss of the oxygenated products, singly doubly bonded oxygen, due to photooxidation [40].

4. Conclusions

The manuscript presents a study that uses hyperspectral imaging to detect coating defects in bridge steel girders. Coating scratch, substrate rust, and topcoat degradation are evaluated. The major findings can be summarized as follows:

i. Scratch profiles can be effectively depicted by scratch depth indicators by applying a critical threshold for each coating layer. The epoxy undercoat can be discriminated against by SDI > 1.33, and the exposed substrate is identified by 0.95 < SDI < 1.02.
ii. The source of the corrosion products can be evaluated by the absorption features at 612, 708, 733, 841, and 950 nm in the VNIR range. Water-based corrosion products yield features at 708 and 950 nm, while chloride-based rust features absorption at 612, 733, and 841 nm.
iii. The rust-stained coating can be estimated by the corrosion rust indicators (CR (R733/R841) > 1.11), and the total area of the corrosion spot can then be calculated by the pixel dimensions.
iv. As for the degraded topcoat, SWIR spectra show significant reduction at 8000 cm^{-1}, 5850 cm^{-1} as well as hydroxyl absorption at 6820 cm^{-1}.

For a more robust inspection of the girder coatings, further work should focus on the quantitative study of how the SWIR spectra can evaluate the severity of the coating degradations. And more types of industrial coatings need to be tested with hyperspectral imaging to determine the corresponding indicator to differentiate their presence from other layers, which can greatly expand the application of hyperspectral imaging in fast nondestructive inspection of the girder coating conditions.

Author Contributions: Conceptualization, methodology, investigation, writing original draft preparation, P.M.; methodology, investigation, J.L.; methodology, Y.Z. and P.J.; review and funding acquisition, G.C. All authors have read and agreed to the published version of the manuscript.

Funding: Financial support to complete this study was provided by the US Department of Transportation, Office of the Assistant Secretary for Research and Technology (USDOT/OST-R) under Grant No. 69A3551747126 through the INSPIRE University Transportation Center (https://inspire-utc.mst.edu, accessed on 23 May 2023) at Missouri University of Science and Technology. The views, findings, and conclusions reflected in this publication are solely those of the authors and do not represent the official policy or position of the USDOT/OST-R, or any state or other entity.

Institutional Review Board Statement: Not applicable.

Informed Consent Statement: Not applicable.

Data Availability Statement: Not applicable.

Acknowledgments: The authors wish to thank Ibrahim Alomari and Peter Ogunjinmi for their assistance during hyperspectral data collection at the bridge site.

Conflicts of Interest: The authors declare no conflict of interest.

References

1. Kitada, T. Considerations on recent trends in, and prospects of, steel bridge construction in Japan. *J. Constr. Steel Res.* **2006**, *62*, 1192–1198. [CrossRef]
2. Ma, P.; An, J.; Zhang, B.; Zhu, P.; Zhao, H. Research on Axle Load Recognition Algorithm Based on U-rib Transverse Influence Line. *Highw. Eng.* **2020**, *45*, 9. [CrossRef]
3. Mustapha, S.; Huynh, C.P.; Runcie, P.; Porikli, F. Paint condition assessment of civil structures using hyper-spectral imaging. In Proceedings of the 7th International Conference on Structural Health Monitoring of Intelligence Infrastructure—SHMII 2015, Torino, Italy, 1–3 July 2015; Intl Society for Structural Health Monitoring of Intelligent Infrastructure: Red Hook, NY, USA, 2015.
4. Yanez, L.M.M. Bridge Maintenance to Enhance Corrosion Resistance and Performance of Steel Girder Bridges. Ph.D. Thesis, Purdue University, West Lafayette, IN, USA, 2016.
5. Zhang, L.; Lv, X.; Lau, K.; Viswanathan, S.; Li, M.; Gosain, P. *Assessment of Structural Steel Coating Applications*; Florida Department of Transportation: Tallahassee, FL, USA, 2021.
6. FHWA; USDOT. *Bridges and Structures—Bridges by Year Built 2013*; Federal Highway Administration; US. Department of Transportation: Washington, DC, USA, 2015. Available online: http://www.fhwa.dot.gov/bridge/structyr.cfm (accessed on 20 April 2023).
7. Menga, A.; Kanstad, T.; Cantero, D.; Bathen, L.; Hornbostel, K.; Klausen, A. Corrosion-induced damage and failures of posttensioned bridges: A literature review. *Struct. Concr.* **2023**, *24*, 84–99. [CrossRef]
8. Ma, P.; Fan, L.; Chen, G. Hyperspectral reflectance for determination of steel rebar corrosion and Cl− concentration. *Constr. Build. Mater.* **2023**, *368*, 130506. [CrossRef]
9. Lazorenko, G.; Kasprzhitskii, A.; Nazdracheva, T. Anti-corrosion coatings for protection of steel railway structures exposed to atmospheric environments: A review. *Constr. Build. Mater.* **2021**, *288*, 123115. [CrossRef]
10. Guo, S.; Si, R.; Dai, Q.; You, Z.; Ma, Y.; Wang, J. A critical review of corrosion development and rust removal techniques on the structural/environmental performance of corroded steel bridges. *J. Clean. Prod.* **2019**, *233*, 126–146. [CrossRef]
11. Cook, D.C. Spectroscopic identification of protective and non-protective corrosion coatings on steel structures in marine environments. *Corros. Sci.* **2005**, *47*, 2550–2570. [CrossRef]
12. Chong, S.L. A Comparison of Accelerated Tests for Steel Bridge Coatings in Marine Environments. *J. Prot. Coat. Linings* **1997**, *14*, 20. Available online: http://worldcat.org/issn/87551985 (accessed on 27 May 2023).
13. Liao, K.W.; Lee, Y.T. Detection of rust defects on steel bridge coatings via digital image recognition. *Autom. Constr.* **2016**, *71*, 294–306. [CrossRef]
14. Corrosionpedia. Coating Failures and Defects. 2016. Available online: https://www.ppcoatings.co.uk/wp-content/uploads/2016/06/Coating-Failure-Defects.pdf (accessed on 23 May 2023).
15. Yao, Y.; Kodumuri, P.; Lee, S.K. *Performance Evaluation of One-Coat Systems for New Steel Bridges*; No. FHWA-HRT-11-046; United States Department of Transportation; Federal Highway Administration: Washington, DC, USA, 2011.
16. Waters, N.; Connolly, R.; Brown, D.; Laskowski, B. Electrochemical impedance spectroscopy for coating evaluation using a micro sensor. In Proceedings of the Annual Conference of the PHM Society, Fort Worth, TX, USA, 29 September–2 October 2014; Volume 6. [CrossRef]
17. Hayashibara, H.; Tada, E.; Nishikata, A. Monitoring the early stage of degradation of epoxy-coated steel for ballast tank by electrochemical impedance spectroscopy. *Mater. Trans.* **2017**, *58*, 1687–1694. [CrossRef]
18. Kanbayashi, T.; Ishikawa, A.; Matsunaga, M.; Kobayashi, M.; Kataoka, Y. Application of confocal raman microscopy for the analysis of the distribution of wood preservative coatings. *Coatings* **2019**, *9*, 621. [CrossRef]
19. Müller, J.; Knop, K.; Thies, J.; Uerpmann, C.; Kleinebudde, P. Feasibility of Raman spectroscopy as PAT tool in active coating. *Drug Dev. Ind. Pharm.* **2010**, *36*, 234–243. [CrossRef]
20. Hayes, P.A.; Vahur, S.; Leito, I. ATR-FTIR spectroscopy and quantitative multivariate analysis of paints and coating materials. *Spectrochim. Acta Part A Mol. Biomol. Spectrosc.* **2014**, *133*, 207–213. [CrossRef] [PubMed]
21. Potenza, F.; Rinaldi, C.; Ottaviano, E.; Gattulli, V. A robotics and computer-aided procedure for defect evaluation in bridge inspection. *J. Civ. Struct. Health Monit.* **2020**, *10*, 471–484. [CrossRef]
22. Feroz, S.; Abu Dabous, S. UAV-Based Remote Sensing Applications for Bridge Condition Assessment. *Remote Sens.* **2021**, *13*, 1809. [CrossRef]
23. Li, Y.; Kontsos, A.; Bartoli, I. Automated rust-defect detection of a steel bridge using aerial multispectral imagery. *J. Infrastruct. Syst.* **2019**, *25*, 04019014. [CrossRef]
24. Chen, M.; Lu, G.; Wang, G. Discrimination of Steel Coatings with Different Degradation Levels by Near-Infrared (NIR) Spectroscopy and Deep Learning. *Coatings* **2022**, *12*, 1721. [CrossRef]

25. Garrett, J.L.; Johansen, T.A.; Orlandić, M.; Bashir, M.A.; Raeissi, B. Detecting Pinholes in Coatings with Hyperspectral Imaging. In Proceedings of the 2021 11th Workshop on Hyperspectral Imaging and Signal Processing: Evolution in Remote Sensing (WHISPERS), Amsterdam, The Netherlands, 24–26 March 2021; IEEE: New York, NY, USA, 2021; pp. 1–5. [CrossRef]
26. Sandak, J.; Sandak, A.; Legan, L.; Retko, K.; Kavčič, M.; Kosel, J.; Poohphajai, F.; Diaz, R.H.; Ponnuchamy, V.; Sajinčič, N.; et al. Nondestructive evaluation of heritage object coatings with four hyperspectral imaging systems. *Coatings* **2021**, *11*, 244. [CrossRef]
27. Dingemans, L.M.; Papadakis, V.M.; Liu, P.; Adam, A.J.; Groves, R.M. Quantitative coating thickness determination using a coefficient-independent hyperspectral scattering model. *J. Eur. Opt. Soc.-Rapid Publ.* **2017**, *13*, 40. [CrossRef]
28. Daikos, O.; Heymann, K.; Scherzer, T. Monitoring of thickness and conversion of thick pigmented UV-cured coatings by NIR hyperspectral imaging. *Prog. Org. Coat.* **2018**, *125*, 8–14. [CrossRef]
29. Huynh, C.P.; Mustapha, S.; Runcie, P.; Porikli, F. Multi-class support vector machines for paint condition assessment on the Sydney Harbour Bridge using hyperspectral imaging. *Struct. Monit. Maint.* **2015**, *2*, 181–197. [CrossRef]
30. Doherty, M.; Sykes, J.M. Micro-cells beneath organic lacquers: A study using scanning Kelvin probe and scanning acoustic microscopy. *Corros. Sci.* **2004**, *46*, 1265–1289. [CrossRef]
31. Lavadiya, D.N.; Sajid, H.U.; Yellavajjala, R.K.; Sun, X. Hyperspectral imaging for the elimination of visual ambiguity in corrosion detection and identification of corrosion sources. *Struct. Health Monit.* **2022**, *21*, 1678–1693. [CrossRef]
32. Greenler, R.G. Infrared study of adsorbed molecules on metal surfaces by reflection techniques. *J. Chem. Phys.* **1966**, *44*, 310–315. [CrossRef]
33. De Kerf, T.; Pipintakos, G.; Zahiri, Z.; Vanlanduit, S.; Scheunders, P. Identification of corrosion minerals using shortwave infrared hyperspectral imaging. *Sensors* **2022**, *22*, 407. [CrossRef]
34. Kızılkonca, E.; Erim, F.B. Development of anti-aging and anticorrosive nanoceria dispersed alkyd coating for decorative and industrial purposes. *Coatings* **2019**, *9*, 610. [CrossRef]
35. Anghelone, M.; Stoytschew, V.; Jembrih-Simbürger, D.; Schreiner, M. Spectroscopic methods for the identification and photostability study of red synthetic organic pigments in alkyd and acrylic paints. *Microchem. J.* **2018**, *139*, 155–163. [CrossRef]
36. Anghelone, M.; Jembrih-Simbürger, D.; Schreiner, M. Influence of phthalocyanine pigments on the photo-degradation of alkyd artists' paints under different conditions of artificial solar radiation. *Polym. Degrad. Stab.* **2016**, *134*, 157–168. [CrossRef]
37. Duce, C.; Della Porta, V.; Tiné, M.R.; Spepi, A.; Ghezzi, L.; Colombini, M.P.; Bramanti, E. FTIR study of ageing of fast drying oil colour (FDOC) alkyd paint replicas. *Spectrochim. Acta Part A Mol. Biomol. Spectrosc.* **2014**, *130*, 214–221. [CrossRef]
38. Christensen, P.A.; Dilks, A.; Egerton, T.A.; Lawson, E.J.; Temperley, J. Photocatalytic oxidation of alkyd paint films measured by FTIR analysis of UV generated carbon dioxide. *J. Mater. Sci.* **2002**, *37*, 4901–4909. [CrossRef]
39. Zahiri, Z.; Laefer, D.F.; Gowen, A. The feasibility of short-wave infrared spectrometry in assessing water-to-cement ratio and density of hardened concrete. *Constr. Build. Mater.* **2018**, *185*, 661–669. [CrossRef]
40. Miller, C.D. Kinetics and Mechanism of Alkyl Photooxidation. *Ind. Eng. Chem.* **1958**, *50*, 125–128. [CrossRef]
41. Fan, L.; Fan, M.; Alhaj, A.; Chen, G.; Ma, H. Hyperspectral imaging features for mortar classification and compressive strength assessment. *Constr. Build. Mater.* **2020**, *251*, 118935. [CrossRef]

coatings

MDPI

Article

Protection of 316L Steel Against LBE Corrosion by a CaO-MgO-Al_2O_3-SiO_2 Glass–Ceramic Coating

Zunqi Xiao [1], Zhizhong Jiang [2], Lin Luo [2], Yi Wan [2], Aixue Liu [1], Bin Zhang [1], Bing Ren [1,*] and Jing Liu [2,*]

[1] School of Electrical and Information, Hunan Institute of Engineering, Xiangtan 411104, China; xiaozunqi123@126.com (Z.X.)
[2] Institute of Nuclear Energy Safety Technology, Hefei Institutes of Physical Science, Chinese Academy of Sciences, Hefei 230031, China
[*] Correspondence: renbing2024@126.com (B.R.); jing.liu@inest.cas.cn (J.L.)

Abstract: A CaO-MgO-Al_2O_3-SiO_2 glass–ceramic coating was prepared by the slurry method and subsequent sintering to improve the corrosion resistance of 316L steel in liquid lead–bismuth eutectic alloy at high temperatures. The glass–ceramic coating, sintered at 884 °C, was dense and demonstrated strong adhesion to the substrate. It was composed of the crystalline phases diopside ($CaMgSi_2O_6$) and anorthite ($CaAl_2Si_2O_8$) and had an average Vickers hardness of 595 HV, which was over three times that of 316L steel. After corrosion in an oxygen-saturated, static lead–bismuth eutectic alloy at 500 °C for 1000 h, the uncoated 316L experienced significant mass gain (0.04 g) due to severe oxidative corrosion, resulting in the formation of Fe_3O_4 and Pb_2O on its surface. In contrast, the glass–ceramic-coated specimens showed a very small mass gain (0.0012 g) after corrosion. The coating maintained good thermal stability; its crystalline phase composition remained largely unchanged after the corrosion test. The glass–ceramic coating still exhibited dense microstructure and tightly adhered to the substrate after corrosion. There was no evident penetration of lead–bismuth into the coating, and no dissolution of the coating's elements into the lead–bismuth alloy was detected. These observations confirm that the glass–ceramic coating possessed superior corrosion resistance in liquid lead–bismuth eutectic environments.

Keywords: glass–ceramic coating; LBE corrosion; protection; 316L steel

1. Introduction

Lead-cooled fast reactors (LFRs) have become one of the most promising reactors for Generation IV nuclear systems, renowned for their favorable neutronics, thermal-hydraulics, and inherent safety features [1]. However, despite these benefits, material challenges continue to pose a significant barrier to the progress of LFR technology [2]. Unlike the structural materials used in the commercially established Generation II and III nuclear systems, the materials used in LFRs face a more rigorous service environment [3]. Notably, corrosion caused by liquid lead, or the lead–bismuth eutectic (LBE) alloy, is a critical factor in the deterioration of structural materials within LFRs over extended periods of service [4–9].

So far, there are three types of reference reactors in the world: SSTAR (Small, Secure Transportable Autonomous Reactor, 20 MWe) in the United States [10], ELFR (European Lead-cooled Fast Reactor, 300 MWe) in the European Union [11], and BREST-OD-300 (Bystriy Reaktor Estestrennoy Bezopasnosti, 600 MWe) in Russia [1]. Furthermore, other LFRs have been conceptualized, including the MYRRHA (Multi-purpose hybrid research reactor for high-tech applications) in the European Union [1] and CLEAR (China LEAd-based Reactor) in China [12]. Candidate structural materials for these reactors encompass a range of options such as ferritic/martensitic steels (e.g., T91), austenitic stainless steels (e.g., 15-15Ti, 316L), ODS steels, FeCrAl alloys, and refractory metals [13–17]. Notably, 316L steel or its equivalents are considered for cladding in MYRRHA and as a potential material for pump impellers in ELFR [11]. However, studies have indicated that 316L steel in LBE was subject to more severe oxidative corrosion at high oxygen concentrations or dissolution corrosion at low oxygen concentrations between 480 and 550 °C, which are the typical design temperatures of LFRs [18,19]. These corrosion issues could significantly compromise the service life of 316L as a structural material in LFR applications. Consequently, there is a pressing need to develop corrosion-resistant coatings for 316L to protect it against lead or LBE corrosion.

Previous studies have developed a variety of coating materials for steels against lead or LBE corrosion, such as ceramic coatings (e.g., Al_2O_3, SiC, Al_2O_3-TiO_2) [5,20], alloy coatings containing aluminum (e.g., FeCrAl, FeCrAlY) [14], high-entropy alloy coatings [21], and ternary MAX cermet coatings [22]. In addition to the above-mentioned types of coatings, glass and glass–ceramic materials, known for their excellent thermal stability, wear resistance, corrosion resistance, and oxidation resistance, are emerging as promising coating materials for steels against high-temperature oxidation and LBE corrosion [23,24]. For instance, Liu et al. developed a glass and ceramic composite coating on 304 stainless steel, which consisted of a SiO_2-Al_2O_3 glass matrix reinforced with Cr_2O_3 particles, demonstrating good corrosion resistance in LBE [23]. However, compared to composite coatings made by simply mixing a glass matrix with ceramic particles, glass–ceramic coatings that contain a significant amount of microcrystalline and glassy phases produced by controlled crystallization of a specific base glass during heating or sintering exhibit superior high-temperature stability, mechanical properties, and corrosion resistance [25–28]. Despite these advantages, there have been relatively few studies on the preparation of glass–ceramic coatings for structural materials considered for use in LFRs.

In this study, a CaO-MgO-Al_2O_3-SiO_2 (CMAS) glass–ceramic coating was prepared on 316L steel by the slurry method and subsequent sintering. Additionally, the corrosion behavior of the 316L steel and the glass–ceramic coatings in LBE at 500 °C for 1000 h was also studied. The findings of this study not only broaden the potential applications of glass–ceramic coatings but also provide significant guidance for the development of coating materials suitable for advanced nuclear energy systems.

2. Experimental

2.1. Specimen Preparation

A 316L stainless steel sheet was machined into 10 mm × 10 mm × 3 mm (length × width × height) specimens by the wire electrical discharge machining method. A 1 mm diameter circular hole was drilled in the upper right corner of each specimen's surface so that the specimens could be suspended on the specimen holder for the high-temperature LBE corrosion test. Before the glass–ceramic coating was prepared, the surfaces of the 316L specimens were mechanically ground using a sequence of #600 to #1500 SiC abrasive papers. Subsequently, the specimens were cleaned by anhydrous ethanol and dried in a drying oven. The chemical compositions of 316L steel are shown in Table 1.

Table 1. Chemical compositions of 316L stainless steel before corrosion.

Element	C	Cr	Ni	Mo	Mn	Si	Fe
Content (wt%)	0.02	16.20	10.03	2.06	1.48	0.48	Bal.

2.2. Glass Powder Preparation

CMAS glass was prepared using the conventional quenching method. All the starting raw materials $CaCO_3$, $Mg(HCO_3)_2$, Al_2O_3, SiO_2, and K_2O were of reagent grade and were purchased from Sinopharm Chemical Reagent Co., Ltd. in Shanghai, China. After thoroughly mixing, the batches were placed in an alundum crucible and then heated to 1600 °C in the electrical furnace. It was held at this temperature for 2 h, and then the molten glass was poured into water to produce glass particles. Then, the water-quenched glass particles, the grinding balls, and the ethanol were put into the tank for ball milling. In the process of ball milling, the mass ratio of glass particle to ball was 1:3, and the mass of glass particle was the same as that of anhydrous ethanol. After milling for 36 h, the glass powder could be obtained by drying and sieving (200 mesh). The chemical compositions of the CMAS glass are listed in Table 2, which shows experimental starting compositions.

Table 2. Chemical compositions of CMAS glass.

Oxide	**CaO**	**MgO**	**Al_2O_3**	**SiO_2**	**K_2O**
Content (wt%)	27.3	9.2	13.3	49.7	0.5

2.3. Coating Preparation

The CMAS glass–ceramic coating was prepared using the slurry method followed by a sintering process. Initially, CMAS glass powder, a binder (methyl cellulose solution), and distilled water were mixed in a mass ratio of 0.75:0.75:1 to form a slurry. This slurry was then air-sprayed onto the surfaces of spare 316L specimens and subsequently dried in an oven at 80 °C for 24 h. The dried specimens were then subjected to a three-stage high-temperature heating process in a muffle furnace. This process included heating the samples to 500 °C and maintaining them for 1 h, followed by 1 h at 735 °C, and finally 1 h at 884 °C for sintering. This meticulous sintering regimen ensured the coating's optimal density and adherence to the substrate.

2.4. LBE Corrosion Tests

The study of material corrosion behavior in liquids mainly includes two methods. The first method is the immersion method, which involves directly immersing the samples in the corrosive medium. By studying the mass changes in samples before and after corrosion, as well as the morphology and phase of the corrosion products, the material corrosion behavior and mechanism can be determined. This paper adopts this method, which is also a commonly used method for studying the corrosion behavior of materials in liquid metal. The second method for material corrosion research is the electrochemical method. However, this method requires the presence of an electrolyte in the corrosive medium (such as water, water containing mixed liquids, molten salts, etc.). However, there are no electrolytes in liquid metal, and materials do not undergo electrochemical corrosion in liquid metals.

The liquid LBE alloy served as the corrosive medium in our corrosion tests, with a composition of 44.5 wt% lead (Pb) and 55.5 wt% bismuth (Bi).

To evaluate the LBE corrosion resistance of the CMAS glass–ceramic coating, the high-temperature static LBE corrosion test was carried out using the LBE corrosion test device, as shown in Figure 1. The test device, as shown in Figure 1a, comprised a stainless-steel tank, a thermocouple for temperature monitoring, and a heating and insulation system. For the corrosion tests, LBE and the specimens were introduced into the steel tank, with the specimens suspended from a stainless-steel specimen holder, as illustrated in Figure 1b, using molybdenum wire. Throughout the corrosion process, the dissolved oxygen content in the liquid LBE was not actively controlled, and it was assumed to be in a state of oxygen saturation.

The corrosion tests were conducted at a temperature of 500 °C with a total duration of 1000 h. This duration could simulate the long-term corrosion behavior of materials in practical applications (such as in lead-cooled fast reactors), as well as evaluate the durability of materials in the LBE environment. Furthermore, previous studies show that a 1000 h corrosion test duration is long enough to observe the corrosion characteristics and trends in materials in the LBE environment, thereby providing a scientific basis for material selection and application. During corrosion, specimens were extracted from the liquid LBE at intervals of 250 h, 500 h, 750 h, and 1000 h for analysis. The temperature of corrosion tests was set at 500 °C because the current design temperature for the cladding of CLEAR

(China LEAd-based Reactor) is 500 °C. The glass–ceramic coating designed in this paper is also intended for potential application in CLEAR in the future.

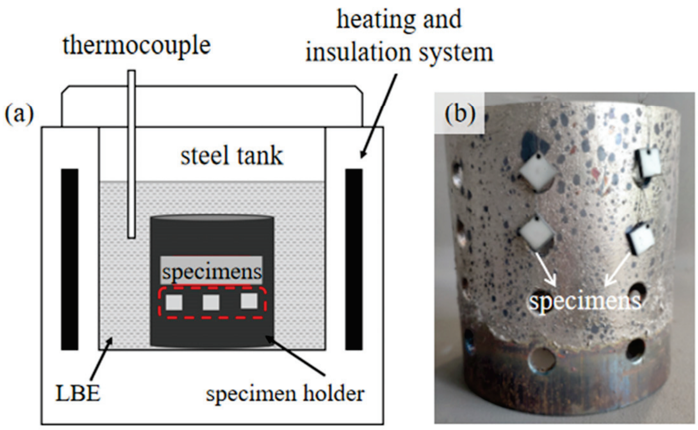

Figure 1. Schematic diagram of LBE corrosion test device (**a**) and physical diagram of specimen holder (**b**).

Post-corrosion, half of the specimens were subjected to surface and mass gain analysis. These were immersed in glycerol at 200 °C to remove any adhering LBE. The other half, designated for cross-sectional analysis, were embedded in resin and then ground and polished to prepare them for further examination.

2.5. Analytical Characterization

The thermal properties of CMAS glasses, such as the glass transition (T_g) and crystallized peak (T_c) temperatures, were determined by differential scanning calorimetry (DSC, NETZSCH in Selb, Genmany) in an inert gas atmosphere (Ar) with a heating rate of 10 °C/min. The surface and cross-sectional morphology and element distribution of specimens were analyzed with a scanning electron microscope (SEM, ZEISS in Oberkochen, Germany) with an EDS spectrometer (Oxford Instruments in Oxford, United Kingdom). The phase composition of specimens was observed by an X-ray diffraction instrument (XRD, PANalytical in Malvern, United Kingdom).

3. Results

3.1. Determination of Coating Sintering Temperature

The DSC curve of CMAS glass powder revealed three distinct exothermic peaks: the glass transition temperature (Tg) at 558.09 °C and two crystallization temperatures (Tc) at 789.14 °C and 951.52 °C. To achieve the desired crystalline phases, the sintering temperature range of CMAS glass–ceramic coating was chosen to be between 789.14 °C and 951.52 °C. We referred to the sintering temperatures of glass ceramics with similar compositions. During sintering, we set the sintering temperatures at 844 °C, 864 °C, 884 °C, 904 °C, and 924 °C, respectively. Eventually, we found that only when the sintering temperature was 884 °C could we achieve a complete coating. Meanwhile, coatings obtained at other sintering temperatures peeled off. However, the reasons for the peeling are not yet clear and require further research. So, after careful consideration of the sintering process, the optimal sintering temperature was set at 884 °C to ensure the coating's adherence without peeling.

3.2. Microstructure of the As-Prepared CMAS Glass–Ceramic Coating

Figure 2 shows the surface and cross-sectional morphology of the CMAS glass–ceramic coating prepared at 884 °C. The surface morphology (Figure 2a) shows that the coating was dense and exhibited a high level of smoothness. However, minor protrusions were observed on the surface, potentially due to the uncontrolled crystal growth during the sintering process. The cross-sectional morphology reveals strong adhesion between the coating and the substrate with no signs of cracking and peeling (Figure 2b). Notably, there was no distinct interface layer visible at the boundary between the coating and the substrate. Some pores within the coating were also observed.

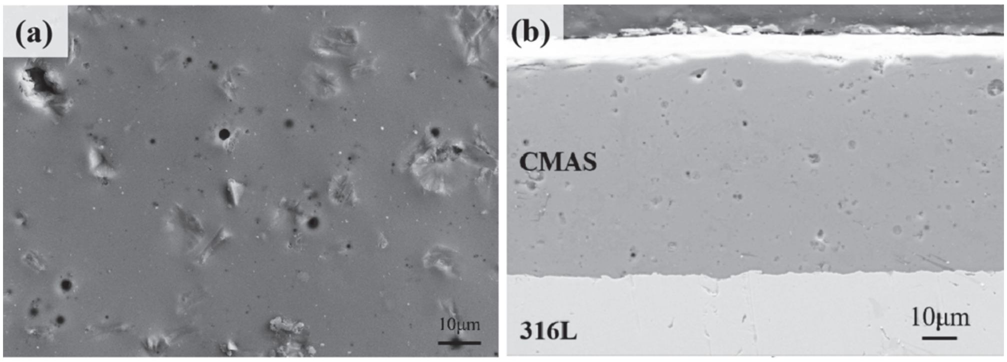

Figure 2. The surface and cross-sectional morphology of the as-prepared CMAS glass–ceramic coating: (**a**) surface morphology; (**b**) cross-sectional morphology.

The XRD pattern of the as-prepared CMAS glass–ceramic coating (Figure 3) confirmed that the main crystalline phases of the coating were diopside ($CaMgSi_2O_6$) and anorthite ($CaAl_2Si_2O_8$), which was consistent with the design objective of this study.

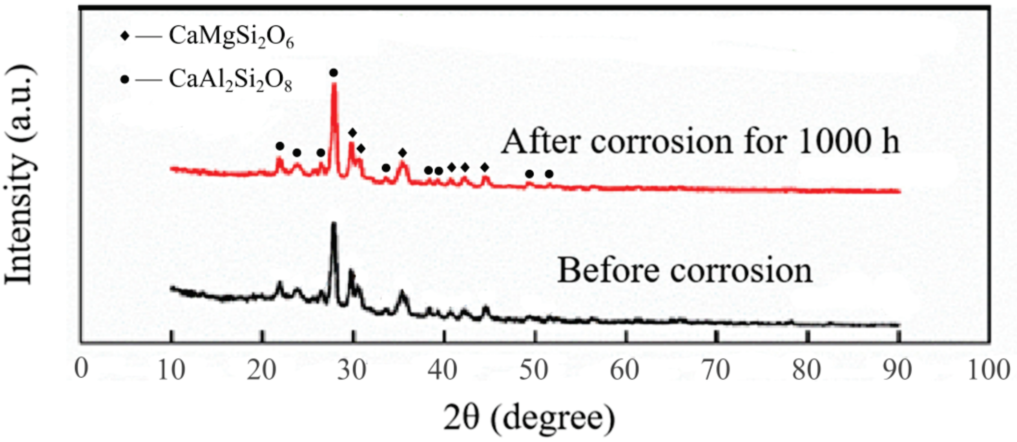

Figure 3. XRD pattern of the CMAS glass–ceramic coating before and after corrosion for 1000 h.

3.3. LBE Corrosion

3.3.1. Mass Gain of Corrosion Specimens

Figure 4 illustrates the mass gain of the 316L and CMAS glass–ceramic-coated specimens after different corrosion times. In our corrosion experiments, the corrosion mass gain at each corrosion time point was derived from the average mass gain of three parallel samples. During the corrosion experiments, we have taken strict control measures to ensure that the initial state of each sample and the corrosion environment remain consistent. Error bars were not added in the diagram of mass gain because we found that the degree of dispersion in the corrosion mass gain data at each time point was very small, within an acceptable range, and will not affect the scientific nature and reliability of this study. Figure 4 shows that the mass of 316L substrate increased with prolonged corrosion time, although the increase rate gradually slowed down. Specifically, after 1000 h of corrosion, the uncoated 316L experienced a mass gain of 0.04 g. In contrast, the CMAS glass–ceramic coating demonstrated minimal mass change throughout the corrosion periods. After 1000 h of corrosion, the coated specimens registered a very small mass gain (0.0012 g). These findings suggest that the CMAS glass–ceramic coating provided effective protection to the substrate.

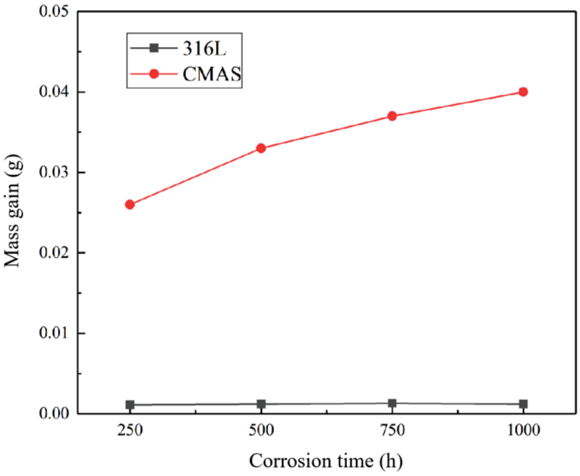

Figure 4. Mass gain of 316L and glass–ceramic coatings after different corrosion times.

3.3.2. Microstructure of Oxide Scales on Bare 316L Steel

Figure 5 presents the surface morphology of 316L steel subjected to varying durations of corrosion (ranging from 250 to 1000 h). Initially, after 250 h of corrosion, numerous corrosion pits were observed on the steel's surface, accompanied by the presence of many protruding substances. Over time, the quantity of these protrusions increased, and their distribution evolved from being scattered to forming continuous patches after 1000 h of corrosion, suggesting a progressive escalation in the severity of corrosion. The EDS scanning analysis depicted in Figure 6 reveals that the predominant elements on the corroded surface after 1000 h were Fe, Cr, Ni, Pb, and O. Notably, the protruding substances exhibited a significant enrichment in O and a marked depletion in Cr and Ni, indicating a change in the surface composition due to the corrosion process. To delve deeper into the composition of the protruding substances, point scanning analysis was conducted on specimens that had been subjected to 1000 h of corrosion. The analysis reveals that the primary constituents of these surface protrusions were Fe at 45.4 wt%, Pb at 19.6 wt%, and O at 23.7wt%, with trace amounts of Ni at 2.3 wt% and Cr at 7.9 wt%. Corroborating these findings with the XRD analysis presented in Figure 7, it was concluded that the surface protrusions on the 316L steel were predominantly composed of Fe_3O_4 and Pb_2O.

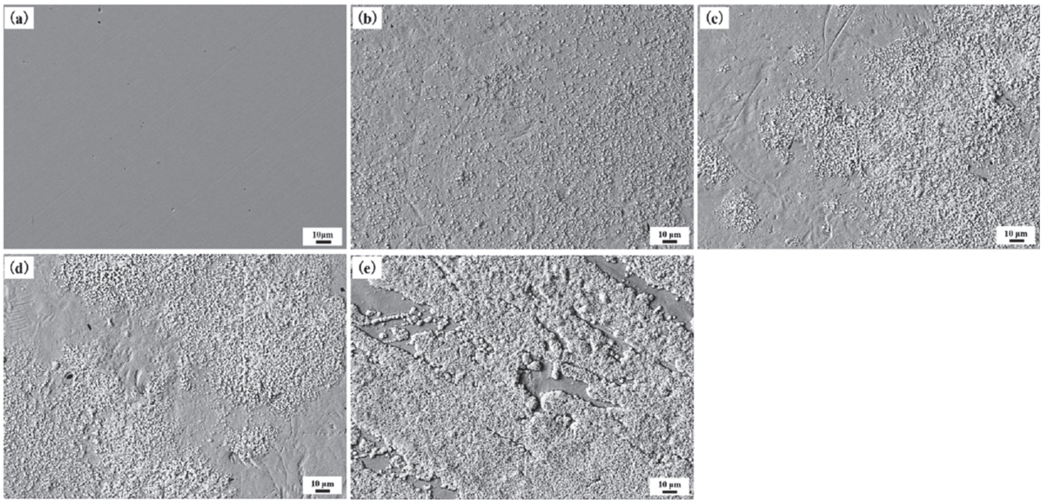

Figure 5. The surface morphology of 316L steel after different corrosion times: (**a**) before corrosion; (**b**) 250 h; (**c**) 500 h; (**d**) 750 h; (**e**) 1000 h.

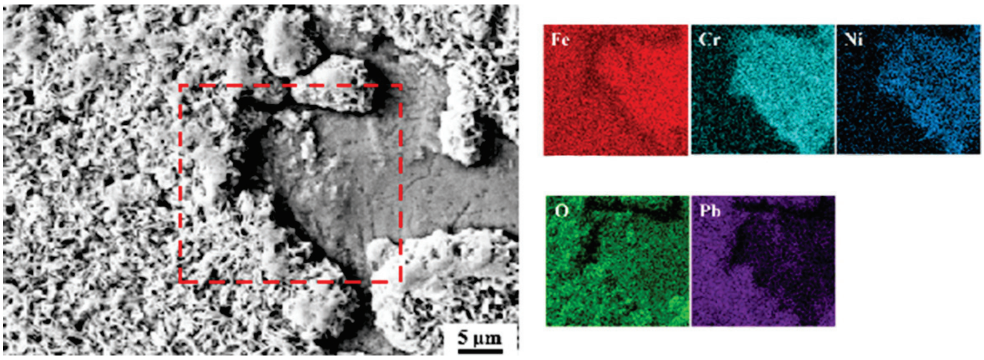

Figure 6. Localized enlarged image of surface morphology of 316L specimens after corrosion for 1000 h and corresponding EDS area scanning results.

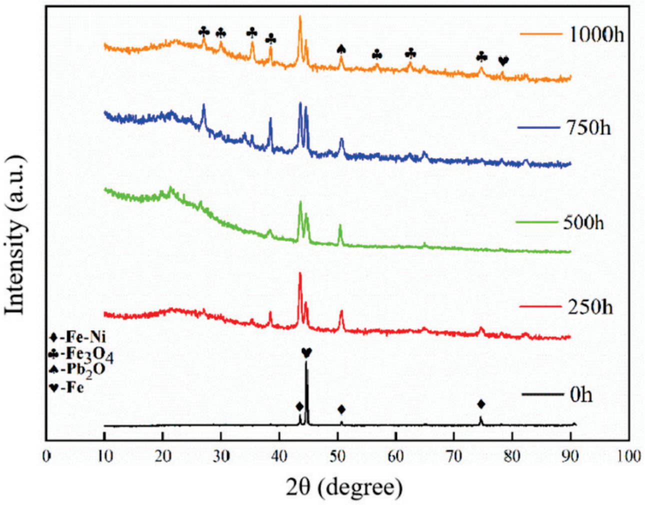

Figure 7. The XRD pattern of the 316L steel before and after corrosion for 250 h, 500 h, 750 h, and 1000 h.

The results of XRD and SEM show that the 316L substrate's surface was predominantly exposed during the early stages of corrosion, with evident oxidation corrosion occurring. As corrosion time increased, the oxide film on the substrate seemed to mitigate further material corrosion to some extent, which was reflected in the decrease in the corrosion rate corresponding to the mass gain data. This suggests that while the initial corrosion was rapid, the formation of the oxide layer helped to slow down the rate of material degradation over time.

3.3.3. Microstructure of the CMAS Glass–Ceramic Coating on 316L Steel After Corrosion

Figure 8 displays the surface and cross-sectional morphology of CMAS glass–ceramic coating after being exposed to liquid LBE for 1000 h. The surface morphology, as depicted in Figure 8a, maintained a dense microstructure post-corrosion, suggesting that the coating remained intact in the high-temperature LBE environment. A comparative examination with pre-corrosion specimens indicates an increase in both the quantity and size of the crystals within the glass–ceramic coating following the corrosion test.

The XRD patterns, as shown in Figure 3, confirm that the crystalline phases of the coating after 1000 h of corrosion were still dominated by diopside ($CaMgSi_2O_6$) and anorthite ($CaAl_2Si_2O_8$), matching the composition of the specimens prior to corrosion. This consistency demonstrates that the CMAS glass–ceramic coating possessed excellent chemical stability against LBE corrosion, retaining its structural integrity and compositional uniformity even after prolonged exposure.

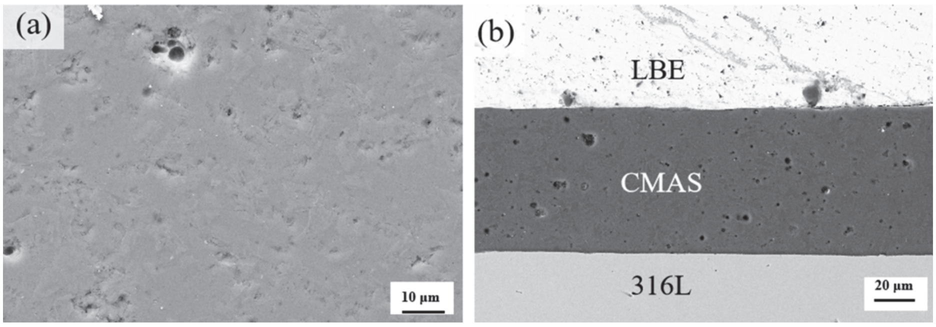

Figure 8. The surface and cross-sectional morphology of the CMAS glass–ceramic coating after corrosion for 1000 h: (**a**) surface morphology; (**b**) cross-sectional morphology.

The cross-sectional morphology of the coating presented in Figure 8b demonstrates that the coating remains firmly bonded to the substrate even after corrosion, with no signs of delamination. Additionally, there was no evident infiltration of lead and bismuth into the coating, suggesting that the coating effectively resisted penetration by these elements. The EDS line scanning analysis, as shown in Figure 9, reveals that lead (Pb) and bismuth (Bi) elements were predominantly localized on the coating's surface, with no indication of them permeating into the coating's bulk. Furthermore, there was no evidence of the coating's constituents dissolving into the lead–bismuth alloy. These observations underscore the CMAS glass–ceramic coating's robust resistance to LBE corrosion, highlighting its potential as a protective barrier in such environments.

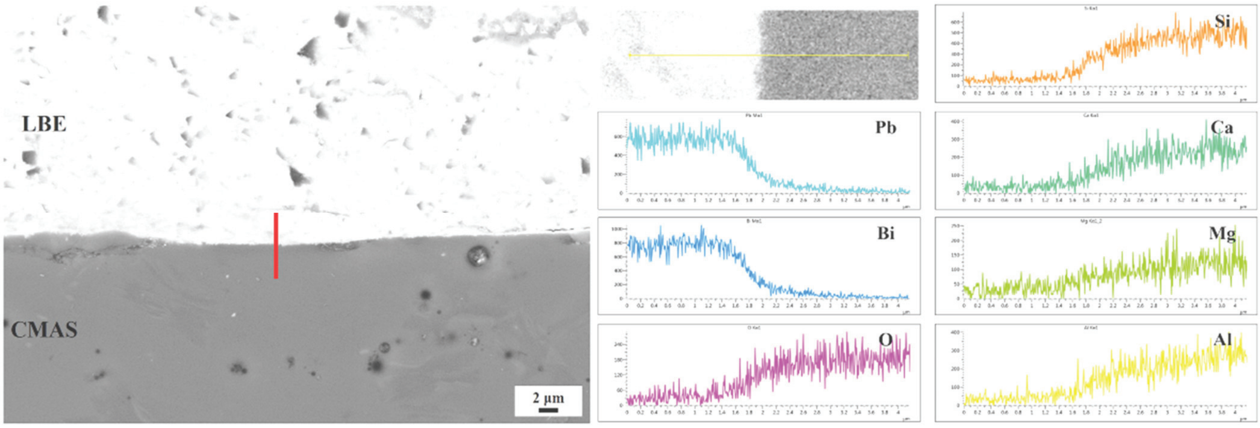

Figure 9. EDS line scan results of the CMAS glass–ceramic coating after corrosion for 1000 h.

4. Discussion

So far, the literature on the development of glass–ceramic coatings for structural materials in LFR is relatively sparse. This paper makes a commendable contribution to the field. The CMAS glass–ceramic coating, characterized by its high hardness, superior thermal stability, and outstanding resistance to LBE, stands out as an ideal candidate for applications like cladding or pump impeller coatings in LFR settings. Its unique combination of properties positions it as a promising material for enhancing the performance and durability of components in such demanding environments.

The CMAS glass–ceramic coating we developed exhibited density and a high level of surface smoothness, which are highly beneficial for enhancing the material's corrosion resistance. Nonetheless, some pores within the coating were observed. These pores are likely attributable to two main factors: first, the pores might come from bubbles within the coating slurry, and second, the bubbles produced in the process of sintering densification of the coating could not be discharged in time, which can also result in pore formation [29,30]. To optimize the density of the glass–ceramic coating and reduce porosity to a minimum, the coating samples must be subjected to a two-stage heat treatment in a muffle furnace before the sintering temperature (884 °C). This involves holding the samples at 500 °C for one hour, followed by a further hour at 735 °C. This procedure was designed to ensure the coating achieves its maximum density and minimizes the presence of pores, thereby enhancing its overall performance and durability.

Previous research yielded a variety of ceramic coating materials for steel protection against lead or LBE corrosion, including coatings of Al_2O_3, SiC, and Al_2O_3-TiO_2 [5,20]. These ceramic coatings have demonstrated effective corrosion resistance. Traditional methods for preparing these coatings include thermal spraying, physical vapor deposition, or chemical vapor deposition. In contrast to these methods, our approach to preparing glass–ceramic coatings is relatively simple. It involves air spraying or brush coating followed by high-temperature sintering processes. More importantly, the preparation process of glass–ceramics is very suitable for the preparation of surface coatings on complex components such as pump impellers, which provides a great opportunity for the widespread application of glass–ceramic coatings in nuclear reactors.

The CMAS glass–ceramic coating we developed is primarily composed of diopside ($CaMgSi_2O_6$) and anorthite ($CaAl_2Si_2O_8$) crystal phases, which are consistent with the design objective of this study. The literature reviews indicate that CMAS glass–ceramic coatings can crystallize into various phases, such as forsterite, diopside, anhydrite, and anorthite. The diopside phase is particularly noted for its excellent wear and corrosion resistance, whereas the anorthite phase is known for its superior corrosion resistance and thermal stability. Research has indicated that a well-balanced ratio of diopside to anorthite can significantly enhance the corrosion and wear resistance of CMAS glass–glass–ceramic coatings [31]. Given that coating materials in lead-fast reactors (LFRs), especially those used for cladding and pump impellers, are subjected to the erosive effects of high-velocity LBE, it is imperative that the coatings exhibit excellent high-temperature stability, resistance to LBE corrosion, and robust wear resistance. Our CMAS glass–ceramic coating, with its specific crystalline composition, is well-suited to meet these demanding requirements.

The formulation of glass–ceramic components is pivotal in creating coatings with the desired crystalline phases. To achieve this, we initially consulted the phase diagram of the CaO-Al_2O_3-SiO_2 system with an addition of 10% MgO to establish a preliminary composition range for the glass–ceramic coating [32]. As shown in Table 2, the CMAS glass–ceramic coating was characterized by a high SiO_2 content, which typically serves as the network-forming component in glass–ceramic coatings. The precipitation of anorthite phase ($CaAl_2Si_2O_8$) requires a certain amount of Al_2O_3. The proportions of CaO and MgO in the CMAS glass–ceramic coatings can be fine-tuned to lower the crystallization temperature, encourage the precipitation of diopside and anorthite phases, and enhance the surface hardness and corrosion resistance of the glass–ceramic coatings. Studies have indicated that maintaining a mass ratio of CaO to MgO close to 3 in CMAS glass–ceramic coatings broadens the crystallization temperature range, thereby improving the crystallization capability and promoting the coexistence of anorthite and diopside phases [33]. Furthermore, to address the limited crystallization propensity of CMAS glass–ceramic coatings, a minor amount of nucleating agent K_2O was incorporated into the composition. This addition aims to reduce the crystallization temperature and facilitate densification post-crystallization, thereby optimizing the overall properties of the glass–ceramic coating.

The corrosion mechanism of coatings in lead–bismuth eutectic (LBE) can be attributed to three primary processes: the dissolution of the coating material by LBE, the oxidation of the coating material by dissolved oxygen in LBE, and the corrosion of the substrate steel material by dissolved oxygen in LBE that permeates through the coating. For metallic coatings like Al-based coating (FeCrAlY, AlTiN) [14,34] and Al-containing high-entropy alloy coatings (FeCrAlTiNb, AlCrMoNbZr) [21,35], when the dissolved oxygen concentration in LBE is controlled within a suitable range, it can diffuse into the coating and react with it to form a protective layer of Al_2O_3, which mitigates the coating's corrosion. Conversely, when the dissolved oxygen concentration in LBE is minimal or too high, the coating material is more susceptible to dissolution or excessive oxidation by LBE, leading to coating corrosion. For our CMAS glass–ceramic coatings, neither dissolution nor oxidation occurs. Our previous research has demonstrated that even at 800 °C, the diffusion rate of oxygen in glass–ceramic coatings was remarkably low [27]. Given that the experimental temperature in this study was 500 °C, the diffusion rate of oxygen through the coating was even lower, making it difficult for dissolved oxygen in LBE to penetrate the glass–ceramic coating and oxidize the 316L substrate. Therefore, the CMAS glass–ceramic coating exhibited good resistance to LBE corrosion.

Looking ahead, our research will delve deeper into the coating's irradiation resistance. This critical assessment will provide further insights into the coating's potential and overall value for use in the demanding conditions of LFR.

5. Conclusions

In this research, we successfully applied a CMAS glass–ceramic coating onto 316L steel to protect it against corrosion by liquid lead–bismuth eutectic (LBE). The as-prepared coating predominantly constituted of diopside ($CaMgSi_2O_6$) and anorthite ($CaAl_2Si_2O_8$) crystal phases. We investigated the corrosion resistance of both the glass–ceramic coatings and the 316L steel when exposed to static LBE at 500 °C for a duration of up to 1000 h. Post-corrosion analysis revealed that the uncoated 316L experienced significant mass gain (0.04 g) due to severe oxidative corrosion with the formation of Fe_3O_4 and Pb_2O on its surface. In contrast, the glass–ceramic coated specimens showed a very small mass gain (0.0012 g) after corrosion. Furthermore, the phase composition of the CMAS glass–ceramic coating remained largely unaffected after the corrosion test, which is a testament to the coating's excellent high-temperature stability. There was no significant evidence of lead–bismuth penetration through the coating, and no dissolution of the coating's elements into the LBE was detected. These findings suggest that the CMAS glass–ceramic coating provides outstanding resistance to LBE corrosion.

Author Contributions: Conceptualization, Z.J.; Investigation, L.L.; Methodology, Y.W.; Validation, J.L.; Writing—original draft, Z.X. and B.R.; Writing—review and editing, A.L. and B.Z. All authors have read and agreed to the published version of this manuscript.

Funding: This work was supported by the National Key R&D Program of China [grant number 2022YFB1902502], the Natural Science Foundation of Hunan Province of China [grant number 2023JJ30194], the CAS-NST Joint Research Projects [grant number 145GJHZ2022028MI], the National Natural Science Foundation of China [grant number 51901224], Youth Innovation Promotion Association of Chinese Academy of Sciences [grant number 2021449], and the Henan Province Key Specialized R&D Breakthrough Program [grant number 242102230054].

Institutional Review Board Statement: Not applicable.

Informed Consent Statement: Not applicable.

Data Availability Statement: Data are contained within this article.

Conflicts of Interest: The authors declare no conflict of interest.

References

1. Alemberti, A.; Smirnov, V.; Smith, C.F.; Takahashi, M. Overview of lead-cooled fast reactor activities. *Prog. Nucl. Energy* **2014**, *77*, 300–307. [CrossRef]
2. Murty, K.; Charit, I. Structural materials for Gen-IV nuclear reactors: Challenges and opportunities. *J. Nucl. Mater.* **2008**, *383*, 189–195. [CrossRef]
3. Yvon, P.; Le Flem, M.; Cabet, C.; Seran, J.L. Structural materials for next generation nuclear systems: Challenges and the path forward. *Nucl. Eng. Des.* **2015**, *294*, 161–169. [CrossRef]
4. Luo, L.; Liu, J.; Tian, S.; Jiang, Z.; Xiao, Z.; Zhang, M.; Huang, W.; Sun, L.; Luo, W. Microstructure evolution of magnetite layer on CLAM steel exposed to lead-bismuth eutectic containing 10^{-6} wt% oxygen at 500 °C. *J. Nucl. Mater.* **2022**, *562*, 153579. [CrossRef]
5. Serag, E.; Caers, B.; Schuurmans, P.; Lucas, S.; Haye, E. Challenges and coating solutions for wear and corrosion inside Lead Bismuth Eutectic: A review. *Surf. Coat. Technol.* **2022**, *441*, 128542. [CrossRef]

6. Tsisar, V.; Gavrilov, S.; Schroer, C.; Stergar, E. Long-term corrosion performance of T91 ferritic/martensitic steel at 400 °C in flowing Pb-Bi eutectic with 2×10^{-7} wt% dissolved oxygen. *Corros. Sci.* **2020**, *174*, 108852. [CrossRef]
7. Shi, H.; Jianu, A.; Fetzer, R.; Szabo, D.V.; Schlabach, S.; Weisenburger, A.; Tang, C.; Heinzel, A.; Lang, F.; Mueller, G. Compatibility and micro-structure evolution of Al-Cr-Fe-Ni high entropy model alloys exposed to oxygen-containing molten lead. *Corros. Sci.* **2021**, *189*, 109593. [CrossRef]
8. Shi, H.; Wang, H.; Fetzer, R.; Heinzel, A.; Weisenburger, A.; Wang, K.; Jianu, A.; Müller, G. Influence of Si addition on the corrosion behavior of 9 wt% Cr ferritic/martensitic steels exposed to oxygen-controlled molten Pb-Bi eutectic at 550 and 600 °C. *Corros. Sci.* **2021**, *193*, 109871. [CrossRef]
9. Charalampopoulou, E.; Lambrinou, K.; Donck, T.V.D.; Paladino, B.; Fonzo, F.D.; Azina, C.; Eklund, P.; Mráz, S.; Schneider, J.M.; Schryvers, D. Early stages of dissolution corrosion in 316L and DIN 1.4970 austenitic stainless steels with and without anticorrosion coatings in static liq-uid lead-bismuth eutectic (LBE) at 500 °C. *Mater. Charact.* **2021**, *178*, 111234. [CrossRef]
10. Smith, C.F.; Halsey, W.G.; Brown, N.W.; Sienicki, J.J.; Moisseytsev, A.; Wade, D.C. SSTAR: The US lead-cooled fast reactor (LFR). *J. Nucl. Mater.* **2008**, *376*, 255–259. [CrossRef]
11. Alemberti, A.; Frogheri, M.; Mansani, L. The lead fast reactor: Demonstrator (ALFRED) and ELFR design. In Proceedings of the International Conference on Fast Reactors and Related Fuel Cycles: Safe Technologies and Sustainable Scenarios, Paris, France, 4–7 March 2013.
12. Wu, Y.; Bai, Y.; Song, Y.; Huang, Q.; Zhao, Z.; Hu, L. Development strategy and conceptual design of China lead-based research reactor. *Ann. Nucl. Energy* **2016**, *87*, 511–516. [CrossRef]
13. Schroer, C.; Konys, J. Quantification of the long-term performance of steels T91 and 316L in oxygen-containing flowing lead-bismuth eutectic at 550 °C. *J. Eng. Gas Turbines Power* **2010**, *132*, 082901. [CrossRef]
14. Weisenburger, A.; Heinzel, A.; Müller, G.; Muscher, H.; Rousanov, A. T91 cladding tubes with and without modified FeCrAlY coatings exposed in LBE at different flow, stress and temperature conditions. *J. Nucl. Mater.* **2008**, *376*, 274–281. [CrossRef]
15. Wang, D.; Liu, S.; Ma, X.; Xiao, C.; Gong, X.; Zhu, H.; Niu, F. Enhanced corrosion resistance of 15–15Ti austenitic steel in liquid lead-bismuth eutectic at 550 °C by shot peening processing. *Corros. Sci.* **2024**, *226*, 111640. [CrossRef]
16. Wang, H.; Yu, H.; Liu, J.; Kondo, S.; Okubo, N.; Kasada, R. Characterization and corrosion behavior of Al-added high Mn ODS austenitic steels in oxygen-saturated lead–bismuth eutectic. *Corros. Sci.* **2022**, *209*, 110818. [CrossRef]
17. Lim, J.; Hwang, I.S.; Kim, J.H. Design of alumina forming FeCrAl steels for lead or lead–bismuth cooled fast reactors. *J. Nucl. Mater.* **2013**, *441*, 650–660. [CrossRef]
18. Heinzel, A.; Weisenburger, A.; Müller, G. Corrosion behavior of austenitic steels in liquid lead bismuth containing 10^{-6} wt% and 10^{-8} wt% oxy-gen at 400–500 °C. *J. Nucl. Mater.* **2014**, *448*, 163–171. [CrossRef]
19. Klok, O.; Lambrinou, K.; Gavrilov, S.; Stergar, E.; Donck, T.V.D.; Huang, S.; Tunca, B.; Graeve, I.D. Influence of plastic deformation on dissolution corrosion of type 316L austenitic stainless steel in static, oxygen-poor liquid lead-bismuth eutectic at 500 °C. *Corrosion* **2017**, *73*, 1078–1090. [CrossRef] [PubMed]
20. Zhong, Y.; Zhang, W.; Chen, Q.; Yang, J.; Zhu, C.; Li, Q.; Yang, J.; Liu, N.; Yang, J. Effect of LBE corrosion on microstructure of amorphous Al_2O_3 coating by magnetron sputtering. *Surf. Coat. Technol.* **2022**, *443*, 128598. [CrossRef]
21. Yang, J.; Liang, J.; Wang, G.; Liao, J.; Qiu, S.; Zhang, W.; Yang, J. Microstructure, mechanical properties and lead-bismuth eutectic corrosion behavior of FeCrAlTiNb high-entropy alloy coatings. *Corros. Sci.* **2023**, *222*, 111407. [CrossRef]
22. Shi, H.; Azmi, R.; Han, L.; Tang, C.; Weisenburger, A.; Heinzel, A.; Maibach, J.; Stüber, M.; Wang, K.; Müller, G. Corrosion behavior of Al-containing MAX-phase coatings exposed to oxygen containing molten Pb at 600 °C. *Corros. Sci.* **2022**, *201*, 110275. [CrossRef]
23. Liu, Z. Study on the Preparation of Glass-Ceramic Coating And Its Corrosion Resistance in Liquid LBE. Master's Thesis, University of South China, Hengyang, China, 2014.
24. Tulyaganov, D.; Ribeiro, M.; Labrincha, J. Development of glass-ceramics by sintering and crystallization of fine powders of calci-um-magnesium-aluminosilicate glass. *Ceram. Int.* **2002**, *28*, 515–520. [CrossRef]
25. Faeghinia, A.; Zamanian, A. Wear behavior of BCS glass ceramic coating on stainless still slab. *Ceram. Int.* **2019**, *45*, 108–114. [CrossRef]
26. Li, Q.; Song, P.; Dong, Q.; Hua, C.; Deng, C.; Li, L.; Zheng, B.; Lu, J. Effect of partial crystallization of an amorphous layer on the mechanical properties of ceramic/metal-glass coating by thermal spraying. *Ceram. Int.* **2019**, *45*, 18803–18813. [CrossRef]
27. Xiao, Z.; Tan, F.; Wang, W.; Lu, H.; Cai, Y.; Qiu, X.; Chen, J.; Qiao, X. Oxidation protection of commercial-purity titanium by Na_2O-CaO-SiO_2 and Na_2O-CaO-Al_2O_3-SiO_2 glass-ceramic coatings. *Ceram. Int.* **2015**, *41*, 325–331. [CrossRef]
28. Zhao, F.; Fu, Q.; Wang, L.; He, S. Wavelike interfacial design and mechanical behaviour of joint between Si-SiC coated carbon/carbon composites and Li_2O-Al_2O_3-SiO_2 glass ceramics. *Ceram. Int.* **2018**, *44*, 5440–5446. [CrossRef]
29. Wang, J.; Vandeperre, L.; Stearn, R.; Clegg, W.J. Pores and cracking in ceramics. *J. Ceram. Process. Res.* **2001**, *2*, 27–30.
30. Jiang, K.; Xu, Y.; Deng, T.; Li, B.; Chen, W. Formation of closed pore structure in CaO-MgO-Al_2O_3-SiO_2 (CMAS) porous glass-ceramics via Fe_2O_3 modified foaming for thermal insulation. *J. Eur. Ceram. Soc.* **2023**, *43*, 1689–1697. [CrossRef]
31. Toya, T.; Tamura, Y.; Kameshima, Y.; Okada, K. Preparation and properties of CaO-MgO-Al_2O_3-SiO_2 glass-ceramics from kaolin clay refining waste (Kira) and dolomite. *Ceram. Int.* **2004**, *30*, 983–989. [CrossRef]
32. Peng, W. Research on CaO-MgO-Al_2O_3-SiO_2 Microcrystalline Glass. Master's Thesis, Hunan University, Changsha, China, 2020.

33. Yang, G. Study on Crystallization and Properties of CaO-MgO-Al_2O_3-SiO_2 Microcrystalline Glass. Master's Thesis, Zhejiang University, Hangzhou, China, 2012.
34. Wu, Z.Y.; Zhao, X.; Liu, Y.; Cai, Y.; Li, J.Y.; Chen, H.; Wan, Q.; Yang, D.; Tan, J.; Liu, H.D.; et al. Lead-bismuth eutectic (LBE) corrosion behavior of AlTiN coatings at 550 and 600 °C. *J. Nucl. Mater.* **2020**, *539*, 152280. [CrossRef]
35. Zhang, W.; Tang, R.; Yang, Z.B.; Liu, C.H.; Chang, H.; Yang, J.J.; Liao, J.L.; Yang, Y.Y.; Liu, N. Preparation; structure, and properties of high-entropy alloy multilayer coatings for nuclear fuel cladding: A case study of AlCrMoNbZr/(AlCrMoNbZr)N. *J. Nucl. Mater.* **2018**, *512*, 15–24. [CrossRef]

MDPI AG
Grosspeteranlage 5
4052 Basel
Switzerland
Tel.: +41 61 683 77 34

Coatings Editorial Office
E-mail: coatings@mdpi.com
www.mdpi.com/journal/coatings

Academic Open
Access Publishing

mdpi.com

ISBN 978-3-7258-4442-5